The Dissertation Committee for Kelli J. Silverstrim Certifies that this is the approved version of the following dissertation:

IMAGE OPTIMIZATION IN DIGITAL DENTAL RADIOGRAPHY

Committee:

Erich Schneider, Supervisor

Sheldon Landsberger

Steven Biegalski

Mark Deinert

Timothy Ritter

IMAGE OPTIMIZATION IN DIGITAL DENTAL RADIOGRAPHY

by

Kelli J. Silverstrim, B.S.; M.S.; M.S.E.

Dissertation

Presented to the Faculty of the Graduate School of

The University of Texas at Austin

in Partial Fulfillment

of the Requirements

for the Degree of

Doctor of Philosophy

The University of Texas at Austin

May 2014

Dedication

I dedicate this report to Jim, for his patience and unfailing support, and to my wonderful children Jacob and Jeni.

And

In loving memory of my father, Ronald E. Copeland, D.D.S.

Acknowledgements

I could not have completed this work without the assistance of several individuals. First, I would like to express my gratitude to my advisor and research committee chairman, Dr. Erich Schneider, for his supervision and guidance throughout the last several years.

I would also like to thank Dr. Sheldon Landsberger for helping me get started in the graduate program ten years ago. Thanks also to the rest of my research committee– Dr. Steven Biegalski, Dr. Mark Deinert, and Dr. Timothy Ritter.

My work couldn't have been completed without access to the equipment at The United States Air Force Academy Cadet Dental Clinic. I also would like to thank Dr. Jonathon Tucker for trusting me with San Antonio Military Medical Center equipment and Dr. William McDavid for the use of the contrast detail phantom.

Most importantly, I want to thank my husband, Jim. His unfailing encouragement and support have kept me motivated to see this project through to completion.

Image Optimization in Digital Dental Radiography

Kelli J. Silverstrim, Ph.D.

The University of Texas at Austin, 2014

Supervisor: Erich Schneider

When the United States Air Force completed a multi-million dollar transition to digital dental radiography in 2010 there was no quantitative method available for establishing the appropriate balance of image quality and radiation dose. The objective of this research was to devise a process to fill this need. Through computer simulation and clinical validation the effect of technical parameters on digital dental radiographic image quality was investigated and an optimization method was devised. The Monte Carlo N-Particle Extended (MCNPX) radiation transport code was used to model the DC Planmeca Intra and AC Gendex 770 dental intraoral radiographic units and a unique anthropomorphic phantom simulating dental bitewing anatomy. The Carestream 6100 RVG sensor signal response, noise response, dose rate dependence and reproducibility were determined experimentally, as were their uncertainties and the inter- and intra-radiographic unit variabilities. The experimental measurements were used to calibrate and scale the MCNPX generated data for the optimization analysis. The technical parameters modified in the simulation were peak kilovoltage, (50 through 90) and tube filtration (inherent, 0.1 mm and 0.2 mm added copper). The entrance air KERMA (~720 μGy) at the current clinical technique (63 kVp at 1 milliAmpere-seconds) was used to establish the reference image quality metrics for comparison. Four figures of merit (FOM) were chosen to encompass the impact of variations in the adjustable parameters.

With equal weighting of all FOMs and given no limitations on the equipment, the optimal combination of kVp and tube filtration for dental bitewing imaging identified was 90 kVp with 0.1 mm added copper filtration. The optimal technique in the radiographic units' operating range was 70 kVp and 0.1 mm added copper filtration, which could be immediately adopted for a ~50% (+/-17%) entrance dose and ~40% effective dose savings (Planmeca units). In general, the optimization method facilitates image quality standardization across different radiographic units and sensors in a dental clinic. The unique computer model and optimization method used could be easily customized to evaluate any adult or pediatric intraoral imaging task. The results underscore the importance of tailoring the technical parameters to the particular imaging devices in service.

Table of Contents

List of Tables

List of Figures

Chapter 1: Introduction and Motivation

The United States Air Force Dental Service recently completed a multi-million dollar deployment of digital imaging technology. The goal was to convert all Air Force dental clinics from a traditional film based imaging system to an entirely digital environment by the end of 2009. The project was completed in 2010 with an estimated cost of more than $25 million. To illustrate the impact of this transition, consider the volume of intraoral radiographic examinations completed in a typical year: 290,000 procedures resulting in more than one million images. Clearly, the proper implementation of this new technology is essential to ensure radiation exposure to the patient is kept to a minimum. At the same time, the full benefits of digital technology must be exploited through careful selection of processing parameters and radiographic technique.

Although digital technology is not new to dentistry-- published articles describing these systems began appearing as early as 1989 (Mouyen)-- widespread implementation has been limited. Brian and Williamson (2007) surveyed a random sample of dentists in Indiana. Of the respondents (51%), only 19.7% had transitioned to digital dentistry. What does this mean for the Air Force? With such a small percentage of clinicians using the new technology, there exists little if any guidance on how to test the systems in the field. At a minimum, a systematic approach is needed to optimize the image quality versus dose relationship for each digital sensor in use. Additionally, the multitude of image processing options available should be tested objectively to maximize the clinical utility of the images for the task at hand. What works well for an endodontist, for example, may not be appropriate for a general dentist. Quality control procedures aimed at ensuring system performance over time and detecting potential problems should also

be developed. In short, the procedures used for traditional dental imaging are not adequate to meet the current needs.

The challenges faced by the Air Force dental community are not unlike those experienced in the radiology community several years ago and continuing today. Digital technology deployment occurred long before standards were in place to test the equipment and optimize performance. Despite these systems being in clinical use throughout the U.S. Air Force for nearly ten years, it wasn't until 2006 that a final standard for testing computed radiography systems was published (American Association of Physicists in Medicine (AAPM) Task Group #93). In 2009, the AAPM published recommendations for standardizing the exposure indicator for digital radiography in an effort to provide technologists and radiologists a consistent means of monitoring image quality and radiographic techniques (AAPM Task Group #116). Historically, each vendor has maintained their own methodology and specifications making it virtually impossible to inter-compare systems. Widespread implementation of the standard has not yet been achieved and it does not address digital dental radiography. However, the methods used for general radiology may serve as a guide.

Several authors have reported techniques for image quality optimization. A number of these studies will be reviewed in an attempt to identify techniques that may be useful in digital dental imaging. Alternative approaches will also be explored.

The dose versus image quality optimization process must be approached in several steps. First, a method must be identified to optimize the technical components of the imaging chain. That is, the appropriate radiographic technique for the chosen digital sensors must be determined with consideration for patient radiation exposure. Careful characterization of the radiation source at each potential x-ray tube setting is essential to accomplish this goal. The x-ray source energy distribution, half-value layer, spatial

intensity distribution, and exposure must be measured. To determine the optimum technique, radiographic parameters such as peak tube kilovoltage, exposure time, total exposure, source to sensor distance, and beam filtration may be altered. The effect of these changes on the image will be assessed with a carefully chosen image quality test tool or phantom; the initial optimization process will be computer generated.

Once the optimum technique(s) is identified through simulation and mathematical optimization, the technical parameters must be clinically validated. A physical phantom will be imaged using the identified optimum technical factors and the resultant image will be scored using predetermined criteria.

The impact of the selected optimum technique on patient dose should also be assessed. The third step in the optimization process is then to determine patient dose through empirical measurements and compare these results against published data.

Proper implementation of all steps in this process is pivotal. The final step, optimizing the image processing through software manipulation of the image, cannot be fully realized without first verifying the basic components of the imaging chain are appropriately configured.

This work will attempt to implement new techniques in dental imaging research to address the first three steps in the optimization process. This author has not discovered any work undertaking the complete dental x-ray source characterization and phantom modeling with the Monte Carlo N-Particle Extended (MCNPX) radiation transport code. Further, a more rigorous mathematical approach to the optimization process will be attempted. Although quantitative optimization methods are being used in general radiology to some extent, published work to date describing such studies for digital dental sensors is lacking. Instead, sensor performance comparisons for a variety of image quality metrics is the norm. This work therefore augments past research by employing

mathematical optimization processes not used in any published dental imaging research to discern their potential value for imaging protocol design.

To begin, current methods employed in general radiology for optimization of the dose/image quality relationship will be reviewed in chapter 2 along with a summary of work describing digital dental sensor performance. Past work completed by this researcher in characterizing a generic radiographic tube will be reviewed as the foundation for a more thorough characterization of the dental tube in chapter 3. The current work and results will be described in chapters 4 through 6. Finally, the conclusions will be discussed in chapter 7. The ultimate goal of this research is to identify a standard set of technical parameters for general use throughout Air Force dental clinics, which will produce an adequate image with the lowest patient radiation burden.

Chapter 2: Literature Review

Before general approaches to image optimization are described, a review of the research specific to digital dental radiography will be accomplished. In general, the studies published can be categorized as either objective evaluations, describing the digital systems in terms of their physical characteristics, or subjective evaluations utilizing anthropomorphic phantoms or human subjects. It is not the goal of this researcher to define the physical attributes of the system under study but rather to devise a simple objective approach to image optimization. As such, the literature review to follow will focus on objective evaluations of image quality.

Implementing an image optimization strategy requires a fundamental knowledge of metrics used to describe an imaging system. This chapter will define image quality metrics as a prelude to the literature review. Geijer (2002) lists several methods by which radiographic system performance can be evaluated:

- A system can be described in terms of its inherent physical properties such as contrast and spatial resolution. The Modulation Transfer Function (MTF) quantifies the spatial resolution of a system. The Noise Power Spectrum (NPS) or Wiener Spectrum assesses the intensity and distribution of noise in an image while the Noise Equivalent Quanta (NEQ) describes the number of quanta needed to produce an image with a certain noise level (Workman and Brettle, 1997).
- The Detective Quantum Efficiency (DQE), which utilizes the system MTF, NPS, and photon fluence to determine the overall system efficiency,

is another important tool that can be used to describe the performance of digital systems and is also valuable for system intercomparisons.

- Over-all system performance can be assessed with a contrast-detail phantom by human observers.
- Anthropomorphic phantoms provide a subjective method to evaluate optimization efforts. Receiver Operator Characteristic (ROC) studies can be used to grade images based upon the observers ability to correctly identify predefined image attributes. The Visual grading analysis (VGA) (Månsson, 2000) method is another objective means to intercompare phantom images.
- Finally, human subject images can be used for the evaluation process also by means of a well-defined ROC or VGA study.

Before the past work is described, a brief review of the digital sensor technology adopted by the U.S. Air Force will be undertaken.

2.1 DIGITAL DENTAL SENSOR TECHNOLOGY

Intraoral digital images in dentistry are acquired through either direct or indirect image capture. Charge-coupled device (CCD) or complementary metal oxide semiconductor (CMOS) technologies have been the direct capture modes of choice for dental applications (Van der Stelt, 2005). CCD detectors utilize solid-state sensors to convert the x-ray photon energy striking the chip to an electrical signal. To increase detector efficiency, a scintillator layer is placed on top of the sensor. In dental detectors, the scintillator material is typically Cesium Iodide (CsI). CMOS is a similar image capture technology, differing from CCD chips in that the electronics controlling signal conversion are manufactured as part of the chip, making their assembly easier and

therefore cheaper. Van der Stelt indicates the image quality of both technologies is analogous. Direct capture sensors communicate directly with a PC via a long cable attached to the sensor. The sensors are quite rigid and can be difficult for some patients to tolerate.

Indirect sensors utilize a thin phosphor plate, similar in size to the traditional dental film. The plate is coated with a photo-stimulable phosphor (PSP) capable of storing x-ray energy. After the plate is exposed to radiation, it is scanned by a laser of the appropriate wavelength releasing the energy stored on the plate. The energy, released in the form of light, is detected by a photomultiplier tube, converted to an electrical signal, and displayed as a digital image. Barium fluorobromide doped with Europium is the most common phosphor used. One of the drawbacks to the phosphor plate system is the time required to process the plates after exposure. Typically, the scanning process takes up to two minutes for a series of plates—comparable to traditional film processing.

The Air Force dental community has selected Carestream Dental Systems RVG 6100 digital sensors (Figure 2-1) as the primary detector. The Carestream sensor utilizes CMOS technology with a CsI crystal. The Air Techniques, Inc. ScanX$^{(R)}$ PSP system was selected as a back-up for situations in which the tethered detector is not practical (Figure 2-2). For a more detailed analysis of digital imaging technology in general, Yaffe and Rowlands (1997) review the direct and indirect sensor systems on the market.

Figure 2-1. Carestream Dental Systems RVG 6100 Direct Capture Sensor
([Figure Source: http://mediaroom.carestreamdental.com/press-materials/image-galleries/digital-intraoral-sensors/rvg-6100)

Figure 2-2. Air Techniques, Inc. PSP System
(Figure Source: https://decs.nhgl.med.navy.mil/ALERTS/PSPAIRTECH.JPG)

2.2 OBJECTIVE IMAGE QUALITY EVALUATIONS

Several studies have been published describing the physical performance of digital dental sensors. A representative sample is included here to highlight the characteristics of sensor technology.

Farman, et al (1995) evaluated the physical properties of the Sens-A-Ray CCD detector. The Signal-to-Noise Ratio (SNR) and MTF of this system were measured along with system dark current. The system was found to produce a linear response to radiation with an overlying dark current signal, analogous to fog on radiographic film. The system contrast was greater than that of film but had lower latitude. An important finding was that the Sens-A-Ray system is so fast it may present problems when trying to select the appropriate exposure time since the appropriate exposure will require a time at the lower end of the settings available on most dental radiographic units.

Welander, et al (1994) compared the resolution of four digital intraoral sensors in terms of the modulation transfer function (MTF). While the authors concede the system MTF is not directly related to the clinical quality of the images they do recommend measurements of system resolution as a valid way to compare radiographic systems.

Wakoh, et al (1995) used low contrast detectability as a means of comparison between two digital sensors. The impact of exposure and added filtration on the perception of defects in an aluminum test object were measured. One observation discussed by the authors was the potential for using higher exposures than necessary with the digital systems as a result of their wide dynamic range.

In 1995, Welander, et al, measured the inherent physical properties of the Sens-A-Ray CCD system. The NPS, NEQ, and DQE were calculated to provide information suitable for comparing this system to other detectors.

Brettle (1996) completed an evaluation of the physical characteristics of the Digora PSP system. The MTF, NPS, and DQE of the Digora system were compared to Carestream Ektaspeed film and the author concluded comparable image quality could be achieved with the Digora system at exposures 80% less than that required for film imaging.

In 1997, Huda, et al, compared a PSP based digital dental imaging system to E speed radiographic film and concluded that the PSP system demonstrated higher low contrast detectability and could produce images with adequate contrast at lower doses than possible with the film used in the study. The limiting spatial resolution of the PSP system, however, was inferior to E speed film by a significant amount: 6.5 lp/mm for the PSP versus >20 lp/mm for E speed film.

Attaelmanan, Borg, and Gröndahl (1999) performed a comparative study of digital sensors. This study sought to determine whether a new generation of detectors showed a marked improvement in image quality over their predecessors. They measured contrast resolution, MTF, and signal-to-noise ratio (SNR), and observed a measurable improvement in performance in the newer detectors.

The technical properties of the Dixel CCD system were investigated by Yoshiura, et al (1999). They also measured the SNR, NPS, NEQ, and DQE and concluded the system was an adequate alternative to traditional radiography.

Borg, Attaelmanan, and Gröndahl (2000) performed another comparative study between two PSP systems. Once again, the contrast resolution, MTF, and SNR of the systems were measured and one system proved to be clearly superior when images were processed at default settings.

In 2000, Stamatakis, Welander, and McDavid measured the physical properties of the Digora PSP system. The MTF, NPS, and DQE of the system were measured and

compared to the work completed by other researchers. They concluded the system was suitable for intra-oral radiography but that studies including viewer performance were necessary to validate clinical performance.

Three CCD based systems and one PSP system were evaluated by Araki, Endo, and Okano (2000). System MTFs and exposure-response curves were determined for each. One system demonstrated the highest system resolution but the narrowest latitude. Conversely, another system tested showed a much wider latitude but lower system resolution. In conclusion, each digital sensor had unique properties, which could be used as a discriminator when selecting the appropriate system for a particular imaging task.

Attaelmanan, Borg, and Gröndahl performed a study in 2001 comparing the signal-to-noise ratio of six intraoral sensors and found that the SNR reaches a peak after which it will either remain constant or start to fall depending upon the system. The exposure level at which the peak SNR was achieved also varied among the sensors tested.

In a similar study, Couture (2003) measured the SNR of two systems and compared his results to those published in the study just described. His conclusions contradict those of Attaelmanan, Borg, and Gröndahl and he presented a potential problem with their methodology as the reason.

Farman and Farman (2005) presented a comparison of 18 different digital sensors. This work concisely described the detector specifications, measured spatial resolution, and practical exposure ranges of all 18 systems for rapid comparison and represents the most comprehensive review of the technology available at the time.

More recently, Hellén-Halme (2011) studied the diagnostic accuracy of observers evaluating digital images acquired at two peak kilovoltages. The author concluded the detection of approximal caries was the same for images acquired at 60 or 70 kVp using

the Schick CDR Wireless 2 sensor but added more research was needed to assess the sensor noise, contrast, and sensitivity responses at different energies.

These approaches are valuable for comparing sensor performance, describing the intrinsic detector properties and providing clinicians the information they need to make informed purchasing decisions. But a comprehensive optimization and implementation methodology is lacking. Over the last few years, several authors have published their approaches to this problem for general radiology. A review of representative techniques will be presented.

2.3 IMAGE OPTIMIZATION APPROACHES IN GENERAL RADIOLOGY

The medical use of radiation is governed by the ALARA (As Low As Reasonably Achievable) principle: keep radiation dose to the patient at a minimum to limit stochastic effects. With this in mind, the goal of image optimization is to adjust the radiographic technique, and thus patient exposure, to obtain the *required* diagnostic information, not the *best* image possible (Geijer, 2002). Different approaches to optimization have been proposed, but some basic steps apply to all:

- A reference set of radiographic parameters is identified (i.e., peak tube voltage, tube current, exposure time, added filtration, detector system, etc.)
- A phantom of some type is used to assess image quality of proposed alternative imaging system or proposed dose reducing technique
- An anthropomorphic phantom or human subjects are imaged to validate the proposed alternative technique for clinical studies

- The radiation burden is measured. Entrance dose, entrance surface dose, or organ dose can be measured and effective dose equivalent can be calculated for the reference and alternative technique
- The dose savings is determined for the proposed technique.

2.3.1 The Image Quality Figure and Visual Grading Analysis

Several authors describe a method to optimize radiographic procedures through use of a contrast-detail phantom. Geijer, et al (2001, 2002) and Jansson, et al (2006) used the CDRAD phantom, which consists of a 26.5 cm x 26.5 cm plexiglass plate one cm thick with 15 rows and 15 columns comprising an array of 225 squares. Each square contains two identical holes, one in the center and the other in an arbitrary corner. In each row the hole depth is increased logarithmically from 0.3 mm to 8.0 mm. In each column the hole diameter is increased logarithmically from 0.3 mm to 8.0 mm. Contrast changes are represented in the horizontal direction and spatial changes in the vertical (Thijssen, 1989). The phantom is sandwiched between Lucite slabs of varying thickness depending upon the imaging task the study is aimed at simulating. The phantom is exposed to a variety of radiographic techniques and then evaluated quantitatively to determine the Image Quality Figure (IQF) for each exposure, which is the sum of the products of the depth and diameter of the just visible holes (Thijssen):

$$IQF = \sum_{i=1}^{15} C_i x D_{i,th} \qquad \text{(Eq. 2-1)}$$

Where:

C_i=contrast (depth of hole)

$D_{i,th}$=threshold diameter in contrast column i

As defined, the radiographic technique producing the lowest IQF represents the best study.

In 2001, Geijer used this method to compare the performance of a flat-panel detector to a storage phosphor plate system and found the flat-panel detector could achieve equivalent image quality at half the dose required for the storage phosphor plate system.

Geijer (2002) also used this method to evaluate lower dose techniques for scoliosis radiography. A traditional screen-film, digital radiography, and digital fluoroscopy system were evaluated. The author identified a technique able to produce an acceptable image at 31% of the baseline dose.

Jansson used the same technique to determine a reduced exposure technique for intravenous urography procedures, performed to assess the functional and morphologic characteristics of the urinary tract. They were able to achieve a 70% reduction in dose with a flat panel detector over the technique used with a storage phosphor plate system.

Additional steps used by these authors included dose verification through Monte Carlo modeling, experimental measurement, or both, and subjective image quality studies using radiographic images of an anthropomorphic phantom or human subjects.

Visual grading analysis (VGA) was employed by both Geijer and Jansson to rank the clinical images in a more quantitative manner than typically used for a subjective comparison. An observer must compare a test image to a reference image and judge which is superior based on a set of established criteria. A score for all observers and all images is then tabulated (Jansson):

$$VGA\_score = \frac{\sum_{O=1}^{O}\sum_{I=1}^{I}\sum_{S=1}^{S} G_{o,i,s}}{OxIxS} \qquad \text{(Eq. 2-2)}$$

Where:

$G_{o,i,s}$=grading for the observer (o), image(i), and structure(s)

A positive VGA score indicates that the test system is superior to the reference system.

Hamer, et al (2004) described a similar procedure to optimize the image quality for chest radiography using a CsI amorphous silicon flat-panel detector. A 25 cm x 25 cm x 25 mm thick contrast detail phantom consisting of a 6 x 6 array of holes was devised. The holes varied in diameter from 0.05 cm to 2.0 cm across the rows and varied in depth from 0.05 to 1.0 cm across the columns. The phantom was placed between thicknesses of Lucite representing individuals of different body size from slim to large and exposed to a range of peak kilovoltages (kVps) with varying amounts of copper filtration in the beam. Human observers had to rank their confidence in detecting each hole in the phantom. Monte Carlo calculations were performed to determine the dose savings achieved with the techniques used and they found a tube voltage of 125 kVp with 0.3 mm added copper filtration allowed for a 33% reduction in patient dose without degrading image quality.

2.3.2 Defining a Figure of Merit (FOM)

Samei, et al (2005) describes an optimization method, which is suitable for any radiographic procedure. The authors first identify differences between traditional analog and digital imaging systems. One key trait of digital systems that differs from analog systems is the decoupling of image capture and image display. This feature makes it possible to optimize the radiographic technique without simultaneously affecting the contrast of the final displayed image. They identify three independent variables: kVp applied to the x-ray tube, patient exposure or dose (E), and added filtration, which can be

further categorized in terms of filter atomic number (Z) and filter thickness (t). Independent variables of the object imaged include tissue thickness, tissue type, lesion type, and lesion thickness. Because the contrast of the digital image can be modified, it can no longer be considered the chief image quality determinant. Instead, Samei defines a new quality metric, the signal-difference-to-noise ratio:

$$SdNR = \frac{|I_B - I_L|}{\sigma_B} \qquad \text{(Eq. 2-3)}$$

Where:

I_B=signal intensity of background

I_L=signal intensity of a lesion

σ_B=standard deviation of detector noise in the background

Given identical processing, the image with the highest SdNR may have improved image quality.

The Rose Model, first described by Dr. Albert Rose in the 1950s relates image contrast to the number of photons detected and the difference in detected photons between the target object and the background (Hasegawa, 1991):

$$C = \frac{\Delta N}{N}$$
$$Signal = \Delta N = CN \qquad \text{(Eq. 2-4)}$$

Where:
C=Contrast
N=Number of detected photons

Since the noise is the square root of the number of detected photons in systems exhibiting Poisson statistics, the signal-to-noise ratio can be described as:

$$k = \frac{Signal}{Noise} = \frac{CN}{\sqrt{N}} = C\sqrt{N} = C\sqrt{\Phi A} = C\sqrt{E} \qquad \text{(Eq. 2-5)}$$

with:

Φ=photon-fluence (photons/unit area)

A=Area imaged

E=Exposure

In other words, the image SdNR is proportional to the square root of the incident exposure. Given this relationship, the figure of merit (FOM) can be defined independent of exposure as:

$$FOM = \frac{SdNR^2}{E} \qquad \text{(Eq. 2-6)}$$

Establishing a FOM to demonstrate the effects of anatomical noise may also be used. For example, the ratio of lesion-to-bone contrast in chest radiography may help identify the radiographic technique that optimizes the lesion contrast in relation to bone. The authors suggest an additional FOM may need to account for the burden placed on the radiographic generator or the heat load of the x-ray tube:

$$nFOM = \frac{\eta_{opt} FOM_{opt}}{\eta_0 FOM_0} \qquad \text{(Eq. 2-7)}$$

Here,

η_{opt}=filter transmission for optimized technique

FOM_{opt}=FOM for optimized technique

η_0=filter transmission for non-optimized or current technique

$FOM_{0=}$FOM for non-optimized or current technique

The nFOM "represents the change in squared SNR after the addition of filtration while milliampere seconds (mAs) are constant (Dobbins, et al,2003, p. 229). In other words, the mAs would have to be increased by 1/nFOM with the filter in place to maintain the same SNR and this would result in a patient exposure of $\frac{\eta_{opt}}{\eta_0 nFOM}$. In conclusion the authors stated that the main purpose of image optimization is to *reduce patient dose without a resultant loss in image quality*, as mentioned previously. By selecting tissue mimicking phantoms specific to the imaging task, the $SdNR^2/E$ value can help achieve that goal.

This technique was used to optimize digital chest radiography where the authors concluded 120-130 kVp with a 0.2 mm copper filter was an optimum technique with a demonstrated 25% reduction in exposure over the non-optimized technique but 50% increase in tube burden. Their results for digital mammography showed a potential 60% reduction in Mean Glandular Dose (MGD) with a tungsten anode and rhodium filter compared to the traditional molybdenum anode/molybdenum filter used for screen/film imaging.

Dobbins et al, also demonstrated the utility of this method in optimizing the image quality for chest radiography using a CsI-amorphous silicon flat-panel detector. In addition to experimental measurements, however, the authors constructed a computer model of the imaging system in order to more efficiently study the effects of varying tube voltage, filter type, and filter thickness. The computer model was used to identify the combinations most likely to produce superior images before experimental measurement was commenced. The end points they selected to assess the quality were SdNR, reduced bone-to-lesion contrast and patient dose. They identified 120 kVp with 0.2 mm added copper filtration as the optimum radiographic technique, which resulted in a 25% dose

savings over the unfiltered technique currently used with this flat-panel detector system; results very close to those reported by Samei.

Williams, et al., (2008) used Samei's technique to optimize the exposure parameters for five commercially available full field digital mammography systems and identified the target/filter combinations, and peak tube voltage resulting in the highest FOM for different breast compositions as defined by:

$$FOM = \frac{SNR^2}{MGD} \qquad \text{(Eq. 2-8)}$$

Where:

MGD= mean breast glandular dose

Another interesting finding of this study was identification of alternative optimal techniques than those proposed by the equipment manufacturers. This provides an opportunity for users to modify their current protocols, in cooperation with equipment service engineers, for improved image quality.

2.3.3 Mathematical Optimization Models

An alternative approach to image optimization not seen in the published dental or general radiology research may be possible using a mathematical algorithm to identify maximum system performance. Simulated annealing is a method used to improve the outcome of a system in which the optimum is approached through a series of trades drawing incrementally closer to the global optimum. The method is based on this simple expression (Carr, 2009):

$$e^{-\Delta D/T} > R(0,1) \qquad \text{(Eq. 2-9)}$$

Where:

D= a cost function

ΔD=a change in the cost function

T=system temperature

R=a random number between 0 and 1

The expression $e^{-\Delta D/T}$ is analogous to the Boltzmann factor used to describe thermodynamic systems. Once an initial state is defined, the system is modified while holding the temperature constant. If the change in the cost function is negative the new arrangement is accepted. If the change is positive, the new arrangement is accepted given a probability determined by the Boltzmann factor. This process is repeated many times until an equilibrium state is reached where T approaches zero.

A classic example illustrating the utility of this technique is the "traveling salesman" problem. Simulated annealing can be used to determine the minimum travel distance between multiple locations for a salesman, thus maximizing the traveler's efficiency and minimizing travel costs.

The harmony search method, which has been used for structural design, vehicle routing, and water distribution design mimics musical improvisation. Zong, et al, (2005) describes how the harmony search method can be used to solve optimization problems. A function variable is analogous to a musician where the range of the musical instrument the musician plays corresponds to the range of values the variable can take. To optimize the function, a solution is tried. If the solution vector is superior to the existing vector it is chosen. This process mimics the method by which musicians will keep a new harmony if it sounds superior to an existing combination of musical notes. The function can continue to be improved iteratively in the same way musicians continually improve their harmony through practice.

A simpler optimization routine may be all that is required for this research project. The steepest descent method, for example, could be applied to find the optimum of a

simple linear function through a stepwise orthogonal search. This procedure is best used when the general location of the optimum point is known (Freund, 2004)

Given a set of well defined image optimization criteria, it may be possible to describe a function defining their relationship. A search algorithm like one described above could then be used to rapidly identify the global optimum.

2.3.4 Dissertations Focused on Image Quality Studies

Recently published doctoral dissertations have focused on studying the image quality and dose relationship.

The objective of Pitcher's work (2004) was to adapt the traditional metrics for assessing the physical performance of imaging systems for use in determining an image quality metric. He hoped to devise a quantitative method of assessing image quality that could be used to optimize the radiographic technique for pediatric computed radiography examinations without the need for time consuming subjective image quality studies using human observers.

The MTF, NPS, and DQE were modified to account for clinical noise added by simulated patient phantoms. New metrics identified as clinical noise power spectrum (NPS_c), clinical modulation transfer function (MTF_c), clinical detective quantum efficiency (DQE_c), and clinical contrast detail score (CDS_c) were calculated and compared to the subjective evaluation of radiographic images of an anthropomorphic pediatric patient. He also devised a computer algorithm for use in identifying the threshold CNR in a phantom with objects of variable size. Pitcher concluded that while these metrics were capable of discriminating between small changes in radiographic technique, because the digital images could be manipulated, a "broad" indicator of image quality could not be determined. However, the threshold CNR proved useful in that its

value was nearly independent of exposure and therefore the minimum CNR required for an object of a particular size to be visible within a clinical image was identified.

Jones (2006) stated the objectives of his work were to: identify and test an appropriate dosimeter for use in a patient simulating phantom, construct a physical newborn phantom integrated with a real-time dosimetry system, develop a means to quantify image quality–in particular, low-contrast detectability in computed tomography (CT)–and use these tools to determine low dose protocols in CT. A computational model of the imaging system to include phantom was also devised using MCNP for depth-dose comparisons. Jones utilized the hybrid software developed by Pitcher to score contrast-detail phantom images acquired using a commercially available CT phantom and once the radiographic technique needed to produce an acceptable CNR was determined, the patient radiation burden of the reduced dose technique was determined.

Like Dobbins, Ullman (2008) also modeled the imaging system. Using Monte Carlo methods, he devised a model of the x-ray tube, patient, image receptor and observer. Two model observers were used in this work ; the "Ideal" observer and the Laguerre-Gauss Hotelling observer concept. The figures of merit selected to grade the physical image quality were nodule-to-bone contrast as described by Samei and Dobbins, and relative contrast. He also described a figure of merit for a VGA study and for the ideal observer. The author found the FOMs determined from the model correlated satisfactorily with measurements made by human observers using ROC and VGA methods, therefore validating the utility of the model for evaluating the effectiveness of image optimization campaigns.

Chapter 3: Past Work

Clearly, both experimental measurements and computer modeling were needed for this project. Prior work by this researcher provided the requisite background in the experimental techniques and methodology required to model the imaging system. A review of work completed modeling a generic radiographic tube along with recent work performed to characterize the dental radiographic tube output will be presented in this chapter.

The objective of the initial project was to create a computer model to simulate x-ray production from a standard radiographic tube. A generic x-ray spectrum file was generated for a 75kVp, 10% voltage ripple and 12^{o} anode angle x-ray source using the *Catalogue of Diagnostic X-ray Spectra and Other Data* spectrum generator (Cranley, et al, 1997) published by the Institute of Physics and Engineering in Medicine (IPEM). This spectrum was utilized to characterize the source with MCNPX. Using a simple geometric model, a photon fluence tally was acquired. From this tally, the radiation exposure was calculated and compared to the calculated IPEM exposure and measured data.

The experimental technique used to acquire radiographic exposure data will be detailed in this chapter along with the computer modeling methodology. A brief description of the MCNPX code will also be given.

3.1 EXPERIMENTAL MEASUREMENTS

3.1.1 Apparatus

A Radcal 9095 (serial number 95-9160) was used with a Radcal model 10X5-6 ionization chamber, (serial number 14169) to measure radiation exposure generated by the source. The ion chamber has a 6 cm^3 active volume and a polycarbonate electrode and walls with a conductive graphite interior coating. The published accuracy for this chamber is +/-4% using x-rays at 60 kVp and 2.8 mm aluminum half-value layer (Radcal, 2004). The theory and operation of ion chambers is well described in the literature (Knoll, 2000).

3.1.2 Source Characterization

Six General Electric Medical Systems (GEMS) radiographic units were used as a radiation source. The x-ray generator for all systems was three-phase with a +/-10% voltage ripple. All radiographic units employed a Maxiray^{TM} 100 X-ray tube, (Serial numbers 6476BI6, 6805BI6, 3705BI5, 3411BI5, S/N for two units not available) with a 100 millimeter diameter rotating polyrhenium anode, 12.5^o target angle and 1.25 millimeter large focal spot (General Electric, 1990). The x-ray source can be approximated as an isotropic point source (Demarco, Sohlberg, and Smathers, 1998) with an energy distribution and total fluence dependent on initial kVp and the product of filament current and time (mAs). The beam spectra will be described in more detail below.

3.1.3 Half-Value Layer Measurement

A 75 kVp beam was selected for testing the MCNPX model because this is a clinically relevant value. The beam quality in terms of the first half-value layer was needed for generating the appropriate spectra and was measured as follows (Figure 3-1):

1. The ion chamber was positioned at a distance of 66 cm from the tightly collimated x-ray source. A mAs value was selected adequate to produce an initial exposure (E_o) of at least 500 milliRoentgens (mR).

2. Aluminum was inserted in increments of 1 millimeter between the source and detector followed by serial exposure measurements until a value of less than $E_o/2$ was achieved.

3. The beam half-value layer was then logarithmically interpolated using the expression (American College of Radiology, 1999):

$$HVL = \frac{t_b \ln(2E_{a/}E_o) - t_a \ln(2E_b / E_o)}{\ln(E_a / E_b)} \qquad \text{(Eq. 3-1)}$$

Where:

t_a=The thickness of aluminum used to achieve an exposure just greater than $E_o/2$

t_b=The thickness of aluminum used to achieve an exposure just less than $E_0/2$

E_a=The exposure closest to but greater than $E_o/2$

E_b=The exposure closest to but less than $E_o/2$

The half-value layer at 75 kVp was measured on one system (General Electric Medical Systems Model XR/d, serial number 11069BC3) but the variance in half-value layer measurements among all units tested was also investigated using historical data acquired during yearly radiographic unit performance assessments.

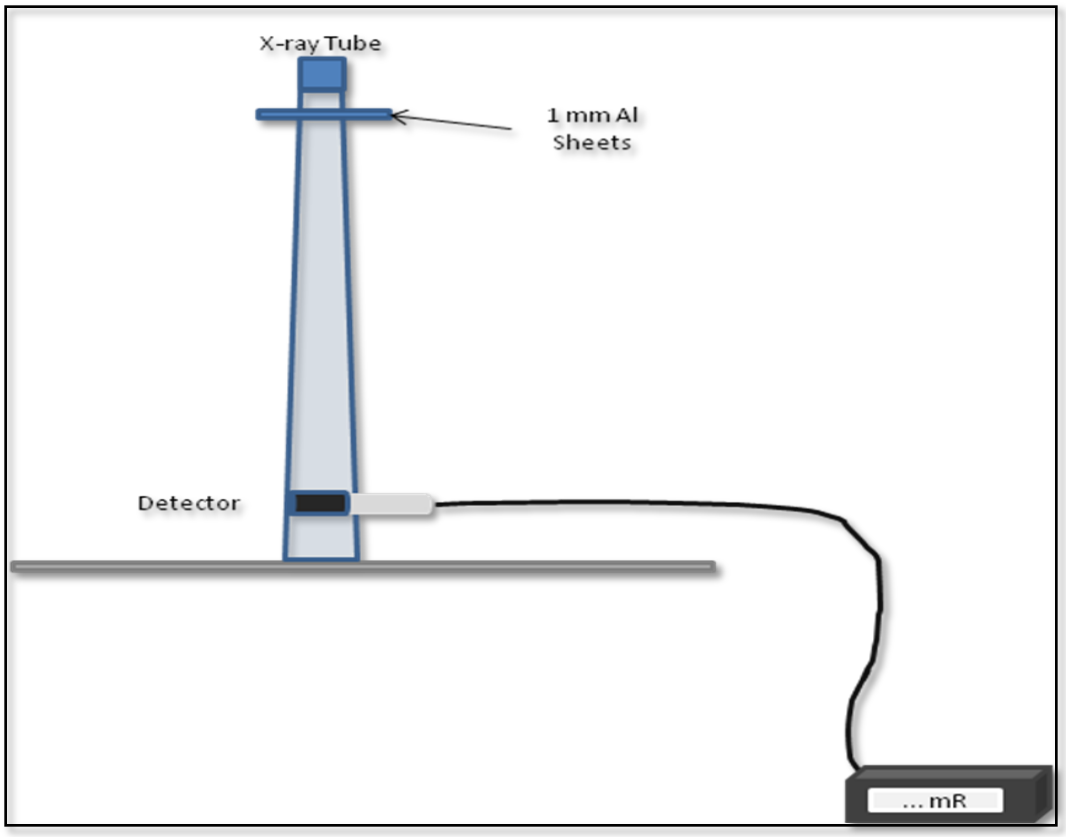

Figure 3-1. Half-Value Layer Measurements

3.1.4 Exposure Measurements

Exposure measurements were needed using a clinically relevant mAs value to provide relevant experimental data for comparison to the modeled data.

1. The detector was positioned a distance of 750 mm from the source (the reason for this distance will be given in the next section)
2. A series of five exposure measurements were recorded using 75 kVp and 25 mAs to assess the reproducibility of the x-ray unit.
3. Measurements were acquired on each of the six radiographic units to determine the degree of variation in tube output among the x-ray systems.

3.2. COMPUTER MODEL

Designing the computer model was a two step process. First, the x-ray energy distribution of the source was determined. Subsequently an MCNPX model was created to simulate the radiation transport.

3.2.1 Theory

The MCNPX code was initially developed for researchers interested in particles of the "intermediate energy" range at Los Alamos National Laboratory but it can now "track nearly all particles at nearly all energies" (Pelowitz (ed.), 2005). It has been used for accelerator shield design projects, cosmochemistry research, and medical physics applications (Waters et al, 2007). Ljungberg (1998) suggests that the powerful geometry tool and extensive variance reduction techniques available in MCNPX make it ideally suited for medical physics problem solving. A more detailed history of the code along with instructions for its use can be found in the user's manuals (Pelowitz (ed.), 2005; Hendricks, et al, 2006). MCNPX version 26c (2006) was used for this project.

3.2.2. Determination of X-Ray Energy Distribution

Consultation with GEMS engineers confirmed the x-ray source energy distribution was not available for the Maxiray^{TM} tube. The IPEM software was used to generate the spectra. The interactive tool generates spectra given a set of user selectable parameters. The following tube configuration was selected, matching as closely as possible the Maxiray^{TM} tube specifications:

- Target Material: Tungsten
- Tube Voltage: 75 kVp
- Anode Angle: 12^{o} (half degree increments cannot be selected)
- Voltage Ripple: 10%

- Attenuation Material: 3.29 mm aluminum (selected through an iterative process to match the IPEM modeled half-value layer calculated as part of the output file to the *measured* half-value layer of the beam). See Figure 3-2 for further explanation.

The percent difference between the IPEM generated HVL and the measured HVL was <0.05%.

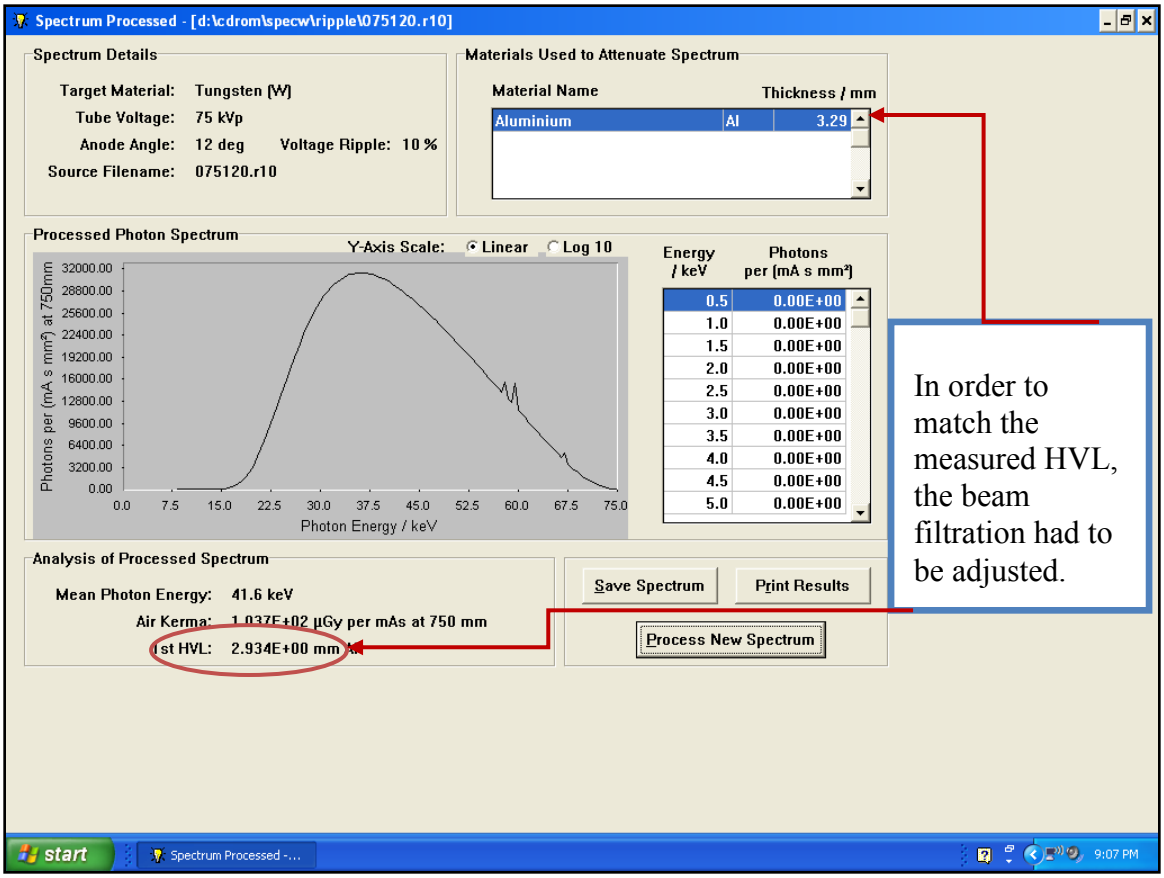

Figure 3-2. IPEM Software Generated Spectrum

Additionally, air could have been included as a beam attenuator. However, a comparison between the spectra generated with aluminum and air versus aluminum alone showed good agreement (Figure 3-3).

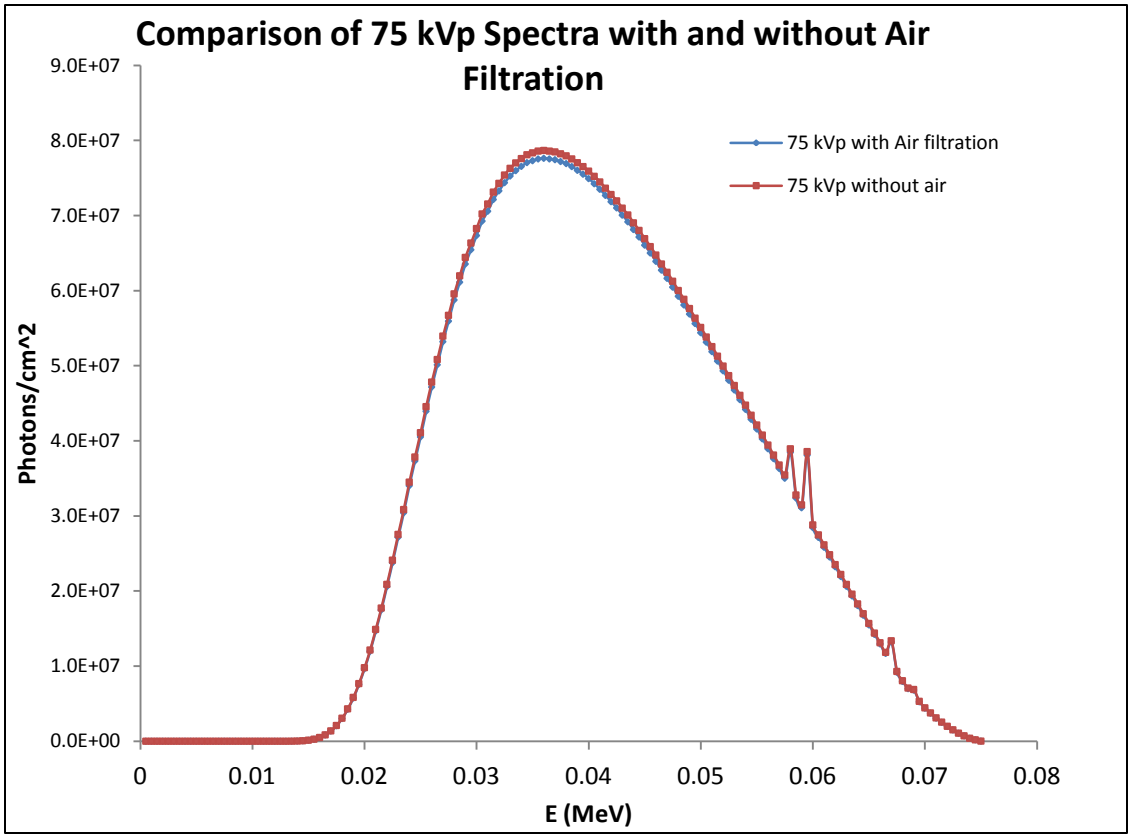

Figure 3-3. Spectra Generated With and Without Air Attenuation

The output file presents the energy distribution in 0.5 keV increments in terms of photons/milliAmpere-seconds/mm^2 at a distance of 750 mm from the source.

3.2.3. MCNPX Model

Once the spectrum file was generated, the data was used to characterize the source for the MCNPX model. First, the photon tallies per energy bin were multiplied by 25

mAs (the value used for the experimental measurements) and divided by the surface area of a 750 mm radius sphere. The photons per energy bin were then summed to determine the total number of source photons. Since the fractional energy distribution was required for the MCNPX input file, the photons per energy increment were then divided by that sum. These values were used to create the source energy distribution card. See **Appendix A** for data generated with the IPEM software and the energy distribution used for MCNPX.

A very simple geometric model was developed to simulate the collimated x-ray source (Figure 3-4). A surface 750 mm from the source was created to provide a location for the photon fluence tally to match the IPEM calculation distance. The cell had a void fill; since the IPEM spectrum was generated post filtration, this was felt to be the best simulation condition. The size of the trapezoid at 750 mm was arbitrarily selected to match a clinically relevant field size (15.5 cm x 34.4 cm; selected to match field size used for scoliosis examinations).

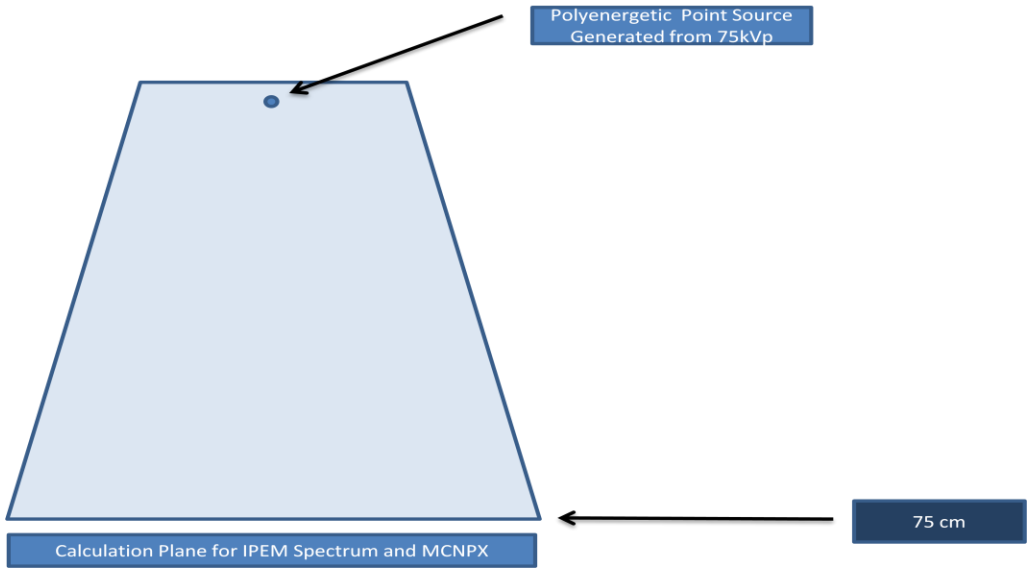

Figure 3-4. MCNPX Geometry for Test Model

The MCNPX input file is given in **Appendix B**. For this initial model, the code was run until the variance per energy bin was below 0.01% (i.e., number of particles started not defined).

Results of the experimental measurements as well as the data generated with the MCNPX model are presented below.

3.3. EXPERIMENTAL MEASUREMENTS

The half-value layer data collected is given in Table 3-1 and 3-2.

Table 3-1. Half-Value Layer Measurements

Half-Value Layer	
kVp:	75
mm Al	**mR**
0.0	615.2
1.0	466.0
2.0	371.1
3.0	303.5
4.0	
5.0	
6.0	
E_o :	613.8
1/2 E_o :	307.6
E_a	371.1
E_b	303.5
t_a	2.0
t_b	3.0
HVL [mm]:	**2.933**

Historical half-value layer data (at 80 kVp) for all units is presented in Table 3-2 below.

Table 3-2. Half-Value Layer Data at 80 kVp

UNIT	HVL (mm Al)
1	3.31
2	2.98
3	3.11
4	3.06
5	2.76
6	2.82
AVERAGE:	3.01
σ:	0.20
σ_{ran}:	0.08

Where the half-value layer is calculated as above and:

σ =standard deviation of independent half-value layer measurements

$\sigma_{ran} = \sigma / \sqrt{N}$ (N=Number of independent measurements)

Exposure data is presented in Figure 3-5 and Table 3-3. The average exposure among all units ranged from 242.6 milliRoentgens (mR) to 323.7 mR (σ_E=29.8 mR). Inter and intra-unit exposure variability is given as well as a determination of measurement error.

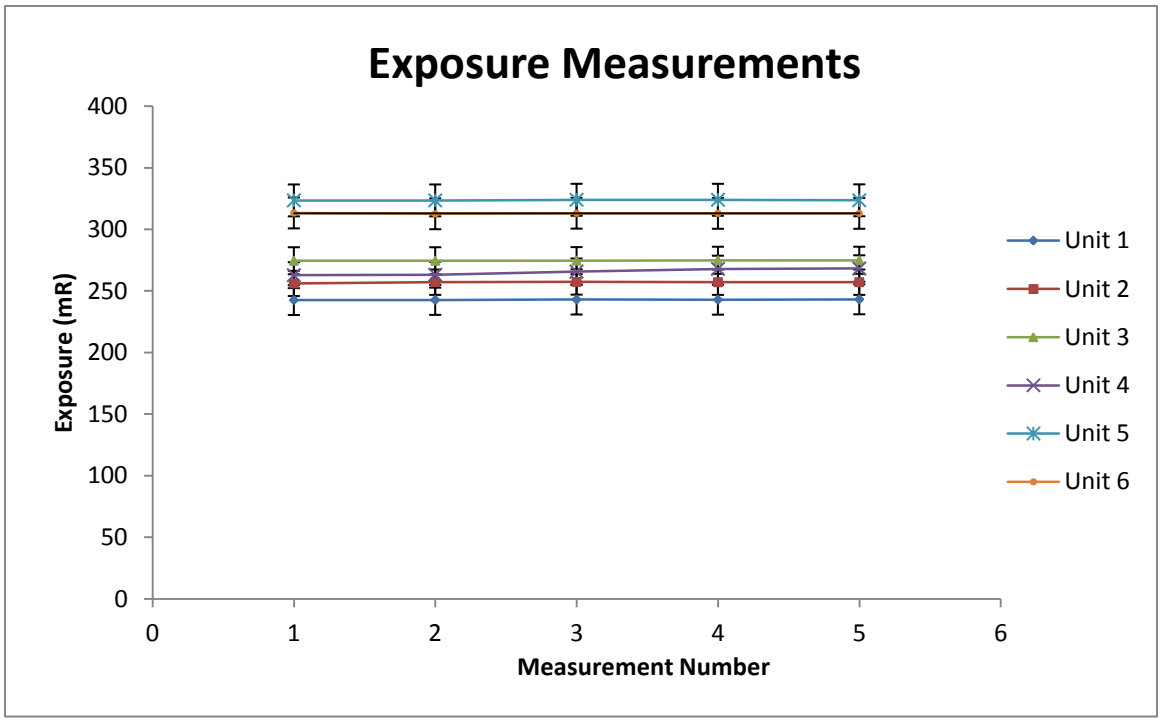

Figure 3-5. Exposure Measurements for Six Independent X-Ray Units

Table 3-3. Exposure Measurements

E (mR)	1	2	3	4	5	6
1	242.6	256.1	274.5	262.8	323.5	313.3
2	242.7	257.1	274.5	263.2	323.5	312.6
3	243.0	257.3	274.6	265.7	324.0	313.1
4	242.9	257.1	274.9	267.9	324.0	313.0
5	243.2	257.1	274.9	268.2	323.6	313.0
$\bar{E}$ **:**	242.9	256.9	274.7	265.6	323.7	313.0
σ_E**:**	0.2387	0.4775	0.2049	2.5324	0.2588	0.2550
$\sigma_{E(sys)}$**:**	9.715	10.28	10.99	10.62	12.95	12.52
$\sigma_{E(TOTAL)}$**:**	**9.72**	**10.28**	**10.99**	**10.63**	**12.95**	**12.52**
$\%\sigma_{E(TOTAL)}$**:**	4.00	4.00	4.00	4.00	4.00	4.00

Where:

σ_E=standard deviation of independent exposure measurements

$\sigma_{E(sys)}$=4% detector measurement uncertainty = $\bar{E} * 0.04$

$\sigma_{E(TOTAL)} = \sqrt{(\sigma_{E(ran)})^2 + (\sigma_{E(sys)})^2}$

$\sigma_{E(random)} = \sigma_E / \sqrt{N}$ (N=Number of independent measurements)

$\%\sigma_{E(Total)} = \sigma_{E(Total)} / \bar{E}$

Average Among all Units:	279.5		
σ_E **among all units:**	29.8		
$\sigma_{E(sys)}$ **among all units:**	11.2		
$\sigma_{E(TOTAL)}$ **among all units:**	**11.2**		
$\%\sigma_{E(TOTAL)}$**:**	4.02		
Range :	242.6	*to*	324.0
Outside Range (+/-4%):	**232.9**		**337.0**

3.4 COMPUTER MODEL

3.4.1 Comparison of IPEM Spectra and MCNPX Spectra at 750 mm from the Source

The number of particles started for the MCNPX run had to be scaled to match the IPEM spectra at 750 mm from the source. In total, 3.45×10^{14} particles were required to generate the photon fluence for the clinical parameters selected: 75 kVp and 25 mAs.

In general, where the number of source particles is defined in the MCNPX input deck, the flux tally will be reported in photon weight per energy bin per source particle. The back calculation will then be performed by multiplying the weighted photon strength by the total number of source particles. In this example, the calculation would be performed as follows:

$$Photons/cm^2 = \left(Photon\_strength\_per\_source\_particle\right) * Total\#\_Source\_Particles$$
$$Photons/cm^2 = (Photon\_strength\_per\_source\_particle) * 3.45x10^{14}$$

The entire data set and percent difference per energy bin between IPEM and MCNPX is shown in **Appendix C.**

3.4.2. Calculated Exposure vs. Measured Exposure

The exposure for a heterogeneous photon beam can be calculated as (Shultis and Faw, 2000):

$$X = \int_E dE \Re_X(E) \Phi(E) \qquad \text{(Eq. 3-2)}$$

Where:

$\Re_X$ = Exposure Response Function

$\Phi(E)$ = Photon flux (photons/cm^2) at energy E (MeV)

For this case, where discrete energies were used, the integral reduces to a simple summation:

$$X = \sum_{i=1}^{n} \Re_X(E_n) * \Phi(E_n) \qquad \text{(Eq. 3-3)}$$

To calculate the exposure in Roentgens (R), the following exposure response function is used (Shultis and Faw):

$$\Re_\chi(E) = 1.835x10^{-8} E\left(\frac{\mu_{en}(E)}{\rho}\right)_{air} \text{ (R-cm}^2\text{)} \qquad \text{(Eq. 3-4)}$$

Where:

μ_{en}/ρ = Mass Energy Absorption Coefficient for Air, Dry (Near Sea Level) (cm^2/g)

E = Energy (MeV)

$1.835x10^{-8}$= conversion factor in units of $\frac{R \cdot g}{MeV}$ roughly calculated as:

$$\frac{1.602x10^{-13} J}{MeV} * \frac{1g}{10^{-3} kg} * \frac{C/kg}{34 J/kg} * \frac{1R}{2.58x10^{-4} C/kg} \cong \frac{1.83x10^{-8} R \cdot g}{MeV}$$

The exposure in mR (10^{-3}R) for both the IPEM and MCNPX modeled x-ray fluence data was calculated using values for the mass energy absorption coefficient obtained from the National Institute of Standards and Technology (Hubbell and Seltzer, 1996). See **Appendix D** for the complete data set.

3.5 RESULTS

3.5.1. Half-Value Layer Measurements

As seen by the data in Table 3-2, the half-value layer of radiographic tubes can vary from one unit to another. The HVL thickness should be inversely proportional to

the x-ray tube output. Increased total tube filtration results in selective absorption of the low energy photons. This in turn increases the average photon energy and thus the beam HVL but also decreases the tube output resulting in a lower exposure. A plot of the HVL versus output for the six units used in this study (Figure 3-6) does demonstrate a correlation (R^2 = 0.804) although other factors appear to be influencing the output. Equipment age and generator design are probably the two leading reasons the relationship between HVL and output is not stronger. Data collection variations may also have contributed to the discrepancy.

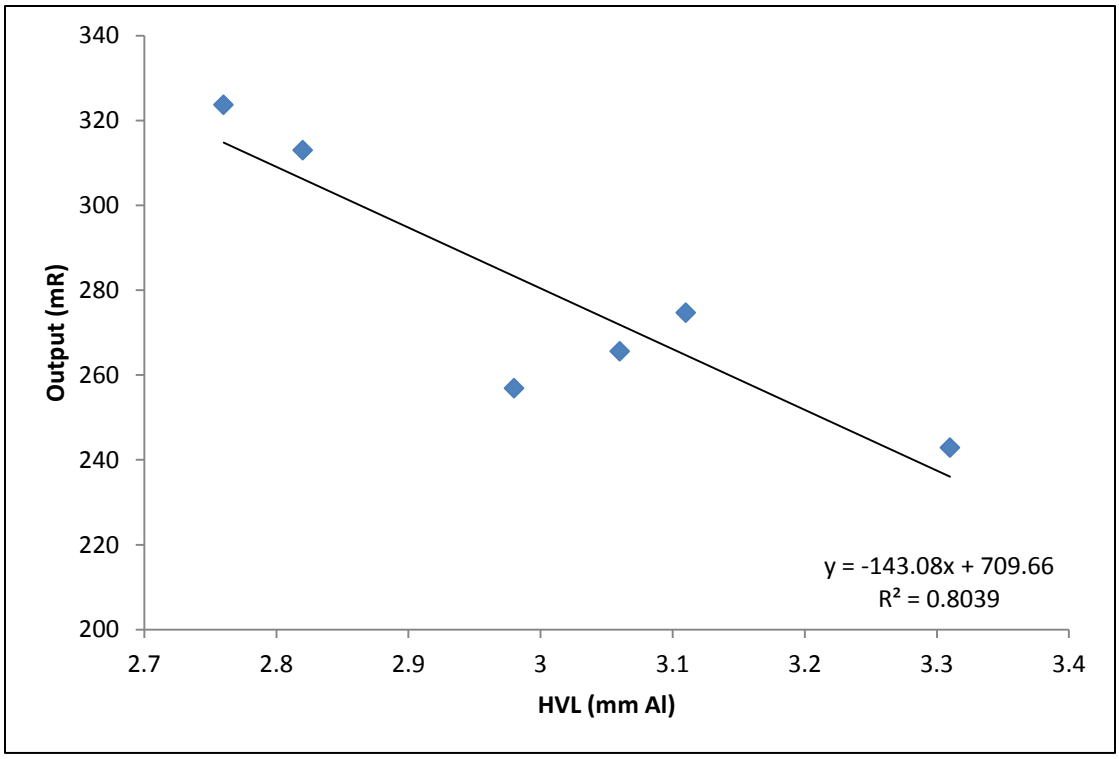

Figure 3-6. X-Ray Unit Output versus Measured Half-Value Layer

3.5.2. Exposure Measurements

Clearly, the output of a given model x-ray tube varies widely among x-ray units, even of the same make, model, and approximate age. In other words, tube-to-tube variations can lead to significant errors in dose estimates. The percent difference among the measurements was (taking into account the measurement uncertainty of the radiation detector):

$$\%Difference = \left(\frac{Max - Min}{Max} \right) * 100$$

$$\%Difference = \left(\frac{337.0 - 232.9}{337.0} \right) * 100$$

$$\%Difference = 30.9\%$$

This value far exceeds the measurement uncertainty of the radiation detector and must be taken into account when comparing modeled data to expected values. Exposure and consequently patient dose can be expected to vary clinically by as much as 30% for a given radiographic procedure. This high degree of exposure variability has an impact on the requirements for the precision of the modeled data since the uncertainty associated with the model must be small in comparison to the measurement uncertainty. In this case, small compared to 30% does not place very rigorous demands on the model.

3.5.3. Comparison of MCNPX Fluence vs. IPEM Generated Fluence at 750 mm

Given the simplicity of the MCNPX model, it was found to be in good agreement with the IPEM data (Table 3-4):

Table 3-4. Fluence Comparison

Fluence Comparison		
	Photons/cm^2	**% Difference**
MCNPX (scaled):	4.88x10^9	**-2.02**
IPEM Spectrum Generator:	4.89x10^9	

This is demonstrated quite well graphically (Figure 3-7):

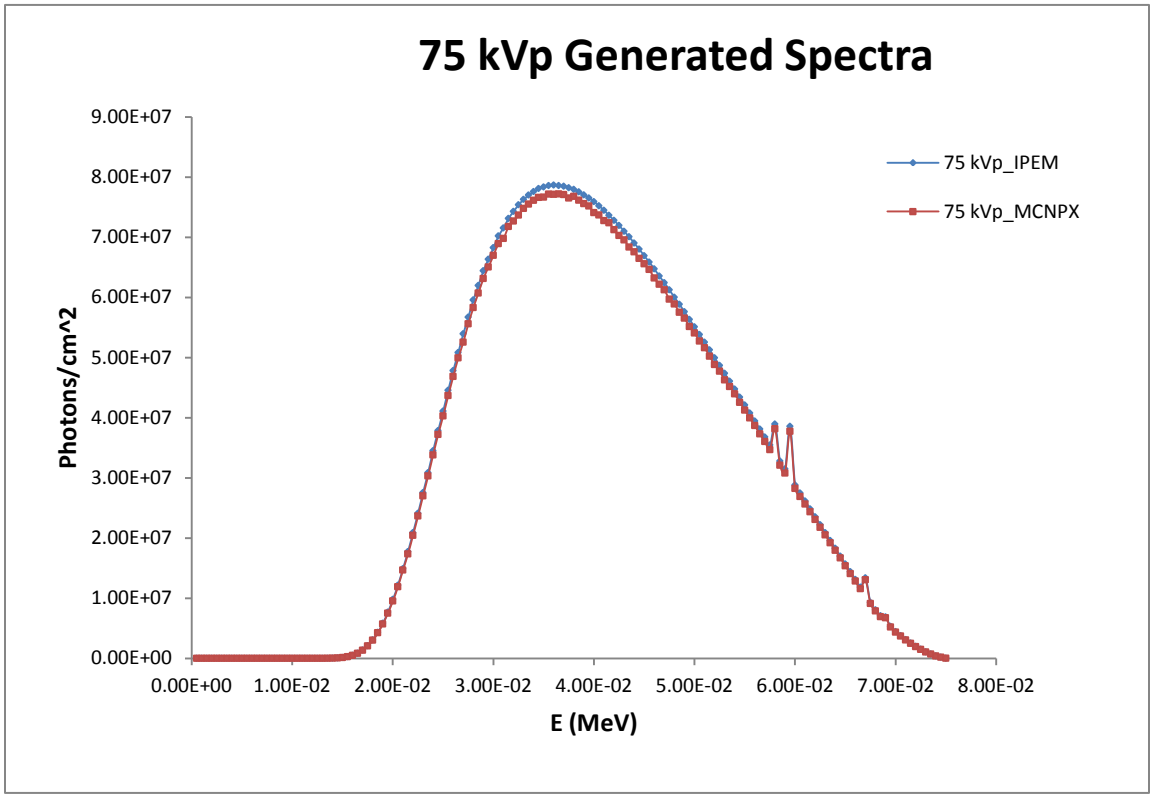

Figure 3-7. Modeled Spectra

3.5.4. Comparison of Measured Exposure to Calculated Exposure

The exposure calculated at 750 mm from the source with both the IPEM and MCNPX data falls well within the range of measured values. It is felt that the generic MCNPX model provides a reasonable representation of a radiographic tube and has

adequately estimated radiation exposure at the tested distance and energy distribution (Table 3-5).

Table 3-5. Calculated versus. Measured Exposure

Calculated vs. Measured Exposure					
	E (mR)		**% Difference**		
Measured Range:	232.9	337.0			
MCNPX:	321.7		**38.12**	*to*	**-4.534**
IPEM Spectrum Generator:	328.3		**40.95**	*to*	**-2.582**

However, some of the statistical checks did not pass (Table 3-6):

Table 3-6. MCNPX Statistical Checks

Results of 10 statistical checks for the estimated answer for the tally fluctuation chart (tfc) bin of tally 2										
tfc bin	--mean--	------	---relative error-----		-------variance of the variance----			--figure of merit--		-pdf-
behavior	behavior	value	decrease	decrease rate	value	decrease	decrease rate	value	behavior	slope
desired	random	<0.10	yes	1/sqrt(nps)	<0.10	yes	1/nps	constant	random	>3.00
observed	decrease	0.00	yes	yes	0.00	yes	yes	constant	decrease	10.00
passed?	**no**	yes	yes	yes	yes	yes	yes	yes	**no**	yes

This problem was easily resolved by increasing the width of the energy bins at the very lowest and highest energy ranges (eliminating the energy bins below 6.5 keV and combining the energy bins between 73.5 and 75 keV). The results of the second MCNPX tally are given in Table 3-7. The run was terminated after 65.51 minutes (1.08×10^9 particles started).

Table 3-7. MCNPX Statistical Checks (Energy Bin Modification)

Results of 10 statistical checks for the estimated answer for the tally fluctuation chart (tfc) bin of tally 2										
tfc bin	--mean--	---------relative error------			------variance of the variance----			--figure of merit--		-pdf-
behavior	behavior	value	decrease	decrease rate	value	decrease	decrease rate	value	behavior	slope
desired	random	<0.10	yes	1/sqrt(nps)	<0.10	yes	1/nps	constant	random	>3.00
observed	random	0.00	yes	yes	0.00	yes	yes	constant	random	10.00
passed?	yes	yes	yes	yes	yes	yes	yes	yes	yes	yes

3.6. MODELING THE DENTAL RADIOGRAPHIC TUBE

For the purposes of this work, a more specific model relevant to dental radiography was needed. A survey of the Air Force dental radiographic unit inventory (Warren, USAF Dental Evaluation and Consultation Service, Great Lakes Naval Station, personal communication, 2008) confirmed over 50% of the intraoral systems in use are direct current (DC) and the remaining systems are older single-phase alternating current (AC) units. The Planmeca Prostyle Intra was selected as a representative DC unit while the Gendex 770 system was used to model the AC systems.

System specifications are listed in Table 3-8 (ECRI, 2002).

Table 3-8. Intraoral Radiographic Unit Specifications

Specification	***Planmeca Prostyle Intra***	***Gendex 770***
Generator	Constant Potential, microprocessor controlled	AC Half-Wave Rectified
Focal Spot Size	0.7 mm	0.6 mm
kV Range	50-70	70
mA Range	2-8	7
Minimum Total Filtration	2.0 mm Al	1.5 mm Al

The IPEM spectral data used to define the energy distribution for a general radiographic tube does not provide enough flexibility to adequately describe the dental units. Specifically, the spectrum analyzer cannot generate data for half-wave rectified

tubes for which the voltage ripple is 100%. Therefore, another method to acquire this information is necessary. The solution will be described in section 4.1.1.

3.6.1. Determining Intensity Variations Across X-Ray Field

Another characteristic of the x-ray field that was ignored for the original MCNPX model is the intensity variation across the irradiated field. Because of x-ray tube design features, a portion of the radiation emitted from the target is self attenuated by the anode. The anode-heel effect is more pronounced at shorter distances from the source. Experimental measurements performed by this researcher showed the radiation intensity was reduced by over 50% under the anode relative to the central axis at 75 cm for the Maxiray^{TM} 100 x-ray tube. Even at the maximum clinically useful distance (182.8 cm—72 inches) the anode heel effect was still significant, resulting in greater than 25% reduction in beam intensity on the anode side of the tube. The intensity variation perpendicular to the anode cathode axis was minimal (less than +/- 15%).

It was assumed that the dental x-ray tube intensity distribution would also be impacted by the anode-heel effect. To measure the magnitude of the effect, radiographs were obtained using Carestream Portal Pack Localization film aligned parallel to the end of the dental cone approximately 5.5 cm from the cone tip (to represent a clinically relevant source to image distance). The film was processed in a Carestream 5000 RA Processor and scanned with a Vidar Dosimetry Pro Advantage scanner (S/N: 3100055). Using Omnipro IMRT software (version 1.3, Scanditronix-Wellhofer) the intensity distribution of the radiation field was mapped. Figure 3-8 is the distribution from a Planmeca Prostyle Intraoral tube, 25.5 cm from the source.

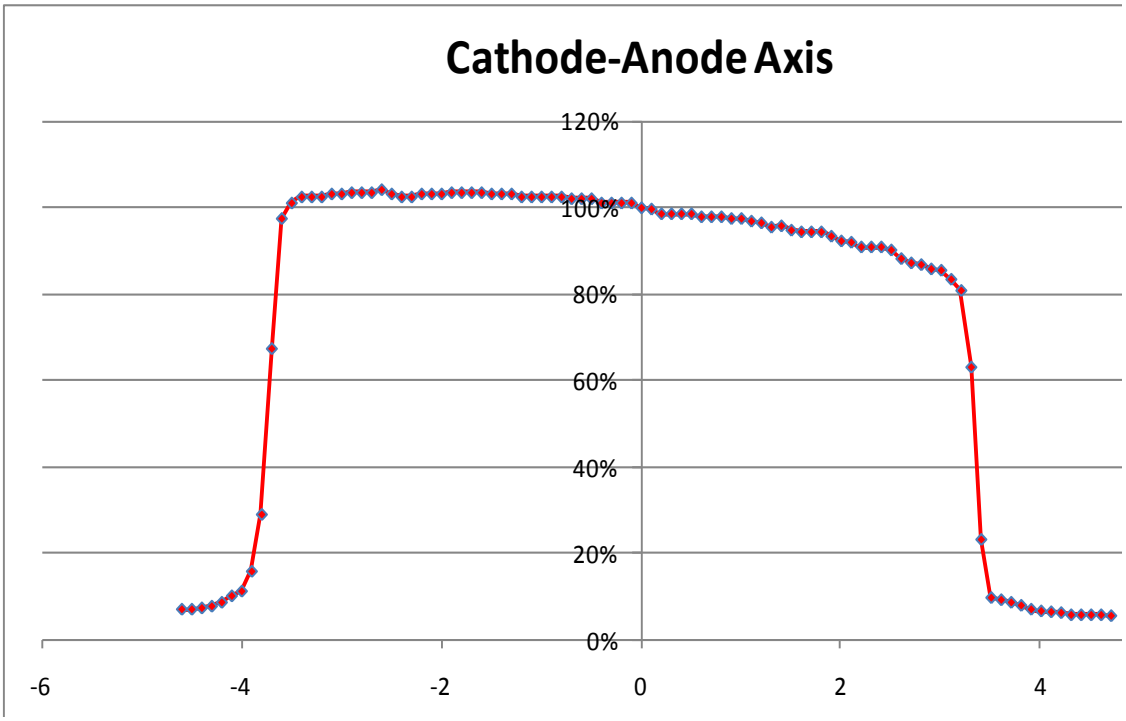

Figure 3-8. Relative Intensity Distribution Planmeca Prostyle Intra, 25.5 cm from Source

The variation across the radiation field perpendicular to the anode-cathode axis is significant: greater than 20% for the Planmeca unit and greater than 40% for the Gendex 770 (Figure 3-9). Perpendicular to the anode-cathode axis, the radiation field for both units is relatively uniform.

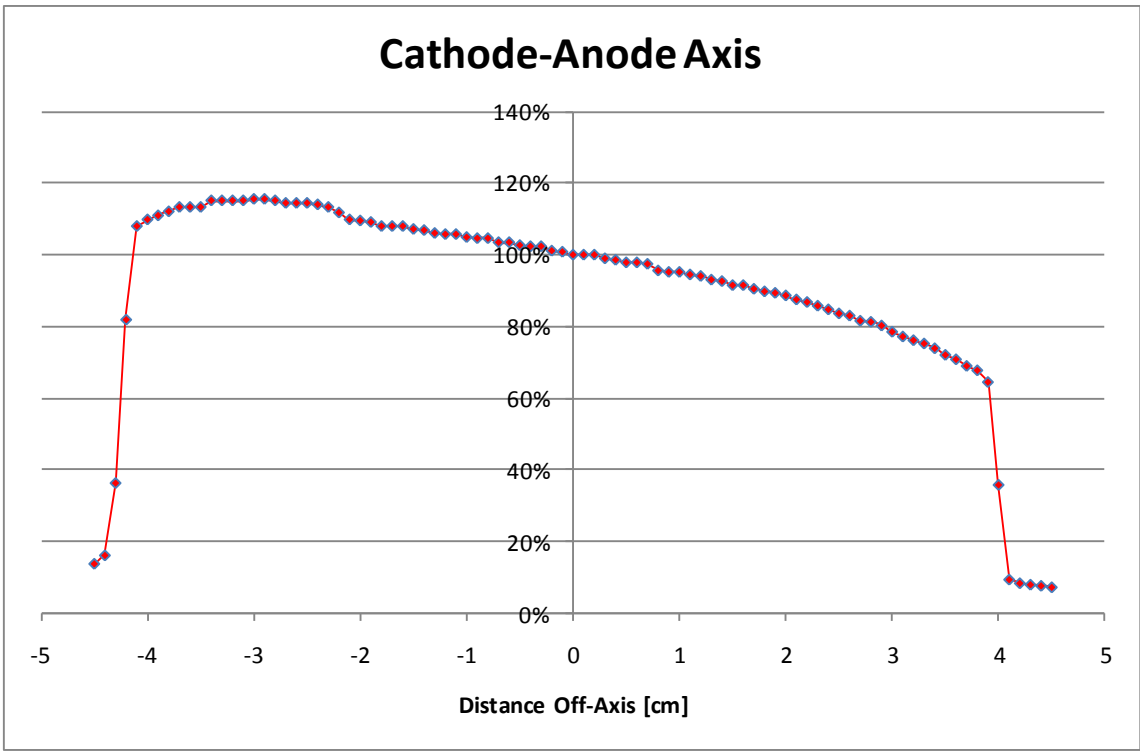

Figure 3-9. Relative Intensity Distribution Gendex 770, 25.5 cm from Source

An attempt will be made to incorporate the spatial intensity variation of the x-ray source into the MCNPX model. Assigning a directional bias to the source or inserting a tungsten wedge into the x-ray field distal to the source will both be considered. The impact of the additional filtration a wedge would produce must be evaluated as it will change the source energy distribution.

Chapter 4: Spectra, Radiographic Unit, Detector Characterization and Results

The computational model served as the data acquisition engine from which the optimization process was launched. To fully develop the model, a clear understanding of the imaging system was needed. This included defining the x-ray spectrum as well as verifying radiographic unit exposure output and reproducibility at all relevant energies. The sensor dose response function and response reproducibility were evaluated to complete the imaging system characterization.

The data acquisition and results can be divided into three distinct categories: spectra, radiographic unit, and sensor characterization. The methods and results are described below.

4.1. SPECTRAL CHARACTERIZATION

4.1.1. Spectral Measurements

Since x-ray interactions are a function of energy and precise optimization depends on an accurate knowledge of the interaction probabilities (Miyajima, 2003), spectral characterization was a critical component of this project. The Amptek, Inc. XR-100T Cadmium Telluride x-ray and gamma ray detector system was used to capture x-ray spectral data for the DC Planmeca Intra and AC Gendex 770 dental intraoral radiographic units. This detector system is designed for measuring the energy distribution of x-ray sources accurately and provides an excellent means to experimentally verify the source distribution rather than relying entirely upon simulations. The efficiency of the CdTe detector at energies between 1 keV and 10 MeV is published (Redus, 2002). Miyajima documented good agreement between corrected x-ray spectra measured with the CdTe detector and a high purity germanium detector. The detector (S/N: A011326) was

operated with the PX4 Digital Pulse Processor and power supply (S/N: 001499) through a software interface.

These steps were followed to acquire each spectrum:

1. The system was calibrated using a 100 μCi Co-57 button source with known gamma peaks at 14.4 and 122 keV. After the intial calibration, the system was set to automatically load the calibration file at start-up.
2. The CdTe detector was aligned with the dental radiographic tube head. Because the detector is susceptible to damage in high radiation flux environments, a 100 micron pinhole camera collimator was placed over the sensor window to limit the photon flux impinging on its surface. The x-ray source to detector distance was adjusted to limit the count rate to a maximum of 9000 counts per second. Higher count rates caused significant dead time losses as well as erroneous low energy channel counts. The experimental set-up is shown in Figure 4-1.
3. Serial exposures were made until a total spectrum count of at least 250,000 was achieved.
4. The raw spectral data was processed to remove the cadmium and telluride characteristic x-ray escape peaks using XRS-FP software (Crossroads Scientific), which is well described (Redus, 2008).

Figure 4-1. Spectrum Acquisition

5. After processing, the spectral data were binned at 0.5 keV increments. The cut-off for the maximum energy was arbitrarily selected where the intensity dropped to 1E-05. This is consistent with the highest IPEM energy bin intensity (nominal kVp). The experimentally measured x-ray unit spectra were then benchmarked against analogous IPEM generated spectra to verify intensity distributions were appropriate.

4.1.2. Results: Measured Spectra

Figures 4-2 through 4-6 represent the measured and processed spectra from five Planmeca intra-oral radiographic units at 60, 63, 66, and 70 kVp and five Gendex intra-oral radiographic units at 70 kVp.

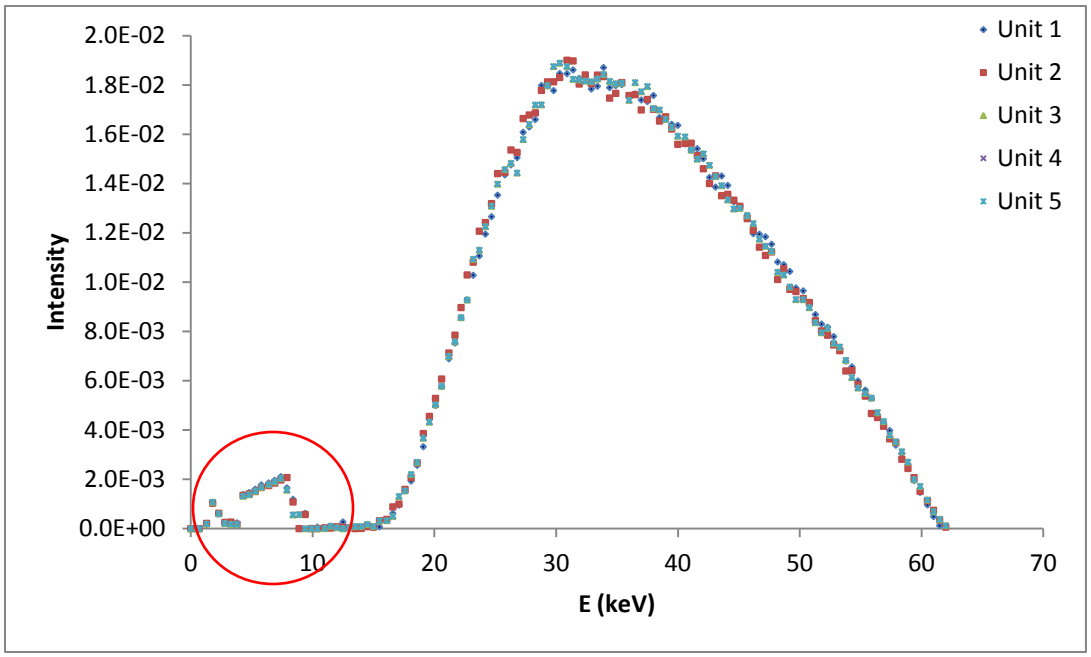

Figure 4-2. 60 kVp Measured Spectra

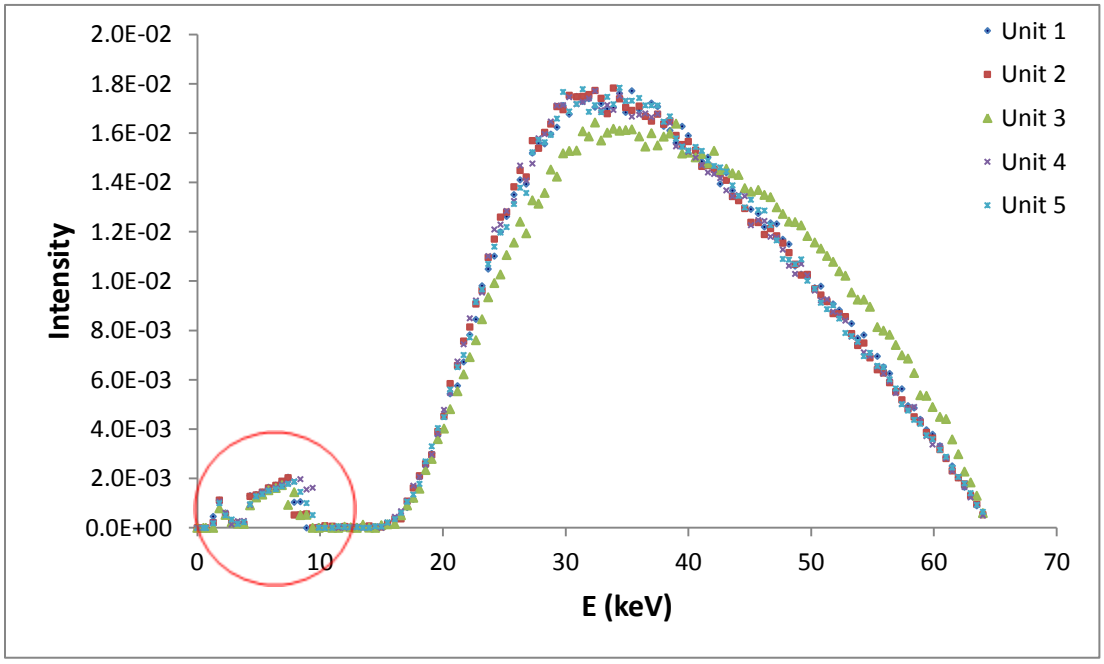

Figure 4-3. 63 kVp Measured Spectra

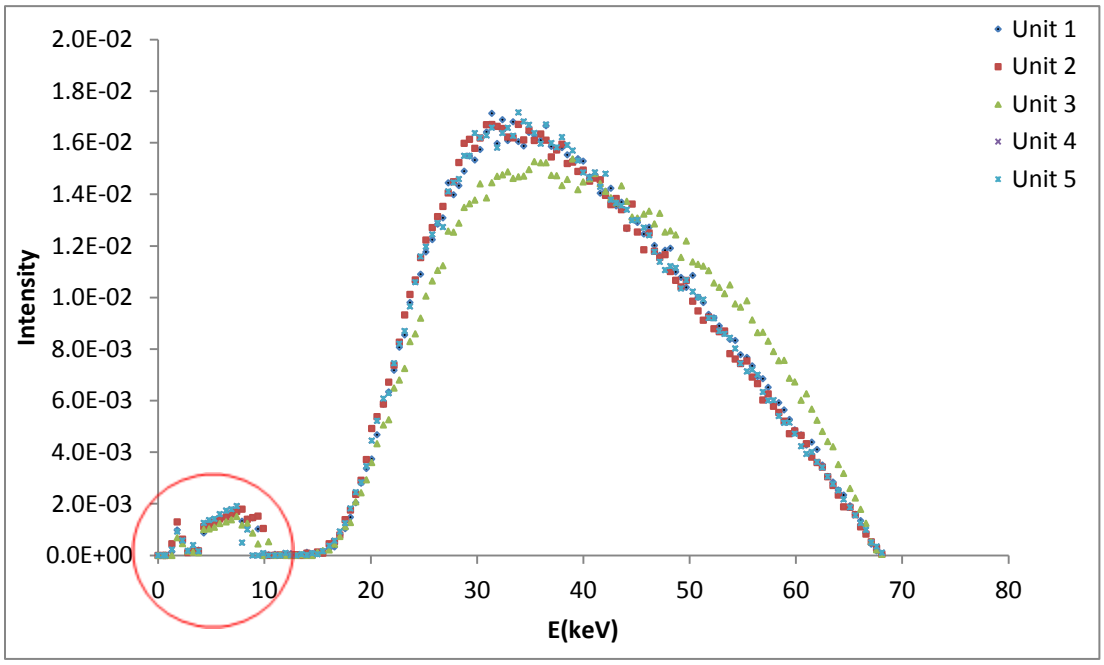

Figure 4-4. 66 kVp Measured Spectra

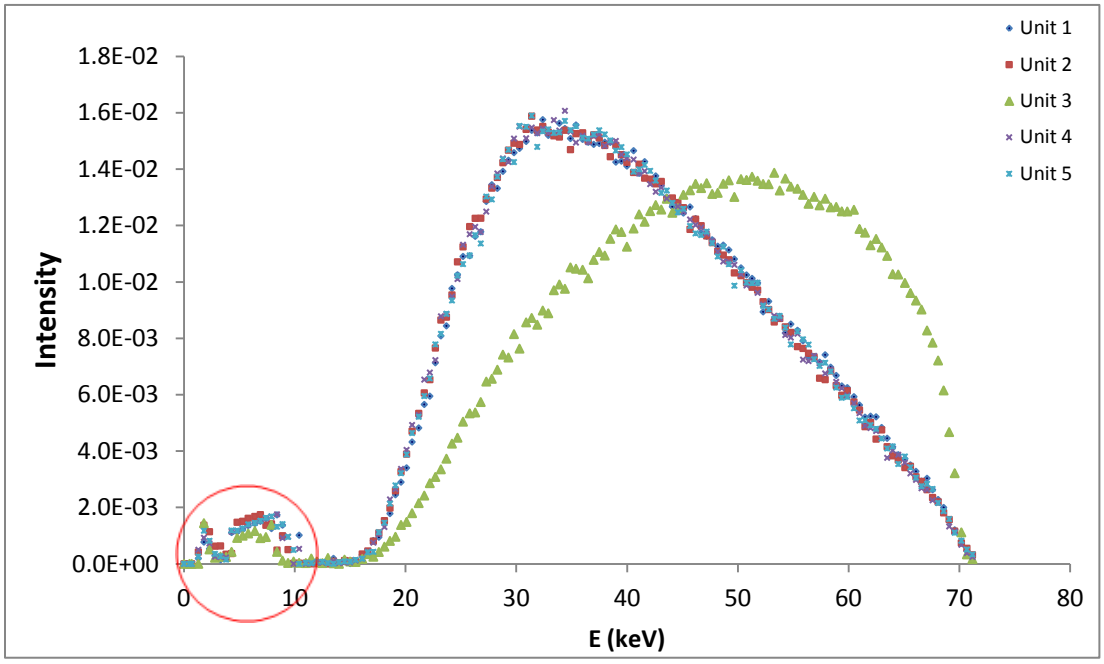

Figure 4-5. 70 kVp Measured Spectra (Planmeca)

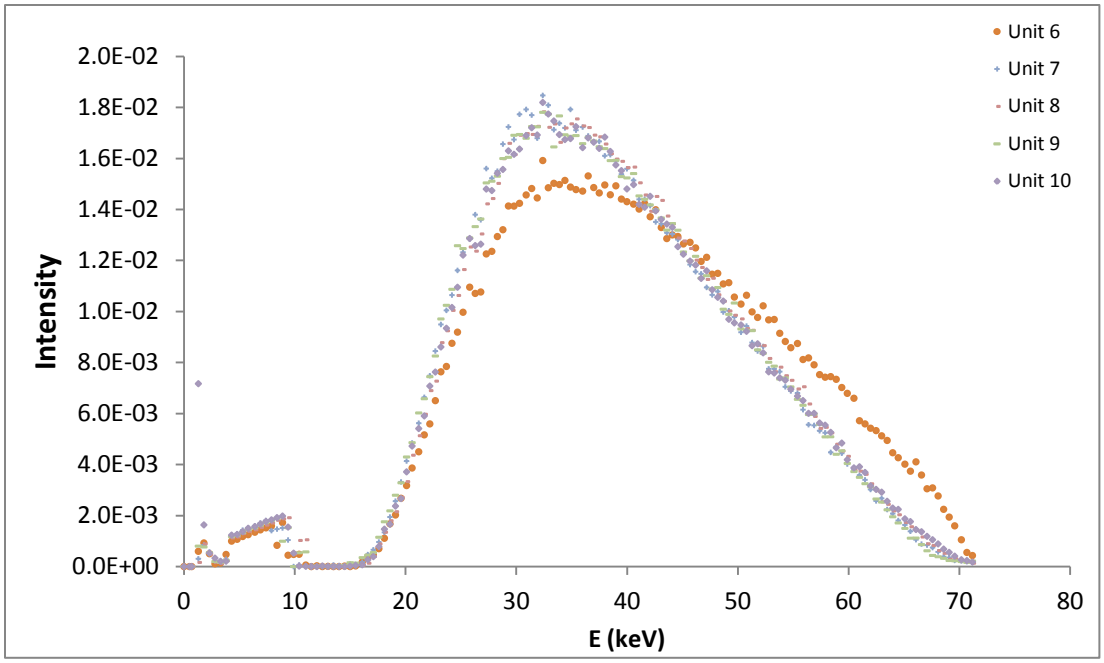

Figure 4-6. 70 kVp Measured Spectra (Gendex)

All spectra exhibit a small peak in the low energy channels (below 10 keV). Since the x-ray tubes contain at least two millimeters aluminum equivalent, the photons below 10 keV will effectively be attenuated before exiting the tube (Bushberg, 2002). The most likely explanation for these low energy counts is incomplete correction for the CdTe escape peaks. Figure 4-7 illustrates the correction algorithm applied to an 80 kVp x-ray spectrum with a 15 keV aluminum filter (Redus, 2008). The green curve shows the escape events of the unprocessed spectrum. The blue curve represents the corrected escape events, which are added back into the unprocessed spectrum. The post-processed spectrum in this example illustrates a residual signal in the low energy channels that should not be present with a 15 keV filter.

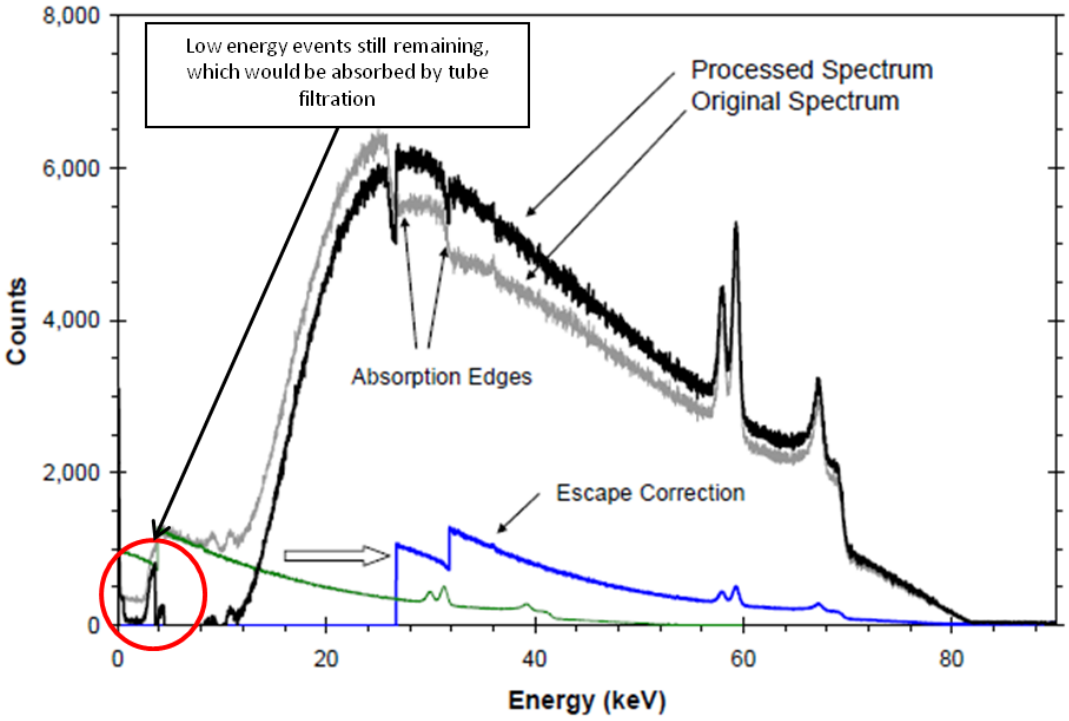

Figure 4-7. Software Correction for CdTe Escape Events (Redus, 2008 p. 2)

To demonstrate the effects of the processing software on the dental x-ray spectra, a representative 60 kVp Planmeca spectrum before and after processing is shown in Figure 4-8. Since the XRS-FP software did not completely remove the low energy escape events, the remaining counts in bins below 10 keV for all spectra were discarded.

With the exception of one Planmeca unit (Unit 3) and one Gendex unit (Unit 6), the spectra display a consistent intensity distribution. The reason for the deviations in these two units is not known. The data from Units 3 and 6 were excluded from further analysis.

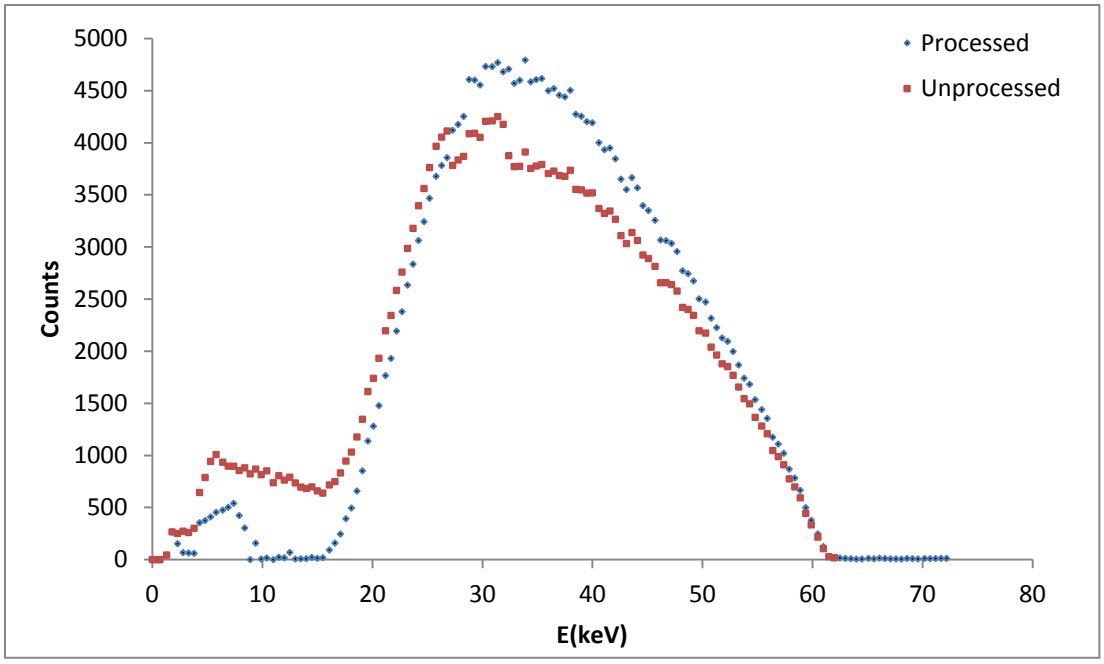

Figure 4-8. Representative Processed and Unprocessed 60 kVp Planmeca Spectra

4.1.3. Results: IPEM vs. Measured Spectra

As described in section 3.2.2, the IPEM spectra were generated using parameters to match the actual radiographic settings as closely as possible. The total beam filtration was selected through an iterative process to match the measured half-value layer of the beam. The Planmeca Intra tube specifications are:

- Target Material: Tungsten
- Anode Angle: 16^{o}
- Voltage Ripple: Nominally, less than 2% for a constant potential generator (Bushberg)
- Attenuation Thickness (aluminum): Adjusted to match average measured half-value layer at each peak kilovoltage

The IPEM software allows voltage ripple selection in 5% increments from 0-30%. Therefore, 0% ripple was used to simulate the Planmeca waveform and 30% voltage ripple had to be used to simulate the Gendex waveform. Figures 4-9 through 4-13 display the average measured and IPEM generated Planmeca spectra at 60, 63, 66, and 70 kVp. Error bars represent the standard deviation of the intensity in each energy bin for the measured spectra.

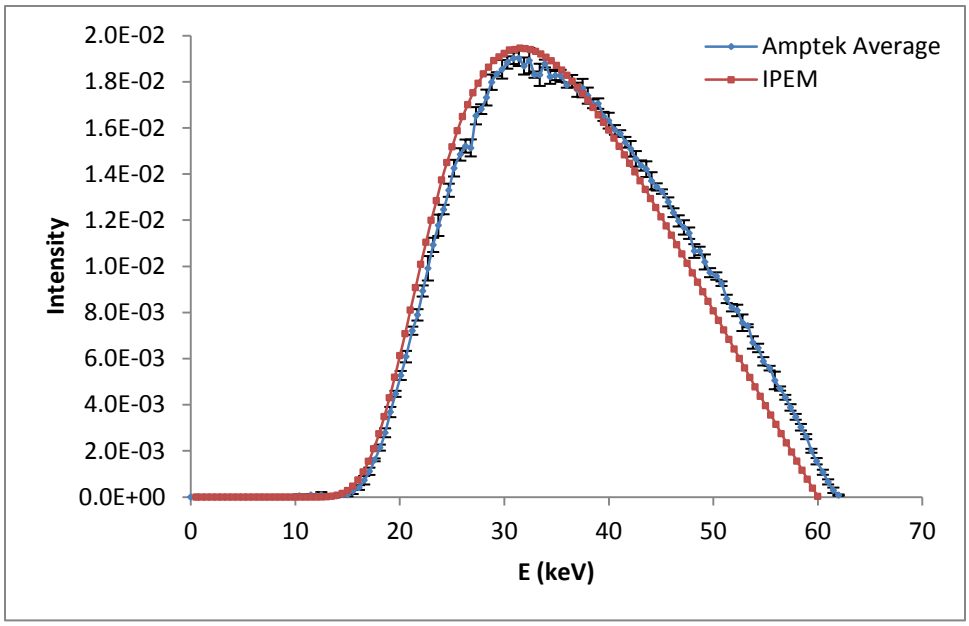

Figure 4-9. 60 kVp Comparison (Measured vs. Software Generated)

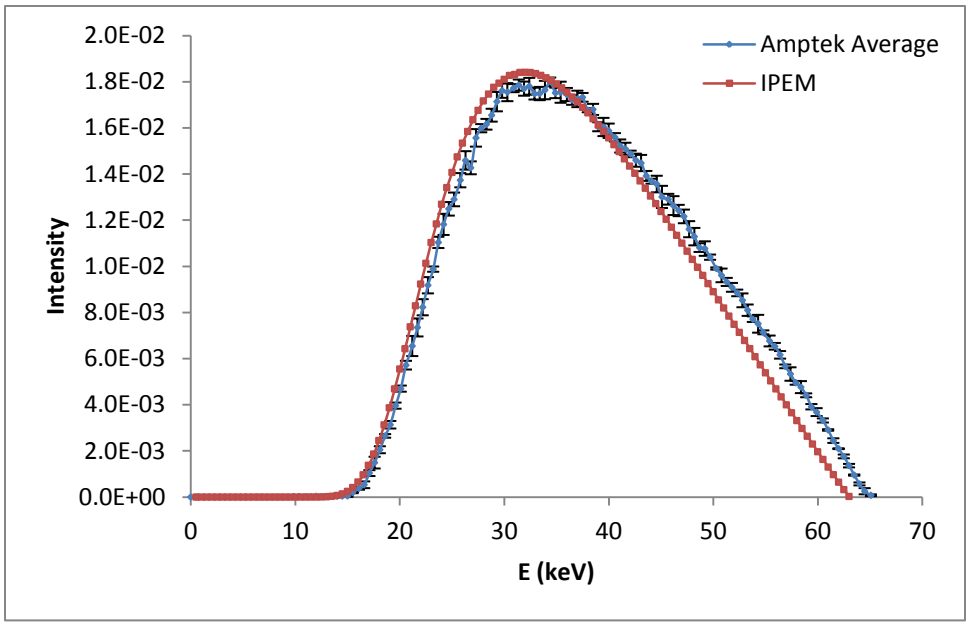

Figure 4-10. 63 kVp Comparison (Measured vs. Software Generated)

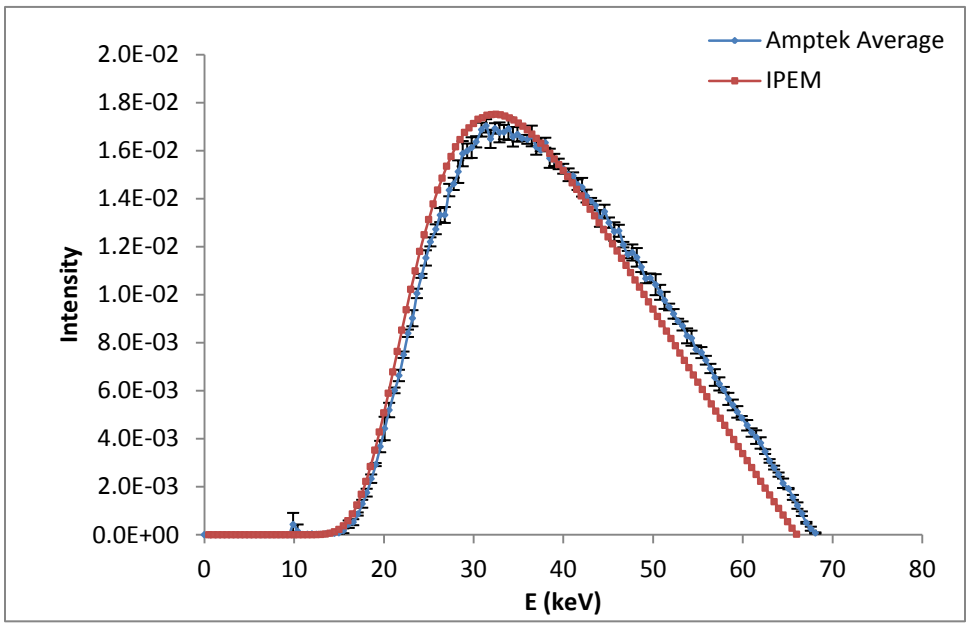

Figure 4-11. 66 kVp Comparison (Measured vs. Software Generated)

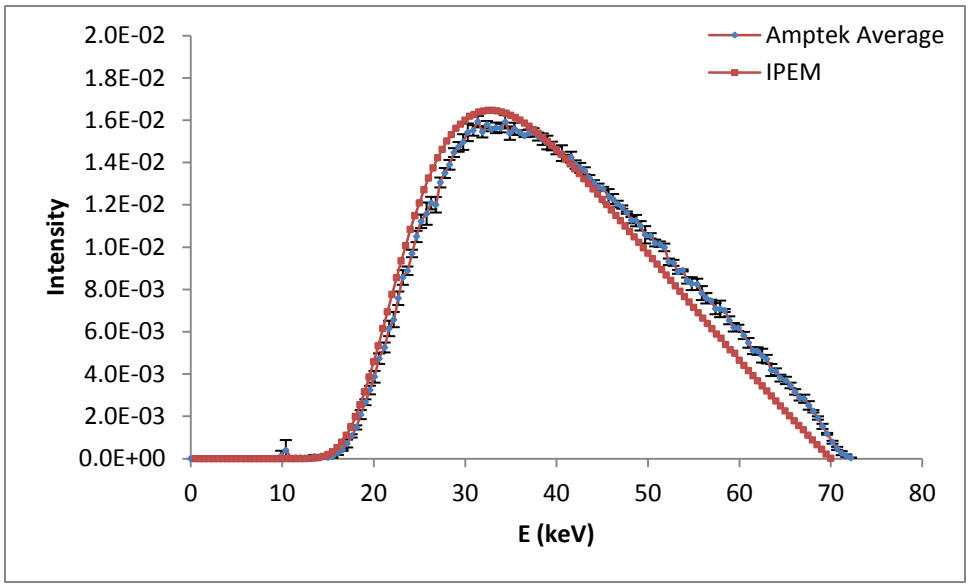

Figure 4-12. 70 kVp Planmeca Comparison (Measured vs. Software Generated)

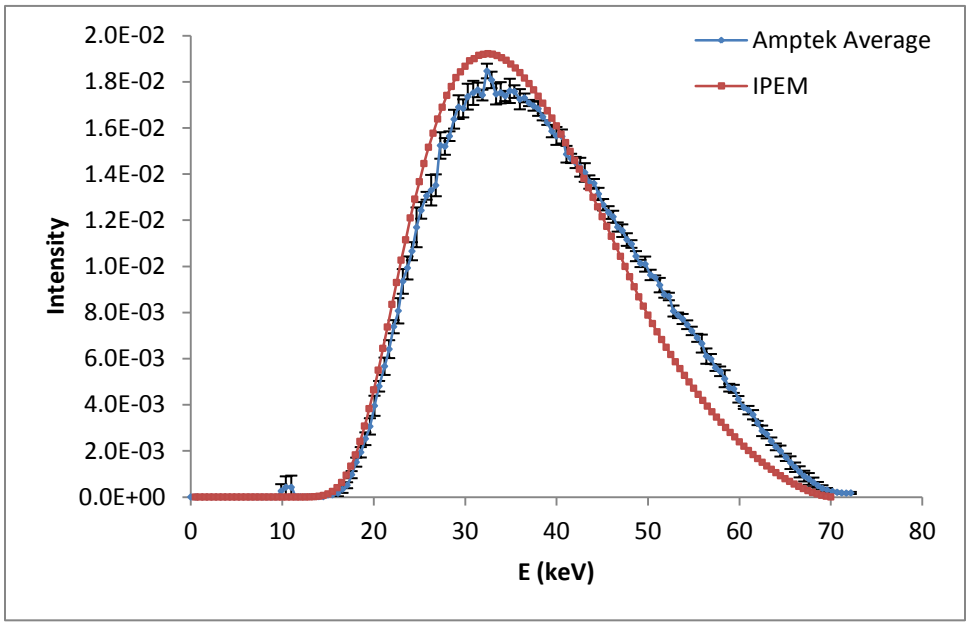

Figure 4-13. 70 kVp Gendex Comparison (Measured vs. Software Generated)

The average energy for all measured spectra was calculated as:

$$E_{Average}(keV) = \sum_{i=1}^{n} E_i I_i \qquad \text{(Eq. 4-1)}$$

Where:

E_i=Energy bin (keV)

I_i=Intensity in bin i

The average energy for all Planmeca measured spectra was approximately 4% higher than the software generated spectra, even when the half-value layers were matched. This could be due to the differences between the equipment used for the IPEM model and the dental radiographic units, variations between nominal and actual kVp or a systematic error introduced during data collection. The IPEM spectra are theoretical with an assumed peak energy cut-off at the nominal kVp. In practice, the kVp can vary by as much as 5% from the nominal value (the measured peak kilovoltages are shown in Table 4-2). The difference between the Gendex measured and modeled spectra was ~5% even though the model waveform does not accurately represent the actual waveform.

An alternative approach to matching the measured spectra was investigated. Instead of matching the nominal kVp and measured half-value layers, the average energy and measured average kVp was used for the model. A comparison of the two methods used to model the 60 kVp measured spectrum is demonstrated in Figure 4-14. The IPEM spectrum was modified to a near perfect match with the measured spectrum by adjusting the beam filtration. However, the half-value layer of this spectrum is 2.34 millimeters aluminum compared to the average measured half-value layer of 2.03 millimeters aluminum. The published uncertainty for HVL measurements is 10%; the modeled HVL exceeds this uncertainty. Given the inconsistencies in measured versus modeled HVL for

this alternative approach, the original IPEM model was considered to be the closest representation of the clinical spectra.

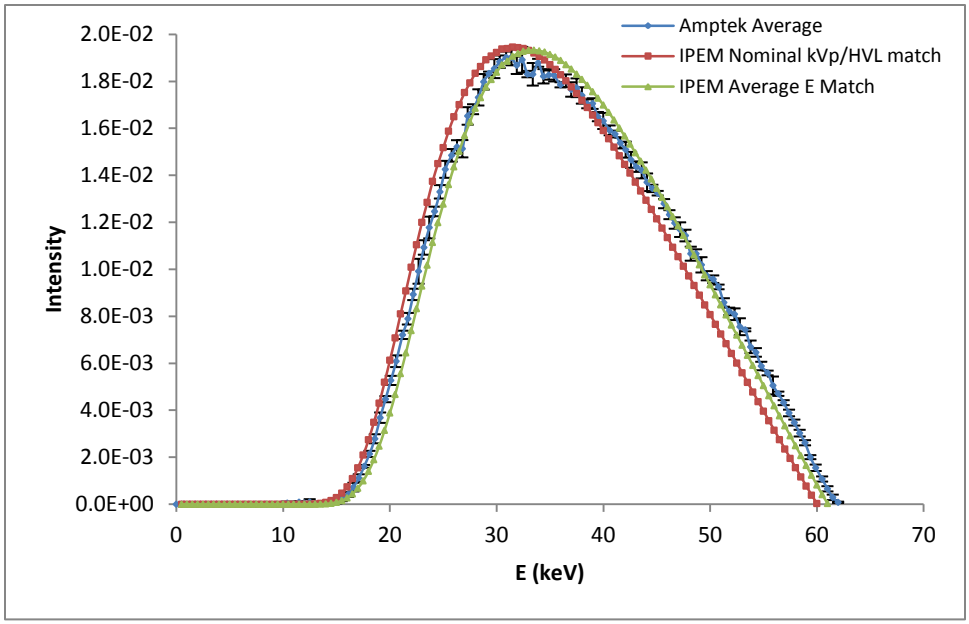

Figure 4-14. Alternative IPEM Model Comparison

Because of the systematic bias in the measured data, the IPEM generated spectra were ultimately used for the MCNPX model. Since it was shown in past work (described in chapter 3) that the IPEM generated spectra could be used to adequately estimate clinical radiation exposures, it was considered to be a valid substitute for experimentally derived spectra. The systematic bias between the IPEM and measured data sets was carried forward in the optimization. A comparison of the average energies of the measured and software spectra are provided in Table 4-1. The systematic bias is shown as the percent difference between the measured and IPEM spectra calculated as:

$$\%Difference = \frac{AvgE_{Amptek} - AvgE_{IPEM}}{AvgE_{IPEM}} * 100 \qquad \text{(Eq. 4-2)}$$

Table 4-1. Comparion of Measured to IPEM Generated Spectra: Mean Energy

Energy (kVp)	Measured Spectra Energy (keV) (σ)	IPEM Generated Spectra Energy (keV)	% Difference
60	37.0 (0.12)	35.6	3.8%
63	38.1 (0.12)	36.7	3.9%
66	39.2 (0.17)	37.7	4.0%
70	40.7 (0.16)	39.0	4.3%
70 (Gendex)	38.9 (0.25)	37.0	5.1%

The standard deviation of the average energy for the measured spectra (shown in parentheses above) was carried through in the uncertainty propagation.

4.1.4. Results: Representative IPEM Generated Spectra

Additional IPEM spectra were generated at 50, 55, 75, 80, 85, and 90 kVp. The Planmeca units can be operated at 50, 52, 55, and 57 kVp but have not been due to patient dose concerns. Because the digital sensors are significantly more sensitive than film, the lower kVps were included in the optimization process because of the potential to increase image contrast. The reason that only 50 and 55 kVp were modeled will be explained in chapter 5. The higher kVps (75 to 90) used for the optimization may be clinically available on some units and were included as the upper end of the diagnostically useful range for dental imaging. The spectra for the kVp range available on the Planmeca units are presented in Figure 4-15. The additional spectra are shown in Figure 4-16.

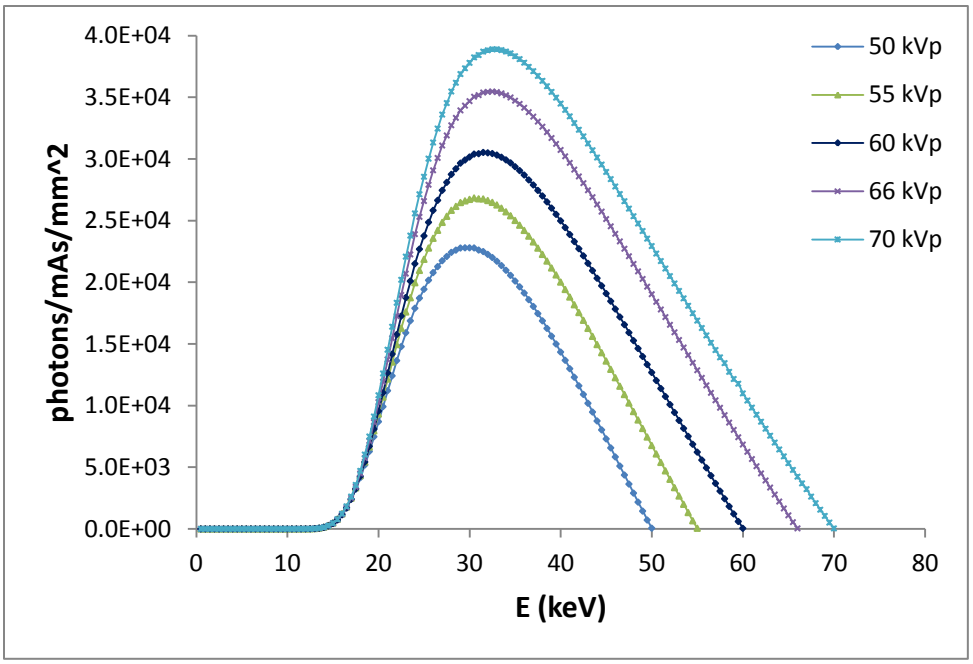

Figure 4-15. IPEM Generated Spectra (Clinically Available on Planmeca)

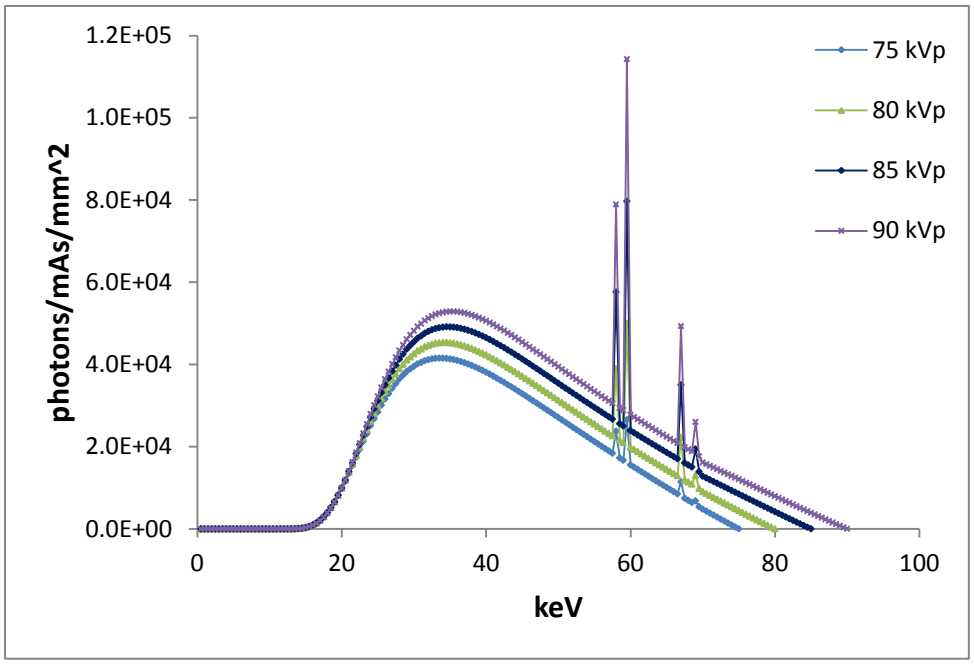

Figure 4-16. IPEM Generated Spectra (Potentially Available in Dental Imaging)

The spectra were plotted in photons per mAs per millimeter squared to illustrate the output differences at each kVp. In Figure 4-17, the IPEM 70 kVp Planmeca model is plotted with the IPEM 70 kVp Gendex model to illustrate the difference between the constant potential versus 30% voltage ripple spectra. Note the differences in both shape and output between the two. The output, defined as (μGy air KERMA)/mAs, is roughly 40% lower for the 30% voltage ripple generator [Exposure from this point forward will be reported as air KERMA. The conversion factor from exposure in milliroentgens to μGy air KERMA is 8.77.]

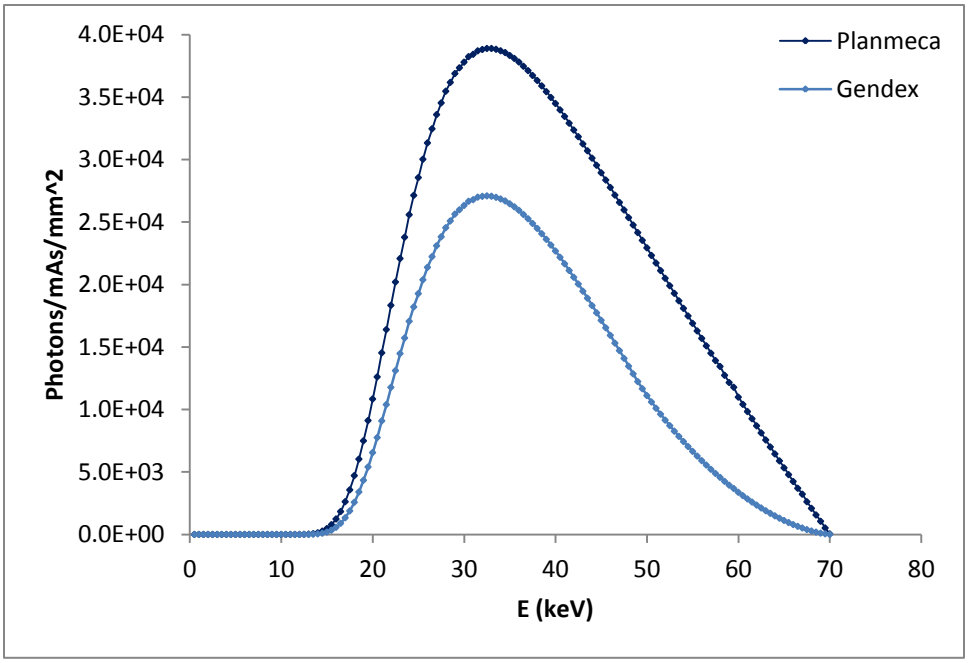

Figure 4-17. Modeled Planmeca and Gendex 70 kVp Spectra

The measured Amptek spectra can be found in **Appendix E**. All IPEM spectra files used for the optimization can be found in **Appendix F**.

4.1.5. Uncertainty Analysis

Analyses of the uncertainties and variability across all components of the system were performed to establish confidence intervals on the final results presented in chapter 6. Uncertainty propagation was performed following standard calculation methods for independent uncertainties in functions of several variables. A detailed description of this method is described in Taylor (1997).

The uncertainties associated with the x-ray spectra will be described in chapter 5 in terms of the MCNPX generated radiographic contrast differences between the Amptek and IPEM spectra (Table 5-12). The data used for uncertainty propagation can be found in **Appendix R.**

4.2. RADIOGRAPHIC UNIT CHARACTERIZATION

4.2.1. Radiographic Output, Beam Quality and Results

To complete the source characterization, the radiographic exposure for each peak kilovoltage was needed. The unit output was used to scale the MCNPX results to a clinically relevant range, which was essential for the optimization. These data were measured following the same methodology outlined in chapter 3, taking serial exposure readings from several radiographic units using an Unfors Xi base unit with a radiographic/fluoroscopic solid-state detector (Model 8201031-C, S/N 136669, calibration date 10 July 2012). The half-value layer and kVp measured directly with the Unfors detector were also recorded. The specified meter uncertainties are:

- kVp: +/-2%
- Dose: +/-5%
- HVL: +/-10%

The exposure measurements for the Planmeca units were acquired at 0.8 milliAmpere-seconds (mAs) and 30.5 cm source to detector distance (SCD) for each kVp. The Gendex exposure measurements were acquired at seven milliAmperes and six pulses (approximately 0.6 mAs) and 20.5 cm SCD.

Figure 4-18 displays the output in μGy air KERMA per mAs for the Planmeca and Gendex units (error bars represent standard deviation of measured values). The Gendex output is approximately 36% lower than the output of the Planmeca units. This is comparable to the modeled output differences between the constant potential and 30% voltage ripple spectra, which also confirms the IPEM model is an adequate representation of the measured Gendex spectrum in terms of both average energy and output.

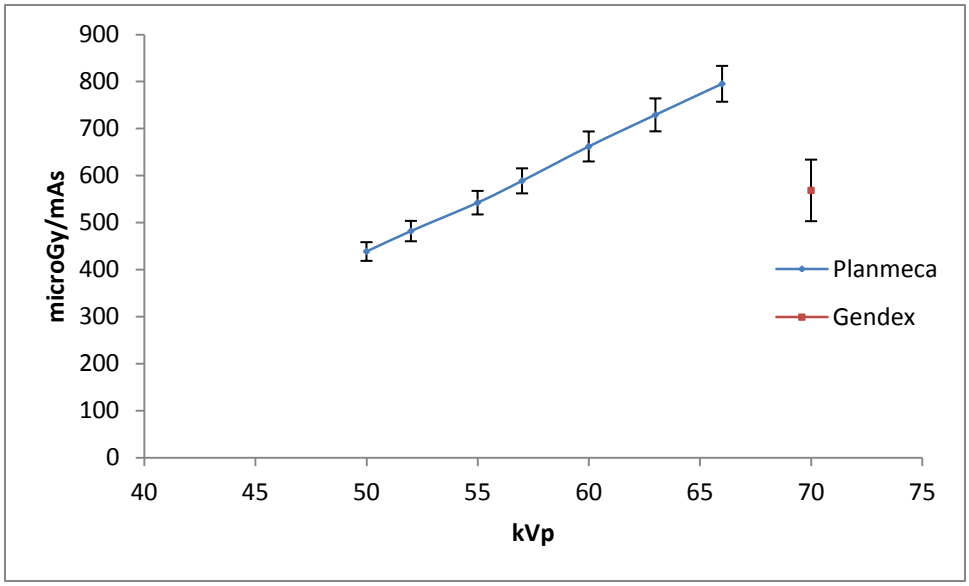

Figure 4-18. Radiographic Unit Output

The intra-unit variability (variation in measurements on individual units) was below the published 5% measurement uncertainty for all units. The inter-unit exposure

variability (variation between all units) was much more significant, approaching the 5% detector uncertainty for the Planmeca units and exceeding the detector uncertainty for the Gendex units.

The average measured kVp and half-value layer at each peak voltage is shown in Table 4-2. The inter-unit variability in half-value layer was well below the published detector uncertainty of 10%. The published uncertainty for both kVp and HVL was used for uncertainty propagation to be conservative.

Table 4-2. Measured Peak Kilovoltage and Half-Value Layer

	kVp								
	50	***52***	***55***	***57***	***60***	***63***	***66***	***70*** *Planmeca*	***70*** *Gendex*
Avg kVp:	50.5	52.8	55.8	58.0	60.8	63.8	66.9	70.7	72.4
σ (kVp):	0.31	0.41	0.43	0.44	0.42	0.49	0.48	0.60	1.50
Uncertainty (+/-) (kVp):	1.01	1.06	1.12	1.16	1.216	1.28	1.34	1.41	1.45
Avg HVL (mm Al):	1.68	1.76	1.85	1.90	2.03	2.12	2.20	2.32	2.22
σ (mm Al):	0.029	0.032	0.034	0.032	0.069	0.070	0.076	0.084	0.170
Uncertainty (+/-) (mm):	0.17	0.18	0.18	0.19	0.20	0.21	0.22	0.23	0.22

The entire exposure reproducibility data set can be found in **Appendix G**.

4.2.2. Kilovolt Waveforms

Both the output and average energy of the 30% voltage ripple generator should be higher than the half-wave rectified Gendex unit with 100% voltage ripple (Bushberg). One possible reason the measured Gendex average energy was so close to the modeled IPEM average energy could be the normal variations in nominal versus actual kVp as described above (the average measured kVp for the Gendex units was 72.4). Another possible reason the Gendex average energy is higher than expected could be due to the generator design. As described in the Gendex 770 user's manual, "the first several x-ray pulses will be high kVp (about 80)…low mA (about 2), and will settle out to 70 kVp and

7 mA (nominal) after 5-10 pulses." (Gendex Corporation, p. 8). This could result in a measured average energy higher than one generated from a theoretical model.

To get a better understanding of the differences between the Planmeca constant potential generator and the Gendex half-wave rectified generator, the kilovolt waveforms were captured with a Barracuda solid state MPD detector (serial number: MPD-07120015). The detector was centered in the x-ray field at the end of the cone, perpendicular to the anode-cathode axis. The waveforms were measured at 70 kVp for each unit. The Planmeca waveform was recorded at 70 kVp, 8 mA and 100 milliseconds. The Gendex waveform was recorded at 70 kVp, 7 mA and 16 pulses. Figure 4-19 displays the Planmeca waveform and Figure 4-20 demonstrates the Gendex waveform.

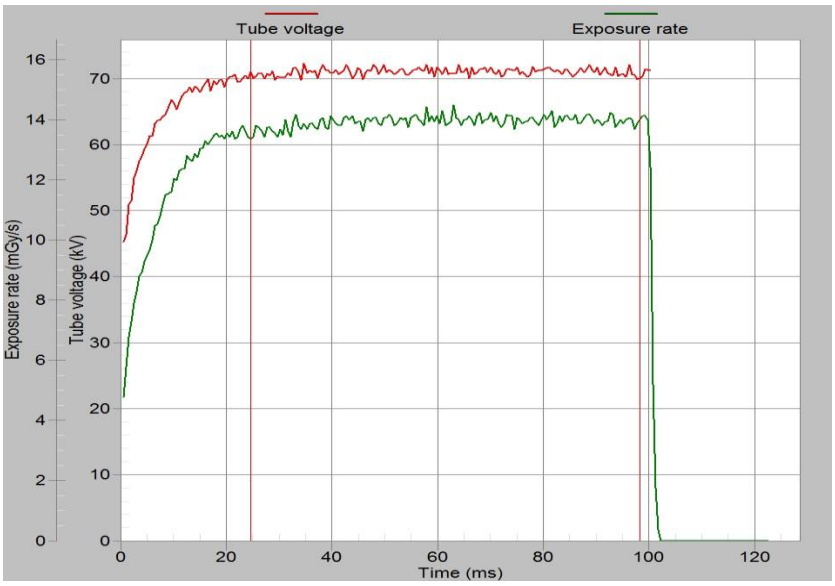

Figure 4-19. Planmeca 70 kVp Waveform

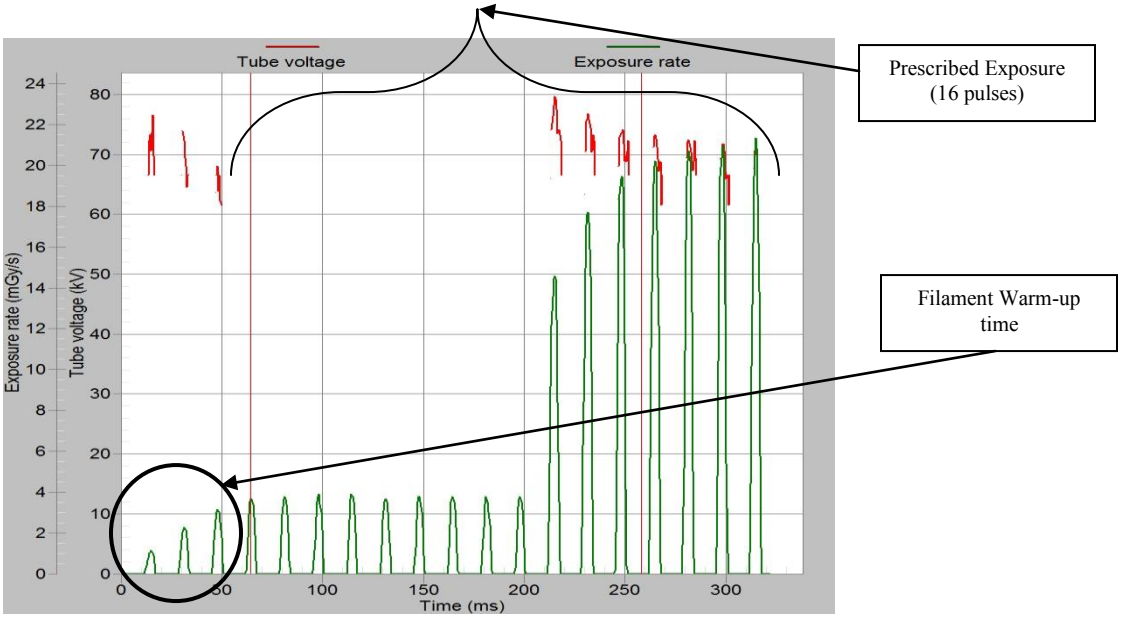

Figure 4-20. Gendex 70 kVp Waveform

The constant potential generator displays a near constant peak kilovoltage across the entire 100 msec exposure. Because of the Barracuda detector limitations, the full kilovoltage waveform for the Gendex unit was not displayed but the measured voltage variations as seen in this example are over 10 kVp. Also note the highest measured kilovoltage is approximately 80 kVp as described in the Gendex user's manual. Additionally, each exposure begins with a ~0.4 second filament warm-up time with kilovoltage varying between 60 and 80 kVp (Gendex), represented in this illustration by the first three pulses (one pulse is 1/60 second). These pulses are low output but produce enough radiation to contribute to the image formation. The warm-up time is followed by the nominal exposure time.

4.2.3. Estimating Entrance Air KERMA

The method described by Harpen (1996) was used to determine a linear fit of the exposure data. Harpen described a power function to estimate the exposure for a

particular radiographic unit at any kVp, mAs, and distance using measured exposure at two kVps.

$$E(mR) = a_1 kVp^{a_2} \qquad \text{(Eq. 4-3)}$$

Where:

$$a_1 = \frac{mR}{kVp_1^{\,a_2} * mAs} * \left(\frac{Distance}{SSD} \right)^2$$

$$a_2 = \frac{\ln\left(\frac{mR_1}{mR_2} \right)}{\ln\left(\frac{kV_1}{kV_2} \right)}$$

The entire data set for all Planmeca units was linearized by taking the natural logarithm of the kVp and exposure then a regression analysis was performed to determine the coefficients, a_1 and a_2. The regression fit is shown in Figure 4-21 (all statistical analyses performed using the Excel Data Analysis Add-in).

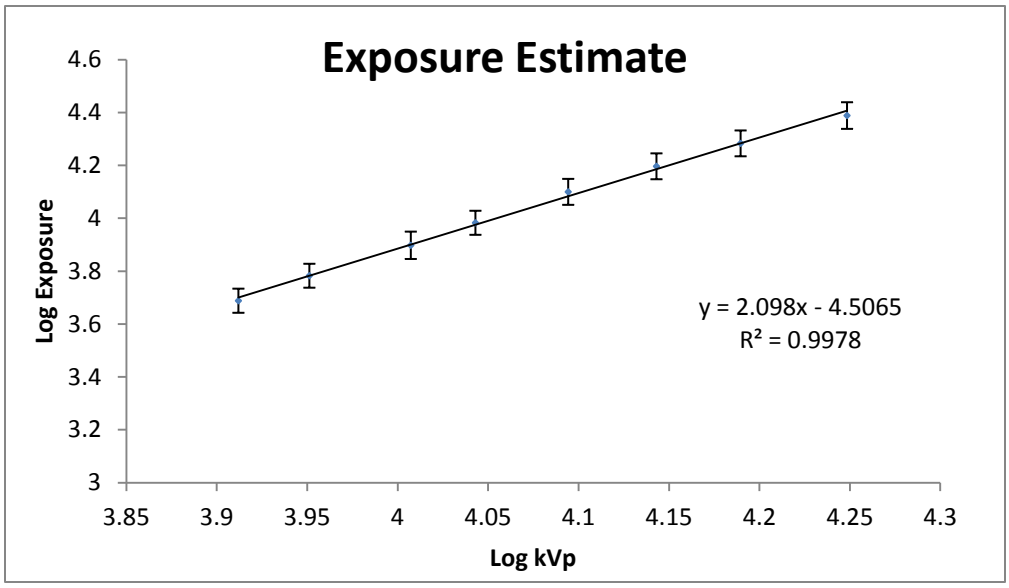

Figure 4-21. Exposure Estimate

Converting this back to a power equation, the estimated coefficients are:

$$E(mR) = 0.011 kVp^{2.10} \qquad \text{(Eq. 4-4)}$$

If the coefficients are normalized to 1 mAs at 1 cm source to skin distance (SSD) by multiplying a_1 by: $\frac{(SCD)^2}{mAs}$ where the SCD for all exposures was 30.5 cm and the mAs was 0.8, the equation can be used to determine the exposure at any technique and distance:

$$E(mR) = 12.8 kVp^{2.10} (cm^2 / mAs) \qquad \text{(Eq. 4-5)}$$

The coefficients and regression statistics for the linearized and power equation are given in Table 4-3.

Table 4-3. Coefficients and Standard Error

	Linearized Regression				Power Equation		Normalized	
	Value	Error	*t Stat*	*P-value*	Value	Error	Value	Error
a_1	-4.51	0.165	-27.3	1.61E-07	0.011	4.05E-04	12.8	0.471
a_2	2.10	4.06E-02	51.7	3.52E-09	2.10	4.06E-02	2.10	4.06E-02

R^2: 0.998

The estimated air KERMA for the Planmeca units at any distance or mAs is then:

$$K_{air}(\mu Gy) = \left(12.8 * kVp^{2.10} * \left(\frac{mAs}{SSD^2}\right)\right) * 8.77 \qquad \text{(Eq. 4-6)}$$

The appropriate mAs to achieve the optimized exposure to the detector was calculated with this equation. Since the Gendex units can only be operated at 70 kVp and 7 mA and all have a 20.5 cm source to skin distance, the entrance air KERMA can be estimated as:

$$K_{air}(\mu Gy) = \frac{1260\,\mu Gy}{mAs} * mAs \quad (\sigma: \text{ +/-158 } \mu Gy) \qquad \text{(Eq. 4-7)}$$

4.2.4. Anode-Heel Effect

The measured anode-heel effect (previously described) was not incorporated into the MCNPX model. The intensity distribution was considered irrelevant to the objectives of this work, which were to optimize the detector response/dose relationship.

4.2.5. Uncertainty Analysis

The uncertainty analysis for Equation 4-6 was calculated as:

$$\sigma_K (= \sqrt{\left(kVp^{a_2}\sigma_{a_1}\right)^2 + \left(a_1 a_2 (kVp)^{a_2-1}\sigma_{kVp}\right)^2 + \left(a_1 (kVp)^{a_2} \ln(kVp)\sigma_{a_2}\right)^2} \qquad \text{(Eq. 4-8)}$$

This uncertainty was needed to calculate the sensor signal and noise response uncertainties as shown in section 4.3.7 and the optimization uncertainties in chapter 6. Table 4-4 defines the Equation 4-8 terms and the text location where the data were presented. The average uncertainties for the exposure response function are shown in Table 4-5.

Table 4-4. Equation 4-8 Definition of Terms

Symbol	Definition	Value (Units)	Location in Text
σ_K	Uncertainty in K_{air}	Multiple values (μGy)	Appendix G
kVp	Peak Kilovoltage	Multiple Values (kVp)	Table 4-2
σ_{kVp}	Uncertainty in Peak Kilovoltage	Multiple Values (kVp)	Table 4-2
a_1	Coefficient	12.8 (Unitless)	Eq. 4-5
σ_{a1}	Coefficient a_1 Standard Error	4.71E-01 (Unitless)	Table 4-3
a_2	Coefficient	2.10 (Unitless)	Eq. 4-5
σ_{a2}	Coefficient a_2 Standard Error	4.06E-02 (Unitless)	Table 4-3

Table 4-5. Exposure Estimate Uncertainties

Error Analysis: Exposure Response Functions			
%σ (kVp)	**%σ Coef a_1**	**%σ Coef a_2**	**Total %σ**
2.1%	3.7%	1.9%	17%

4.3. SENSOR CHARACTERIZATION

4.3.1. Sensor Response Function

Because the sensors cannot be modeled accurately in MCNPX, detector response functions were acquired experimentally for both the Carestream digital sensors and the Air Techniques ScanX® PSP plates. The detector response functions were used to scale the radiography tally results across a range of exposures for the optimization.

The Carestream images were acquired as follows:

1. Through trial and error, it was determined the lowest radiation dose capable of initiating an image acquisition for the Carestream sensors was approximately 5 μGy air KERMA. The Unfors radiographic/fluoroscopic detector was used to determine the appropriate radiographic techniques to achieve an air KERMA between approximately 5 and 300 μGy at 50, 55, 60, 66, and 70 kVp with the Planmeca radiographic units and 70 kVp with the Gendex radiographic units.
2. The Carestream sensor was positioned in the test stand (Figure 4-23) on a custom Styrofoam tray. A one millimeter lead foil was placed behind the styrofoam to minimize backscatter. The source to detector distance was 30.5 cm (sensor positioned at the end of the dental extension cone as shown).
3. Two centimeters of PMMA and seven millimeters of aluminum were placed on the detector to simulate clinical imaging conditions. The short axis of the sensor was positioned parallel to the anode-cathode axis of the x-ray tube to minimize the anode-heel effect.
4. A series of exposures to the Carestream sensors were made at each kVp and 12-bit images were acquired without image enhancement.
5. The images were exported from the digital archive and analyzed with ImageJ, version 1.37 (National Institutes of Health, 2013). The images were opened, inverted, and the mean pixel value (PV_{mean}) and standard deviation within a 100 x 100 pixel region of interest (ROI) centered on the image was recorded at each dose. A two mm square area in the contrast deficit and adjacent to the deficit was used for the signal measurements from the radiography tally. This is approximately a 100 x 100 pixel area in the sensors (Carestream pixel spacing: 0.0185 mm).
6. The data were plotted and analyzed to achieve an optimized curve fit.

The ScanX® image plates (Size 2, model 6244) could not be evaluated in the same way because the "auto-ranging" function could not be disabled. Auto-ranging shifts the mean pixel values in the image to approximately the middle of the dynamic range regardless of radiation dose to the plate. In an attempt to bypass the auto-ranging feature, a five-step aluminum step wedge and lead sheet were used. The lead sheet was placed across one end of the image plate. The aluminum step wedge was placed flush against the lead sheet, and a margin of the plate was left uncovered. The objective was to utilize the full dynamic range of the image plate by saturating the uncovered portion of the plate and permitting very little radiation to reach the image plate beneath the lead. An example test image is shown in Figure 4-22.

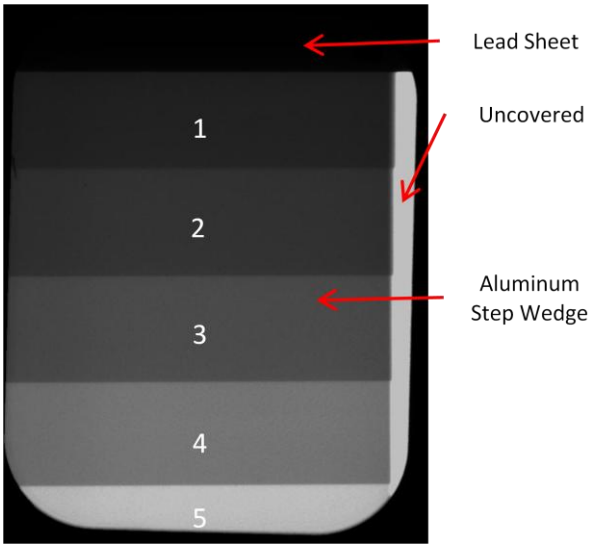

Figure 4-22. Example ScanX® Image with Aluminum Step Wedge and Lead Sheet

The ScanX® test acquisition was then performed as follows:

1. The attenuation through five millimeters of aluminum was measured at 50, 60, and 70 kVp. The attenuation factor was then used to estimate attenuation through each of the five steps in the step wedge. The steps were 3, 6, 9, 12, and 15 mm thick.

2. The image plates were erased to remove any residual signal and then exposed with the aluminum step wedge and lead sheet in place at 50, 60, and 70 kVp. The air KERMA was set high enough to saturate the uncovered portion of the image plates.
3. The image plates were processed on the Air Techniques processor, (Model ScanX IO ILE, serial number 2305). They can be processed in three resolution modes: intraoral standard (50 micron pixels), intraoral high (30 micron pixels), and intraoral very high (21 micron pixels). The intraoral standard setting was used for this analysis because this is the mode recommended by the manufacturer. Image enhancement was turned off and the images were acquired at 12 bits.
4. The images were exported from the digital archive and analyzed with ImageJ as previously described. The mean pixel value and standard deviation within a 100 x 100 pixel region of interest (ROI) centered on each step of the step wedge was recorded.
5. The data were plotted and analyzed to determine an optimized curve fit.

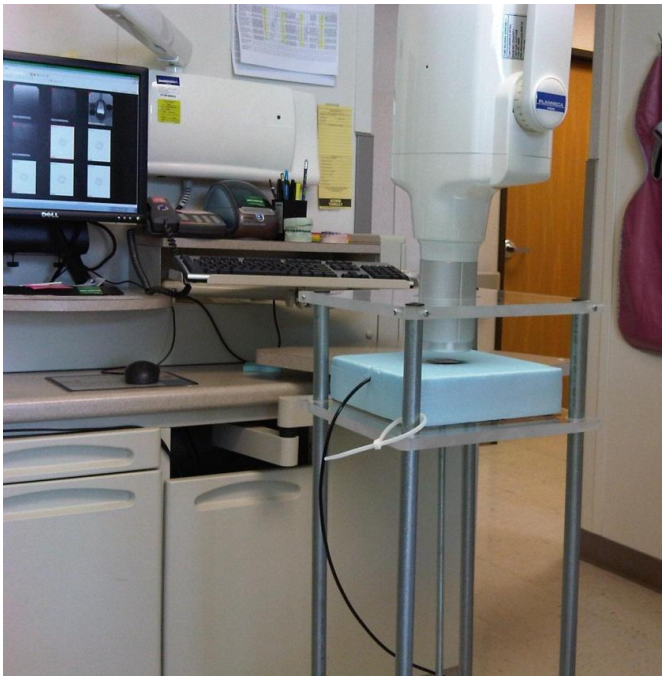

Figure 4-23. Sensor Response Image Acquisition

4.3.2. Results: Carestream Sensor Response

The detector response from five Carestream sensors coupled with the Planmeca radiographic units and five Carestream sensors coupled with the Gendex radiographic units is shown in Figure 4-24. These response curves represent the composite response of all sensors tested in each group and not the response of any single detector. The Carestream Product Line Manager of Intra-Oral Digital Imaging (personal communication, 18 Jan 2013) confirmed the manufacturer does not model or predict the response function and they expect variability between sensors. The responses were not identical but similar among the devices tested and for images acquired on both radiographic units. The response across the useful exposure range appears to be a linear function, with measurable energy dependence in the 50 to 70 kVp range, which will be described below. An air KERMA of approximately 140 and 155 μGy produced a mid-

range signal with the Planmeca and Gendex units respectively. The sensors approached saturation at around 300 μGy.

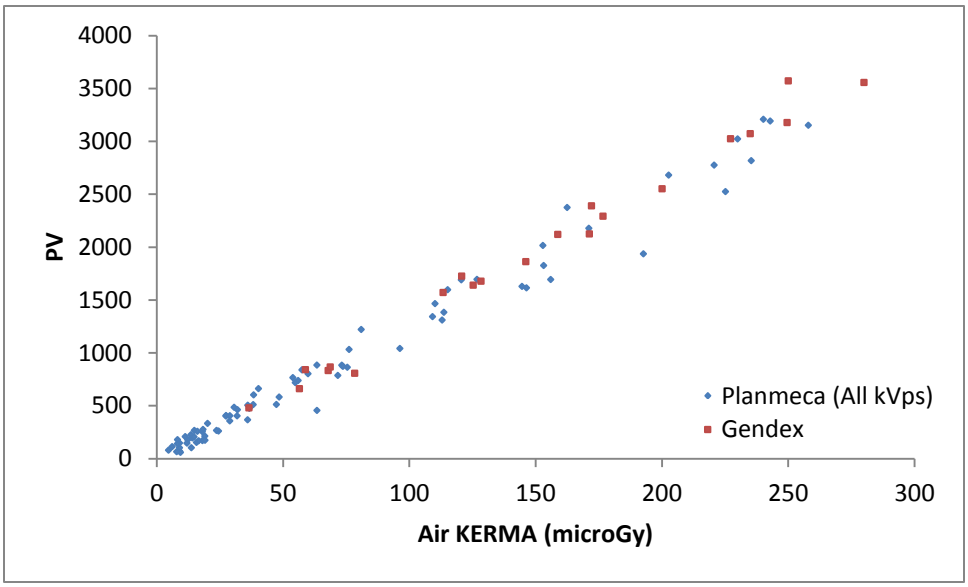

Figure 4-24. Carestream Sensor Response Function

An image acquired at ~140 μGy air KERMA is shown in Figure 4-25.

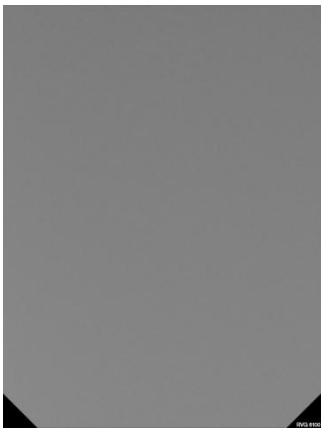

Figure 4-25. Carestream Sensor Image (140 μGy air KERMA)

To evaluate the degree of energy dependence, the Carestream sensor/Planmeca unit response data was sorted by kVp and a single factor analysis of variance (ANOVA) was performed (alpha = 0.05). The ANOVA results are shown in Table 4-6. The sensor response was normalized to PV per μGy air KERMA to minimize signal variabilities attributable to sensor dose differences.

Table 4-6. Carestream Sensor Single Factor ANOVA: By kVp

Source of Variation	*SS*	*df*	*MS*	*F*	*P-value*	*F crit*
Between Different kVps	250	4	62.4	11.2	8.44E-08	2.45
Within a single kVp	677	122	5.55	677	122	
Total	927	126				

Where:

SS = Sum of Squares

MS = Mean Square

df = degrees of freedom

F = F-test statistic

F_{crit} = Minimum F-value required to reject the null hypothesis that no difference exists between the groups

The ANOVA results suggest a measurable energy dependent response. (F-value exceeds F_{crit} and P-value indicating less than $8x10^{-6}$% chance there is no difference between the groups). The Carestream sensor/Planmeca unit response plotted by kVp is shown in Figure 4-26. A linear fit of the data at each kVp was also performed to demonstrate the response differences (the curve fits at 50, 60, and 70 kVp are shown).

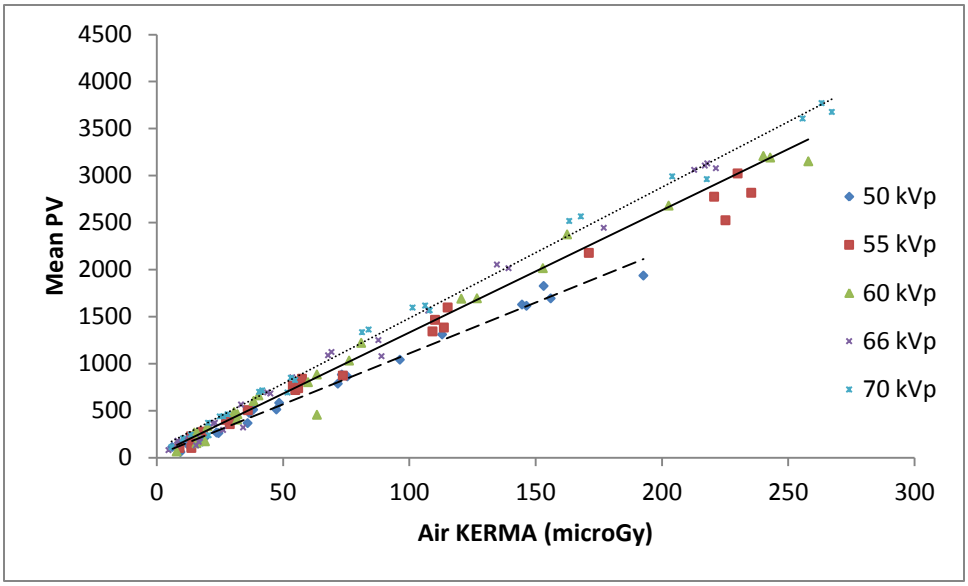

Figure 4-26. Carestream Sensor/Planmeca Unit Response by kVp

Ultimately, a generalized fit was required for the optimization. The following function form for this fit was proposed:

$$PV_{mean} = a_1(kVp * K_{air})^{a_2} \qquad \text{(Eq. 4-9)}$$

The data were linearized and a regression was performed to estimate coefficients a_1 and a_2. The regression statistics are shown in Table 4-7 and the final form of the equation used was:

$$PV_{mean} = 0.272 * (kVp * K_{air})^{0.976} \qquad \text{(Eq. 4-10)}$$

Table 4-7. Carestream/Planmeca Unit Curve Fit Regression Statistics

	Linearized Regression				Power Equation	
	Value	Error	*t Stat*	*P-value*	Value	Error
a_1	-1.30	0.123	-10.6	4.58E-19	0.272	0.026
a_2	0.976	0.015	64.0	2.14E-97	0.976	0.015

R^2: 0.970

Figure 4-27 demonstrates the actual versus predicted response.

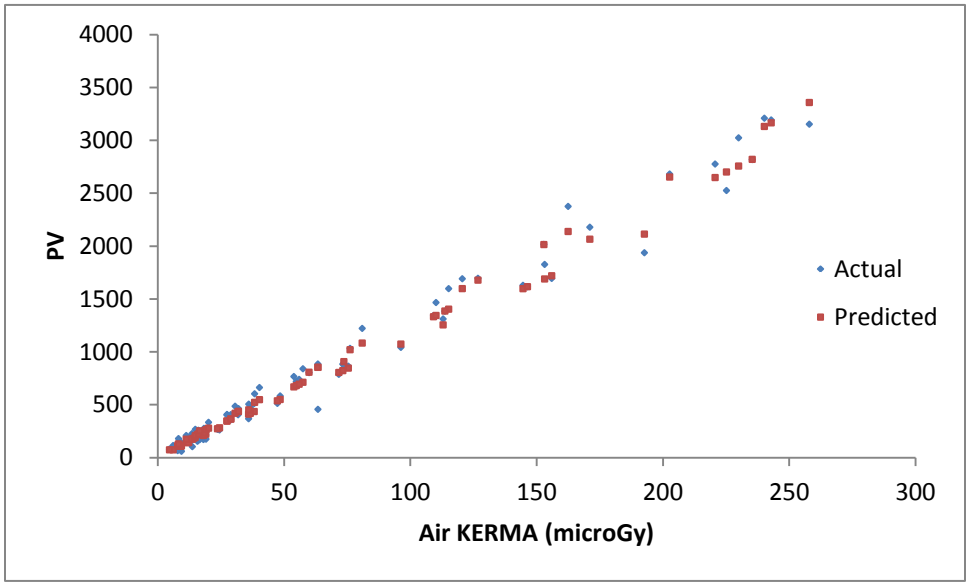

Figure 4-27. Carestream Sensor/Planmeca Unit Sensor Response

The 70 kVp data for the Carestream sensor/Planmeca units and Carestream sensor/Gendex units were also compared to evaluate radiographic unit dependent response. The ANOVA results are shown in Table 4-8 (data normalized to PV per μGy air KERMA as above) and suggest the sensor response is slightly greater for exposures acquired with the Planmeca units compared to the Gendex units at the same kVp and relative air KERMA to the detector.

Table 4-8. Planmeca/Gendex Single Factor ANOVA (70 kVp Comparison)

ANOVA

Source of Variation	*SS*	*df*	*MS*	*F*	*P-value*	*F crit*
Between Radiographic Units	91.0	1	91.0	38.6	1.63E-07	4.06
Within Same Unit	104	44	2.36			
Total	195	45				

The 70 kVp data for the Carestream sensors acquired with each radiographic unit are shown in Figure 4-28 with the linear curve fits. The Gendex response function is:

$$PV_{mean} = a_1 * K_{air} + a_2 \qquad \text{(Eq. 4-11)}$$

Where:
$a_1 = 13.3$
$a_2 = -33.7$

The regression statistics are given in Table 4-9.

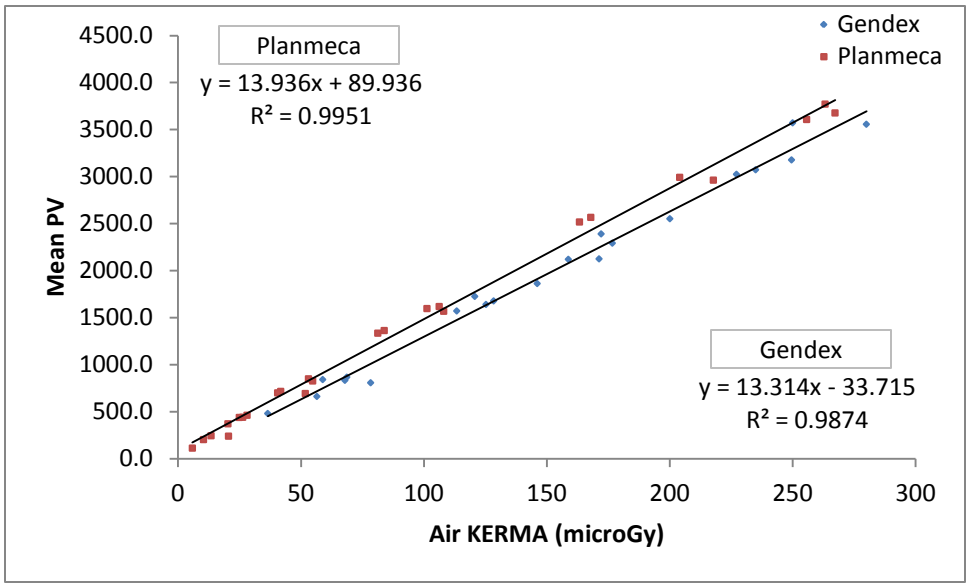

Figure 4-28. Detector Response Comparison: Planmeca and Gendex at 70 kVp

Table 4-9. Gendex Linear Regression Statistics

Regression Statistics					
Coefficients		Standard Error	t Stat	P-value	R^2
a_1	13.3	0.345	38.6	1.65E-19	
a_2	-33.7	56.9	-0.593	0.560	0.987

4.3.3. Results: ScanX® Sensor Response

The ScanX® detectors also demonstrated a linear energy dependent response. The data indicate a mid-range response would require nearly 1 mGy entrance air KERMA but this is unrealistically high. More likely, the ScanX® sensors are probably half the sensitivity of the Carestream sensors meaning it would require approximately twice the dose for the same signal response.

The ScanX® sensor response data for all detectors at 50, 60, and 70 kVp are plotted in Figure 4-29. The response plotted by kVp is shown in Figure 4-30. It is

possible the estimated air KERMA to the detector through each portion of the step wedge is not correct since a precise attenuation coefficient was not known. The auto-ranging feature may still be affecting the results as well. Given the uncertainty in these data, the ScanX® sensors were not considered further in the optimization.

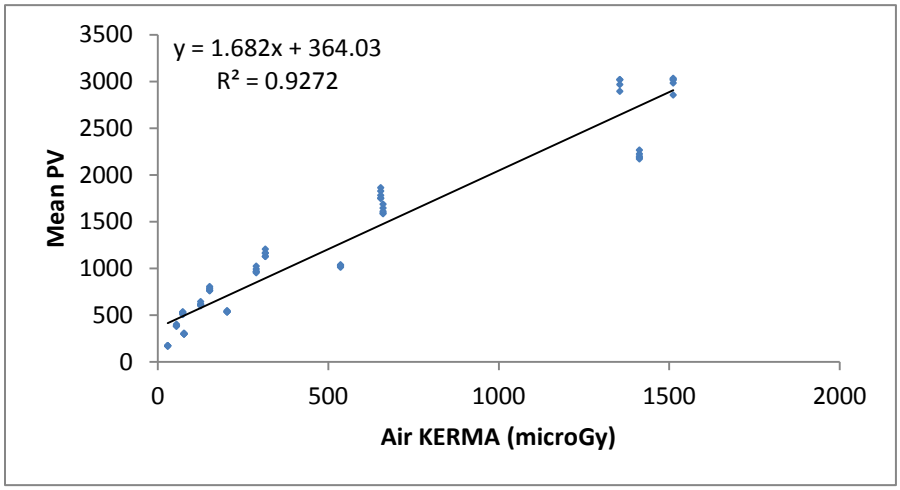

Figure 4-29. ScanX® Sensor Response

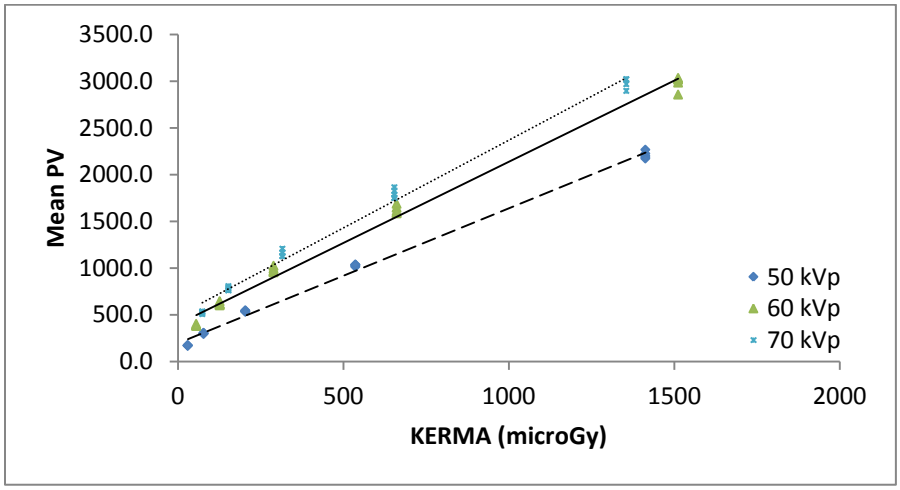

Figure 4-30. ScanX® Sensor Response by kVp

4.3.4. Noise Response

To complete the optimization, the noise response of each sensor was also needed. The standard deviation of the sensor signal in the 100 x 100 ROI placed in the center of each image was used for the noise measurements. This is equivalent to the size of the areas evaluated in the MCNPX model. The noise response for the Carestream/Planmeca and Carestream/Gendex units are shown in Figure 4-31. A linear regression of the noise response was used to determine a curve fit. The noise response function for both the Carestream/Planmeca and Carestream/Gendex units takes the form:

$$N = a_1 K_{air} + a_2 \qquad \text{(Eq. 4-12)}$$

Where:
a_1= 0.058 (Planmeca)
a_2= 6.53 (Planmeca)
a_1= 0.047 (Gendex)
a_2= 8.36 (Gendex)

The regression statistics are given in Tables 4-10 and 4-11.

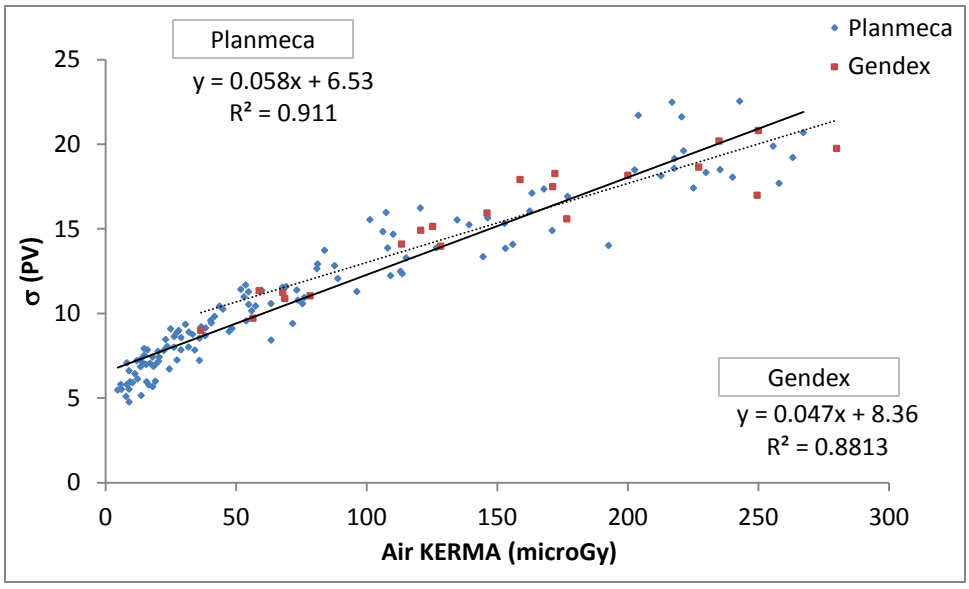

Figure 4-31. Carestream Noise Response

Table 4-10. Carestream Sensor/Planmeca Noise Regression Statistics

	Coefficients	*Standard Error*	*t Stat*	*P-value*
a_1	0.0575	1.61E-03	35.8	1.64E-67
a_2	6.53	0.177	36.8	6.03E-69

R^2: 0.911

Table 4-11. Carestream Sensor/Gendex Noise Regression Statistics

	Coefficients	*Standard Error*	*t Stat*	*P-value*
a_1	0.0466	3.93E-03	11.9	3.09E-10
a_2	8.36	0.647	12.9	7.35E-11

R^2: 0.881

A statistically significant energy dependence for the noise response was not demonstrated. The signal-to-noise ratio (SNR) for the Carestream sensors was also plotted where the SNR is defined as:

$$SNR = \frac{Mean\_PV(100x100ROI)}{\sigma(100x100ROI)} \qquad \text{(Eq 4-13)}$$

Where:

N = the standard deviation of the pixel values in the 100x100 pixel ROI (noise)

"N" will be used to represent noise throughout this and subsequent chapters.

The data are graphed in Figure 4-32. The SNR curves were not used for the optimization but were helpful in visualizing differences in response between the sensor/radiographic unit combinations.

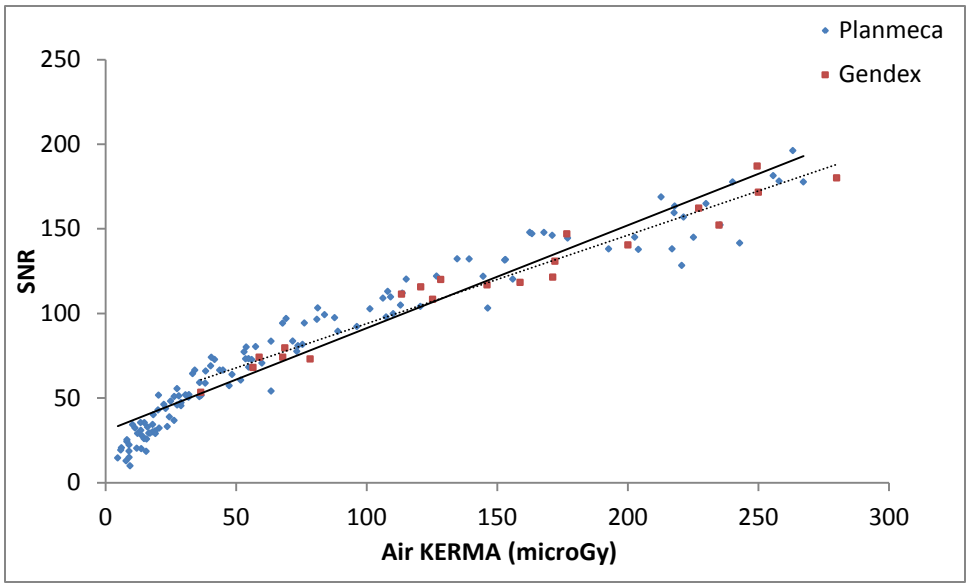

Figure 4-32. Signal-to-Noise Response for Carestream Sensors

4.3.5. Dose Rate Effects

A significant reduction in sensor response was observed when the Carestream sensors were imaged at dose rates below approximately 300 μGy/mAs. Since the average dose rate at all kVps was greater than ~400 μGy/mAs, this was not a clinically significant finding (see Appendix G for average measured dose rates at all kVps), and this effect was not incorporated into the sensor response function. Figure 4-33 demonstrates the observed effect for images acquired at approximately 300 μGy air KERMA. The exposure times were approximately 38 msecs, 105 msecs, and 1.4 seconds). The source to sensor distance was adjusted to maintain the same detector dose and normalized to microGray per milli-Ampere seconds.

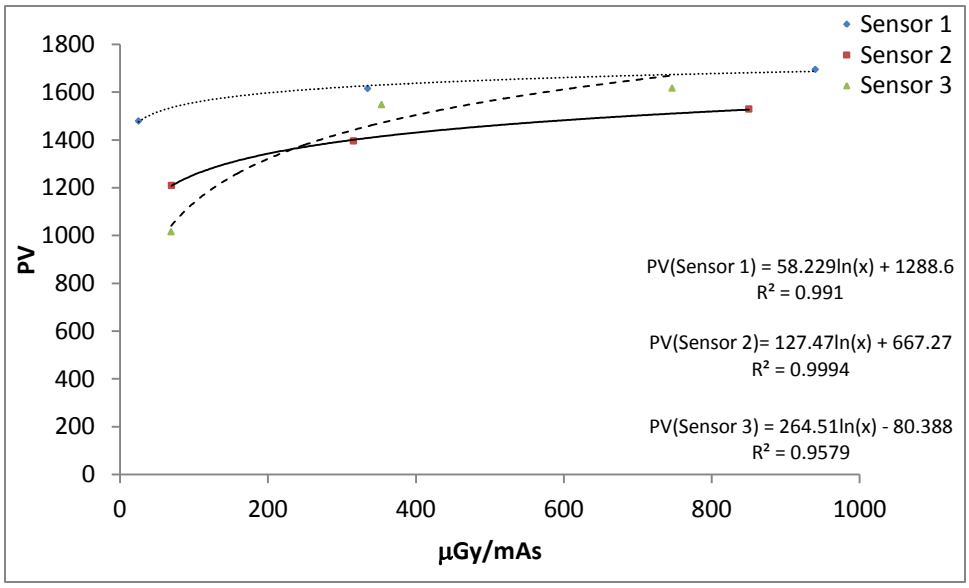

Figure 4-33. Carestream Dose Rate Effects

4.3.6. Detector Reproducibility and Results

Five images per sensor were acquired with five Carestream sensors/Gendex units at an air KERMA adequate to produce a mean pixel value of approximately 2000 (mid-range of response). The mean and standard deviation of the pixel values in a 100 x 100 pixel ROI centered on each of the five images was recorded. The Carestream intra-sensor reproducibility (reproducibility of response on individual sensors) is shown in Table 4-12 and inter-sensor variability is presented in Table 4-13. Since the data were acquired with different radiographic units at slightly different exposures, the average pixel value per µGy air KERMA instead of the average pixel value was used to evaluate the inter-sensor response.

Table 4-12. Carestream Intra-Sensor Reproducibility (Acquired with Gendex Unit)

Intra-Sensor Reproducibility							
Sensor ID	Air KERMA to Sensor (μGy)	Average Signal	σ Signal	%σ (Signal)	Average Noise	σ Noise	%σ (Noise)
Sensor 1	250	1646	43.0	2.6%	12.2	0.3	2.4%
Sensor 2	250	1528	36.7	2.4%	14.6	0.3	2.1%
Sensor 3	240	1427	32.5	2.3%	12.5	0.3	2.1%
Sensor 4	230	1451	31.0	2.1%	13.6	0.3	2.1%
Sensor 5	230	1408	31.3	2.2%	13.4	0.2	1.4%
			AVG:	**2.3%**		**AVG:**	**2.0%**

Table 4-13. Carestream Inter-Sensor Reproducibility (Acquired with Gendex Unit)

Inter-Sensor Reproducibility						
Average Signal	Average PV/μGy	σ PV/μGy	%σ (Signal)	Average Noise	σ Noise	%σ (Noise)
1492	6.2	0.3	4.7%	13.3	1.0	7.6%

The measured sensor response variability was utilized as a benchmark for comparison to the calculated signal response uncertainty presented below.

4.3.7. Uncertainty Analysis

The uncertainty analysis associated with the Carestream/Planmeca sensor response function (Eq. 4-10) was calculated as:

(Eq 4-14)

$$\sigma_{PV} = \sqrt{\begin{aligned}&\left[\left(kVp^{*}K_{air}\right)^{a_2}\sigma_{a_1}\right]^2 + \left[\left(a_1a_2\left(kVp^{*}K_{air}\right)^{a_2-1}\right)\sigma_{kVp}\right]^2 \\ &+\left[\left(a_1a_2kVp\left(kVp^{*}K_{air}\right)^{a_2-1}\right)\sigma_{K_{air}}\right]^2 + \left[\left(a_1\left(kVp^{*}K_{air}\right)^{a_2} * \ln\left(kVp^{*}K_{air}\right)\right)\sigma_{a_2}\right]^2\end{aligned}}$$

The uncertainty analysis for the Carestream/Gendex sensor response function (Eq 4-11) was calculated as:

$$\sigma_{PV} = \sqrt{\left(K_{air}\sigma_{a_1}\right)^2 + \left(a_1\sigma_{K_{air}}\right)^2 + \left(\sigma_{a_2}\right)^2} \qquad \text{(Eq. 4-15)}$$

The uncertainty analysis for the Carestream/Planmeca and Carestream/Gendex sensor noise response functions (Eq. 4-12) were calculated as:

$$\sigma_{Noise} = \sqrt{\left(K_{air}\sigma_{a_1}\right)^2 + \left(a_1\sigma_{K_{air}}\right)^2 + \left(\sigma_{a_2}\right)^2} \qquad \text{(Eq. 4-16)}$$

Table 4-14 defines the terms for Equations 4-15 and 4-16; Table 4-15 defines the terms for Equation 4-17. The location in the text where the values were presented is also shown. The average uncertainties for the sensor signal and noise response functions are given in Table 4-16.

Table 4-14. Definition of Terms (Equations 4-10 and 4-11)

Symbol	Definition	Value (Units)	Location in Text
Carestream/Planmeca Sensor Response Function			
kVp	Peak Kilovoltage	Multiple Values (kVp)	Table 4-2
σ_{kVp}	Uncertainty in Peak Kilovoltage	Multiple Values (kVp)	Table 4-2
K_{air}	Entrance air KERMA	Multiple Values (μGy)	Appendix H
σ_{Kair}	Uncertainty in measured K_{air}	Multiple Values (μGy)	Appendix G
a_1	Coefficient	0.272 (Unitless)	Eq. 4-10
σ_{a1}	Coefficient a_1 Standard Error	2.60E-02 (Unitless)	Table 4-7
a_2	Coefficient	0.976 (Unitless)	Eq. 4-10
σ_{a2}	Coefficient a_2 Standard Error	1.50E-02 (Unitless)	Table 4-7
Carestream/Gendex Sensor Response Function			
K_{air}	Entrance air KERMA	Multiple Values (μGy)	Appendix H
σ_{Kair}	Uncertainty in measured K_{air}	Multiple Values (μGy)	Appendix G
a_1	Coefficient (X Variable)	13.3 (Unitless)	Table 4-9
σ_{a1}	Coefficient a_1 Standard Error	3.45E-01(Unitless)	Table 4-9
a_2	Coefficient (Intercept)	-33.7 (Unitless)	Table 4-9
σ_{a2}	Coefficient a_2 Standard Error	5.69E+01(Unitless)	Table 4-9

Table 4-15. Definition of Terms (Equation 4-12)

Carestream/Planmeca Noise Response Function			
$\mathbf{K_{air}}$	Entrance air KERMA	Multiple Values (μGy)	Appendix H
$\boldsymbol{\sigma_{Kair}}$	Uncertainty in measured K_{air}	Multiple Values (μGy)	Appendix G
$\mathbf{a_1}$	Coefficient (X Variable)	0.058 (Unitless)	Table 4-12
$\boldsymbol{\sigma_{a1}}$	Coefficient a_1 Standard Error	1.61E-03(Unitless)	Table 4-12
$\mathbf{a_2}$	Coefficient (Intercept)	6.53 (Unitless)	Table 4-12
$\boldsymbol{\sigma_{a2}}$	Coefficient a_2 Standard Error	0.177 (Unitless)	Table 4-12
Carestream/Gendex Noise Response Function			
$\mathbf{K_{air}}$	Entrance air KERMA	Multiple Values (μGy)	Appendix H
$\boldsymbol{\sigma_{Kair}}$	Uncertainty in measured K_{air}	Multiple Values (μGy)	Appendix G
$\mathbf{a_1}$	Coefficient (X Variable)	0.0476 (Unitless)	Table 4-12
$\boldsymbol{\sigma_{a1}}$	Coefficient a_1 Standard Error	3.93E-03(Unitless)	Table 4-12
$\mathbf{a_2}$	Coefficient (Intercept)	8.36 (Unitless)	Table 4-12
$\boldsymbol{\sigma_{a2}}$	Coefficient a_2 Standard Error	6.47E-01(Unitless)	Table 4-12

Table 4-16. Sensor Signal and Noise Response Uncertainties

	Error Analysis: Signal Response Functions				
	%σ (kVp)	**%σ (K_{air})**	**%σ Coef a_1**	**%σ Coef a_2**	**Total %σ**
Carestream/Planmeca	2.1%	7.0%	9.5%	1.5%	17%
Carestream/Gendex	N/A	13%	2.6%	170%	8.9%

	Error Analysis: Noise Response Functions				
	%σ (K_{air})	**%σ Coef a_1**	**%σ Coef a_2**		**Total %σ**
Carestream/Planmeca	7.0%	2.8%	2.7%		3.4%
Carestream/Gendex	8.4%	7.7%	7.0%		6.7%

The Carestream/Gendex calculated sensor signal and noise response uncertainties are comparable to the measured inter-sensor variabilities (Table 4-13).

Chapter 5: Computer Modeling and Results

The development and validation of the computer model to include the proposed anthropomorphic and clinical validation phantoms will be described in this chapter. A brief description of the post-processing steps needed to format the data for analysis will also be given.

5.1. INPUT DECK

The input deck was finalized after the appropriate phantom design, source characterization, and radiography tally configuration was devised. The input parameters used for the optimization were selected in parallel with development of the input deck. The optimization parameters themselves will be discussed in chapter 6. A description of the input deck and post-processing is given below.

5.1.1. Phantom Models

The composition and dimensions of an appropriate dental phantom have been discussed by several authors. In an early study, Manson-Hing (1961) concluded that type 1100 aluminum appropriately simulates dentin and is an excellent material to study radiographic contrast. He recommended a step wedge ranging in thickness from one to eight millimeters to evaluate the system contrast scale.

The phantom described by Attaelmanan, et al (2001) could be easily fabricated to measure the SNR. It was simply a 1 mm diameter 1.25 mm deep hole drilled in a 10 mm block of aluminum.

McDavid, et al (1982) describes a contrast-detail phantom consisting of a 25 mm x 25 mm by 7 mm aluminum block with ten flat-bottomed cylindrical holes two mm in diameter ranging in depth from 0.05 to 0.5 mm drilled in a random array on the phantom.

Wakoh, et al emulated this design changing nothing but the hole depths and Shibuya, et al (2000) also designed a similar phantom.

Based upon these findings, two phantoms, an anthropomorphic phantom and a clinical validation phantom, were employed in this work. The clinically realistic anthropomorphic phantom was necessary for the optimization to ensure the results were relevant. The clinical validation phantom was used to verify the radiation transport simulation results for the selected optimization parameters.

5.1.1.1. Anthropomorphic Phantom

The phantom used for the optimization was designed to simulate the patient anatomy in a simple yet clinically realistic manner. A typical intraoral radiograph captures an image of the molars with overlying cheek tissue. As a rough approximation, the model design simulates the cheek and molar. For the purposes of this study, the roots of the molar and jaw (maxilla or mandible) were not considered. Figure 5.1 demonstrates the anatomical plane of the molar modeled in this study.

The appropriate thickness and density of the cheek was determined through review of clinical sinus computed tomography studies. A total of 40 studies, 20 male and 20 female patients ranging in age from 18 to 40, were reviewed. The thickness of the cheek between the molars and skin surface was measured. The average CT number in an approximately 500 mm^2 ROI within this area was recorded. An example CT image with representative measurements is shown in Figure 5-2. The average cheek thickness of the patient population sampled was 22 mm (σ: 2.5 mm). The average CT number within the ROI was -5.11 (σ: 101.7). The large standard deviation for the CT numbers in this area is consistent with the variety of tissues present including skin, muscle, and fat.

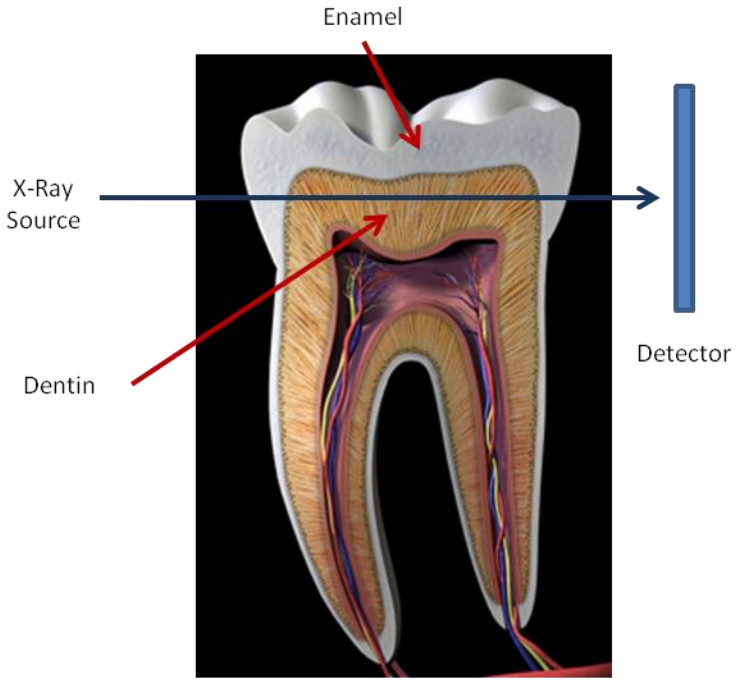

Figure 5-1. Anatomical Plane for Anthropormorphic Phantom (Figure Source: Zygote Media Group)

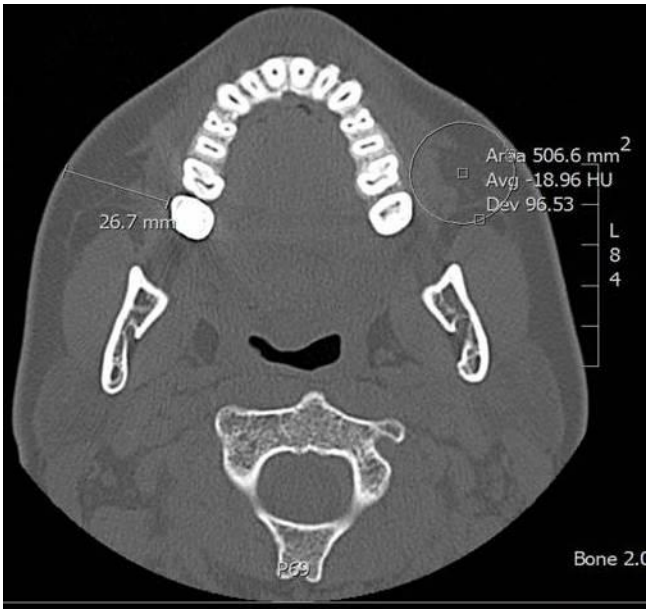

Figure 5-2. Example CT Image

The tissue density was calculated using the linear relationship established between material density and CT number for the CT scanner at this facility. This relationship was measured using the CT number module of the American College of Radiology (ACR) CT Accreditation phantom (ACR, 2013). The materials and material density for the phantom are shown in Table 5-1. The measured CT numbers for these materials were plotted, and a linear regression was performed to find the best curve fit for the data points. The data are plotted in Figure 5-3 and the regression statistics are shown in Table 5-2.

Table 5-1. ACR CT Accreditation Phantom CT Number Module Materials

Object	Expected CT number	CT number measured	Physical Density (g/cm^3)	Linear Attenuation Coefficient (cm^{-1}) @ 75 keV
Bone, Cortical	+850 to +970	947.7	1.92	0.4721
Air	-1005 to -970	-1002.6	1.21E-03	0.0002
Acrylic (PMMA)	+110 to +130	119.9	1.19	0.2135
Polyethylene	-107 to -84	-95.4	0.93	0.1730
Water	-7 to +7	0.9	1	0.1890

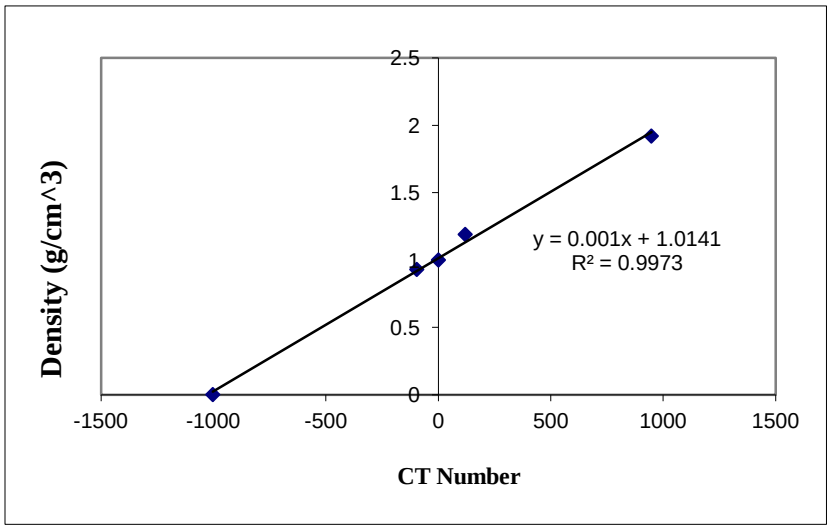

Figure 5-3. CT Number vs Density

Table 5-2. CT Number vs. Density Curve Fit Statistics

	Coefficients	*Standard Error*	*t Stat*	*P-value*
Intercept	1.01	0.0184	55.3	1.31E-05
X Variable	9.88E-04	2.96E-05	33.4	5.89E-05

R^2: 0.997

The average cheek tissue density, estimated using the linear curve fit, is 1.01 g/cm^3. Four component soft tissue was selected to represent the cheek tissue in the final anthropomorphic phantom (International Commission on Radiation Units and Measurements (ICRU), 1989). The material composition and density is presented in Table 5-3.

Table 5-3. ICRU Soft Tissue (Four Component) Composition by Weight Fraction

Element	**Weight Fraction**
H	0.101174
C	0.111000
N	0.026000
O	0.761826

Density (g/cm^3) =1.0000E+00

The composition of enamel and dentin was obtained from the literature. Gutierrez-Salazar and Reyes-Gasga (2003) measured the chemical composition of the human tooth (enamel and dentin) using characteristic x-ray dispersive spectroscopy. The composition in atom percent was given at three anatomical locations in both materials. For enamel, the outer surface, middle, and enamel-dentin junction (EDJ) composition was provided. The dentin composition was specified at the EDJ, middle, and inner portion. The composition of the middle enamel and middle dentin portions of the tooth were selected for the phantom and the data in atom percent was converted to weight fraction used for the phantom (Table 5-4).

Table 5-4. Composition of Enamel and Dentin (Gutierrez-Salazar and Reyes-Gasga)

		Enamel Middle (EM)		[1]Dentin Middle (DM)	
Element	**Atomic Weight**	**Atom % (σ)**	**Weight Fraction**	**Atom % (σ)**	**Weight Fraction**
C	12.0096	36.28 (0.84)	0.2120	52.81 (3.16)	0.3705
O	15.999	34.21(0.67)	0.2663	30.89 (2.14)	0.2886
Na	22.989	0.44(0.13)	0.0049	0.42(0.07)	0.0057
Mg	24.305	0.23(0.07)	0.0027	0.34(0.06)	0.0049
P	30.973	10.86(0.14)	0.1636	6.29 (0.46)	0.1139
Cl	35.446	0.25(0.08)	0.0043	0	0
Ca	40.078	17.74	0.3459	9.24 (0.70)	0.2164
TOTAL:		100	100	100	100

Accurate estimates of enamel and dentin density and thickness were difficult to acquire from the CT studies because of inconsistent positioning of the teeth within the scanned volume and difficulty defining the two materials within the tooth. Instead, density and thickness estimates were also obtained from the literature. The densities reported by Coklica, et al (1969) and Weidmann, et al (1967) were used as a starting point for the model. Coklica reported the density distribution of dentin varies with the location in the tooth, tooth age, and fluoride content. The measured density ranged from less than 2.22 to greater than 2.31 g/cm^3. Weidmann concluded enamel density varies from tooth to tooth and also from region to region in each tooth. The authors reported an enamel density range of 2.87 to 2.97 g/cm^3. Neither of these studies presented a way to calculate a representative average density for dentin and enamel but Willner, et al (2013) published preliminary results using quantitative x-ray phase-contrast CT to measure the dentin and enamel density at multiple locations in a single tooth. A weighted average of the dentin and enamel densities measured with this technique (2.19 and 2.92 g/cm^3 respectively) was used for the computational model.

[1] The atom% for the middle dentin composition was normalized because the published composition was less than 100% (98.98%).

Smith, et al (2006) studied the molar enamel thickness and enamel-dentin junction shape of modern human populations. Enamel thickness and dentin area vary with tooth position but for the purposes of this study, a representative average was desired. The phantom tooth was modeled using the average enamel thickness (EAT) of the sampled population molars (1.25 mm). The dentin thickness was calculated as the average bicervical diameter minus the average EAT of the sampled population molars (7.3 mm).

5.1.1.2. Clinical Validation Phantom

The contrast phantom used for clinical validation was donated by McDavid, described above. A photograph of the phantom is shown in Figure 5-4.

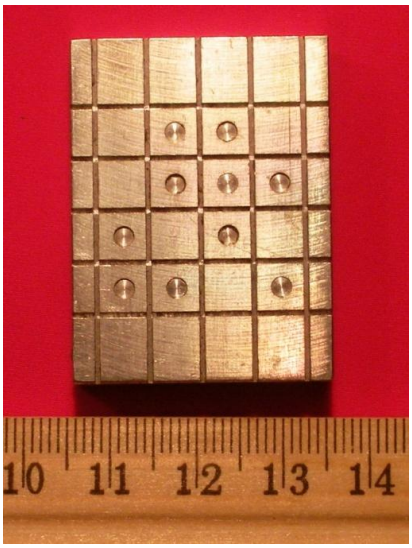

Figure 5-4. Aluminum Phantom for Clinical Validation (McDavid)

The cheek tissue for the clinical phantom was simulated with polymethylmethacrylate (PMMA) and compared to the attenuation properties of the ICRU tissue using the relationship:

$$e^{-\frac{\mu}{\rho}\rho x_A} = e^{-\frac{\mu}{\rho}\rho x_B} \quad \text{(Eq 5-1)}$$

Where:

ρ(A=PMMA)=1.19 g/cm^3

μ/ρ(A=PMMA)= 0.3032 cm^2 /g (at 30 keV)

ρ(B=ICRU Soft Tissue)= 1.0 g/cm^3

μ/ρ (B=ICRU Soft Tissue)= 0.3604 cm^2 /g (at 30 keV)

x(PMMA)= 2.2 cm

PMMA in two cm sheets was clinically available, which is the thickness used in the model.

5.1.1.3. Contrast Object

To perform the optimization, measurement points were needed in the phantoms. Clinical images of the aluminum phantom without added PMMA were acquired and evaluated first to estimate a contrast-detail threshold. The phantom was imaged using the current clinical techniques for bitewings at this facility: 63 kVp and 1 mAs with ten Planmeca radiographic unit/sensor combinations and 70 kVp, 0.5 mAs with eight Gendex radiographic unit/sensor combinations. For this survey no attempt was made to control for variations in radiographic unit output. The average entrance air KERMA for the Gendex units was 630 μGy (+/- 70) and for the Planmeca units 720 μGy (+/- 30). A representative image of the phantom is shown in Figure 5-5. The location of a particular well depth, which was not known *a priori,* was determined after signal-difference-to-noise ratios were calculated using Equation 2.3 where the mean signal in a 100x100 pixel circular ROI placed adjacent to each well (background) was subtracted from the mean

signal of the ROI centered in each well and divided by the standard deviation of the background signal.

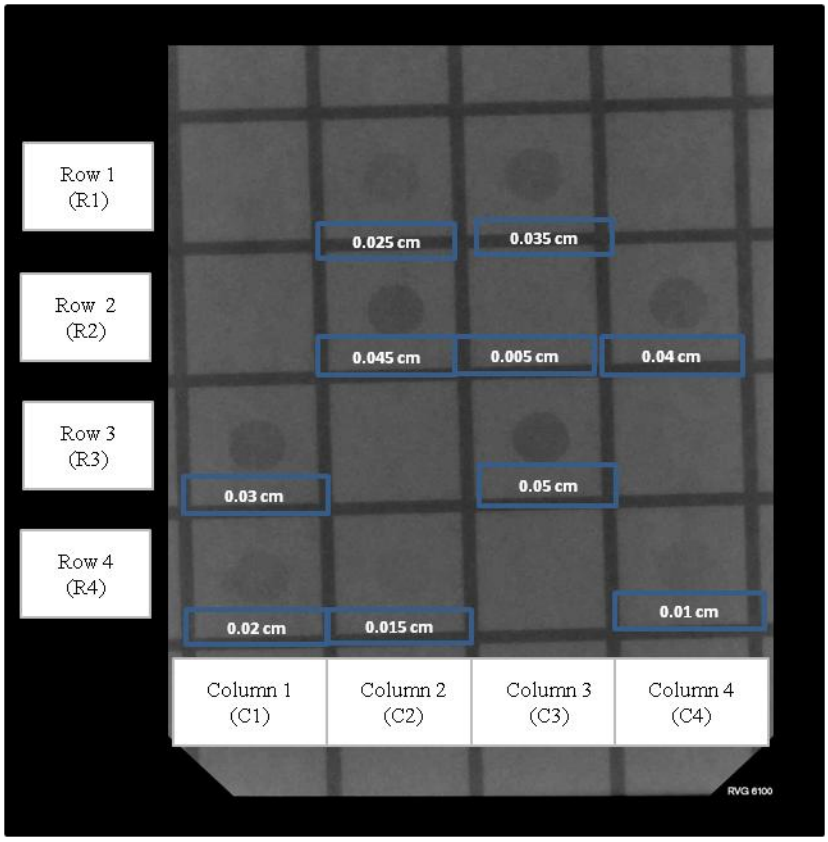

Figure 5-5. Contrast Detail Phantom Image Object Depths

The average SdNRs and standard deviations for the Gendex and Planmeca units by contrast object position are plotted in Figures 5-6 and 5-7 (full data sets in **Appendix K**). The positions are indicated by horizontal row and vertical column, as labeled in Figure 5-5. The relative SdNR for positions R3C1 and R2C4 (0.03 and 0.04 cm object depths) were reversed for the Gendex and Planmeca units. Since the values were more consistent for the sensors exposed with Planmeca units, the object depths were assigned based on the relative SdNRs calculated with the Carestream/Planmeca data.

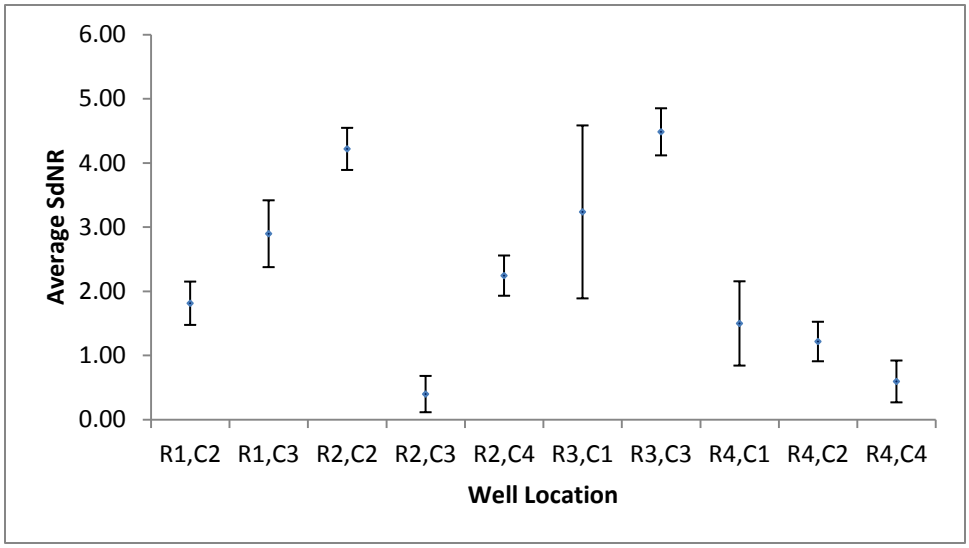

Figure 5-6. Gendex Unit/Sensor Mean SdNR

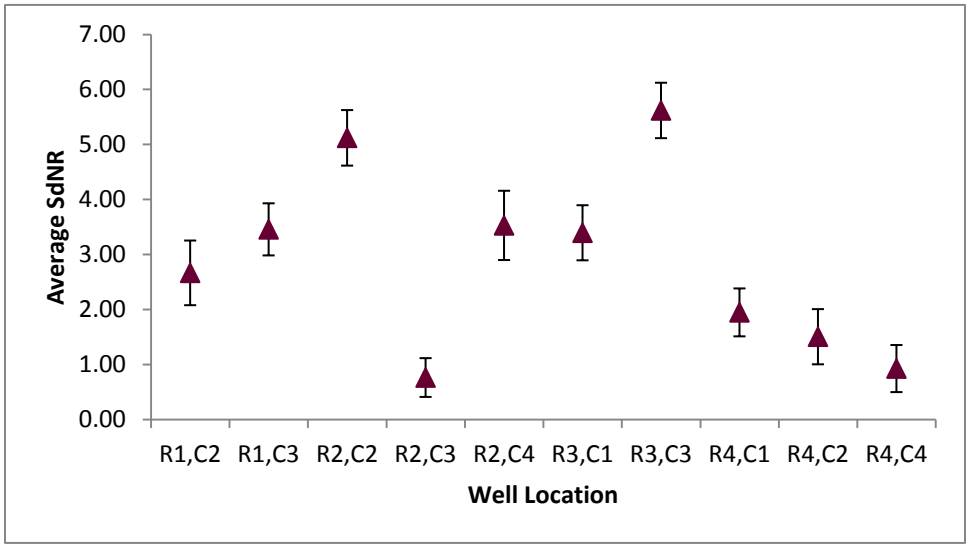

Figure 5-7. Planmeca Unit/Sensor SdNR

Based on this survey, the initial MCNPX phantom model was constructed using a single air-filled contrast object deficit. Early trials with a full representation of the

aluminum phantom proved a large radiography tally matrix would be required to adequately capture the phantom details and the size of the tally grid would necessitate excessive processing time to acquire results with acceptable bin uncertainties. For this reason, it was impractical to generate random variations of the phantom geometry as originally proposed. Instead, a realistic range of well depths to investigate was identified. This work is discussed in section 5.1.3.

The phantoms used for the optimization and clinical validation are shown in Figures 5-8 and 5-9.

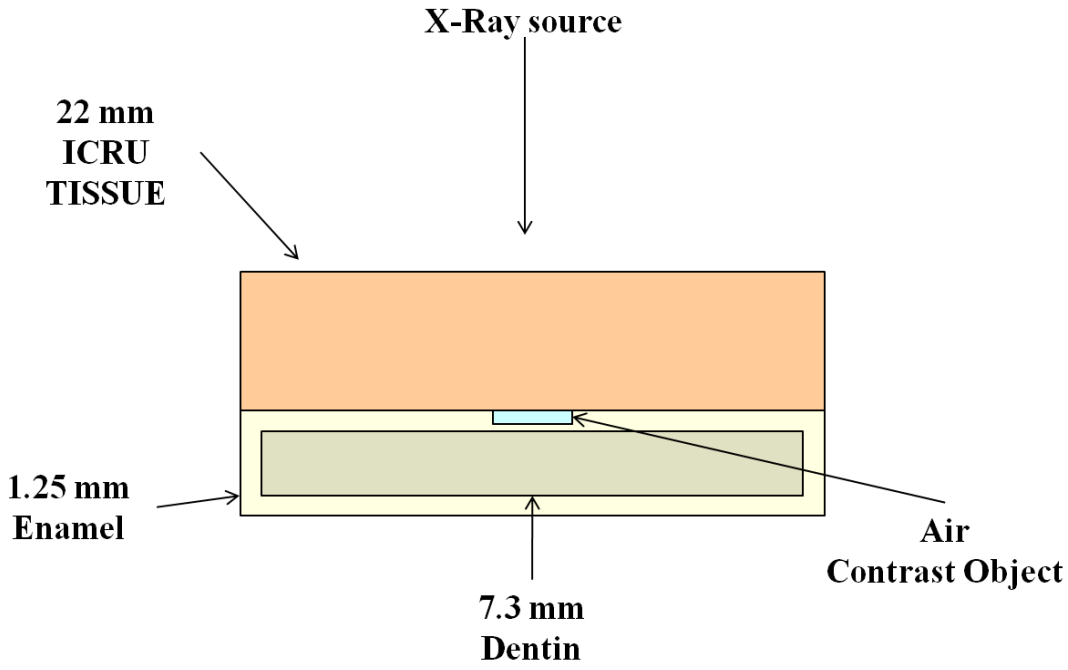

Figure 5-8. Anthropomorphic Phantom

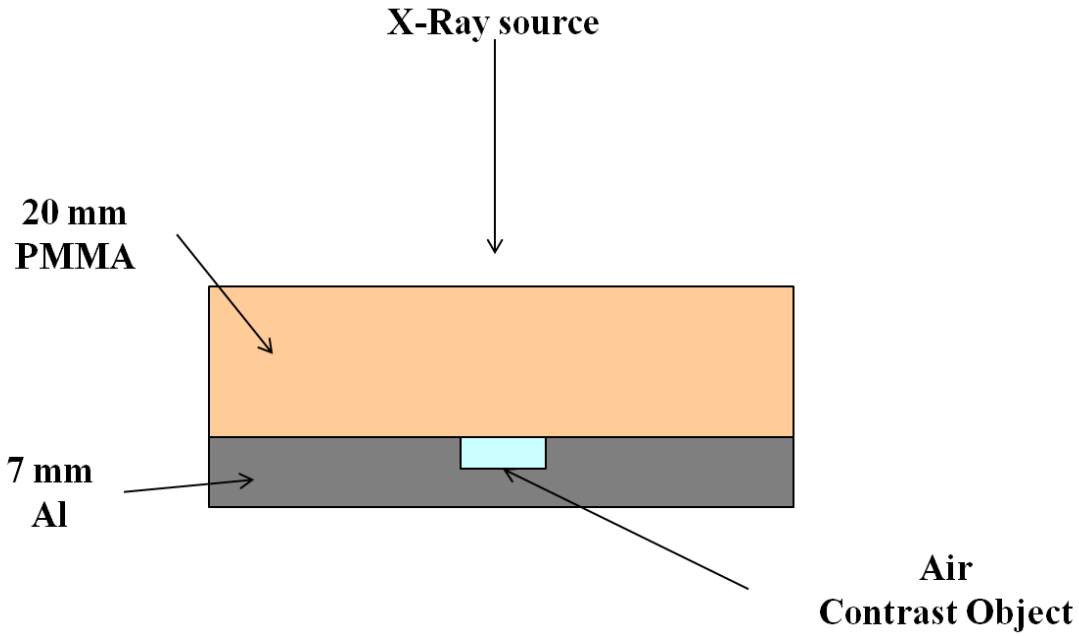

Figure 5-9. Clinical Validation Phantom

5.1.2. Source Characterization

As previously described, the IPEM generated spectra were used for the MCNPX model. The peak energies were selected based on clinically available or potentially available settings. The interval between peak energies was chosen once acceptable interpolation statistics were established.

5.1.2.1. Selection of Peak Energies

MCNPX trials with the aluminum phantom were performed to investigate the uncertainties associated with interpolating results between kVps. The objective was to keep the number of kVps used in the simulation at a minimum because of the time required to complete each run but an uncertainty tolerance had to be established. The allowable interpolation uncertainty was required to be less than the measured intra-sensor mean signal variation, 2.3% (Table 4-12). The average signal in four bins centered on the contrast well and four bins adjacent to the contrast well (background) were compared for

a run at 60 kVp versus the mean well and background at 60 kVp calculated via linear interpolation from runs performed at 50 and 70 kVp. A 10x10 matrix with a 0.5 cm radius was used for the radiography tally. The results–presented in Table 5-5–show an uncertainty of approximately 4%, which is higher than the established limit. Therefore, linear interpolation between potentials as widely spaced as 50 to 70 kVp was rejected.

Table 5-5. Interpolation Results (50 to 70 kVp Interval)

	Mean Well		
	Interpolation	Rad Tally	% Diff
	2.61E-05	2.72E-05	-4.0
60 kVp	Mean Background		
	Interpolation	Rad Tally	% Diff
	2.51E-05	2.61E-05	-3.9

Additional runs were performed with an interpolation interval of 60 to 66 kVp. The radiography tally versus interpolated well and background signals at 63 kVp were compared to validate whether the uncertainty could be reduced further. The results are shown in Table 5-6.

Table 5-6. Interpolation Results (60 to 66 kVp Interval)

	Mean Well		
	Interpolation	Rad Tally	% Diff
	2.90E-05	2.91E-05	-0.3
63 kVp	Mean Background		
	Interpolation	Rad Tally	% Diff
	2.80E-05	2.80E-05	-0.3

Because the interpolation uncertainties at the reduced kVp interval were less than the limit of 2.3%, the MCNPX runs were ultimately performed at 50, 55, 60, 66, 70, 75, 80, 85, and 90 kVp. Tally estimates at 52, 57, and 63 kVp were calculated through linear interpolation.

5.1.2.2. Source Angular Distribution

The source in the MCNPX simulations was assigned an angular distribution in order to maximize the problem efficiency. The source particles were directed in a cone toward the phantom and confined to a two cm radius, adequate to cover the phantom and radiography tally grid.

An illustration of the source distribution is shown in Figure 5-10.

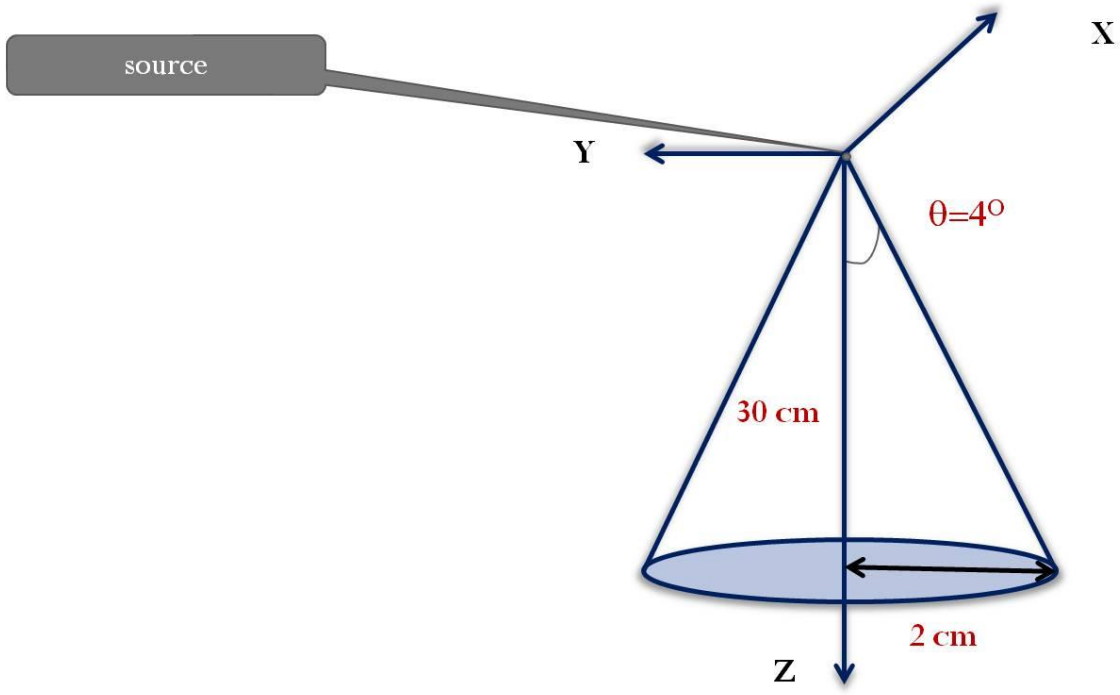

Figure 5-10. Source Angular Distribution

5.1.3. Radiography Tally

The radiography tally card is described in the MCNPX user's manual (Pelowitz, ed.). The tally plane was positioned parallel to the posterior (in relation to the x-ray source) side of the phantom. Figure 5-11 is a visual representation of the radiography tally and required input parameters (grid center, reference point, and image grid bins).

The final phantom design, in particular the contrast object depth, was chosen to maximize relevance to clinical conditions through the process defined below.

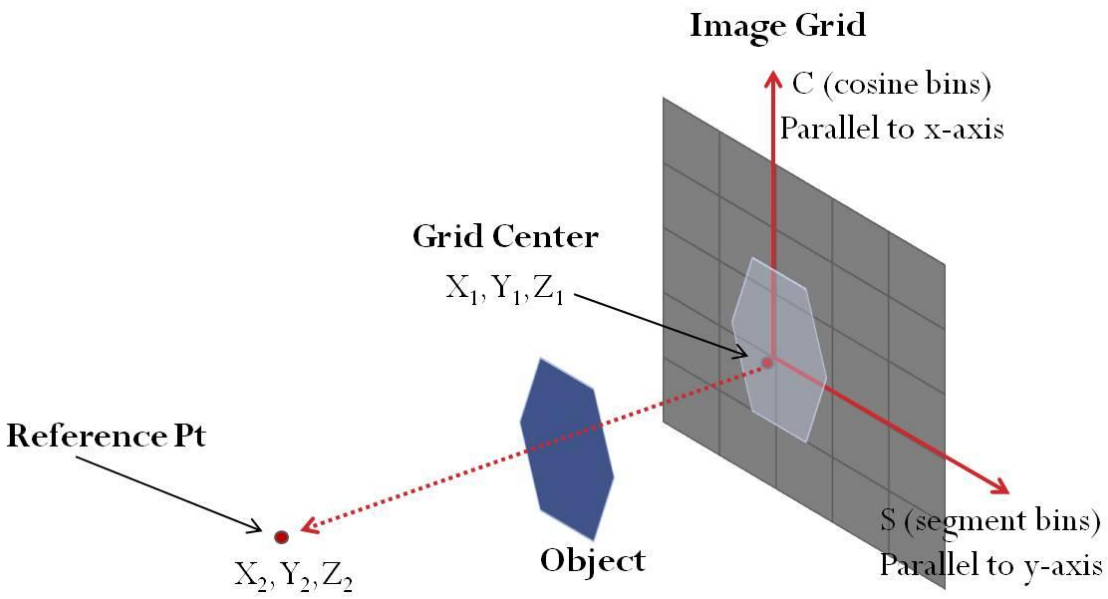

Figure 5-11. Radiography Tally (Fensin, et al, 2007)

Using the Rose Criterion as a guide, one would expect to reliably visualize objects as long as the SdNR is at least five. Quantitatively, the clinical trial suggests the 0.045 cm well depth may be the threshold. However, shallower depths are visible, although some are not clearly defined. Based on a *qualitative* assessment of the images, the contrast threshold depth was tentatively set to 0.03 cm. Trial runs were performed to discern the MCNPX threshold using the radiography tally before the final well depth was selected.

A series of MCNPX runs with the aluminum phantom were accomplished at 60 kVp while varying the contrast well depth from 0.01 to 0.1 cm. This range was used to clearly define the lower contrast limit as well as provide an object depth that should be reliably visualized on clinical images. A 5x5 radiography tally grid with a 0.5 cm radius was used to minimize processing time. The mean well signal and signal difference (mean well minus mean background signal) are shown in Table 5.7.

Table 5-7. Radiography Tally Data (60 kVp)

Depth (cm)	Mean Well Signal	Signal Difference	% Difference
0.1	3.290E-05	4.059E-06	12.3%
0.05	3.082E-05	1.986E-06	6.4%
0.04	3.043E-05	1.598E-06	5.3%
0.03	3.005E-05	1.219E-06	4.1%
0.02	2.968E-05	8.480E-07	2.9%
0.01	2.931E-05	4.769E-07	1.6%

For a 95% confidence level, and assuming a normal distribution of the average bin signal, the bin uncertainties should not exceed one-fourth the signal difference between the well and background signal. Similarly, the bin uncertainties should not exceed one-sixth the signal difference between the well and background signal to assure a 99% confidence level. Given in terms of percent standard deviation for the 60 kVp data, Table 5-8 provides the maximum acceptable bin uncertainties for the contrast well depths.

Table 5-8. Maximum Acceptable Bin Uncertainty for 95% and 99 % Confidence Levels

60 kVp		
Disk depth (cm)	**% Uncertainty (2σ)**	**% Uncertainty (3σ)**
0.1	3.1%	2.1%
0.05	1.6%	1.1%
0.04	1.3%	0.9%
0.03	1.0%	0.7%
0.02	0.7%	0.5%
0.01	0.4%	0.3%

The 0.02 cm and 0.01 cm well depths were excluded from further investigation for two reasons. The low uncertainty limits would have required a very large number of source particle histories for the MCNPX runs and well depths less than 0.03 cm were not reliably visible on the clinical images. The same input deck was also executed at 50 and 90 kVp (lowest and potentially highest peak kilovoltage of interest) for 0.03 cm to 0.1 cm well depths. The acceptable upper limits for bin uncertainty at each kVp are shown in Table 5-9.

Table 5-9. Maximum allowable Bin Uncertainties for Investigational kVp Range

kVp	**Disk depth (cm)**	**2σ**	**3σ**
50	0.1	4.1%	2.7%
	0.05	2.1%	1.4%
	0.04	1.7%	1.1%
	0.03	1.3%	0.9%
90	0.1	2.3%	1.5%
	0.05	1.2%	0.8%
	0.04	1.0%	0.6%
	0.03	0.8%	0.5%

The most conservative value, no more than 0.5% uncertainty (99% confidence level) was ultimately established as the maximum allowable bin uncertainty for the optimization runs. To achieve an acceptable level of phantom detail at a reasonable time, a 10x10 radiography tally grid with a 0.5 cm radius was used. This configuration was tested with the aluminum phantom and the 0.03 cm well depth at 50, 60, and 70 kVp. To confirm a statistically significant signal difference existed between the means, a t-test comparing the mean well and background signals was performed at each kVp (α=0.05, T-critical = 3.18 for Table 5-10 and 5-11). The radiography tally and t-test results are given in Table 5-10.

Table 5-10. Results for 10x10 Radiography Tally with 0.5 cm Radius

kVp	Mean Well	Mean Background	Max Bin Uncertainty	t Stat	P (two Tail)
50	1.93E-05	1.83E-05	0.13%	107	1.82E-06
60	2.72E-05	2.61E-05	0.09%	97.4	2.39E-06
70	3.30E-05	3.18E-05	0.08%	94.8	2.59E-06

The t-statistic is above the T-critical value of 3.18, and the p-value is below the required significance level (α= 0.05) indicating a statistically significant difference does exist between the well and background signals at each kVp.

The optimization phantoms were designed to simulate human anatomy more closely than the aluminum phantom alone and will consequently generate more scatter radiation. A test run at 60 kVp with the phantom and the tentative contrast well depth of 0.03 cm was performed to ensure the additional scatter would not significantly increase the bin uncertainties or decrease the contrast difference to an unacceptable level. The

tally results and t-test statistics confirming a statistically significant difference between the well and background signals are shown in Table 5-11.

Finally, clinical factors were also considered in the selection of the phantom well depth. Dental caries are not visible radiographically until 30-50% demineralization of the enamel has occurred (The Ohio State University, 2013). The contrast well for the anthropomorphic phantom should roughly mimic threshold demineralization at approximately 0.038 cm (1.25mm x 30%) depth. The 0.03 cm well depth tentatively selected was considered sufficient to simulate the demineralization threshold while also meeting the statistical standards described above. This depth was ultimately used for both the clinical validation and anthropomorphic phantoms to be consistent.

Table 5-11. Anthropomorphic Phantom Test Run at 60 kVp (0.03 cm well depth)

kVp	Mean Well Signal	Mean Bkgrd Signal	% Difference	Max Bin Uncertainty	t Stat	P (T<=t) (two Tail)
60	5.08E-06	4.85E-06	4.4%	0.39%	71.1	6.138E-06

5.2. ADDITIONAL FILTRATION

Sandborg, et al (1994) investigated the impact of several filter materials on image contrast, relative tube load, and mean patient absorbed dose for intraoral radiology with conventional radiographic film. Of the materials tested, copper proved to be the most suitable, performing better than standard aluminum and niobium filtration, which is marketed for dental radiography. They concluded copper was best suited to decreasing patient dose with minimal contrast loss due to increased photoelectric absorption in the diagnostic energy range.

Shibuya tested gadolinium, niobium, and the KEY filter (presumably containing copper, aluminum, and tin) with a CCD-based digital intraoral sensor. The KEY filter or similar high-pass filters to include copper were considered the best for the digital intraoral sensors used in their study.

Given the similar conclusions of both studies, the filtration material selected for this optimization was copper. In the Sandborg study, all manufacturer installed filtration except inherent filtration (anode, housing oil, and glass envelope) was removed for testing. Since it was not possible to modify the equipment for this study, the total added filtration had to include the approximately 2.5 mm aluminum already present, which is equivalent to approximately 0.05 mm copper for the kVps used in the simulation. Therefore, instead of adding an additional 0.15 and 0.25 mm copper, 0.10 and 0.20 mm copper was added to the inherent aluminum filtration. Aluminum thicknesses equivalent to the added copper were also considered, but IPEM generated spectra with copper and aluminum produced nearly identical results as shown in Figure 5-12. The additional filtration significantly reduced output compared to the standard inherent filtration and this is also evident.

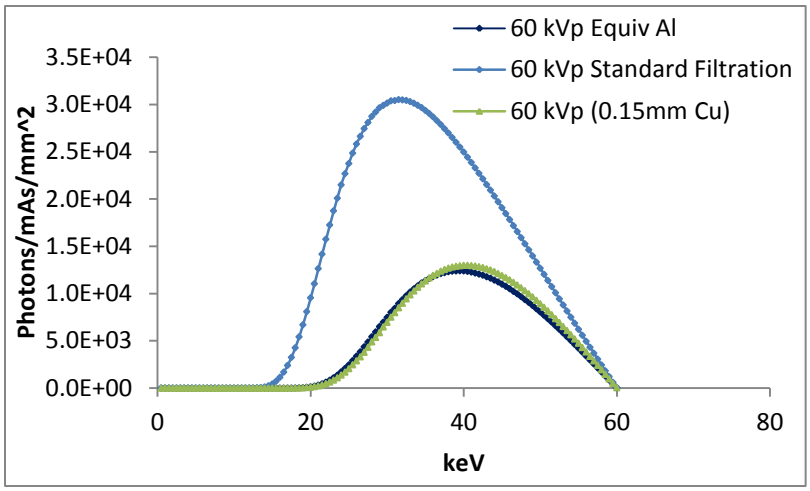

Figure 5-12. Comparison of Copper to equivalent Aluminum Filtration

The IPEM spectra were generated with the additional copper filtration at 50, 55, 60, 66, 70, 75, 80, 85, and 90 kVp.

5.3. SPECTRUM VALIDATION

The differences between the Amptek measured radiographic spectra and IPEM generated spectra were compared through modeling and clinical measurements. The transmission through two cm PMMA and seven mm Type 1100 aluminum (substituting for the McDavid contrast detail phantom) was measured at 50, 55, 60, 66, and 70 kVp for the Planmeca units and at 70 kVp for the Gendex units. The McDavid phantom was too small to adequately cover the detector and could not be used for the attenuation measurements. The measured transmission was compared to the modeled clinical validation phantom transmission for both the IPEM and Amptek spectra.

As shown in Figure 5-13, the IPEM modeled Planmeca spectra underestimated the transmission at all energies (mean: -8.9%, σ: 3.2%) while the Amptek measured spectra overestimated the transmission (mean: 5%, σ: 2.7%). The IPEM Gendex spectra

underestimated the transmission by 13% while the Amptek spectra overestimated the transmission by only 1% (not shown on graph).

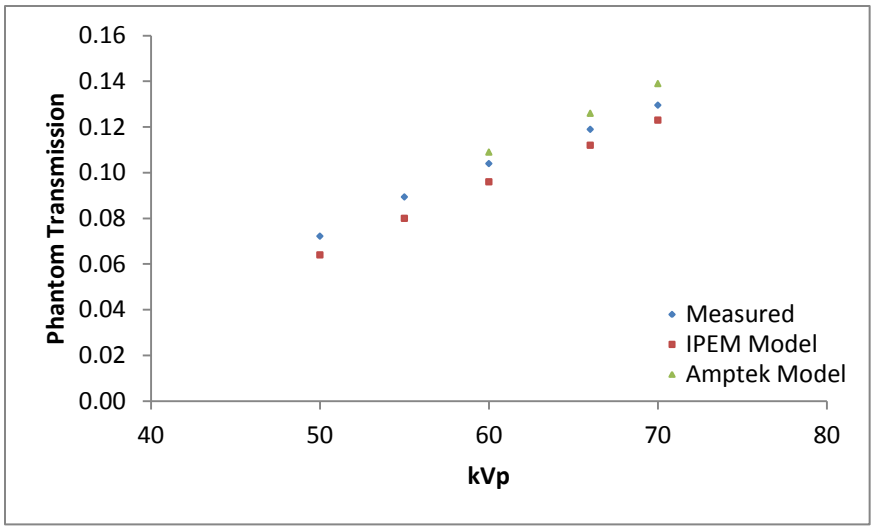

Figure 5-13. Transmission through Clinical Validation Phantom

The significance of the differences was assessed by comparing the modeled radiographic contrast for both spectra as shown in Table 5-12. On average, Amptek modeled radiographic contrast was 6% lower than the IPEM modeled radiographic contrast.

Table 5-12. Radiographic Contrast Comparison

kVp	Modeled Contrast Ratio (IPEM Spectra)	Modeled Contrast Ratio (AMPTEK Spectra)	% Difference
50	0.044	N/A	N/A
55	0.039	N/A	N/A
60	0.036	0.034	-6.46%
63	0.034	0.032	-7.75%
66	0.033	0.031	-4.05%
70(Planmeca)	0.031	0.030	-6.34%
70(Gendex)	0.034	0.032	-5.97%
		Average:	-6.11%
		σ:	1.33%

5.4. SENSOR RESPONSE FUNCTION VALIDATION

To ensure the validity of the sensor response function, the mean pixel value measured in a 100x100 cm ROI through the clinical validation phantom was compared to the predicted response calculated with the sensor response function (Eq.4-10) for nine separate sensors. The predicted response matched the measured response to within 5% on average (σ: 4%). The results are shown in Table 5-13.

Table 5-13. Sensor Response Function Validation

Sensor	Sensor Dose (μGy)	Mean PV Measured	Mean PV Predicted	% Difference
WFGQ214	218	2752.3	3050.4	11%
ZBGQ264	139	1806.8	1965.7	9%
BFGQ199	175	2491.3	2461.4	1%
ZBGQ259	171	2298.8	2406.5	5%
ZBGQ216	170	2204.9	2392.7	9%
ZBGQ217	162	2391.9	2282.7	5%
ZBGQ246	174	2520.8	2447.7	3%
AFG7338	165	2223.8	2324.0	5%
BFGQ254	177	2476.6	2488.9	0.5%
			Average:	**5%**
			σ:	**4%**

5.5. PHANTOM VALIDATION

The validity of the anthropomorphic phantom was also evaluated. The transmission through the phantom model as generated in MCPNX was compared to clinical images of the Center for Devices and Radiological Health (CDRH) Dental Image Quality Test Tool (Fluke Biomedical). This phantom consists of approximately four cm of PMMA with an embedded human premolar. The mean pixel value through the tooth crown was measured for 14 images acquired at 63 kVp, which was chosen because it is currently the peak kilovoltage used clinically, with 14 separate sensors. The entrance dose to the phantom was known and the transmission through the phantom was calculated with the sensor response function. The measured transmission at 63 kVp was estimated to be 7% (σ: 0.9%). This is comparable to the modeled transmission at 63 kVp through the anthropomorphic phantom of 5.6%.

The modeled intensity transmitted through both the clinical validation phantom and anthropomorphic phantom were also compared at 63 kVp to evaluate the difference

in radiographic properties between the two. The average energy of the exiting spectra and radiographic contrast calculated as the quotient of the signal intensity through the well and background were calculated and compared. Figure 5-14 displays the entrance versus exit intensities of both phantoms. The average energies of the exiting spectra as well as the calculated radiographic contrast are shown in Table 5-14.

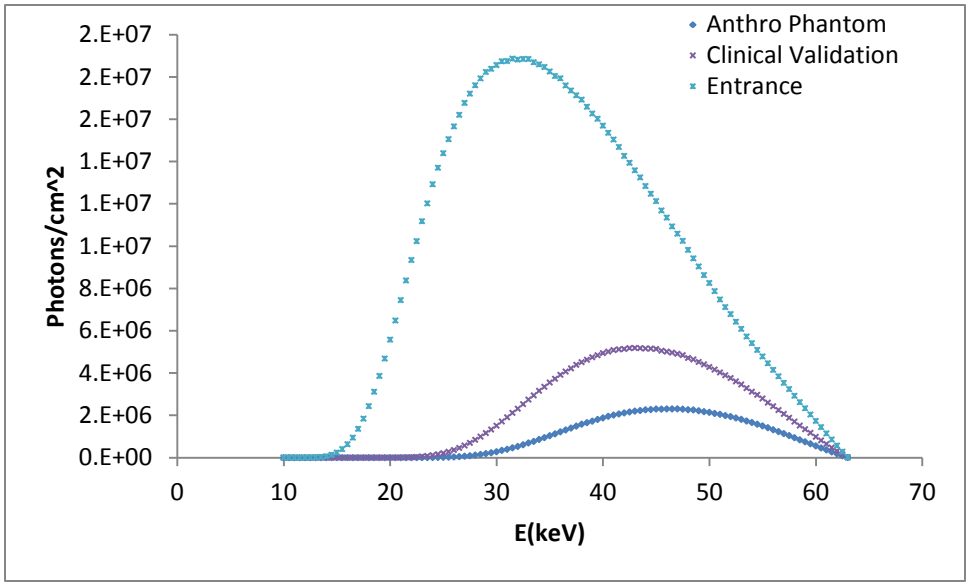

Figure 5-14. Entrance versus Exit Intensity Comparison at 63 kVp

Table 5-14. Average Transmitted Spectral Energy and Radiographic Contrast at 63 kVp

Phantom	Avg Energy (keV)	Contrast Ratio
Clin Val	43.97	0.033
Anthro	45.94	0.047
% Difference	4.3%	29.5%

Given the higher density and greater thickness of the molar compared to the aluminum phantom, the lower output and higher average exit beam energy through the anthropomorphic phantom is logical. Note the radiographic contrast ratio for the

modeled anthropomorphic phantom is 30% higher than the contrast ratio of the clinical validation phantom.

Although the clinical validation phantom is adequate to clinically verify the radiation transport, which is its purpose, it would be difficult to perform an optimization using this phantom alone. It does represent a good starting point, from which a more realistic phantom could be designed; one that more closely matches the true clinical conditions.

5.6. ADDITIONAL TALLIES AND POST-PROCESSING

To calculate the air KERMA to the phantom surface and to the detector, the energy distribution of the photons entering and exiting the phantom was needed. The F2 card was used for this purpose. The data were collected in 0.5 keV energy bins for each peak kilovoltage used in the optimization.

An F6 tally was added to the input deck to track the energy deposited in the tissue cell of the anthropomorphic phantom and PMMA cell of the clinical validation phantom. The tally results were used to calculate the skin dose as described below.

Finally, several post-processing steps were required to format the data for interpretation.

1. A radiography tally output file suitable for analysis was generated.
2. The output files were imported into a spreadsheet and used to generate three dimensional plots.
3. The average tallies (photons/cm^2/source particle) of four bins in the center of the well and adjacent to the well were calculated.

4. The number of source particles was appropriately scaled for the desired entrance exposure using the method described in Section 3.4.2, Equation 3.4 and the phantom entrance F2 tally.
5. The F6 tally output in MeV/gm was converted to dose (μGy): (Eq. 5-2)

$$Skin\_Dose(\mu Gy) = MeV/gm * 1.6022E-13 \frac{J}{MeV} * 1000 \frac{gm}{Kg} * \frac{1Gy}{J/Kg} * 1E6 \frac{\mu Gy}{Gy}$$

6. The scaled radiography and F6 tallies were used to calculate the figures of merit described in chapter 6.

The data generated with the MCNPX output files are tabulated in **Appendix M** for the optimization runs and **Appendix Q** for the clinical validation runs.

Chapter 6: Protocol Optimization and Clinical Validation

The MCNPX model described provided the raw data needed to meet the goal of this research, which was to quantitatively find an "effective" radiographic technique for digital dental radiography. This chapter presents the metrics used to define and quantify effective, as well as a set of potential optimal techniques. The MCNPX generated data provided the input for figures of merit calculations and the optimization analysis. A description of the selected radiographic parameters, figures of merit, and results is presented here.

6.1. Reference Radiographic Parameter Selection

The reference radiographic parameters were described in the preceding chapters. In summary, the variables modified in the MCNPX model were:

- kVp: 50 through 90
- Tube Filtration: Inherent, 0.1 mm added copper, 0.2 mm added copper
- Dose: The entrance air KERMA (~720 μGy) at the current clinical technique (63 kVp at 1 mAs) was used to establish the reference signal response for comparison.

6.2. FOM Definition

Four figures of merit were chosen to encompass the impact of variations in the adjustable parameters–kVp, tube filtration, and dose–on the overall effectiveness of the protocol. The term effective is used here to indicate an FOM value greater than or equal to the reference FOM, which by definition means a clinical technique superior to the reference by some measure. The FOMs are defined below with an explanation of why they were selected and how they can be used to identify optima.

1. **FOM_S.** A modification to the FOM_{SdNR} described in chapter 2 was selected for the optimization because it has been effectively employed to optimize other imaging tasks and is well described in the literature (Samei, 2005; Williams, et al). The noise term was modified to include contributions from both the well and the background (Willner). The signal difference to noise ratio is a fundamental and easily measured metric, which conveys meaningful information about the image quality. The ratio of SdNR to dose normalizes the values for comparison. This FOM was defined as:

$$FOM_S = \frac{SdNR^2}{Dose} \qquad \text{(Eq 6-1)}$$

Where:

$$SdNR = \frac{\mu_{well} - \mu_{bckgrnd}}{\sqrt{(N_{well})^2 + (N_{bckgrnd})^2}}$$

μ_{well} = Mean signal in the well, calculated in two parts:

a. Radiography tally in well (average of four bins centered on well) scaled to dose (μGy):

$$Well\_Dose(\mu Gy) = \frac{Photons/cm^2}{Source\_particle} * NPS * \frac{Dose(\mu Gy)_{Detector}}{(Photons/cm^2)_{Detector\_Plane}}$$

Where:

NPS=number of particles scaled to desired entrance dose (calculated as described in section 3.4.2)

$(Photons/cm^2)_{Detector\_Plane}$ = F2 tally results at detector

$Dose_{Detector}$= Calculated as described in section 3.4.2.

The radiography tally doses had to be estimated by using the F2 Tally results at the detector plane because the radiography tally results are not energy binned.

b. μ_{well} calculated with the Carestream/Planmeca or Carestream/Gendex signal response functions (equations 4-10 and 4-11)

$\mu_{bckgrnd}$ = Mean signal in the background calculated as described using the radiography tally background dose (average of four bins in the background adjacent to the well) and the Carestream/Planmeca or Carestream/Gendex signal response functions (equations 4-10 and 4-11)

N_{well} = Well noise calculated as described using the radiography tally well dose and the Carestream/Planmeca or Carestream/Gendex noise response function (equations 4-13 and 4-14)

$N_{bckgrnd}$ = Background noise calculated as described using the radiography tally background dose and the Carestream/Planmeca or Carestream/Gendex noise response function (equations 4-13 and 4-14)

Dose (μGy) = The skin dose calculated using the F6 tally appropriately scaled to the number of source particles (equation 5-2)

2. **FOM_C.** Because caries detection is highly dependent on contrast resolution (Sogur, et al, 2011), the radiographic contrast between the modeled lesion and tooth, independent of the sensor response function, was chosen as an FOM and defined as:

$$FOM_C = \frac{Well_{Tally} - Background_{Tally}}{Background_{Tally}} \qquad \text{(Eq. 6-2)}$$

Where:

$Well_{Tally}$ = Radiography tally in well scaled to the number of source particles (photons/cm^2)

$Background_{Tally}$ = Radiography tally in the background scaled to the number of source particles (photons/cm^2)

3. **FOM_E.** The total energy deposited is another measure of the potential biological impact a radiation dose may have on the patient. Sandborg warns results may be misinterpreted if only the entrance air KERMA and not total energy deposited is considered in an optimization study. The total energy deposited on the phantom surface was used as a surrogate for the measurement of total energy deposited within a human patient as the modeled phantom was confined to a small volume proximal to the image receptor. Conservatively assuming that the deposited energy is entirely absorbed by the patient, the FOM was defined as:

$$FOM_E = \frac{SdNR^2}{\varepsilon(mJ/cm^2)} \qquad \text{(Eq. 6-3)}$$

Where: $\varepsilon = \left(\sum_{i=1}^{n} E_i(meV/photon) * \Phi_i(photons/cm^2) \right) * 1.602x10^{-10}\, mJ/MeV$

This FOM is similar to the FOM_S, but provides a unique dose-related measure. The change in total energy deposited changes steeply with increased incident energy at a fixed entrance air KERMA as compared to the skin dose. Figure 6-1 illustrates the percent change with respect to the reference technique of both values while entrance air KERMA is held constant. While both increase with increasing kVp, the rates of change are quite different. Over the 50 to 90 kVp range, the skin dose increased approximately 15% while the energy deposited increased nearly 95%.

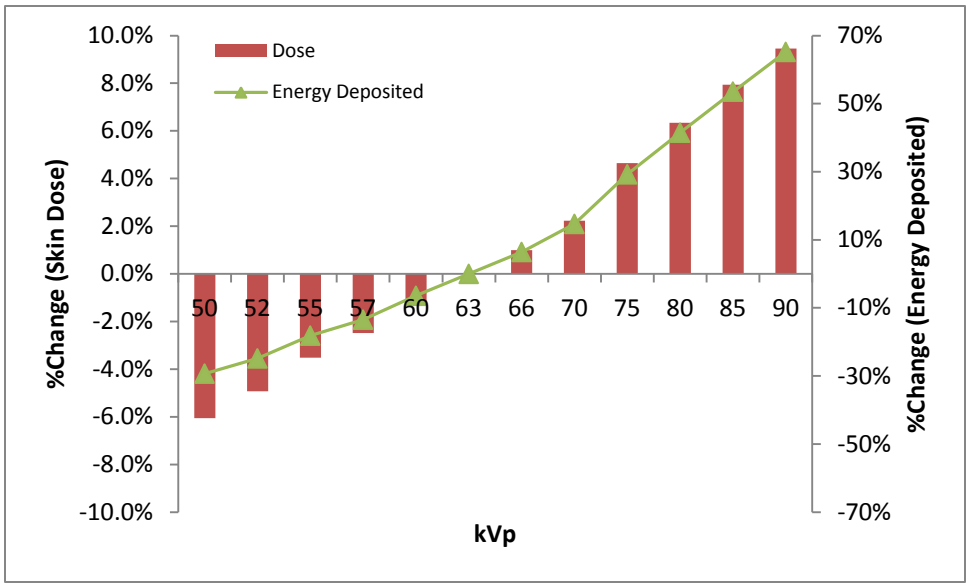

Figure 6-1. Percent Change of Skin Dose and Energy Deposited across 50-90 kVp

4. **FOM_F.** This is a modification of equation 2-7, which considers the impact added filtration will have on the tube workload as well as the effectiveness of the added filtration: does the added filtration improve or at least maintain the image quality/dose ratio of the reference technique and what is the equipment heat load compared to the reference technique?

$$FOM_F = \frac{FOM_{S\_F}}{FOM_{S\_ref}} * \frac{(kVp * mAs)_{ref}}{(kVp * mAs)_F} \qquad \text{(Eq. 6-4)}$$

Where:

FOM_{S_ref} = The FOM_S at the refererence technique (63 kVp, 1 mAs, inherent filtration)

FOM_{s_F} = The FOM_S at all other kVp/filter combinations

$(kVp*mAs)_{ref}$ = The tube workload for the reference technique

$(kVp*mAs)_F$ = The tube workload for the technique at all other kVp/filter combinations

By definition, this FOM is normalized to the reference technique.

6.3. FOM CALCULATION

The radiography tally results generated with the MCNPX runs were used to calculate the signal and noise values in the modeled tooth. Once these values were obtained, the FOMs were calculated. The entrance dose (and number of source particles) was adjusted to maintain the same signal difference to noise ratio at each kVp and filter combination as that obtained with the reference technique (63 kVp and 1 mAs), which produced an SdNR of 2.0 for the Carestream sensors. Equations 4-6 and 4-7 were used to estimate the mAs for the target dose. The measured filter attenuation factor was used to estimate the required mAs with the added copper filtration. The MCNPX and calculated SdNR data are given in **Appendices M** and **N**. The unnormalized FOMs with associated error are shown in Tables 6-1 through 6-3.

Table 6-1. Unnormalized FOMs (Inherent Filtration)

Inherent Filtration	$x10^3$							
kVp	**FOM_S**	**σ_s**	**FOM_C**	**σ_c**	**FOM_E**	**σ_E**	**FOM_F**	**σ_F**
50	5.52	0.77	0.068	9.0E-04	0.57	0.073	0.28	0.047
52	5.99	0.84	0.064	8.6E-04	0.59	0.076	0.35	0.059
55	6.84	0.96	0.059	7.9E-04	0.63	0.080	0.49	0.083
57	7.35	1.03	0.057	7.5E-04	0.65	0.083	0.60	0.100
60	8.24	1.15	0.052	7.0E-04	0.68	0.087	0.81	0.135
63	8.87	1.24	0.049	6.5E-04	0.69	0.088	1.00	0.168
66	9.43	1.32	0.046	6.1E-04	0.70	0.089	1.20	0.201
70	10.34	1.45	0.043	5.7E-04	0.72	0.092	1.56	0.261
75	11.72	1.64	0.039	5.2E-04	0.74	0.095	2.21	0.370
80	13.12	1.84	0.037	4.9E-04	0.77	0.098	3.02	0.506
85	14.63	2.05	0.035	4.6E-04	0.80	0.103	4.07	0.683
90	16.00	2.24	0.033	4.4E-04	0.83	0.106	5.26	0.882
70 (Gendex)	6.98	0.96	0.049	6.5E-04	0.534	0.038	0.98	0.14

Table 6-2. Unnormalized FOMs (0.1 mm Cu Filtration)

0.1 mm Cu	$x10^3$							
kVp	**FOM_S**	**σ_s**	**FOM_C**	**σ_c**	**FOM_E**	**σ_E**	**FOM_F**	**σ_F**
50	8.50	1.19	0.063	8.4E-04	0.668	0.085	0.232	0.039
52	9.06	1.27	0.060	7.9E-04	0.678	0.087	0.282	0.047
55	10.01	1.40	0.054	7.2E-04	0.693	0.089	0.380	0.064
57	10.67	1.49	0.052	6.9E-04	0.707	0.090	0.479	0.080
60	11.79	1.65	0.049	6.5E-04	0.731	0.093	0.678	0.114
63	12.56	1.76	0.046	6.1E-04	0.738	0.094	0.853	0.143
66	13.42	1.88	0.043	5.7E-04	0.745	0.095	1.074	0.180
70	14.31	2.00	0.040	5.3E-04	0.747	0.096	1.386	0.232
75	15.97	2.23	0.037	4.9E-04	0.768	0.098	2.326	0.390
80	17.11	2.40	0.034	4.5E-04	0.769	0.098	3.018	0.506
85	18.56	2.60	0.032	4.3E-04	0.786	0.101	3.996	0.670
90	20.46	2.86	0.031	4.1E-04	0.824	0.105	5.393	0.904
70 (Gendex)	9.57	1.32	0.044	5.9E-04	0.559	0.039	0.822	0.12

Table 6-3. Unnormalized FOMs (0.2 mm Cu Filtration)

0.2 mm Cu	x10^3							
kVp	**FOM$_S$**	**σ$_s$**	**FOM$_C$**	**σ$_c$**	**FOM$_E$**	**σ$_E$**	**FOM$_F$**	**σ$_F$**
50	10.23	2.76	0.060	7.9E-04	0.695	0.089	0.163	0.027
52	10.90	2.94	0.056	7.5E-04	0.703	0.090	0.205	0.034
55	12.04	3.25	0.051	6.8E-04	0.717	0.092	0.288	0.048
57	12.60	3.40	0.049	6.5E-04	0.718	0.092	0.359	0.060
60	13.51	3.65	0.045	6.0E-04	0.720	0.092	0.495	0.083
63	14.28	3.86	0.042	5.6E-04	0.722	0.092	0.633	0.106
66	15.13	4.08	0.039	5.3E-04	0.723	0.092	0.806	0.135
70	16.27	4.39	0.037	4.9E-04	0.732	0.094	1.082	0.181
75	17.61	4.76	0.034	4.5E-04	0.733	0.094	1.830	0.307
80	18.87	5.10	0.032	4.2E-04	0.737	0.094	2.451	0.411
85	20.96	5.66	0.031	4.1E-04	0.776	0.099	3.484	0.584
90	22.45	6.06	0.029	3.9E-04	0.795	0.102	4.559	0.764
70 (Gendex)	11.22	3.37	0.042	5.6E-04	0.563	0.040	0.692	0.10

6.3.1. Uncertainty Analysis

To establish the confidence intervals shown on the FOMs, the uncertainty and variability for each FOM was calculated as described below.

SdNR: (Eq. 6-5)

$$\sigma_{SdNR} = \sqrt{\left[\left(\frac{1}{\sqrt{N_{well}^2 + N_{bckgrnd}^2}}\right)\sigma_{\mu\_well}\right]^2 + \left[\left(\frac{-1}{\sqrt{N_{well}^2 + N_{bckgrnd}^2}}\right)\sigma_{\mu\_bckgrnd}\right]^2 + \left[\left(\frac{(\mu_{well} - \mu_{bckgrnd})N_{well}}{(N_{well}^2 + N_{bckgrnd}^2)^{3/2}}\right)\sigma_{N\_well}\right]^2 + \left[\left(\frac{(\mu_{well} - \mu_{bckgrnd})N_{bckgrnd}}{(N_{well}^2 + N_{bckgrnd}^2)^{3/2}}\right)\sigma_{N\_bckgrnd}\right]^2}$$

Table 6-4 defines the Equation 6-5 terms and the text location where the data were presented. Note the signal uncertainty and noise uncertainty calculated and shown in Table 4-17 were scaled to the 100x100 pixel ROI used for image analysis since the radiography tally was the mean of only four bins. The scaling factor was $\frac{1}{\sqrt{10{,}000}} = \frac{1}{100}$.

Table 6-4. Signal Difference to Noise Ratio Uncertainties

Symbol	Definition	Value (Units)	Location in Text
SdNR: Carestream/Planmeca			
μ_{well}	Mean signal in the Well	Multiple Values (Unitless)	Appendix H
$\sigma_{\mu\ well}$	Uncertainty in well signal	0.17% (Unitless)	Table 4-17
$\mu_{bckgrnd}$	Mean signal in the background	Multiple Values (Unitless)	Appendix H
$\sigma_{\mu\ bckgrnd}$	Uncertainty in the background signal	0.17% (Unitless)	Table 4-17
N_{well}	Noise in the well	Multiple Values (Unitless)	Appendix H
$\sigma_{N\ well}$	Uncertainty in the well noise	0.034% (Unitless)	Table 4-17
$N_{bckgrnd}$	Noise in the background	Multiple Values (Unitless)	Appendix H
$\sigma_{N\ bckgrnd}$	Uncertainty in the background noise	0.034% (Unitless)	Table 4-17
SdNR: Carestream/Gendex			
μ_{well}	Mean signal in the Well	Multiple Values (Unitless)	Appendix I
$\sigma_{\mu\ well}$	Uncertainty in well signal	0.089% (Unitless)	Table 4-17
$\mu_{bckgrnd}$	Mean signal in the background	Multiple Values (Unitless)	Appendix I
$\sigma_{\mu\ bckgrnd}$	Uncertainty in the background signal	0.089% (Unitless)	Table 4-17
N_{well}	Noise in the well	Multiple Values (Unitless)	Appendix I
$\sigma_{N\ well}$	Uncertainty in the well noise	0.067% (Unitless)	Table 4-17
$N_{bckgrnd}$	Noise in the background	Multiple Values (Unitless)	Appendix I
$\sigma_{N\ bckgrnd}$	Uncertainty in the background noise	0.067% (Unitless)	Table 4-17

FOM_S:

$$\sigma_{FOM(S)} = \sqrt{\left[\left(\frac{2SdNR}{Dose}\right)\sigma_{SdNR}\right]^2 + \left[\left(\frac{-SdNR^2}{Dose^2}\right)\sigma_{dose}\right]^2} \quad \text{(Eq. 6-6)}$$

Table 6-5 defines the Equation 6-6 terms and the text location where the data were presented.

Table 6-5. FOM_S Uncertainties

Symbol	Definition	Value (Units)	Location in Text
FOM_S Carestream/Planmeca			
SdNR	Calculated signal difference to noise ratio	2.0 (Unitless)	Appendix N, R
σ_{SdNR}	Uncertainty in SdNR	6% (Unitless)	Appendix R
Dose	F6 Tally Skin Dose	Multiple Values (μGy)	Appendix M,R
σ_{Dose}	Uncertainty in F6 Tally Skin Dose	7% (μGy)	Table 4-17
FOM_S Carestream/Gendex			
SdNR	Calculated signal difference to noise ratio	2.0 (Unitless)	Appendix N, R
σ_{SdNR}	Uncertainty in SdNR	3% (Unitless)	Appendix R
Dose	F6 Tally Skin Dose	Multiple Values (μGy)	Appendix M,R
σ_{Dose}	Uncertainty in F6 Tally Skin Dose	13% (μGy)	Table 4-17

FOM_C:

The uncertainty in the radiographic contrast is dependent upon the spectral characteristics used for the simulation. The best estimate is the standard deviation of the contrast bias given in Table 5-12. This uncertainty is approximately 1.3%.

FOM_E:

$$\sigma_{FOM(E)} = \sqrt{\left[\left(\frac{2SdNR}{\varepsilon}\right)\sigma_{SdNR}\right]^2 + \left[\left(\frac{-SdNR^2}{\varepsilon^2}\right)\sigma_{\varepsilon}\right]^2} \quad \text{(Eq. 6-7)}$$

Table 6-6 defines the equation 6-7 terms and the text location where the data were presented.

Table 6-6. FOM_E Uncertainties

Symbol	Definition	Value (Units)	Location in Text
FOM_E Carestream/Planmeca			
SdNR	Calculated signal difference to noise ratio	2.0 (Unitless)	Appendix N, R
σ_{SdNR}	Uncertainty in SdNR	6% (Unitless)	Appendix R
ε	Energy Deposited	Multiple Values (mJ/cm^2)	Appendix M,R
σ_ε	Uncertainty in energy deposited	4% (mJ/cm^2)	Table 4-1
FOM_E Carestream/Gendex			
SdNR	Calculated signal difference to noise ratio	2.0 (Unitless)	Appendix N, R
σ_{SdNR}	Uncertainty in SdNR	3% (Unitless)	Appendix R
ε	Energy Deposited	Multiple Values (mJ/cm^2)	Appendix M,R
σ_ε	Uncertainty in energy deposited	4% (mJ/cm^2)	Table 4-1

Uncertainty in calculated energy deposited is dependent upon spectral characteristics. As an estimate, the variation in energy deposited would be approximately equivalent to the difference between average measured and modeled energy. The comparisons between the Amptek and IPEM generated spectra are the best estimate (Table 4-1).

FOM_F: (Eq 6-8)

$$\sigma_{FOM_F} = \sqrt{\left[\left(\frac{1}{FOM_{S\_ref}} * \frac{(kVp*mAs)_{ref}}{(kVp*mAs)_F}\right)\sigma_{FOM(S\_F)}\right]^2 + \left[\left(\frac{-FOM_{S\_F}}{FOM^2_{S\_ref}} * \frac{(kVp*mAs)_{ref}}{(kVp*mAs)_F}\right)\sigma_{FOM(S\_ref)}\right]^2}$$

Where:

$\sigma_{FOM(S\_ref)}$ = The uncertainty of the FOM_{S_ref} values

$\sigma_{FOM(S\_F)}$ = The uncertainty of the FOM_{S_F} values

Table 6-7 defines the equation 6-8 terms and the text location where the data were presented.

Table 6-7. FOM_F Uncertainties

Symbol	Definition	Value (Units)	Location in Text
FOM_F Carestream/Planmeca and Carestream/Gendex			
FOM_{S_ref}	FOM_S at reference technique	Multiple Values (unitless)	Appendix N
$\sigma_{FOM(S\_ref)}$	Uncertainty in calcualted FOM_{S_ref}	14% (Unitless)	Appendix R
FOM_F	FOM_S at other kVp/filter combinations	Multiple Values (unitless)	Appendix N
$\sigma_{FOM(S\_F)}$	Uncertainty in calcualted FOM_{S_F}	14% (Unitless)	Appendix R
$(kVp*mAs)_{ref}$	Workload at reference technique	Multiple Values	Appendix M
$(kVp*mAs)_F$	Workload at other kVp/filter combinations	Multiple Values	Appendix M

A summary of the average uncertainties for all FOMs is shown in Table 6-8. The measured inter-sensor signal and noise variability was ~5% and ~8% respectively (Table 4-13) for images acquired with Gendex units. The vendor specified tolerance on non-uniformities across an individual sensor is 20% (Carestream Product Line Manager of Intra-Oral Digital Imaging personal communication, 18 Jan 2013). In comparison, the estimated uncertainty of the signal response function is 17% (Planmeca) and 9% (Gendex) and the noise response function uncertainties are 3% (Planmeca) and 7% (Gendex).

Table 6-8. Estimated FOM Uncertainties

	Error Analysis: FOM_S				
	Signal %σ	**Noise %σ**	**SdNR %σ**	**Dose %σ**	**Total %σ**
Carestream/Planmeca	17%	3%	6%	7%	14%
Carestream/Gendex	9%	7%	3%	13%	14%

	Error Analysis: FOM_C
	Total %σ
All Radiographic Units	1.3%

	Error Analysis: FOM_E				
	Signal %σ	**Noise %σ**	**SdNR %σ**	**ε %σ**	**Total %σ**
Carestream/Planmeca	17%	3%	6%	4%	13%
Carestream/Gendex	9%	7%	3%	4%	7%

	Error Analysis: FOM_F			
	FOM_S %σ	**Dose %σ**		**Total %σ**
Carestream/Planmeca	14%	7%		17%
Carestream/Gendex	14%	13%		14%

The FOMs were then normalized with respect to the FOMs at the reference technique (63 kVp at 1 mAs). The data for the Carestream/Planmeca units with one standard deviation confidence intervals are shown in Figures 6-2 through 6-5.

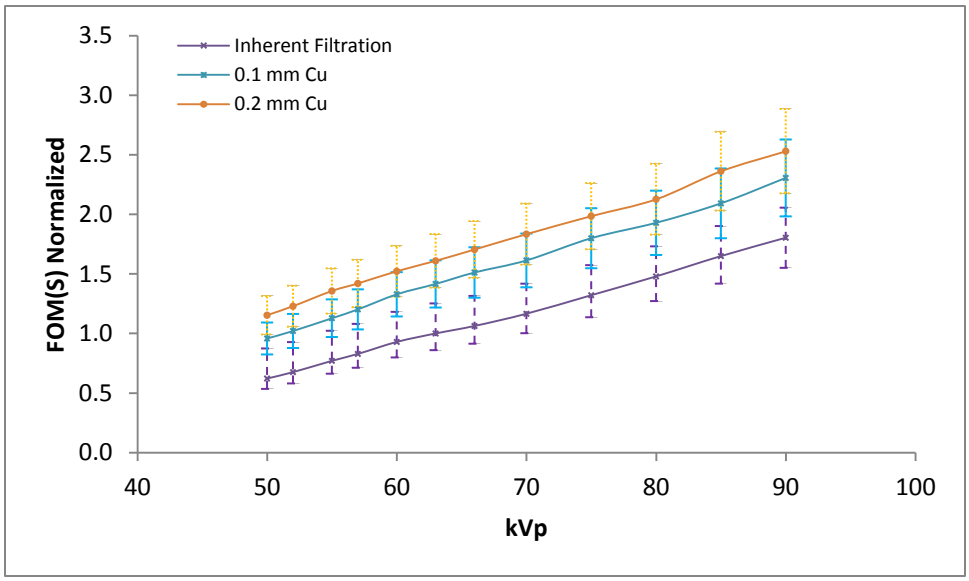

Figure 6-2. FOM_S (Carestream/Planmeca)

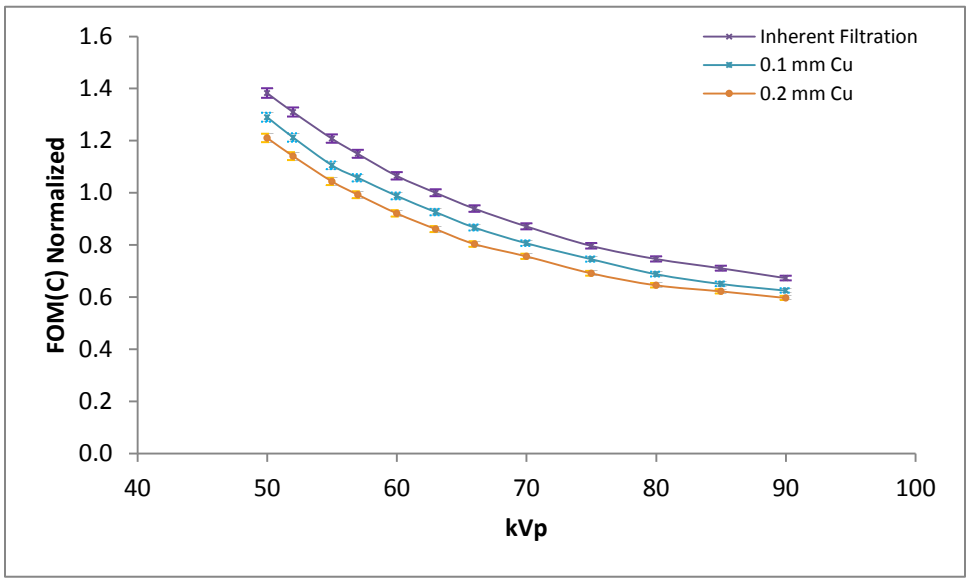

Figure 6-3. FOM_C (Carestream/Planmeca)

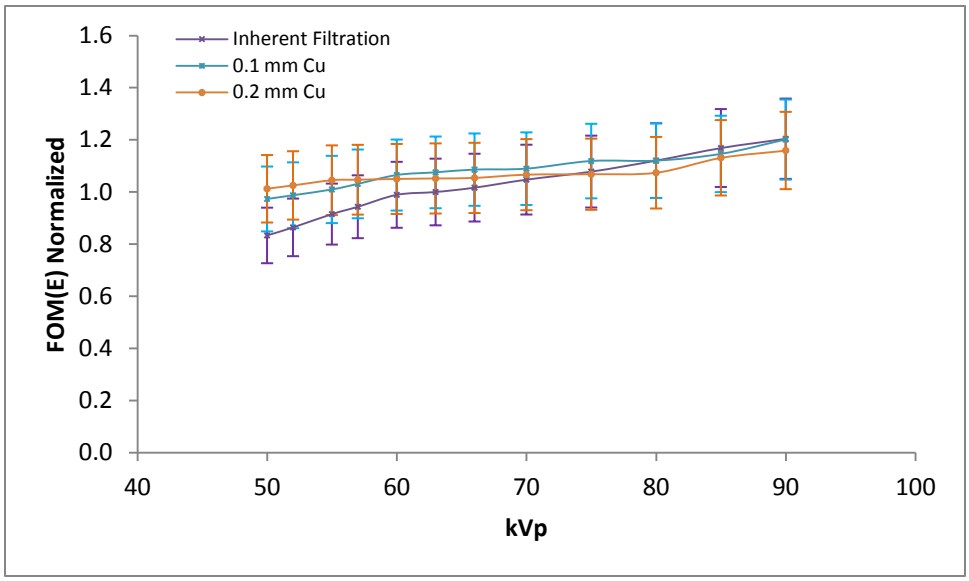

Figure 6-4. FOM_E (Carestream/Planmeca)

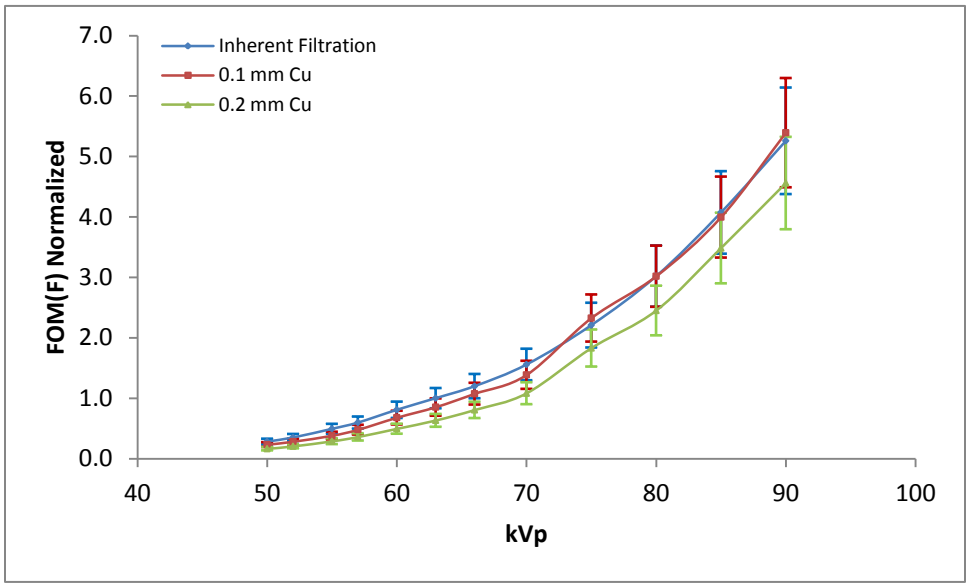

Figure 6-5. FOM_F (Carestream/Planmeca)

FOM_S: The FOM_S plot demonstrates the advantage of added tube filtration and increased peak kilovoltage on image quality, which is counterintuitive. At higher energies, the inherent radiographic contrast diminishes. However, by definition, the

FOM_S includes the dose required to achieve the SdNR and at higher energies, it was possible to achieve the reference SdNR at much lower doses. The largest improvement in the FOM_S is seen with 0.1 mm added copper filtration. By removing a large portion of the low energy photons from the spectra, the entrance dose needed to obtain the reference SdNR for the copper filtered spectra was lower than that need with inherent filtration alone.

FOM_C: As expected, the radiographic contrast is best at the lowest energies. The added filtration reduces contrast but at the highest peak kilovoltages, the disadvantage of added filtration is negligible.

FOM_E: The behavior of this metric can be explained by noting the total energy deposited varied slowly over the range of peak kilovoltages and filtration configurations tested (shown in Figure 6-6). Additionally, the entrance dose and consequently number of source particles needed for the target SdNR was not a unique value. For example, at 70 kVp, the target SdNR (2.0) could be maintained at an entrance dose of ~560 to 610 μGy. To be conservative, the maximum entrance dose that produced the target SdNR was used. The slope of this curve indicates that, in general, the total energy deposited decreased at increased energy and increased tube filtration because the entrance dose required to attain the reference SdNR decreased. However, above 70 kVp, added tube filtration made little impact on reducing patient radiation burden.

FOM_F: Added filtration will increase the heat load on the radiographic unit. This is more apparent when comparing the heat load at a fixed entrance dose. Since the dose required to maintain a given SdNR decreased at both higher kVps and higher tube filtration, the impact of heat load is minimal except at the highest added tube filtration (0.2 mm copper).

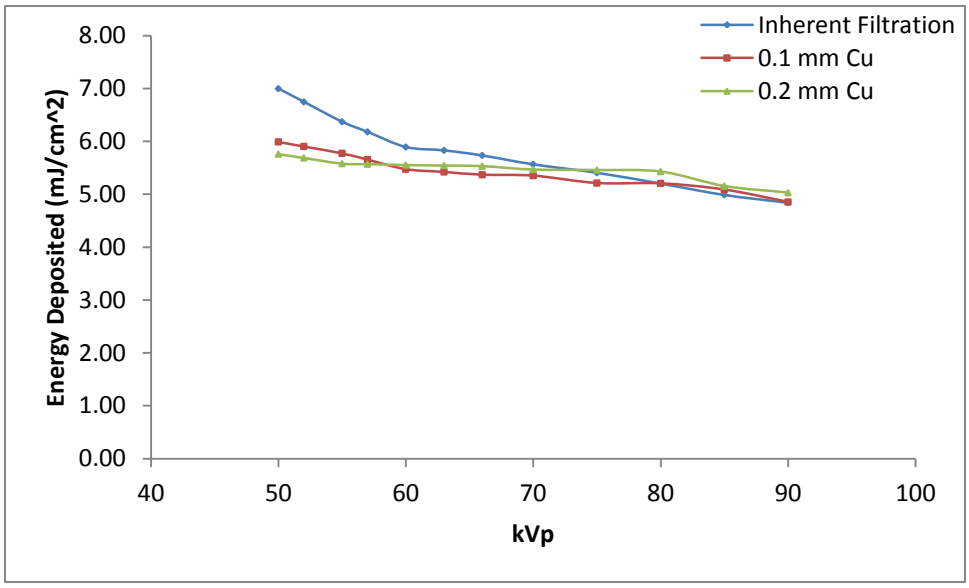

Figure 6-6. Energy Deposition for Fixed SdNR

6.4. FOM Sensitivity Analysis and Optimization

Once the FOMs were established, they were combined into a single metric for optimization. A weighted average of the image quality FOMs was chosen as the simplest and most logical approach to create this metric. Before the selected weighting is discussed, the results of a sensitivity analysis on the weighting factors will be described.

6.4.1. Sensitivity Analysis

The weight of a single FOM was varied from 100% to 0% in 25% increments with the remaining weight distributed evenly among the remaining three FOMs. The technique with the highest metric across the entire range of kVps (50 to 90) as well as the highest metric within the range of kVps clinically available (50 to 70) was identified. The results are shown in Tables 6-9 and 6-10.

Table 6-9. Sensitivity Analysis: FOM_S and FOM_C

	FOM_S				FOM_C			
	100%	75%	50%	0%	100%	75%	50%	0%
50-70 kVp	70 kVp 0.2 mm Cu	70 kVp 0.2 mm Cu	70 kVp 0.2 mm Cu	70 kVp Inherent	50 kVp Inherent	50 kVp Inherent	70 kVp 0.1 mm Cu	70 kVp 0.1 mm Cu
50-90 kVp	90 kVp 0.2 mm Cu	90 kVp 0.2 mm Cu	90 kVp 0.1 mm Cu	90 kVp 0.1 mm Cu	50 kVp Inherent	90 kVp 0.1 mm Cu	90 kVp 0.1 mm Cu	90 kVp 0.1 mm Cu

Table 6-10. Sensitivity Analysis: FOM_E and FOM_F

	FOM_E				FOM_F			
	100%	75%	50%	0%	100%	75%	50%	0%
50-70 kVp	70 kVp 0.1 mm Cu	70 kVp 0.1 mm Cu	70 kVp 0.1 mm Cu	70 kVp 0.1 mm Cu	70 kVp Inherent	70 kVp Inherent	70 kVp Inherent	70 kVp 0.1 mm Cu
50-90 kVp	90 kVp 0.1 mm Cu	90 kVp 0.1 mm Cu	90 kVp 0.1 mm Cu	90 kVp 0.1 mm Cu	90 kVp 0.1 mm Cu	90 kVp 0.1 mm Cu	90 kVp 0.1 mm Cu	90 kVp 0.1 mm Cu

Weighted sums were also calculated with two FOMs at a time. The kVp/filtration combination with the highest metric for each combination across the full kVp range as well as the clinically available range is shown in Figures 6-7 and 6-8.

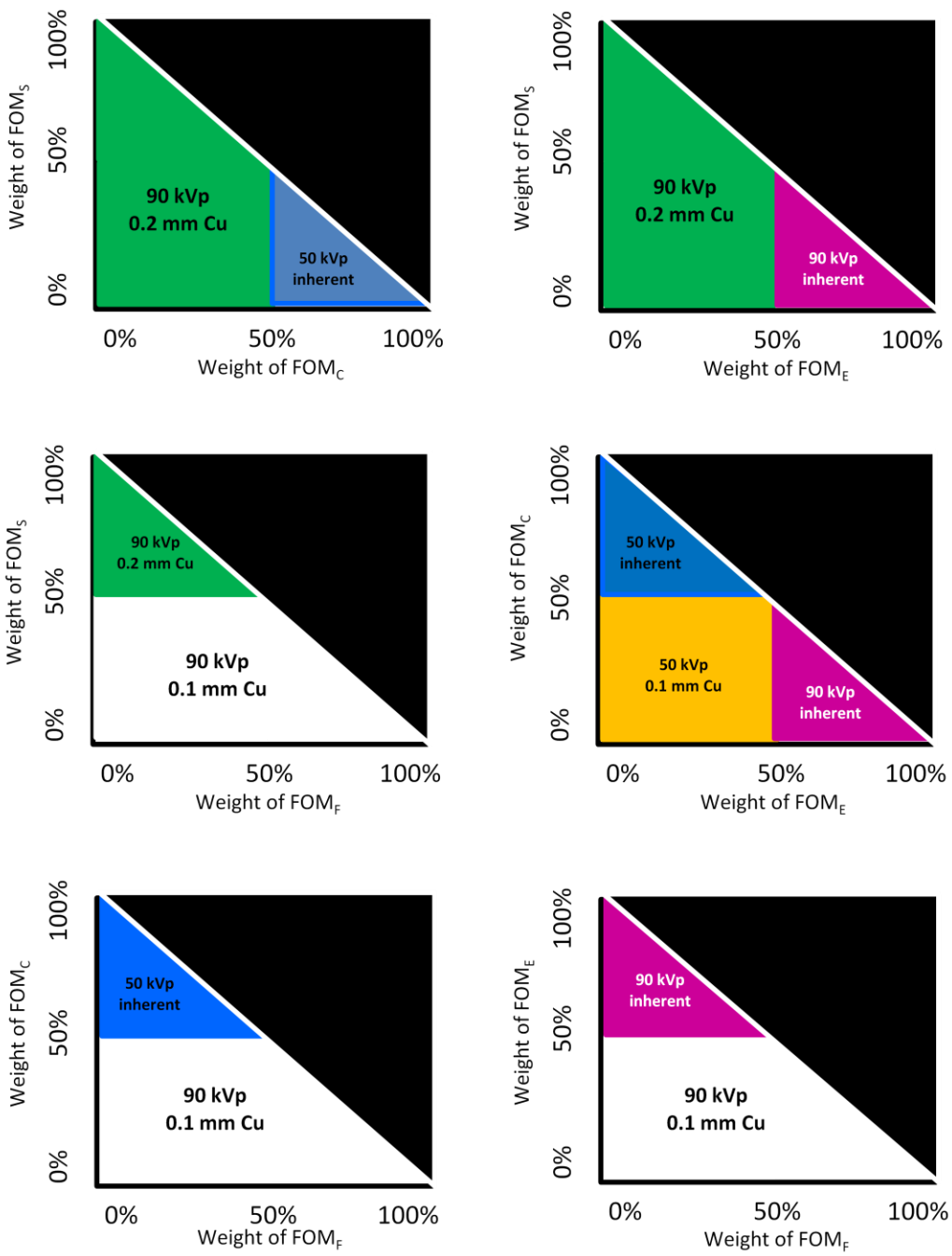

Figure 6-7. Paired Sensitivity Analysis: 50-90 kVp

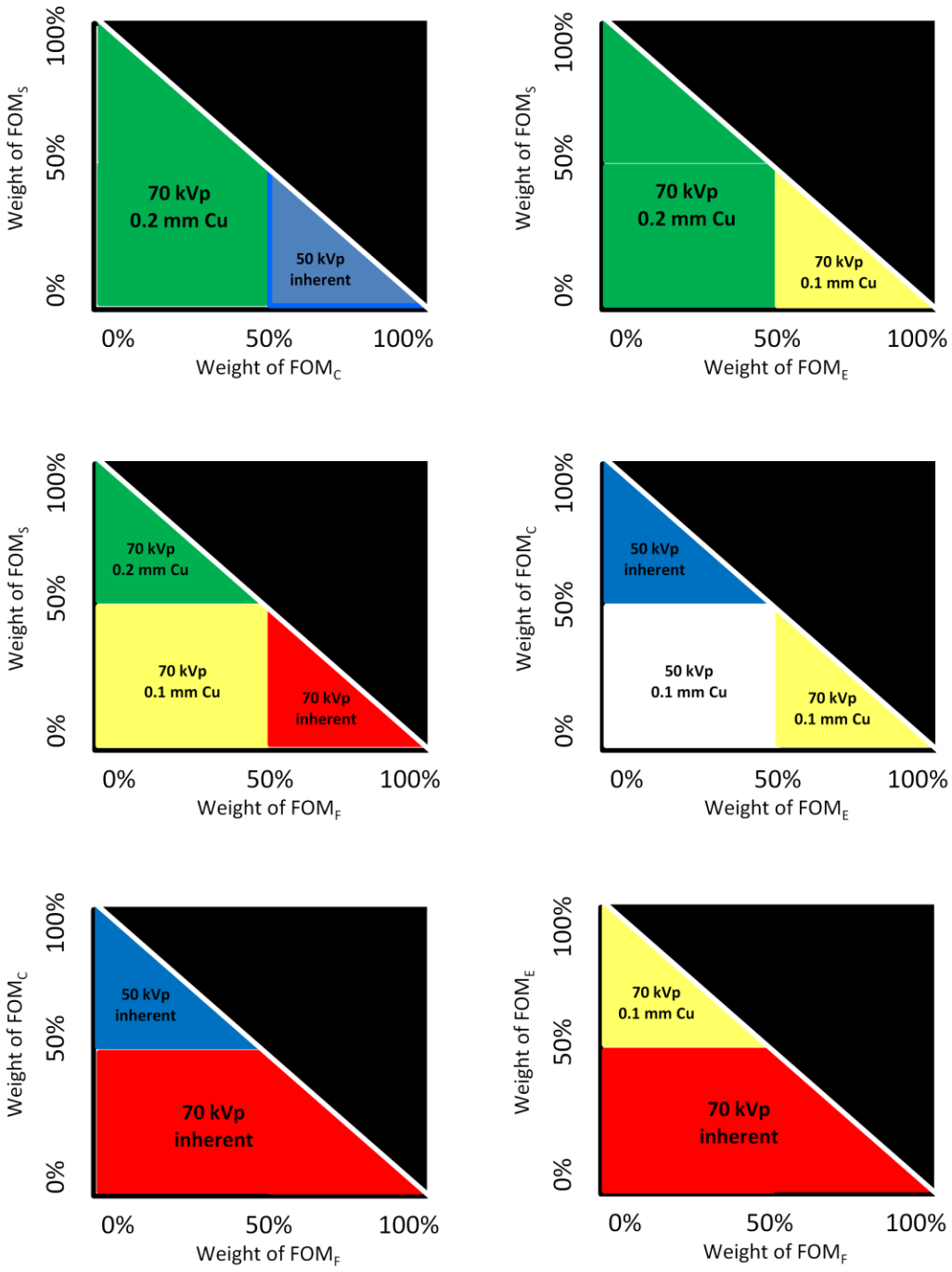

Figure 6-8. Paired Sensitivity Analysis: 50-70 kVp

Both the FOMs used and the FOM weighting have an impact on the result. If one desires to maximize radiographic contrast, the lowest kVp, least filtered spectrum will emerge as the optimum. Weighting the metric in favor of FOM_C would then be the goal. On the contrary, if the highest SdNR to dose ratio is the primary goal, regardless of tube workload, high kVp with heavy filtration will prove to be optimum and preference should be given to FOM_S when weighting the FOMs. Ultimately, the clinical goals of the optimization will drive the FOM weighting process.

The complete datasets can be found in **Appendix O**.

6.4.2. FOM Weighting

The goal of this project was to compare the dose and image quality (defined as the SdNR) of the current clinical technique to a variety of alternatives. The figures of merit consider entrance dose, energy deposition, inherent radiographic contrast, and the equipment workload. These factors were of equal importance to the researcher and equal weighting of all FOMs was used to define the metric to be optimized. The optimal technique will thus be the one that maximizes the following metric:

$$f(x)_{optimum} = 0.25FOM_S + 0.25FOM_C + 0.25FOM_E + 0.25FOM_F \qquad \text{(Eq. 6-9)}$$

6.5. Selection of Optimal Technical Factors

With equal weighting of all FOMs and given no limitations on the equipment, the optimal combination of kVp and tube filtration for dental bitewing imaging was identified to be ***90 kVp*** with ***0.1 mm added copper filtration***. Kaeppler, et al (2007) concluded an increase in peak tube kilovoltage from 60 to 90 kVp produced a limited dose savings (~8%). This study indicates a more substantial savings may be possible at

increased tube potential under the conditions tested and merits further investigation to verify the sensor response function at peak kilovoltages greater than 70 kVp.

The optimal technique in the radiographic units' operating range is ***70 kVp*** with ***0.1 mm added copper filtration***. This simple modification to the equipment could be immediately adopted at relatively low cost for a significant dose savings (Planmeca units). The achievable dose savings for both proposed techniques is shown in Table 6-11.

Table 6-11. Potential Dose Savings with Optimized Technical Parameters (Planmeca)

	63 kVp Inherent Filtration	**90 kVp 0.1 mm Cu**	**% Decrease**	**70 kVp 0.1 mm Cu**	**% Decrease**	**70 kVp** Inherent Filtration	**% Decrease**
Entrance Dose (μGy)	723	260	**64%**	392	**46%**	606	**16%**
Skin Dose (μGy)	451	196	**57%**	279	**38%**	387	**14%**
Energy Dep (mJ/cm^2)	5.83	4.85	**17%**	5.35	**8%**	5.57	**5%**

Sandborg used 59 kVp for the intraoral radiography spectrum shaping study. He compared the mean absorbed dose, defined as $\frac{\varepsilon}{m}$, for the test filter material to the 59 kVp spectrum filtered with 2.0 mm aluminum.

Where:

ε = energy imparted to the patient (fraction of the incident radiation absorbed)

m= patient mass

At equivalent contrast to the reference spectrum, Sandborg observed an approximately 10% decrease in mean absorbed dose with 0.15 mm added copper filtration. Although differences in phantom design, image receptor, and calculation of energy deposited make direct comparisons between this study and Sandborg difficult, the 60 kVp results for this work are presented in Table 6-12 for comparison.

Table 6-12. Dose Comparison for Constant SdNR at 60 kVp

	60 kVp Inherent Filtration	60 kVp 0.1 mm Cu	% Decrease
Entrance Dose (μGy)	786	492	**37%**
Skin Dose (μGy)	485	339	**30%**
Energy Deposited (mJ/cm^2)	5.89	5.47	**7%**

A 7% decrease in energy deposited was observed with 0.1 mm added copper filtration in this study, which is in rough agreement with Sandborg.

Re-considering the sensitivity analysis, Figures 6-9 and 6-10 demonstrate the space over which both the 90 kVp and 70 kVp techniques are optimal.

The identified optimum technique would satisfy most weighting schemes. Clearly, unless the metric was heavily weighted in favor of a single FOM, the optimal technique would be the same. This indicates a precise weighting, which would be difficult to determine, is probably not necessary. More likely, careful consideration should be given to defining the FOMs, which as previously mentioned is dependent on the optimization objectives.

It is also worth investigating whether the identified optimum technique would be different if the radiographic units or sensors had suboptimal performance. This is a clinically relevant question as a large dental clinic has multiple devices, which are presumed to produce similar images. If, for example, a particular sensor produced images with a noise level at two standard deviations above the mean, would the metric result be the same? To answer this question, the optimization was re-calculated after the well and background noise was increased by 15% (Table 4-13: Inter-Sensor Reproducibility average noise $\%\sigma = 7.6\%$). The estimated uncertainty in the noise response for images acquired with the Planmeca units is lower but this higher uncertainty

was used to be conservative. The optimization outcome did not change, however, the SdNR value across all kVps and filter combinations dropped from 2.0 to 1.8. To maintain the reference SdNR for a sensor operating with this noise level, the dose at the reference technique would have to be increased ~18% and at the optimized technique (90 kVp, 0.1 mm added copper) it would have to be increased ~15%. This underscores the necessity of measuring the response of each imaging system (radiographic unit and sensor) and setting the technical factors accordingly rather than establishing a standard technique for the entire clinic, which is the common practice.

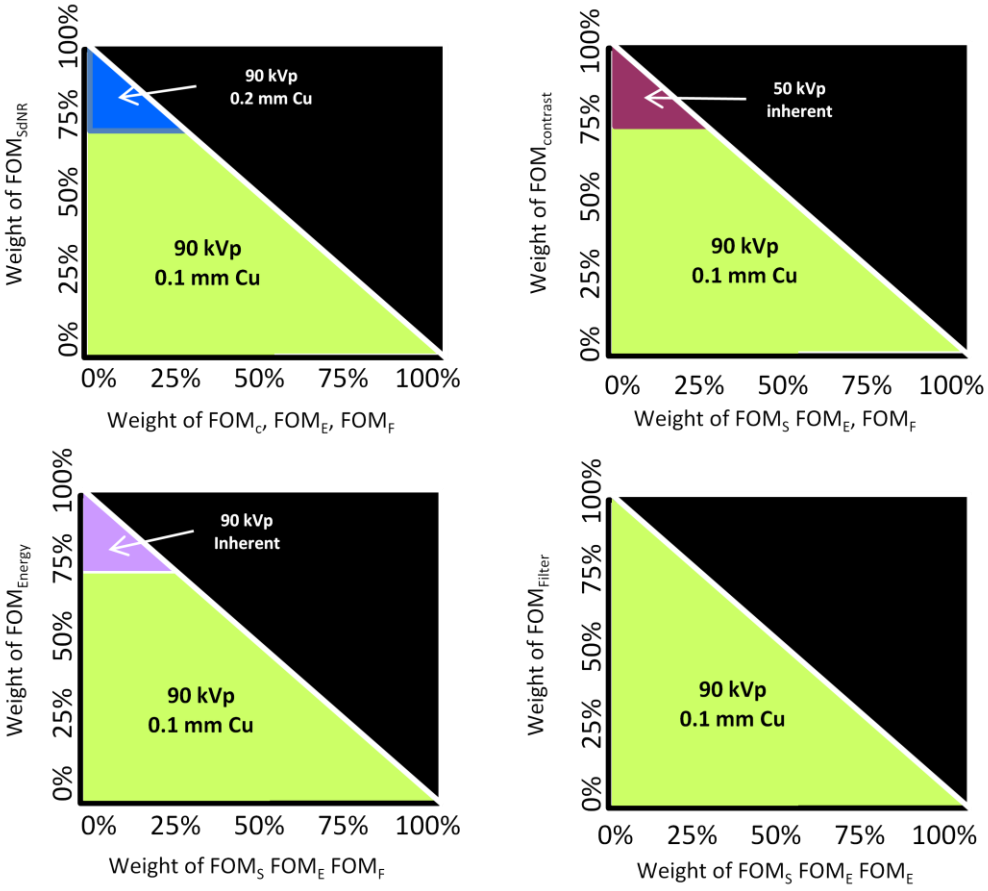

Figure 6-9. Sensitivity Analysis: 50-90 kVp (All FOMs)

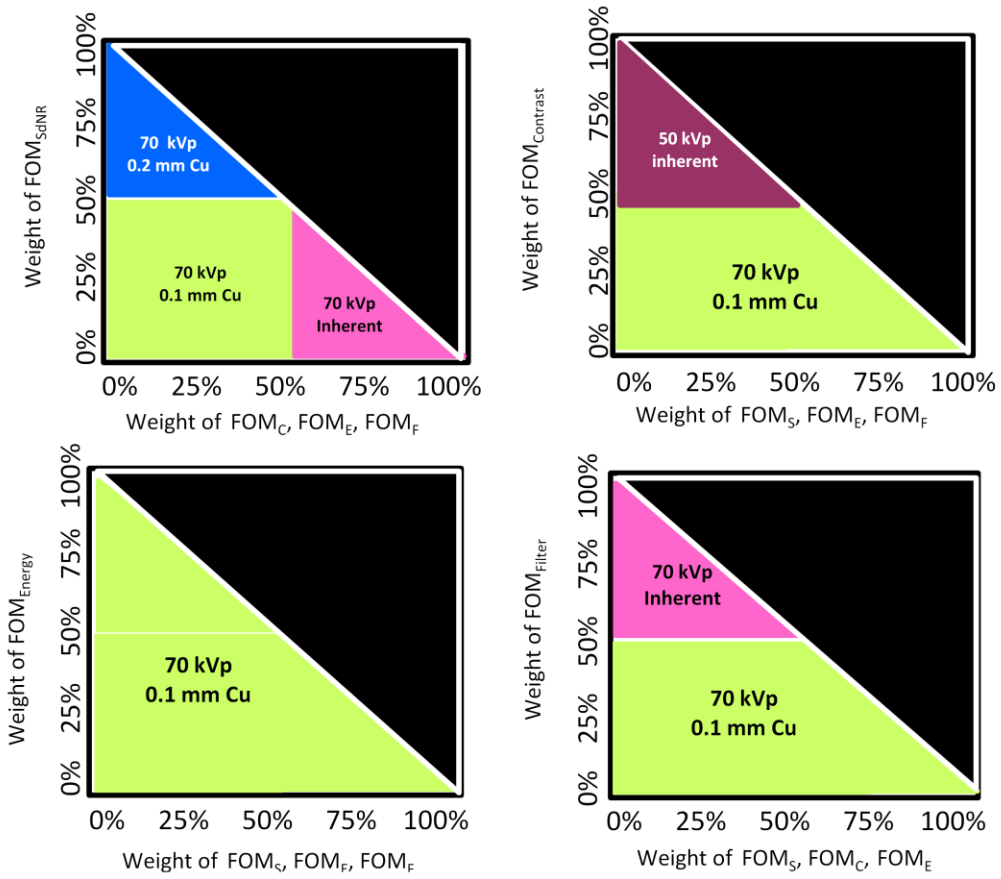

Figure 6-10. Sensitivity Analysis: 50-70 kVp (All FOMs)

The proposed optimization will require a modest modification to the existing equipment but an immediate dose savings could be achieved by using 70 kVp with the Planmeca units. For the same SdNR, the skin dose could be decreased by approximately 14%, and total energy deposited could be decreased by 5%. The proposed techniques also yield entrance air KERMA doses below the NCRP Report #172 (2012) median value for digital intraoral radiology (Table 5.2: Michigan Department of Community Health 2005-2009 survey of dental bitewing images) as shown in Table 6-13.

Table 6-13. Comparison of Proposed Technique to Published Data for Digital Intraoral Imaging (Planmeca)

	NCRP Median (Table 5-2)	90 kVp 0.1 mm Cu	% Decrease	70 kVp 0.1 mm Cu	% Decrease	70 kVp Inherent Filtration	% Decrease
Entrance Air KERMA (μGy)	800	260	**67%**	392	**51%**	606	**24%**

In contrast, the Gendex units underperformed the Planmeca units. Without added filtration, a higher patient dose was required to attain equivalent image quality (SdNR). The best response was observed with 0.1 mm added copper filtration, which yielded an entrance dose 17% lower than the reference technique but with 23% higher total energy deposited. The results are summarized in Table 6-14. All values in red indicate an increase over the reference technique.

Table 6-14. Gendex Optimization Results relative to Planmeca Reference Technique

	63 kVp Inherent Filtration	70 kVp 0.1 mm Cu	% Difference	70 kVp Inherent Filtration	% Difference
Entrance Air KERMA (μGy)	723	599	**17%**	907	**26%**
Skin Dose (μGy)	451	418	**7%**	573	**27%**
Energy Deposited (mJ/cm^2)	5.83	7.19	**23%**	7.48	**28%**

Adding 0.1 mm copper filtration to the Gendex spectrum will, however, decrease the dose from the current clinical technique needed to match the Carestream/Planmeca reference SdNR (Table 6-15).

Table 6-15. Gendex Optimization Results

	70 kVp Inherent Filtration	70 kVp 0.1 mm Cu	% Decrease
Entrance Dose (μGy)	907	599	**34%**
Skin Dose (μGy)	573	418	**27%**
Energy Deposited (mJ/cm^2)	7.48	7.19	**4%**

Since a typical dental clinic may have both DC and AC units, it is critical to understand the implications. To attain consistent image quality among all units may require higher doses with a single-phase AC radiographic unit, such as the Gendex 770.

6.6. CLINICAL VALIDATION

MCNPX runs were performed with the modeled clinical validation phantom (two cm PMMA and McDavid low contrast detail phantom shown in Figure 5-9) at the reference and optimized techniques. As described in section 6.3, the entrance dose, and number of source particles, was adjusted to maintain the same signal difference to noise ratio at each kVp and filter combination as that obtained with the reference technique (63 kVp and 1 mAs). Images were then acquired clinically with five Carestream sensor/Planmeca units and four Carestream sensor/Gendex units using as close to the calculated entrance dose as possible. The mean and standard deviation of the signal in a 100x100 pixel region was measured inside the 0.03 cm well. The average background mean and standard deviation were calculated from the average of four 100x100 pixel regions of interest positioned on each side of the well. The measured SdNR was compared to the predicted value at each kVp/filter combination. The average results are summarized in Table 6-16.

Table 6-16. Measured versus Predicted SdNR values with Clinical Validation Phantom

	kVp	Average K_{air} (μGy)	Filter	Average Measured SdNR	Predicted SdNR	% Difference
Carestream/Planmeca	63	729	Inherent	1.9	2.1	**-10%**
	70	612	Inherent	1.9	2.1	**-10%**
	70	451	0.1 mm Cu	1.9	2.1	**-10%**
Carestream/Gendex	70	868	Inherent	1.8	2.1	**-14%**
	70	626	0.1 mm Cu	2.0	2.1	**-5%**

The sensor response function was validated (Table 5-13) and on average the difference between the measured and predicted mean signal was 5% (+/-4%). Here, the measured SdNR is systematically lower than the predicted SdNR. In an effort to understand why, a more detailed evaluation of the predicted versus measured differences was conducted. The background signal-to-noise ratio , $\frac{\mu_{bckgrnd}}{N_{bckgrnd}}$, was calculated for both the predicted and measured response and is shown in Table 6-17.

Table 6-17. Predicted versus Measured Signal to Noise Ratios

	kVp	Filter	Bkgrd Signal (Predicted)	Bkgrd Noise (Predicted)	SNR (Predicted)	Bkgrd Signal (Meas)	Bkgrd Noise (Meas)	SNR (Meas)	% Diff
Planmeca	63	Inherent	942.2	10.4	90.6	1060.2	12.8	83.1	**-8%**
	70	Inherent	967.4	10.1	95.8	1143.2	13.2	86.7	**-9%**
		Inherent +0.1mm Cu	1138.9	10.7	106.4	1511.3	15.2	99.4	**-7%**
Gendex	70(G)	Inherent	978	11.9	82.2	1039.8	12.9	80.9	**-2%**
		Inherent +0.1mm Cu	1139	12.5	91.1	1499.9	15.3	98.0	**8%**

For all but the Gendex unit with 0.1 mm added copper, the measured SNRs are once again lower than the predicted values although the measured mean signal and noise values are higher. This suggests the lower than predicted response was due in part to higher than predicted relative noise and not a lower signal difference (contrast) between

the well and background for the Carestream sensors/Planmeca units evaluated. The predicted versus measured signal differences were also compared and are shown in Table 6-18.

Table 6-18. Comparison of Actual Versus Measured Signal Difference

	kVp	Filter	Well Signal (Predicted)	Bkgrd Signal (Predicted)	Diff	Well Signal (Meas)	Bkgrd Signal (Meas)	Diff
Planmeca	63	Inherent	973.5	942.2	**31.3**	1094.8	1060.2	**34.6**
	70	Inherent	998.2	967.4	**30.8**	1177.8	1143.2	**34.6**
		Inherent +0.1mm Cu	1171.6	1138.9	**32.7**	1552.3	1511.3	**41.0**
Gendex	70(G)	Inherent	1013.9	978	**35.9**	1071.9	1039.8	**32.2**
		Inherent +0.1mm Cu	1177.1	1139	**38.1**	1542.9	1499.9	**43.0**

On average, the measured signal differences (3.0%) were 10% lower than the predicted signal differences (3.3%).

A few factors could be responsible for the systematic difference between the measured and predicted SdNR. One possible reason could be a disparity between the modeled Type 1100 aluminum and the McDavid aluminum phantom. A potential composition for Type 1100 aluminum was used for the model. The precise composition of the aluminum phantom is not known. The attenuation was measured through both at 70 kVp (although it was difficult to completely cover the detector with the McDavid phantom as previously mentioned): PMMA/Type 1100 aluminum and PMMA/McDavid phantom. The transmission through the PMMA/McDavid phantom was 8% lower than through the PMMA/Type 1100 aluminum suggesting the McDavid phantom contained a slightly different aluminum alloy blend. Differences between the modeled and actual

phantom would lead to differences in the modeled versus measured SdNR. Non-uniformities in the phantom would also affect the measured noise.

As described in chapter 5 (section 5.1.1.3), the contrast analysis performed with the aluminum phantom alone demonstrated a high degree of uncertainty for Gendex acquired images in the 0.03 cm well (mean 3.2, σ 1.3, Appendix K). The results were more consistent with the Planmeca acquired images but some variability did exist (mean 3.4, σ 0.5, Appendix K). The difference between the actual and predicted responses shown in Table 6-18 is less than this previously measured uncertainty.

The systematic bias between the Amptek and IPEM spectra may also be contributing to the difference between the measured and predicted SdNRs. The contrast ratio for the measured spectra was on average 6% lower than the contrast ratio for the IPEM spectra (Table 5-12). Adjusting the predicted SdNR to account for this bias reduces the difference between the predicted and measured SdNR to on average 4%, which is within the expected range of error for the Carestream/Planmeca units (Table 6-8).

Individual variations in sensor uniformity could also have contributed to both the SdNR and SNR differences. In particular, the 0.03 cm well was not in the center of the sensor because it was not in the center of the phantom. The sensor response function was estimated based on measurements from the center of the sensor. To eliminate the measurement location as a contributing factor, a check of the sensor uniformity was completed following the manufacturer's recommendations.

Each sensor was imaged at 70 kVp with a two cm PMMA and seven mm aluminum phantom placed directly on it. Twelve-bit images without image enhancement were acquired and imported into ImageJ as previously described. A 400 x 350 pixel ROI was placed in 15 locations across each of the images and the mean and standard deviation

(noise) in each ROI was recorded (see Figure 6-11). From these data, the averages and variation across the sensor were calculated. The results are shown in Tables 6-19 and 6-20.

Table 6-19. Uniformity Analysis Carestream/Planmeca

Room	Sensor ID	Sensor Dose (μGy)	Mean Signal	σ Signal	%σ Signal	Mean N	σ N	%σ N	Mean SNR	σ SNR	%σ (SNR)
409	ZBGQ249	106	1612.9	22.3	**1.4%**	16.1	0.7	**4.5%**	100.5	4.6	**5%**
433	BGQA043	84	1359.3	22.4	**1.7%**	14.3	0.8	**5.6%**	95.5	6.3	**7%**
435	ZBGQ262	81	1335.0	10.7	**0.8%**	13.3	0.4	**3.1%**	101.1	2.4	**2%**
481	BFGQ140	101	1586.4	12.9	**0.8%**	17.0	1.1	**6.4%**	93.7	6.2	**7%**
483	WFGQ214	108	1562.3	21.0	**1.3%**	15.2	0.7	**4.8%**	102.8	4.4	**4%**

Table 6-20. Uniformity Analysis: Carestream/Gendex

Room	Sensor ID	Sensor Dose (μGy)	Mean Signal	σ Signal	%σ Signal	Mean N	σ N	%σ N	Mean SNR	σ SNR	%σ (SNR)
377	ZBGQ161	125	3267.1	51.9	**1.6%**	18.2	4.7	**25.7%**	189.0	42.1	**22%**
378	WFGQ211	129	1672.1	37.2	**2.2%**	16.3	1.3	**7.9%**	103.3	9.3	**9%**
425	ZBGQ255	121	1711.4	11.8	**0.7%**	16.3	0.5	**3.4%**	104.9	4.1	**4%**
457	ZBGQ250	159	2104.1	44.8	**2.1%**	20.2	4.7	**23.1%**	108.0	19.0	**18%**

The sensors imaged with the Planmeca units showed minor signal variations (<2%σ). The noise variations were higher ranging from 3 to 6.5 %σ.

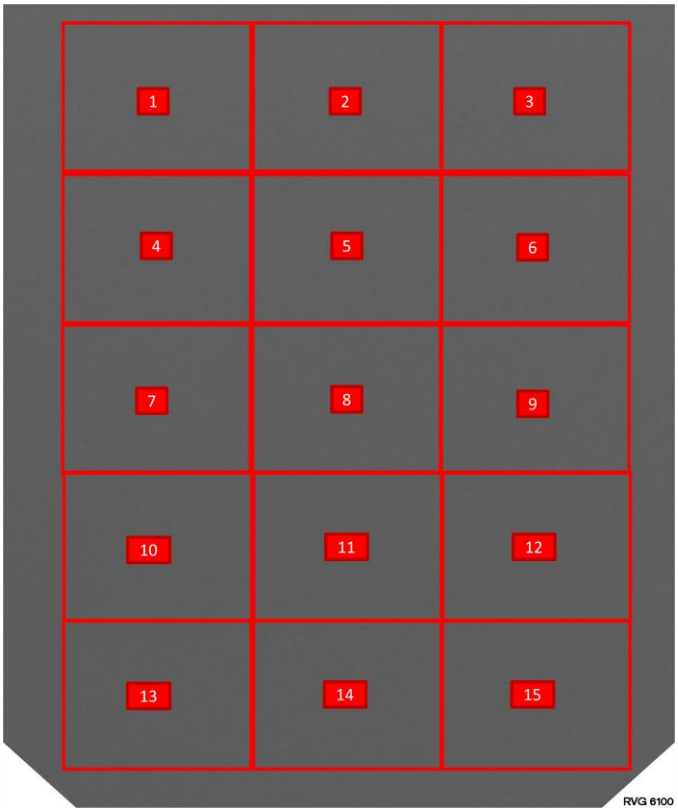

Figure 6-11. Uniformity Analysis

The sensor non-uniformities may have contributed to the disparity between predicted and measured SdNR, particularly the images acquired with the Gendex units, which showed significant noise variations.

The 15% difference between predicted and measured SdNR for the Carestream sensor/Gendex units (with inherent filtration) is probably due in part to the inadequacy of the IPEM modeled spectra as described in chapter 4.

Note the mean signal for both image sets was considerably higher than predicted with 0.1 mm added copper filtration (~30%). This could be due to the demonstrated energy dependence of the Carestream sensors.

The measured SdNR values at the optimized techniques were also compared to the measured SdNR values at the reference technique and are given in Table 6-21.

Table 6-21. Optimized versus Reference SdNR

	kVp	Target K_{air} (μGy)	Average K_{air} (μGy)	Filter	Average SdNR	Comparison to Reference (average)
Carestream/Planmeca	63	723	729	Inherent	1.9	
	70	637	612	Inherent	1.9	0%
	70	466	451	0.1 mm Cu	1.9	0%
Carestream/Gendex	70	883	868	Inherent	1.8	-5%
	70	669	626	0.1 mm Cu	2.0	5%

The relative measured SdNR values are consistent with the optimization prediction. For the Planmeca units, equivalent SdNR values were achieved with 16% lower entrance air KERMA at 70 kVp (inherent filtration) and 38% lower entrance air KERMA (K_{air}) with 0.1 mm added copper filtration. The Gendex units did not meet the SdNR target with inherent filtration alone but showed higher than predicted performance with 0.1 mm added copper filtration. An example of each image series acquired without image enhancement is presented in Figures 6-12 and 6-13. The 0.03 cm well is difficult to visualize, as expected, since it was selected to be at the threshold of perceptibility.

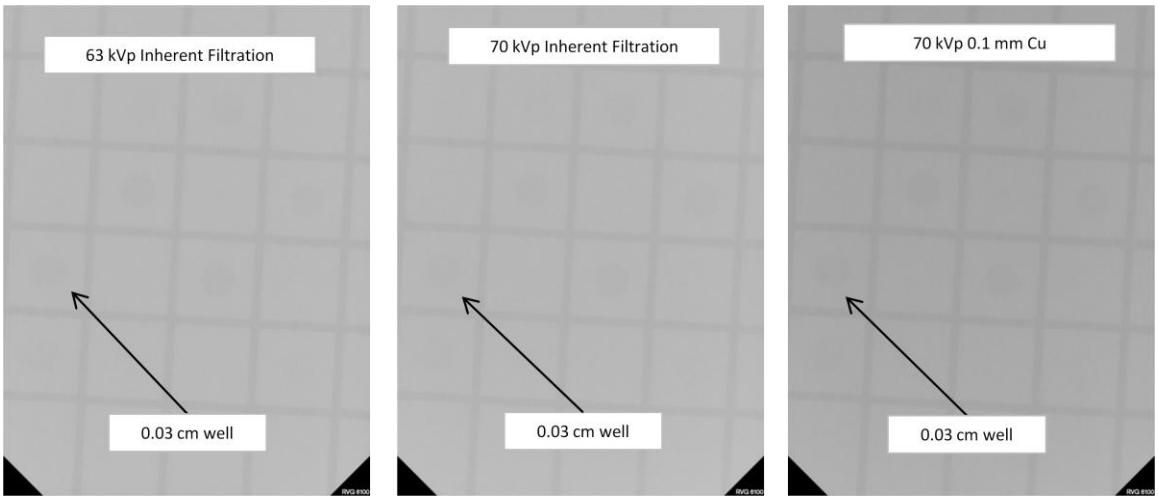

Figure 6-12. Carestream/Planmeca Clinical Validation Images

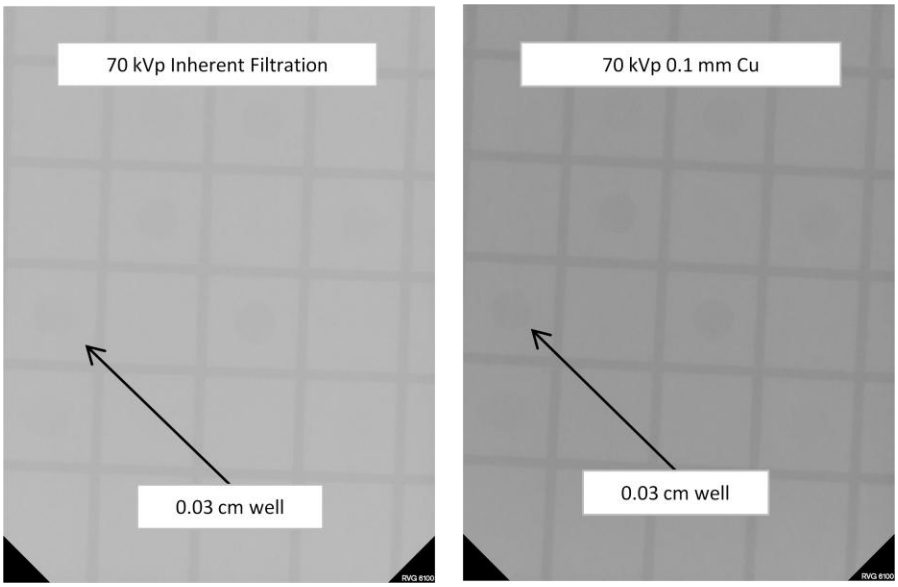

Figure 6-13. Carestream/Gendex Clinical Validation Images

The clinical validation MCNPX input deck can be found in **Appendix P** and the clinical data can be found in **Appendix R**.

6.7. Effective Dose Estimate and Comparison to Reference Technique

Thilander-Klang and Helmrot (2010) caution effective dose as a risk estimator for dental radiographic procedures must be used carefully as uncertainties may be as high as +/- 40%. With this caveat, the dose-area-product (DAP) to effective dose conversion coefficient published by Looe, et al, (2008) was employed to estimate the effective dose for the reference and proposed techniques. The authors calculated the effective dose for intraoral radiography at 65 kVp using ICRP 103 dose coefficients. Looe, et al, also published the kVp dependent DAP to effective dose dependence conversion factors for panoramic dental radiography. A linear regression (R^2= 0.986) of these data was performed to estimate a kVp correction factor for the bitewing ("back") dose coefficient at the clinical reference and proposed techniques and are summarized in Table 6-22.

Table 6-22. kVp Corrected Dose-Area-Product to Effective Dose Conversion Factors

	0.107(+/-0.030) μSv mGy^{-1}cm^{-2} at 65 kVp (Looe, et al)			
kVp	**63**	**70**	**90**	
Estimated E(ICRP103/DAP)	0.103(+/-0.034)	0.116(+/-0.041)	0.154(+/-0.054)	**μSv mGy^{-1}cm^{-2}**

The estimated effective dose of the reference and proposed techniques are given in Tables 6-23 (Planmeca) and 6-24 (Gendex). The values in red represent an increase over the reference technique.

Table 6-23. Estimated Effective Doses for Reference and Proposed Techniques (Planmeca)

Field Size (cm^2)	28.3						
	63 kVp Inherent Filtration	**90 kVp 0.1 mm Cu (σ)**	**% Decrease**	**70 kVp 0.1 mm Cu (σ)**	**% Decrease**	**70 kVp Inherent Filtration (σ)**	**% Decrease**
Entrance Dose (µGy)	723	260	**64%**	392	**46%**	606	**16%**
Effective Dose (µSv)	2.1(+/- 0.70)	1.1(+/-0.40)	**44%**	1.3(+/-0.45)	**38%**	2.0(+/-0.70)	**4%**

Table 6-24. Gendex Estimated Effective Doses Relative to Planmeca Reference Technique

	70 kVp Inherent Filtration	**% Decrease**	**70 kVp 0.1 mm Cu**	**% Decrease**
Entrance Dose (µGy)	907	**25%**	599	17%
Effective Dose (µSv)	3.5 (+/- 1.23)	**66%**	2.3 (+/- 0.81)	**10%**

At 90 kVp with 0.1 mm added copper filtration, the effective dose could potentially be decreased by over 40%. A nearly 40% decrease in effective dose may be possible using the existing equipment at 70 kVp with 0.1 mm added copper filtration. Although the dose for equivalent SdNR on the Gendex units exceeds the reference, by adding 0.1 mm copper filtration, the effective dose could be lowered by over 30% with respect to the current technique on that unit (3.5 µSv versus 2.3 µSv).

6.8. Limitations and Recommendations

6.8.1. Limitations

Limitations to the results described in this study must be acknowledged.

Modeling the Detector Response: It was not possible to acquire ScanX® images without post-processing applied and was difficult to acquire unprocessed (or minimally processed) images with the Carestream sensor. A combination of factors is probably to blame. The sensors are networked through a third-party vendor picture archiving and communications system. Features that may be available with the sensor manufacturer's software are absent. This problem has been addressed in general radiography. All manufacturers of general purpose digital radiographic units and computed radiography readers provide specific processing menus for testing purposes and instructions on how to access those menus. These menus allow the user to test the system linearity over a range of exposures and evaluate the detector uniformity. The same requirements should be imposed on the manufacturers of digital dental sensors. Given this limitation, the sensor response functions described should only be considered valid under the conditions tested.

Systematic shift in Amptek measured spectrum. Because the Amptek measured spectra were systematically shifted to higher energies (on average 4%) the IPEM spectra were used for the MCNPX simulation. This problem may have been the result of the software post-processing or a set-up error. The IPEM spectrum generator had its own limitations as it could not model a half-wave rectified system. Further investigation of the Amptek for clinical use in dental applications is warranted as this system provides a means to measure directly what may not be well modeled. Other products are also available on the market for modeling radiographic spectra. Since the optimization analysis was dependent on relative and not absolute performance comparisons, the energy shift would not have altered the results and the Amptek spectra could have been used for the model.

6.8.2. Recommendations

A simple anthropomorphic dental phantom was designed and presented in this study. This model could be readily modified to assess a variety of dental imaging tasks. For example, a two tooth model could be used to optimize the image quality for the evaluation of interproximal caries. Child-size tooth models could also be developed to appropriately scale down the dose for pediatric patients. A physical model of this phantom would be very valuable to assist the medical physicist in optimizing dental radiographic procedures in the clinic.

The MCNPX simulation could be improved by modeling the sensors, obviating the need for an experimental sensor response function. This would require detailed information, which the sensor manufacturer's may or may not be willing to provide.

Chapter 7: Conclusion

This research illustrates a new and original method for optimizing digital dental radiography using radiation transport simulation and a unique anthropomorphic phantom. The findings add to the body of literature describing optimal techniques for dental radiography but also provide specific and actionable clinical recommendations.

Acceptable digital image quality can be achieved at radiation doses lower than previously possible with film radiography. But unlike film, adequate digital sensor dose is not readily apparent. Using the basic steps described here, a well executed approach to image optimization in dentistry can be achieved. The workflow developed in this work proceeds as follows:

- Characterize the radiographic units,
- experimentally determine the sensor response, noise response, and response reproducibility of the digital sensors,
- develop a realistic computer model of the relevant anatomy,
- generate the appropriate data through Monte Carlo modeling,
- devise meaningful image quality metrics and perform a sensitivity analysis to evaluate weighting options,
- identify the optimal technique,
- validate the results clinically.

The key findings of this research were:

1. With equal weighting of all FOMs and given no limitations on the equipment, the optimal combination of kVp and tube filtration for dental bitewing imaging identified was ***90 kVp with 0.1 mm added copper filtration***. This modification to the current technique could reduce entrance dose ~60% and effective dose ~45%. The optimal

technique in the radiographic units' operating range was ***70 kVp with 0.1 mm added copper filtration***, which could be immediately adopted for a ~50% entrance dose and ~40% effective dose savings (Planmeca units). This simple modification to the existing equipment could be accomplished at relatively low cost.

2. The Gendex units underperformed the Planmeca units. Without added filtration, a higher patient dose was required to attain equivalent image quality (SdNR). The best response was observed with 0.1 mm added copper filtration, which yielded an entrance dose ~17% lower than the reference technique but with ~11% higher effective dose.
3. Single-factor ANOVA disclosed statistically significant energy dependent and radiographic unit dependent responses for the Carestream RVG 6100 sensor.

In summary, the goal of this research was to appropriately model a dental radiographic system, establish figures of merit, use the FOMs to mathematically optimize the system, and validate the optimized technique clinically. This represents a unique approach to evaluating digital dental sensors. To date, the published research has primarily focused on detector comparisons, sensor characteristics, or general imaging guidelines. A rigorous method for fully characterizing and modeling the dental imaging system to include a realistic simulated anthropomorphic dental phantom has not been well described.

In general, the optimization method proposed facilitates image quality standardization across different radiographic units and sensors in a dental clinic. The unique optimization method combining radiation transport simulations, calibration, and validation with an anthropomorphic phantom could be customized to evaluate any adult or pediatric intraoral imaging task. The results underscore the importance of tailoring the technical parameters to the particular imaging devices in service.

The conclusion of this work represents the first step in the process of image optimization. Although not considered here, post-processing plays a significant role in the appearance and diagnostic quality of digital images. Follow-on studies could be performed to optimize post-processing parameters (i.e., edge enhancement, noise reduction, etc.), to compare the performance of other sensors and radiographic units, or to refine and customize the simulated anthropomorphic phantom for other dental radiographic procedures.

Appendix A

Spectral Data Used for MCNPX Source Definition (Chapter Three)

File Name: 075K12D0W2R10%
Source: Catalogue of X-Ray Spectra
HVL: 2.933 mm Al
Filtration: 3.29 mm Al
Tube Potential: 75 kVp
mAs: 25
Distance: 75 cm
Sphere area at 75 cm 70685.8 cm^2

E (keV)	E (MeV)	Photons/mAs/ mm^2	Photons/mAs/ cm^2	Photons/cm^2 (at 75 cm)	Photons (at source)	Fraction
0.5	5.00E-04	0.00E+00	0.00E+00	0.00E+00	0.00E+00	0.00E+00
1	1.00E-03	0.00E+00	0.00E+00	0.00E+00	0.00E+00	0.00E+00
1.5	1.50E-03	0.00E+00	0.00E+00	0.00E+00	0.00E+00	0.00E+00
2	2.00E-03	0.00E+00	0.00E+00	0.00E+00	0.00E+00	0.00E+00
2.5	2.50E-03	0.00E+00	0.00E+00	0.00E+00	0.00E+00	0.00E+00
3	3.00E-03	0.00E+00	0.00E+00	0.00E+00	0.00E+00	0.00E+00
3.5	3.50E-03	0.00E+00	0.00E+00	0.00E+00	0.00E+00	0.00E+00
4	4.00E-03	0.00E+00	0.00E+00	0.00E+00	0.00E+00	0.00E+00
4.5	4.50E-03	0.00E+00	0.00E+00	0.00E+00	0.00E+00	0.00E+00
5	5.00E-03	0.00E+00	0.00E+00	0.00E+00	0.00E+00	0.00E+00
5.5	5.50E-03	0.00E+00	0.00E+00	0.00E+00	0.00E+00	0.00E+00
6	6.00E-03	0.00E+00	0.00E+00	0.00E+00	0.00E+00	0.00E+00
6.5	6.50E-03	3.86E-31	3.86E-29	9.64E-28	6.81E-23	1.97E-37
7	7.00E-03	2.66E-24	2.66E-22	6.65E-21	4.70E-16	1.36E-30
7.5	7.50E-03	4.42E-19	4.42E-17	1.11E-15	7.82E-11	2.26E-25
8	8.00E-03	4.92E-15	4.92E-13	1.23E-11	8.69E-07	2.52E-21
8.5	8.50E-03	9.88E-11	9.88E-09	2.47E-07	1.75E-02	5.05E-17
9	9.00E-03	2.56E-09	2.56E-07	6.41E-06	4.53E-01	1.31E-15
9.5	9.50E-03	2.20E-06	2.20E-04	5.49E-03	3.88E+02	1.12E-12
10	1.00E-02	8.37E-05	8.37E-03	2.09E-01	1.48E+04	4.28E-11
10.5	1.05E-02	1.18E-04	1.18E-02	2.95E-01	2.08E+04	6.03E-11
11	1.10E-02	1.66E-03	1.66E-01	4.14E+00	2.93E+05	8.48E-10
11.5	1.15E-02	4.01E-02	4.01E+00	1.00E+02	7.09E+06	2.05E-08
12	1.20E-02	6.82E-02	6.82E+00	1.70E+02	1.20E+07	3.49E-08
12.5	1.25E-02	2.84E-01	2.84E+01	7.11E+02	5.02E+07	1.45E-07
13	1.30E-02	1.14E+00	1.14E+02	2.84E+03	2.01E+08	5.82E-07
13.5	1.35E-02	3.80E+00	3.80E+02	9.49E+03	6.71E+08	1.94E-06

E (keV)	E (MeV)	Photons/mAs/ mm^2	Photons/mAs/ cm^2	Photons/cm^2	Photons	Fraction
14	1.40E-02	1.02E+01	1.02E+03	2.55E+04	1.80E+09	5.23E-06
14.5	1.45E-02	2.49E+01	2.49E+03	6.23E+04	4.40E+09	1.27E-05
15	1.50E-02	5.43E+01	5.43E+03	1.36E+05	9.60E+09	2.78E-05
15.5	1.55E-02	1.08E+02	1.08E+04	2.70E+05	1.91E+10	5.53E-05
16	1.60E-02	2.00E+02	2.00E+04	4.99E+05	3.53E+10	1.02E-04
16.5	1.65E-02	3.39E+02	3.39E+04	8.49E+05	6.00E+10	1.74E-04
17	1.70E-02	5.51E+02	5.51E+04	1.38E+06	9.74E+10	2.82E-04
17.5	1.75E-02	8.39E+02	8.39E+04	2.10E+06	1.48E+11	4.29E-04
18	1.80E-02	1.23E+03	1.23E+05	3.07E+06	2.17E+11	6.28E-04
18.5	1.85E-02	1.73E+03	1.73E+05	4.31E+06	3.05E+11	8.83E-04
19	1.90E-02	2.33E+03	2.33E+05	5.84E+06	4.12E+11	1.19E-03
19.5	1.95E-02	3.07E+03	3.07E+05	7.68E+06	5.43E+11	1.57E-03
20	2.00E-02	3.92E+03	3.92E+05	9.80E+06	6.93E+11	2.00E-03
20.5	2.05E-02	4.86E+03	4.86E+05	1.21E+07	8.59E+11	2.49E-03
21	2.10E-02	5.96E+03	5.96E+05	1.49E+07	1.05E+12	3.05E-03
21.5	2.15E-02	7.09E+03	7.09E+05	1.77E+07	1.25E+12	3.63E-03
22	2.20E-02	8.36E+03	8.36E+05	2.09E+07	1.48E+12	4.27E-03
22.5	2.25E-02	9.65E+03	9.65E+05	2.41E+07	1.70E+12	4.93E-03
23	2.30E-02	1.10E+04	1.10E+06	2.75E+07	1.95E+12	5.64E-03
23.5	2.35E-02	1.23E+04	1.23E+06	3.09E+07	2.18E+12	6.31E-03
24	2.40E-02	1.38E+04	1.38E+06	3.45E+07	2.44E+12	7.06E-03
24.5	2.45E-02	1.51E+04	1.51E+06	3.79E+07	2.68E+12	7.75E-03
25	2.50E-02	1.64E+04	1.64E+06	4.11E+07	2.90E+12	8.41E-03
25.5	2.55E-02	1.78E+04	1.78E+06	4.46E+07	3.15E+12	9.12E-03
26	2.60E-02	1.91E+04	1.91E+06	4.78E+07	3.38E+12	9.79E-03
26.5	2.65E-02	2.03E+04	2.03E+06	5.08E+07	3.59E+12	1.04E-02
27	2.70E-02	2.16E+04	2.16E+06	5.40E+07	3.81E+12	1.10E-02
27.5	2.75E-02	2.27E+04	2.27E+06	5.67E+07	4.01E+12	1.16E-02
28	2.80E-02	2.38E+04	2.38E+06	5.96E+07	4.21E+12	1.22E-02
28.5	2.85E-02	2.48E+04	2.48E+06	6.20E+07	4.38E+12	1.27E-02
29	2.90E-02	2.58E+04	2.58E+06	6.44E+07	4.55E+12	1.32E-02
29.5	2.95E-02	2.65E+04	2.65E+06	6.63E+07	4.69E+12	1.36E-02
30	3.00E-02	2.73E+04	2.73E+06	6.83E+07	4.83E+12	1.40E-02
30.5	3.05E-02	2.81E+04	2.81E+06	7.02E+07	4.96E+12	1.44E-02
31	3.10E-02	2.86E+04	2.86E+06	7.15E+07	5.06E+12	1.46E-02
31.5	3.15E-02	2.93E+04	2.93E+06	7.31E+07	5.17E+12	1.50E-02

E (keV)	E (MeV)	Photons/mAs/ mm^2	Photons/mAs/ cm^2	Photons/cm^2	Photons	Fraction
32	3.20E-02	2.97E+04	2.97E+06	7.43E+07	5.25E+12	1.52E-02
32.5	3.25E-02	3.02E+04	3.02E+06	7.54E+07	5.33E+12	1.54E-02
33	3.30E-02	3.05E+04	3.05E+06	7.63E+07	5.39E+12	1.56E-02
33.5	3.35E-02	3.08E+04	3.08E+06	7.70E+07	5.44E+12	1.58E-02
34	3.40E-02	3.10E+04	3.10E+06	7.76E+07	5.48E+12	1.59E-02
34.5	3.45E-02	3.12E+04	3.12E+06	7.81E+07	5.52E+12	1.60E-02
35	3.50E-02	3.13E+04	3.13E+06	7.84E+07	5.54E+12	1.60E-02
35.5	3.55E-02	3.14E+04	3.14E+06	7.86E+07	5.56E+12	1.61E-02
36	3.60E-02	3.15E+04	3.15E+06	7.87E+07	5.56E+12	1.61E-02
36.5	3.65E-02	3.14E+04	3.14E+06	7.86E+07	5.56E+12	1.61E-02
37	3.70E-02	3.14E+04	3.14E+06	7.85E+07	5.55E+12	1.61E-02
37.5	3.75E-02	3.13E+04	3.13E+06	7.82E+07	5.53E+12	1.60E-02
38	3.80E-02	3.12E+04	3.12E+06	7.80E+07	5.51E+12	1.60E-02
38.5	3.85E-02	3.10E+04	3.10E+06	7.75E+07	5.48E+12	1.59E-02
39	3.90E-02	3.08E+04	3.08E+06	7.70E+07	5.45E+12	1.58E-02
39.5	3.95E-02	3.06E+04	3.06E+06	7.65E+07	5.41E+12	1.57E-02
40	4.00E-02	3.04E+04	3.04E+06	7.59E+07	5.37E+12	1.55E-02
40.5	4.05E-02	3.01E+04	3.01E+06	7.52E+07	5.32E+12	1.54E-02
41	4.10E-02	2.98E+04	2.98E+06	7.45E+07	5.26E+12	1.52E-02
41.5	4.15E-02	2.95E+04	2.95E+06	7.36E+07	5.21E+12	1.51E-02
42	4.20E-02	2.91E+04	2.91E+06	7.28E+07	5.15E+12	1.49E-02
42.5	4.25E-02	2.88E+04	2.88E+06	7.20E+07	5.09E+12	1.47E-02
43	4.30E-02	2.84E+04	2.84E+06	7.10E+07	5.02E+12	1.45E-02
43.5	4.35E-02	2.80E+04	2.80E+06	7.01E+07	4.95E+12	1.43E-02
44	4.40E-02	2.76E+04	2.76E+06	6.90E+07	4.88E+12	1.41E-02
44.5	4.45E-02	2.72E+04	2.72E+06	6.80E+07	4.81E+12	1.39E-02
45	4.50E-02	2.68E+04	2.68E+06	6.69E+07	4.73E+12	1.37E-02
45.5	4.55E-02	2.63E+04	2.63E+06	6.59E+07	4.66E+12	1.35E-02
46	4.60E-02	2.59E+04	2.59E+06	6.47E+07	4.58E+12	1.32E-02
46.5	4.65E-02	2.54E+04	2.54E+06	6.36E+07	4.49E+12	1.30E-02
47	4.70E-02	2.50E+04	2.50E+06	6.24E+07	4.41E+12	1.28E-02
47.5	4.75E-02	2.45E+04	2.45E+06	6.13E+07	4.33E+12	1.25E-02
48	4.80E-02	2.40E+04	2.40E+06	6.00E+07	4.24E+12	1.23E-02
48.5	4.85E-02	2.35E+04	2.35E+06	5.89E+07	4.16E+12	1.20E-02
49	4.90E-02	2.30E+04	2.30E+06	5.76E+07	4.07E+12	1.18E-02
49.5	4.95E-02	2.25E+04	2.25E+06	5.63E+07	3.98E+12	1.15E-02

E (keV)	E (MeV)	Photons/mAs/ mm^2	Photons/mAs/ cm^2	Photons/cm^2	Photons	Fraction
50	5.00E-02	2.20E+04	2.20E+06	5.51E+07	3.90E+12	1.13E-02
50.5	5.05E-02	2.15E+04	2.15E+06	5.38E+07	3.80E+12	1.10E-02
51	5.10E-02	2.10E+04	2.10E+06	5.26E+07	3.71E+12	1.08E-02
51.5	5.15E-02	2.05E+04	2.05E+06	5.13E+07	3.62E+12	1.05E-02
52	5.20E-02	2.00E+04	2.00E+06	5.00E+07	3.53E+12	1.02E-02
52.5	5.25E-02	1.95E+04	1.95E+06	4.87E+07	3.44E+12	9.96E-03
53	5.30E-02	1.90E+04	1.90E+06	4.74E+07	3.35E+12	9.69E-03
53.5	5.35E-02	1.84E+04	1.84E+06	4.61E+07	3.26E+12	9.43E-03
54	5.40E-02	1.79E+04	1.79E+06	4.48E+07	3.16E+12	9.16E-03
54.5	5.45E-02	1.74E+04	1.74E+06	4.34E+07	3.07E+12	8.88E-03
55	5.50E-02	1.68E+04	1.68E+06	4.21E+07	2.98E+12	8.62E-03
55.5	5.55E-02	1.63E+04	1.63E+06	4.08E+07	2.88E+12	8.34E-03
56	5.60E-02	1.58E+04	1.58E+06	3.94E+07	2.79E+12	8.07E-03
56.5	5.65E-02	1.52E+04	1.52E+06	3.81E+07	2.69E+12	7.80E-03
57	5.70E-02	1.47E+04	1.47E+06	3.68E+07	2.60E+12	7.53E-03
57.5	5.75E-02	1.42E+04	1.42E+06	3.55E+07	2.51E+12	7.26E-03
58	5.80E-02	1.56E+04	1.56E+06	3.89E+07	2.75E+12	7.97E-03
58.5	5.85E-02	1.31E+04	1.31E+06	3.28E+07	2.32E+12	6.71E-03
59	5.90E-02	1.26E+04	1.26E+06	3.15E+07	2.23E+12	6.44E-03
59.5	5.95E-02	1.54E+04	1.54E+06	3.86E+07	2.73E+12	7.89E-03
60	6.00E-02	1.15E+04	1.15E+06	2.88E+07	2.04E+12	5.90E-03
60.5	6.05E-02	1.10E+04	1.10E+06	2.75E+07	1.94E+12	5.62E-03
61	6.10E-02	1.05E+04	1.05E+06	2.62E+07	1.85E+12	5.35E-03
61.5	6.15E-02	9.94E+03	9.94E+05	2.48E+07	1.76E+12	5.08E-03
62	6.20E-02	9.41E+03	9.41E+05	2.35E+07	1.66E+12	4.81E-03
62.5	6.25E-02	8.89E+03	8.89E+05	2.22E+07	1.57E+12	4.55E-03
63	6.30E-02	8.36E+03	8.36E+05	2.09E+07	1.48E+12	4.27E-03
63.5	6.35E-02	7.83E+03	7.83E+05	1.96E+07	1.38E+12	4.01E-03
64	6.40E-02	7.32E+03	7.32E+05	1.83E+07	1.29E+12	3.74E-03
64.5	6.45E-02	6.79E+03	6.79E+05	1.70E+07	1.20E+12	3.48E-03
65	6.50E-02	6.27E+03	6.27E+05	1.57E+07	1.11E+12	3.21E-03
65.5	6.55E-02	5.76E+03	5.76E+05	1.44E+07	1.02E+12	2.95E-03
66	6.60E-02	5.25E+03	5.25E+05	1.31E+07	9.27E+11	2.68E-03
66.5	6.65E-02	4.73E+03	4.73E+05	1.18E+07	8.37E+11	2.42E-03
67	6.70E-02	5.35E+03	5.35E+05	1.34E+07	9.46E+11	2.74E-03
67.5	6.75E-02	3.72E+03	3.72E+05	9.29E+06	6.57E+11	1.90E-03

E (keV)	E (MeV)	Photons/mAs/ mm^2	Photons/mAs/ cm^2	Photons/cm^2	Photons	Fraction
68	6.80E-02	3.22E+03	3.22E+05	8.06E+06	5.70E+11	1.65E-03
68.5	6.85E-02	2.83E+03	2.83E+05	7.08E+06	5.01E+11	1.45E-03
69	6.90E-02	2.76E+03	2.76E+05	6.89E+06	4.87E+11	1.41E-03
69.5	6.95E-02	2.12E+03	2.12E+05	5.31E+06	3.76E+11	1.09E-03
70	7.00E-02	1.78E+03	1.78E+05	4.45E+06	3.14E+11	9.10E-04
70.5	7.05E-02	1.51E+03	1.51E+05	3.77E+06	2.67E+11	7.72E-04
71	7.10E-02	1.25E+03	1.25E+05	3.11E+06	2.20E+11	6.37E-04
71.5	7.15E-02	1.02E+03	1.02E+05	2.54E+06	1.80E+11	5.20E-04
72	7.20E-02	7.96E+02	7.96E+04	1.99E+06	1.41E+11	4.07E-04
72.5	7.25E-02	6.09E+02	6.09E+04	1.52E+06	1.08E+11	3.11E-04
73	7.30E-02	4.30E+02	4.30E+04	1.08E+06	7.60E+10	2.20E-04
73.5	7.35E-02	2.89E+02	2.89E+04	7.23E+05	5.11E+10	1.48E-04
74	7.40E-02	1.58E+02	1.58E+04	3.94E+05	2.79E+10	8.07E-05
74.5	7.45E-02	7.62E+01	7.62E+03	1.91E+05	1.35E+10	3.90E-05
75	7.50E-02	6.35E+00	6.35E+02	1.59E+04	1.12E+09	3.25E-06
			TOTAL:	**4.89E+09**	**3.45E+14**	**1.00E+00**

Appendix B

MCNPX Input Deck (Chapter 3)

```
Point Source in Trapezoid.  SURFACE TALLY AT 750 MM
c Cell Cards
8  0   -8
9  0    8

c Surface Cards
8 arb -1 1 -1
      -1 -1 -1
       1 1 -1
       1 -1 -1
      -7.25 17.2 75
      -7.25 -17.2 75
       7.25 17.2 75
       7.25 -17.2 75
       1234 1256 1357 2468 3478 5678   $Trapezoid to match f/s at 182.22

c Data Cards
sdef par=p erg=d1  pos=0 0 0
si1 h 0.006 0.0065 0.007 0.0075 0.008 0.0085 0.009 0.0095 0.01 0.0105 0.011
      0.0115 0.012 0.0125 0.013 0.0135 0.014 0.0145 0.015 0.0155 0.016 0.0165
      0.017 0.0175 0.018 0.0185 0.019 0.0195 0.02 0.0205 0.021 0.0215 0.022
      0.0225 0.023 0.0235 0.024 0.0245 0.025 0.0255 0.026 0.0265 0.027 0.0275
      0.028 0.0285 0.029 0.0295 0.03 0.0305 0.031 0.0315 0.032 0.0325 0.033
      0.0335 0.034 0.0345 0.035 0.0355 0.036 0.0365 0.037 0.0375 0.038 0.0385
      0.039 0.0395 0.04 0.0405 0.041 0.0415 0.042 0.0425 0.043 0.0435 0.044
      0.0445 0.045 0.0455 0.046 0.0465 0.047 0.0475 0.048 0.0485 0.049 0.0495
      0.05 0.0505 0.051 0.0515 0.052 0.0525 0.053 0.0535 0.054 0.0545 0.055
      0.0555 0.056 0.0565 0.057 0.0575 0.058 0.0585 0.059 0.0595 0.06 0.0605
      0.061 0.0615 0.062 0.0625 0.063 0.0635 0.064 0.0645 0.065 0.0655 0.066
      0.0665 0.067 0.0675 0.068 0.0685 0.069 0.0695 0.07 0.0705 0.071 0.0715
      0.072 0.0725 0.073 0.0735 0.074 0.0745 0.075
sp1 d 0 1.97E-37 1.36E-30 2.26E-25 2.52E-21 5.05E-17 1.31E-15 1.12E-12 4.28E-11
      6.03E-11 8.48E-10 2.05E-08 3.49E-08 1.45E-07 5.82E-07 1.94E-06 5.23E-06
      1.27E-05 2.78E-05 5.53E-05 1.02E-04 1.74E-04 2.82E-04 4.29E-04 6.28E-04
      8.83E-04 1.19E-03 1.57E-03 2.00E-03 2.49E-03 3.05E-03 3.63E-03 4.27E-03
      4.93E-03 5.64E-03 6.31E-03 7.06E-03 7.75E-03 8.41E-03 9.12E-03 9.79E-03
      1.04E-02 1.10E-02 1.16E-02 1.22E-02 1.27E-02 1.32E-02 1.36E-02 1.40E-02
      1.44E-02 1.46E-02 1.50E-02 1.52E-02 1.54E-02 1.56E-02 1.58E-02 1.59E-02
      1.60E-02 1.60E-02 1.61E-02 1.61E-02 1.61E-02 1.61E-02 1.60E-02 1.60E-02
      1.59E-02 1.58E-02 1.57E-02 1.55E-02 1.54E-02 1.52E-02 1.51E-02 1.49E-02
```

```
41-         1.47E-02 1.45E-02 1.43E-02 1.41E-02 1.39E-02 1.37E-02 1.35E-02 1.32E-02
42-         1.30E-02 1.28E-02 1.25E-02 1.23E-02 1.20E-02 1.18E-02 1.15E-02 1.13E-02
43-         1.10E-02 1.08E-02 1.05E-02 1.02E-02 9.96E-03 9.69E-03 9.43E-03 9.16E-03
44-         8.88E-03 8.62E-03 8.34E-03 8.07E-03 7.80E-03 7.53E-03 7.26E-03 7.97E-03
45-         6.71E-03 6.44E-03 7.89E-03 5.90E-03 5.62E-03 5.35E-03 5.08E-03 4.81E-03
46-         4.55E-03 4.27E-03 4.01E-03 3.74E-03 3.48E-03 3.21E-03 2.95E-03 2.68E-03
47-         2.42E-03 2.74E-03 1.90E-03 1.65E-03 1.45E-03 1.41E-03 1.09E-03 9.10E-04
48-         7.72E-04 6.37E-04 5.20E-04 4.07E-04 3.11E-04 2.20E-04 1.48E-04 8.07E-05
49-         3.90E-05 3.25E-06
50-     mode p e
51-     imp:p,e 1 0
52-     phys:e
53-     f2:p 8.6
54-     e2 0.0065 0.007 0.0075 0.008 0.0085 0.009 0.0095 0.01 0.0105 0.011 0.0115
55-         0.012 0.0125 0.013 0.0135 0.014 0.0145 0.015 0.0155 0.016 0.0165 0.017
56-         0.0175 0.018 0.0185 0.019 0.0195 0.02 0.0205 0.021 0.0215 0.022 0.0225
57-         0.023 0.0235 0.024 0.0245 0.025 0.0255 0.026 0.0265 0.027 0.0275 0.028
58-         0.0285 0.029 0.0295 0.03 0.0305 0.031 0.0315 0.032 0.0325 0.033 0.0335
59-         0.034 0.0345 0.035 0.0355 0.036 0.0365 0.037 0.0375 0.038 0.0385 0.039
60-         0.0395 0.04 0.0405 0.041 0.0415 0.042 0.0425 0.043 0.0435 0.044 0.0445
61-         0.045 0.0455 0.046 0.0465 0.047 0.0475 0.048 0.0485 0.049 0.0495 0.05
62-         0.0505 0.051 0.0515 0.052 0.0525 0.053 0.0535 0.054 0.0545 0.055 0.0555
63-         0.056 0.0565 0.057 0.0575 0.058 0.0585 0.059 0.0595 0.06 0.0605 0.061
64-         0.0615 0.062 0.0625 0.063 0.0635 0.064 0.0645 0.065 0.0655 0.066 0.0665
65-         0.067 0.0675 0.068 0.0685 0.069 0.0695 0.07 0.0705 0.071 0.0715 0.072
66-         0.0725 0.073 0.0735 0.074 0.0745 0.075
```

Appendix C

Comparison of IPEM vs. MCNPX Photon Fluence at 750 mm from Source

$$\%Dif = \frac{IPEM\_Value - MCNPX\_Value}{IPEM\_Value} * 100$$

E(MeV)	MCNPX Photons/cm^2	MCNPX Scaled to IPEM Photons/cm^2	IPEM Data Photons/cm^2	% Difference
5.00E-04	0.00E+00	0.00E+00	0.00E+00	#DIV/0!
1.00E-03	0.00E+00	0.00E+00	0.00E+00	#DIV/0!
1.50E-03	0.00E+00	0.00E+00	0.00E+00	#DIV/0!
2.00E-03	0.00E+00	0.00E+00	0.00E+00	#DIV/0!
2.50E-03	0.00E+00	0.00E+00	0.00E+00	#DIV/0!
3.00E-03	0.00E+00	0.00E+00	0.00E+00	#DIV/0!
3.50E-03	0.00E+00	0.00E+00	0.00E+00	#DIV/0!
4.00E-03	0.00E+00	0.00E+00	0.00E+00	#DIV/0!
4.50E-03	0.00E+00	0.00E+00	0.00E+00	#DIV/0!
5.00E-03	0.00E+00	0.00E+00	0.00E+00	#DIV/0!
5.50E-03	0.00E+00	0.00E+00	0.00E+00	#DIV/0!
6.00E-03	0.00E+00	0.00E+00	0.00E+00	#DIV/0!
6.50E-03	0.00E+00	0.00E+00	9.64E-28	100.00
7.00E-03	0.00E+00	0.00E+00	6.65E-21	100.00
7.50E-03	0.00E+00	0.00E+00	1.11E-15	100.00
8.00E-03	0.00E+00	0.00E+00	1.23E-11	100.00
8.50E-03	0.00E+00	0.00E+00	2.47E-07	100.00
9.00E-03	0.00E+00	0.00E+00	6.41E-06	100.00
9.50E-03	0.00E+00	0.00E+00	5.49E-03	100.00
1.00E-02	0.00E+00	0.00E+00	2.09E-01	100.00
1.05E-02	0.00E+00	0.00E+00	2.95E-01	100.00
1.10E-02	0.00E+00	0.00E+00	4.14E+00	100.00
1.15E-02	4.11E-03	1.78E+02	1.00E+02	-77.28
1.20E-02	2.01E-03	8.67E+01	1.70E+02	49.11
1.25E-02	3.24E-02	1.40E+03	7.11E+02	-97.07
1.30E-02	6.06E-02	2.62E+03	2.84E+03	7.83
1.35E-02	2.19E-01	9.45E+03	9.49E+03	0.46

E(MeV)	MCNPX Photons/cm^2	MCNPX Scaled to IPEM Photons/cm^2	IPEM Data Photons/cm^2	% Difference
1.40E-02	5.85E-01	2.53E+04	2.55E+04	1.03
1.45E-02	1.48E+00	6.41E+04	6.23E+04	-2.92
1.50E-02	3.04E+00	1.31E+05	1.36E+05	3.42
1.55E-02	6.24E+00	2.69E+05	2.70E+05	0.31
1.60E-02	1.13E+01	4.88E+05	4.99E+05	2.17
1.65E-02	1.93E+01	8.35E+05	8.49E+05	1.66
1.70E-02	3.11E+01	1.34E+06	1.38E+06	2.65
1.75E-02	4.78E+01	2.07E+06	2.10E+06	1.51
1.80E-02	6.99E+01	3.02E+06	3.07E+06	1.50
1.85E-02	9.85E+01	4.26E+06	4.31E+06	1.33
1.90E-02	1.32E+02	5.71E+06	5.84E+06	2.13
1.95E-02	1.74E+02	7.50E+06	7.68E+06	2.23
2.00E-02	2.21E+02	9.54E+06	9.80E+06	2.66
2.05E-02	2.75E+02	1.19E+07	1.21E+07	2.05
2.10E-02	3.40E+02	1.47E+07	1.49E+07	1.45
2.15E-02	4.02E+02	1.74E+07	1.77E+07	2.15
2.20E-02	4.73E+02	2.04E+07	2.09E+07	2.14
2.25E-02	5.48E+02	2.37E+07	2.41E+07	1.87
2.30E-02	6.25E+02	2.70E+07	2.75E+07	1.95
2.35E-02	7.02E+02	3.03E+07	3.09E+07	1.73
2.40E-02	7.83E+02	3.38E+07	3.45E+07	2.01
2.45E-02	8.61E+02	3.72E+07	3.79E+07	1.67
2.50E-02	9.33E+02	4.03E+07	4.11E+07	1.94
2.55E-02	1.01E+03	4.37E+07	4.46E+07	1.97
2.60E-02	1.08E+03	4.69E+07	4.78E+07	2.04
2.65E-02	1.16E+03	4.99E+07	5.08E+07	1.74
2.70E-02	1.22E+03	5.26E+07	5.40E+07	2.58
2.75E-02	1.29E+03	5.56E+07	5.67E+07	1.96
2.80E-02	1.35E+03	5.83E+07	5.96E+07	2.13
2.85E-02	1.41E+03	6.07E+07	6.20E+07	2.03
2.90E-02	1.46E+03	6.31E+07	6.44E+07	2.00
2.95E-02	1.51E+03	6.51E+07	6.63E+07	1.95
3.00E-02	1.55E+03	6.70E+07	6.83E+07	1.88
3.05E-02	1.60E+03	6.89E+07	7.02E+07	1.83
3.10E-02	1.62E+03	6.98E+07	7.15E+07	2.45
3.15E-02	1.66E+03	7.18E+07	7.31E+07	1.84

E(MeV)	MCNPX Photons/cm^2	MCNPX Scaled to IPEM Photons/cm^2	IPEM Data Photons/cm^2	% Difference
3.20E-02	1.68E+03	7.27E+07	7.43E+07	2.16
3.25E-02	1.71E+03	7.37E+07	7.54E+07	2.28
3.30E-02	1.73E+03	7.48E+07	7.63E+07	1.97
3.35E-02	1.75E+03	7.55E+07	7.70E+07	1.96
3.40E-02	1.76E+03	7.61E+07	7.76E+07	1.87
3.45E-02	1.77E+03	7.66E+07	7.81E+07	1.90
3.50E-02	1.77E+03	7.67E+07	7.84E+07	2.15
3.55E-02	1.79E+03	7.72E+07	7.86E+07	1.81
3.60E-02	1.79E+03	7.71E+07	7.87E+07	1.97
3.65E-02	1.79E+03	7.72E+07	7.86E+07	1.77
3.70E-02	1.78E+03	7.71E+07	7.85E+07	1.77
3.75E-02	1.77E+03	7.65E+07	7.82E+07	2.18
3.80E-02	1.78E+03	7.68E+07	7.80E+07	1.49
3.85E-02	1.76E+03	7.62E+07	7.75E+07	1.79
3.90E-02	1.75E+03	7.56E+07	7.70E+07	1.89
3.95E-02	1.74E+03	7.52E+07	7.65E+07	1.74
4.00E-02	1.71E+03	7.41E+07	7.59E+07	2.41
4.05E-02	1.71E+03	7.37E+07	7.52E+07	2.03
4.10E-02	1.68E+03	7.28E+07	7.45E+07	2.31
4.15E-02	1.68E+03	7.24E+07	7.36E+07	1.69
4.20E-02	1.65E+03	7.13E+07	7.28E+07	2.14
4.25E-02	1.63E+03	7.03E+07	7.20E+07	2.32
4.30E-02	1.61E+03	6.96E+07	7.10E+07	2.02
4.35E-02	1.58E+03	6.84E+07	7.01E+07	2.45
4.40E-02	1.56E+03	6.76E+07	6.90E+07	2.11
4.45E-02	1.54E+03	6.65E+07	6.80E+07	2.27
4.50E-02	1.52E+03	6.56E+07	6.69E+07	2.01
4.55E-02	1.50E+03	6.46E+07	6.59E+07	1.86
4.60E-02	1.46E+03	6.32E+07	6.47E+07	2.34
4.65E-02	1.44E+03	6.22E+07	6.36E+07	2.16
4.70E-02	1.42E+03	6.13E+07	6.24E+07	1.90
4.75E-02	1.38E+03	5.97E+07	6.13E+07	2.53
4.80E-02	1.36E+03	5.89E+07	6.00E+07	1.87
4.85E-02	1.33E+03	5.75E+07	5.89E+07	2.26
4.90E-02	1.31E+03	5.66E+07	5.76E+07	1.86
4.95E-02	1.28E+03	5.52E+07	5.63E+07	2.10

E(MeV)	MCNPX Photons/cm^2	MCNPX Scaled to IPEM Photons/cm^2	IPEM Data Photons/cm^2	% Difference
5.00E-02	1.25E+03	5.41E+07	5.51E+07	1.85
5.05E-02	1.22E+03	5.27E+07	5.38E+07	2.02
5.10E-02	1.19E+03	5.16E+07	5.26E+07	1.76
5.15E-02	1.16E+03	5.02E+07	5.13E+07	2.06
5.20E-02	1.13E+03	4.88E+07	5.00E+07	2.25
5.25E-02	1.10E+03	4.77E+07	4.87E+07	1.96
5.30E-02	1.07E+03	4.63E+07	4.74E+07	2.31
5.35E-02	1.05E+03	4.52E+07	4.61E+07	1.92
5.40E-02	1.02E+03	4.40E+07	4.48E+07	1.77
5.45E-02	9.85E+02	4.25E+07	4.34E+07	1.99
5.50E-02	9.55E+02	4.13E+07	4.21E+07	2.03
5.55E-02	9.25E+02	4.00E+07	4.08E+07	1.98
5.60E-02	8.96E+02	3.87E+07	3.94E+07	1.88
5.65E-02	8.64E+02	3.73E+07	3.81E+07	2.09
5.70E-02	8.34E+02	3.60E+07	3.68E+07	2.02
5.75E-02	8.03E+02	3.47E+07	3.55E+07	2.17
5.80E-02	8.83E+02	3.82E+07	3.89E+07	2.01
5.85E-02	7.43E+02	3.21E+07	3.28E+07	2.12
5.90E-02	7.13E+02	3.08E+07	3.15E+07	2.17
5.95E-02	8.73E+02	3.77E+07	3.86E+07	2.15
6.00E-02	6.54E+02	2.82E+07	2.88E+07	1.98
6.05E-02	6.22E+02	2.69E+07	2.75E+07	2.12
6.10E-02	5.93E+02	2.56E+07	2.62E+07	1.96
6.15E-02	5.64E+02	2.44E+07	2.48E+07	1.93
6.20E-02	5.34E+02	2.31E+07	2.35E+07	1.89
6.25E-02	5.04E+02	2.18E+07	2.22E+07	1.98
6.30E-02	4.75E+02	2.05E+07	2.09E+07	1.78
6.35E-02	4.44E+02	1.92E+07	1.96E+07	1.95
6.40E-02	4.15E+02	1.80E+07	1.83E+07	1.85
6.45E-02	3.86E+02	1.67E+07	1.70E+07	1.70
6.50E-02	3.56E+02	1.54E+07	1.57E+07	1.95
6.55E-02	3.26E+02	1.41E+07	1.44E+07	2.24
6.60E-02	2.97E+02	1.28E+07	1.31E+07	2.04
6.65E-02	2.68E+02	1.16E+07	1.18E+07	2.20
6.70E-02	3.02E+02	1.31E+07	1.34E+07	2.39
6.75E-02	2.11E+02	9.12E+06	9.29E+06	1.92

E(MeV)	MCNPX Photons/cm^2	MCNPX Scaled to IPEM Photons/cm^2	IPEM Data Photons/cm^2	% Difference
6.80E-02	1.82E+02	7.88E+06	8.06E+06	2.21
6.85E-02	1.60E+02	6.92E+06	7.08E+06	2.30
6.90E-02	1.56E+02	6.74E+06	6.89E+06	2.22
6.95E-02	1.20E+02	5.20E+06	5.31E+06	2.02
7.00E-02	1.01E+02	4.35E+06	4.45E+06	2.12
7.05E-02	8.58E+01	3.71E+06	3.77E+06	1.76
7.10E-02	7.07E+01	3.06E+06	3.11E+06	1.82
7.15E-02	5.76E+01	2.49E+06	2.54E+06	2.05
7.20E-02	4.50E+01	1.94E+06	1.99E+06	2.34
7.25E-02	3.42E+01	1.48E+06	1.52E+06	2.77
7.30E-02	2.44E+01	1.05E+06	1.08E+06	2.05
7.35E-02	1.63E+01	7.04E+05	7.23E+05	2.60
7.40E-02	9.06E+00	3.91E+05	3.94E+05	0.74
7.45E-02	4.23E+00	1.83E+05	1.91E+05	4.05
7.50E-02	3.24E-01	1.40E+04	1.59E+04	11.87
TOTAL:	**1.11E+05**	**4.79E+09**	**4.89E+09**	

Appendix D

Exposure Calculations (Chapter 3)

Exposure (mR) per energy bin calculated as:

$$X = \sum_{i=1}^{n} \Re_X(E_n) * \Phi(E_n)$$

$$\Re_\chi(E) = 1.835x10^{-8} E\left(\frac{\mu_{en}(E)}{\rho}\right)_{air} * 10^3 (mR \cdot cm^2)$$

Where:

μ_{en}/ρ = Mass Energy Absorption Coefficient for Air, Dry (Near Sea Level) (g/cm^2)
E= Energy in MeV
$\Phi(E)$ = Photon fluence ($photons/cm^2$) at energy E

Values in **bold** published data [Hubbell, J.H., and Seltzer, S.M, 1996]. All other values determined by linear interpolation.

E(MeV)	$(\mu_{En}/\rho)_{air}$	IPEM X (mR)	MCNPX X (mR)
5.00E-04		0.00E+00	0.00E+00
1.00E-03		0.00E+00	0.00E+00
1.50E-03		0.00E+00	0.00E+00
2.00E-03		0.00E+00	0.00E+00
2.50E-03		0.00E+00	0.00E+00
3.00E-03		0.00E+00	0.00E+00
3.50E-03		0.00E+00	0.00E+00
4.00E-03		0.00E+00	0.00E+00
4.50E-03		0.00E+00	0.00E+00
5.00E-03		0.00E+00	0.00E+00
5.50E-03		0.00E+00	0.00E+00
6.00E-03	**2.270E+01**	0.00E+00	0.00E+00
6.50E-03	1.939E+01	2.23E-33	0.00E+00
7.00E-03	1.608E+01	1.37E-26	0.00E+00

E(MeV)	$(\mu_{En}/\rho)_{air}$	IPEM X (mR)	MCNPX X (mR)
7.50E-03	1.276E+01	1.94E-21	0.00E+00
8.00E-03	**9.446E+00**	1.70E-17	0.00E+00
8.50E-03	8.270E+00	3.18E-13	0.00E+00
9.00E-03	7.094E+00	7.51E-12	0.00E+00
9.50E-03	5.918E+00	5.67E-09	0.00E+00
1.00E-02	**4.742E+00**	1.82E-07	0.00E+00
1.05E-02	4.401E+00	2.50E-07	0.00E+00
1.10E-02	4.060E+00	3.40E-06	0.00E+00
1.15E-02	3.720E+00	7.87E-05	1.40E-04
1.20E-02	3.379E+00	1.27E-04	6.45E-05
1.25E-02	3.038E+00	4.95E-04	9.76E-04
1.30E-02	2.697E+00	1.83E-03	1.69E-03
1.35E-02	2.356E+00	5.54E-03	5.52E-03
1.40E-02	2.016E+00	1.32E-02	1.31E-02
1.45E-02	1.675E+00	2.77E-02	2.86E-02
1.50E-02	**1.334E+00**	4.99E-02	4.82E-02
1.55E-02	1.318E+00	1.01E-01	1.01E-01
1.60E-02	1.175E+00	1.72E-01	1.68E-01
1.65E-02	1.095E+00	2.81E-01	2.77E-01
1.70E-02	1.016E+00	4.37E-01	4.25E-01
1.75E-02	9.365E-01	6.31E-01	6.21E-01
1.80E-02	8.569E-01	8.68E-01	8.55E-01
1.85E-02	7.774E-01	1.14E+00	1.12E+00
1.90E-02	6.979E-01	1.42E+00	1.39E+00
1.95E-02	6.184E-01	1.70E+00	1.66E+00
2.00E-02	**5.389E-01**	1.94E+00	1.89E+00
2.05E-02	5.196E-01	2.37E+00	2.33E+00
2.10E-02	5.004E-01	2.87E+00	2.83E+00
2.15E-02	4.811E-01	3.37E+00	3.29E+00
2.20E-02	4.619E-01	3.90E+00	3.81E+00
2.25E-02	4.426E-01	4.41E+00	4.32E+00
2.30E-02	4.233E-01	4.92E+00	4.83E+00
2.35E-02	4.041E-01	5.38E+00	5.28E+00
2.40E-02	3.848E-01	5.85E+00	5.73E+00
2.45E-02	3.656E-01	6.22E+00	6.12E+00
2.50E-02	3.463E-01	6.53E+00	6.40E+00

E(MeV)	$(\mu_{En}/\rho)_{air}$	IPEM X (mR)	MCNPX X (mR)
2.55E-02	3.270E-01	6.82E+00	6.68E+00
2.60E-02	3.078E-01	7.02E+00	6.88E+00
2.65E-02	2.885E-01	7.13E+00	7.01E+00
2.70E-02	2.693E-01	7.20E+00	7.01E+00
2.75E-02	2.500E-01	7.16E+00	7.02E+00
2.80E-02	2.307E-01	7.06E+00	6.91E+00
2.85E-02	2.115E-01	6.86E+00	6.72E+00
2.90E-02	1.922E-01	6.59E+00	6.46E+00
2.95E-02	1.730E-01	6.21E+00	6.09E+00
3.00E-02	**1.537E-01**	5.78E+00	5.67E+00
3.05E-02	1.494E-01	5.87E+00	5.76E+00
3.10E-02	1.452E-01	5.91E+00	5.77E+00
3.15E-02	1.409E-01	5.96E+00	5.85E+00
3.20E-02	1.366E-01	5.96E+00	5.83E+00
3.25E-02	1.324E-01	5.95E+00	5.82E+00
3.30E-02	1.281E-01	5.92E+00	5.80E+00
3.35E-02	1.238E-01	5.86E+00	5.75E+00
3.40E-02	1.196E-01	5.79E+00	5.68E+00
3.45E-02	1.153E-01	5.70E+00	5.59E+00
3.50E-02	1.110E-01	5.59E+00	5.47E+00
3.55E-02	1.067E-01	5.46E+00	5.36E+00
3.60E-02	1.025E-01	5.33E+00	5.22E+00
3.65E-02	9.821E-02	5.17E+00	5.08E+00
3.70E-02	9.394E-02	5.01E+00	4.92E+00
3.75E-02	8.967E-02	4.83E+00	4.72E+00
3.80E-02	8.540E-02	4.64E+00	4.57E+00
3.85E-02	8.114E-02	4.45E+00	4.37E+00
3.90E-02	7.687E-02	4.24E+00	4.16E+00
3.95E-02	7.260E-02	4.03E+00	3.96E+00
4.00E-02	**6.833E-02**	3.81E+00	3.72E+00
4.05E-02	6.696E-02	3.74E+00	3.67E+00
4.10E-02	6.560E-02	3.68E+00	3.59E+00
4.15E-02	6.423E-02	3.60E+00	3.54E+00
4.20E-02	6.286E-02	3.53E+00	3.45E+00
4.25E-02	6.149E-02	3.45E+00	3.37E+00
4.30E-02	6.013E-02	3.37E+00	3.30E+00

E(MeV)	$(\mu_{En}/\rho)_{air}$	IPEM X (mR)	MCNPX X (mR)
4.35E-02	5.876E-02	3.29E+00	3.21E+00
4.40E-02	5.739E-02	3.20E+00	3.13E+00
4.45E-02	5.602E-02	3.11E+00	3.04E+00
4.50E-02	5.466E-02	3.02E+00	2.96E+00
4.55E-02	5.329E-02	2.93E+00	2.88E+00
4.60E-02	5.192E-02	2.84E+00	2.77E+00
4.65E-02	5.055E-02	2.74E+00	2.68E+00
4.70E-02	4.919E-02	2.65E+00	2.60E+00
4.75E-02	4.782E-02	2.55E+00	2.49E+00
4.80E-02	4.645E-02	2.46E+00	2.41E+00
4.85E-02	4.508E-02	2.36E+00	2.31E+00
4.90E-02	4.372E-02	2.27E+00	2.22E+00
4.95E-02	4.235E-02	2.17E+00	2.12E+00
5.00E-02	**4.100E-02**	2.07E+00	2.03E+00
5.05E-02	4.045E-02	2.02E+00	1.98E+00
5.10E-02	3.992E-02	1.96E+00	1.93E+00
5.15E-02	3.939E-02	1.91E+00	1.87E+00
5.20E-02	3.887E-02	1.85E+00	1.81E+00
5.25E-02	3.834E-02	1.80E+00	1.76E+00
5.30E-02	3.781E-02	1.74E+00	1.70E+00
5.35E-02	3.728E-02	1.69E+00	1.65E+00
5.40E-02	3.675E-02	1.63E+00	1.60E+00
5.45E-02	3.622E-02	1.57E+00	1.54E+00
5.50E-02	3.570E-02	1.52E+00	1.49E+00
5.55E-02	3.517E-02	1.46E+00	1.43E+00
5.60E-02	3.464E-02	1.40E+00	1.38E+00
5.65E-02	3.411E-02	1.35E+00	1.32E+00
5.70E-02	3.358E-02	1.29E+00	1.27E+00
5.75E-02	3.305E-02	1.24E+00	1.21E+00
5.80E-02	3.252E-02	1.35E+00	1.32E+00
5.85E-02	3.200E-02	1.13E+00	1.10E+00
5.90E-02	3.147E-02	1.07E+00	1.05E+00
5.95E-02	3.094E-02	1.30E+00	1.27E+00
6.00E-02	**3.041E-02**	9.65E-01	9.45E-01
6.05E-02	3.025E-02	9.23E-01	9.03E-01
6.10E-02	3.009E-02	8.81E-01	8.64E-01

E(MeV)	$(\mu_{En}/\rho)_{air}$	IPEM X (mR)	MCNPX X (mR)
6.15E-02	2.993E-02	8.39E-01	8.23E-01
6.20E-02	2.978E-02	7.97E-01	7.82E-01
6.25E-02	2.962E-02	7.55E-01	7.40E-01
6.30E-02	2.946E-02	7.11E-01	6.99E-01
6.35E-02	2.930E-02	6.69E-01	6.56E-01
6.40E-02	2.914E-02	6.26E-01	6.14E-01
6.45E-02	2.898E-02	5.83E-01	5.73E-01
6.50E-02	2.883E-02	5.39E-01	5.29E-01
6.55E-02	2.867E-02	4.96E-01	4.85E-01
6.60E-02	2.851E-02	4.53E-01	4.44E-01
6.65E-02	2.835E-02	4.09E-01	4.00E-01
6.70E-02	2.819E-02	4.64E-01	4.53E-01
6.75E-02	2.803E-02	3.23E-01	3.16E-01
6.80E-02	2.787E-02	2.80E-01	2.74E-01
6.85E-02	2.772E-02	2.47E-01	2.41E-01
6.90E-02	2.756E-02	2.40E-01	2.35E-01
6.95E-02	2.740E-02	1.86E-01	1.82E-01
7.00E-02	2.724E-02	1.56E-01	1.52E-01
7.05E-02	2.708E-02	1.32E-01	1.30E-01
7.10E-02	2.692E-02	1.09E-01	1.07E-01
7.15E-02	2.676E-02	8.93E-02	8.74E-02
7.20E-02	2.661E-02	6.99E-02	6.83E-02
7.25E-02	2.645E-02	5.36E-02	5.21E-02
7.30E-02	2.629E-02	3.79E-02	3.71E-02
7.35E-02	2.613E-02	2.55E-02	2.48E-02
7.40E-02	2.597E-02	1.39E-02	1.38E-02
7.45E-02	2.581E-02	6.73E-03	6.45E-03
7.50E-02	2.566E-02	5.61E-04	4.94E-04
		328.26	**321.68**

Appendix E

Average Amptek Spectral Data (Post-Processed)

60 kVp				63 kVp			
E(keV)	Average Photons	Average Intensity	Average Energy	E(keV)	Average Photons	Average Intensity	Average Energy
9.9	2.00E+00	7.83E-06	7.76E-05	9.9	5.50E+00	2.18E-05	2.16E-04
10.4	1.28E+01	4.99E-05	5.19E-04	10.4	6.00E+00	2.38E-05	2.47E-04
11	4.75E+00	1.86E-05	2.05E-04	11	5.00E+00	1.98E-05	2.18E-04
11.5	2.25E+01	8.81E-05	1.01E-03	11.5	4.25E+00	1.68E-05	1.94E-04
12	1.30E+01	5.09E-05	6.11E-04	12	8.25E+00	3.27E-05	3.92E-04
12.5	2.45E+01	9.60E-05	1.20E-03	12.5	5.75E+00	2.28E-05	2.85E-04
13	7.25E+00	2.84E-05	3.69E-04	13	7.75E+00	3.07E-05	3.99E-04
13.5	8.00E+00	3.13E-05	4.23E-04	13.5	7.75E+00	3.07E-05	4.15E-04
14	1.33E+01	5.19E-05	7.27E-04	14	8.50E+00	3.37E-05	4.71E-04
14.5	2.78E+01	1.09E-04	1.58E-03	14.5	1.05E+01	4.16E-05	6.03E-04
15	2.60E+01	1.02E-04	1.53E-03	15	1.20E+01	4.75E-05	7.13E-04
15.5	6.38E+01	2.50E-04	3.87E-03	15.5	4.93E+01	1.95E-04	3.02E-03
16.1	1.05E+02	4.12E-04	6.64E-03	16.1	9.53E+01	3.77E-04	6.08E-03
16.6	1.86E+02	7.29E-04	1.21E-02	16.6	1.34E+02	5.32E-04	8.83E-03
17.1	2.85E+02	1.12E-03	1.91E-02	17.1	2.62E+02	1.04E-03	1.78E-02
17.6	4.12E+02	1.61E-03	2.84E-02	17.6	3.77E+02	1.49E-03	2.63E-02
18.1	5.47E+02	2.14E-03	3.88E-02	18.1	5.18E+02	2.05E-03	3.71E-02
18.6	7.11E+02	2.79E-03	5.18E-02	18.6	6.69E+02	2.65E-03	4.93E-02
19.1	9.41E+02	3.68E-03	7.04E-02	19.1	7.91E+02	3.13E-03	5.99E-02
19.6	1.14E+03	4.47E-03	8.77E-02	19.6	1.00E+03	3.96E-03	7.76E-02
20.1	1.35E+03	5.27E-03	1.06E-01	20.1	1.19E+03	4.70E-03	9.44E-02
20.6	1.55E+03	6.09E-03	1.25E-01	20.6	1.44E+03	5.72E-03	1.18E-01
21.2	1.84E+03	7.21E-03	1.53E-01	21.2	1.65E+03	6.55E-03	1.39E-01
21.7	2.02E+03	7.90E-03	1.71E-01	21.7	1.86E+03	7.35E-03	1.59E-01
22.2	2.28E+03	8.93E-03	1.98E-01	22.2	2.08E+03	8.23E-03	1.83E-01
22.7	2.53E+03	9.92E-03	2.25E-01	22.7	2.32E+03	9.18E-03	2.08E-01
23.2	2.79E+03	1.09E-02	2.54E-01	23.2	2.49E+03	9.88E-03	2.29E-01
23.7	3.01E+03	1.18E-02	2.79E-01	23.7	2.79E+03	1.10E-02	2.62E-01
24.2	3.18E+03	1.25E-02	3.02E-01	24.2	2.98E+03	1.18E-02	2.86E-01
24.7	3.40E+03	1.33E-02	3.28E-01	24.7	3.15E+03	1.25E-02	3.09E-01
25.2	3.64E+03	1.43E-02	3.59E-01	25.2	3.26E+03	1.29E-02	3.25E-01
25.8	3.79E+03	1.48E-02	3.83E-01	25.8	3.47E+03	1.37E-02	3.54E-01
26.3	3.88E+03	1.52E-02	4.00E-01	26.3	3.68E+03	1.46E-02	3.84E-01

26.8	3.86E+03	1.51E-02	4.06E-01	26.8	3.60E+03	1.43E-02	3.82E-01
27.3	4.22E+03	1.65E-02	4.51E-01	27.3	3.93E+03	1.56E-02	4.25E-01
27.8	4.29E+03	1.68E-02	4.67E-01	27.8	4.04E+03	1.60E-02	4.44E-01
28.3	4.42E+03	1.73E-02	4.90E-01	28.3	4.08E+03	1.62E-02	4.57E-01
28.8	4.59E+03	1.80E-02	5.18E-01	28.8	4.18E+03	1.66E-02	4.77E-01
29.3	4.68E+03	1.83E-02	5.37E-01	29.3	4.33E+03	1.71E-02	5.02E-01
29.8	4.73E+03	1.85E-02	5.53E-01	29.8	4.45E+03	1.76E-02	5.25E-01
30.3	4.81E+03	1.88E-02	5.71E-01	30.3	4.43E+03	1.75E-02	5.32E-01
30.9	4.86E+03	1.90E-02	5.88E-01	30.9	4.47E+03	1.77E-02	5.48E-01
31.4	4.86E+03	1.90E-02	5.97E-01	31.4	4.51E+03	1.79E-02	5.61E-01
31.9	4.77E+03	1.87E-02	5.96E-01	31.9	4.47E+03	1.77E-02	5.65E-01
32.4	4.83E+03	1.89E-02	6.13E-01	32.4	4.49E+03	1.78E-02	5.77E-01
32.9	4.67E+03	1.83E-02	6.02E-01	32.9	4.41E+03	1.75E-02	5.75E-01
33.4	4.67E+03	1.83E-02	6.11E-01	33.4	4.41E+03	1.75E-02	5.84E-01
33.9	4.80E+03	1.88E-02	6.37E-01	33.9	4.45E+03	1.76E-02	5.98E-01
34.4	4.65E+03	1.82E-02	6.27E-01	34.4	4.54E+03	1.80E-02	6.19E-01
34.9	4.66E+03	1.83E-02	6.38E-01	34.9	4.42E+03	1.75E-02	6.11E-01
35.4	4.66E+03	1.83E-02	6.46E-01	35.4	4.43E+03	1.75E-02	6.21E-01
36	4.56E+03	1.79E-02	6.43E-01	36	4.40E+03	1.74E-02	6.28E-01
36.5	4.60E+03	1.80E-02	6.58E-01	36.5	4.34E+03	1.72E-02	6.28E-01
37	4.51E+03	1.77E-02	6.53E-01	37	4.36E+03	1.73E-02	6.38E-01
37.5	4.53E+03	1.77E-02	6.65E-01	37.5	4.37E+03	1.73E-02	6.50E-01
38	4.44E+03	1.74E-02	6.61E-01	38	4.23E+03	1.68E-02	6.37E-01
38.5	4.35E+03	1.70E-02	6.56E-01	38.5	4.24E+03	1.68E-02	6.47E-01
39	4.35E+03	1.71E-02	6.65E-01	39	4.05E+03	1.60E-02	6.26E-01
39.5	4.21E+03	1.65E-02	6.52E-01	39.5	4.05E+03	1.60E-02	6.34E-01
40	4.17E+03	1.63E-02	6.53E-01	40	4.01E+03	1.59E-02	6.35E-01
40.6	4.06E+03	1.59E-02	6.46E-01	40.6	3.94E+03	1.56E-02	6.33E-01
41.1	4.02E+03	1.58E-02	6.48E-01	41.1	3.84E+03	1.52E-02	6.25E-01
41.6	3.93E+03	1.54E-02	6.40E-01	41.6	3.81E+03	1.51E-02	6.28E-01
42.1	3.85E+03	1.51E-02	6.35E-01	42.1	3.75E+03	1.49E-02	6.26E-01
42.6	3.74E+03	1.47E-02	6.24E-01	42.6	3.68E+03	1.46E-02	6.22E-01
43.1	3.67E+03	1.44E-02	6.19E-01	43.1	3.65E+03	1.45E-02	6.24E-01
43.6	3.63E+03	1.42E-02	6.20E-01	43.6	3.51E+03	1.39E-02	6.07E-01
44.1	3.50E+03	1.37E-02	6.04E-01	44.1	3.46E+03	1.37E-02	6.04E-01
44.6	3.43E+03	1.34E-02	5.99E-01	44.6	3.42E+03	1.36E-02	6.05E-01
45.1	3.38E+03	1.32E-02	5.97E-01	45.1	3.28E+03	1.30E-02	5.87E-01
45.7	3.27E+03	1.28E-02	5.85E-01	45.7	3.26E+03	1.29E-02	5.90E-01

46.2	3.15E+03	1.23E-02	5.69E-01	46.2	3.19E+03	1.26E-02	5.84E-01
46.7	3.06E+03	1.20E-02	5.59E-01	46.7	3.13E+03	1.24E-02	5.80E-01
47.2	2.98E+03	1.17E-02	5.52E-01	47.2	3.07E+03	1.22E-02	5.74E-01
47.7	2.92E+03	1.14E-02	5.45E-01	47.7	2.93E+03	1.16E-02	5.54E-01
48.2	2.72E+03	1.07E-02	5.14E-01	48.2	2.85E+03	1.13E-02	5.44E-01
48.7	2.72E+03	1.07E-02	5.19E-01	48.7	2.73E+03	1.08E-02	5.27E-01
49.2	2.60E+03	1.02E-02	5.01E-01	49.2	2.72E+03	1.08E-02	5.30E-01
49.7	2.48E+03	9.73E-03	4.83E-01	49.7	2.62E+03	1.04E-02	5.17E-01
50.3	2.45E+03	9.58E-03	4.82E-01	50.3	2.50E+03	9.91E-03	4.98E-01
50.8	2.36E+03	9.25E-03	4.70E-01	50.8	2.43E+03	9.61E-03	4.88E-01
51.3	2.19E+03	8.59E-03	4.41E-01	51.3	2.35E+03	9.32E-03	4.78E-01
51.8	2.10E+03	8.21E-03	4.25E-01	51.8	2.29E+03	9.09E-03	4.71E-01
52.3	2.06E+03	8.09E-03	4.23E-01	52.3	2.23E+03	8.85E-03	4.63E-01
52.8	1.93E+03	7.56E-03	3.99E-01	52.8	2.15E+03	8.53E-03	4.50E-01
53.3	1.90E+03	7.42E-03	3.96E-01	53.3	2.04E+03	8.10E-03	4.32E-01
53.8	1.71E+03	6.70E-03	3.60E-01	53.8	1.95E+03	7.71E-03	4.15E-01
54.3	1.65E+03	6.46E-03	3.51E-01	54.3	1.90E+03	7.51E-03	4.08E-01
54.8	1.50E+03	5.88E-03	3.22E-01	54.8	1.80E+03	7.14E-03	3.91E-01
55.4	1.43E+03	5.59E-03	3.10E-01	55.4	1.71E+03	6.77E-03	3.75E-01
55.9	1.29E+03	5.05E-03	2.83E-01	55.9	1.65E+03	6.53E-03	3.65E-01
56.4	1.20E+03	4.70E-03	2.65E-01	56.4	1.56E+03	6.16E-03	3.48E-01
56.9	1.10E+03	4.32E-03	2.46E-01	56.9	1.43E+03	5.66E-03	3.22E-01
57.4	9.92E+02	3.88E-03	2.23E-01	57.4	1.35E+03	5.33E-03	3.06E-01
57.9	8.88E+02	3.48E-03	2.01E-01	57.9	1.25E+03	4.95E-03	2.87E-01
58.4	7.73E+02	3.03E-03	1.77E-01	58.4	1.20E+03	4.76E-03	2.78E-01
58.9	6.68E+02	2.62E-03	1.54E-01	58.9	1.11E+03	4.41E-03	2.60E-01
59.4	5.12E+02	2.00E-03	1.19E-01	59.4	9.88E+02	3.91E-03	2.33E-01
59.9	3.96E+02	1.55E-03	9.30E-02	59.9	9.29E+02	3.68E-03	2.21E-01
60.5	2.74E+02	1.07E-03	6.50E-02	60.5	8.38E+02	3.32E-03	2.01E-01
61	1.68E+02	6.57E-04	4.01E-02	61	7.34E+02	2.91E-03	1.77E-01
61.5	7.48E+01	2.93E-04	1.80E-02	61.5	6.18E+02	2.45E-03	1.50E-01
62	2.10E+01	8.23E-05	5.10E-03	62	5.29E+02	2.09E-03	1.30E-01
				62.5	4.45E+02	1.76E-03	1.10E-01
				63	3.44E+02	1.36E-03	8.57E-02
				63.5	2.40E+02	9.52E-04	6.04E-02
				64	1.44E+02	5.70E-04	3.65E-02
				64.5	6.35E+01	2.52E-04	1.62E-02
	2.55E+05		**3.70E+01**		**2.52E+05**		**3.83E+01**

66 kVp				70 kVp			
E(keV)	Average Photons	Average Intensity	Average Energy	E(keV)	Average Photons	Average Intensity	Average Energy
9.9	1.09E+02	4.28E-04	4.24E-03	9.9	3.33E+01	1.30E-04	1.29E-03
10.4	3.75E+01	1.48E-04	1.54E-03	10.4	1.01E+02	3.97E-04	4.13E-03
11	3.25E+00	1.28E-05	1.41E-04	11	4.00E+00	1.57E-05	1.73E-04
11.5	6.00E+00	2.36E-05	2.72E-04	11.5	9.75E+00	3.83E-05	4.40E-04
12	8.50E+00	3.35E-05	4.02E-04	12	1.00E+01	3.92E-05	4.71E-04
12.5	4.75E+00	1.87E-05	2.34E-04	12.5	7.75E+00	3.04E-05	3.80E-04
13	4.50E+00	1.77E-05	2.30E-04	13	3.00E+00	1.18E-05	1.53E-04
13.5	9.00E+00	3.54E-05	4.78E-04	13.5	2.45E+01	9.61E-05	1.30E-03
14	1.55E+01	6.10E-05	8.55E-04	14	8.00E+00	3.14E-05	4.39E-04
14.5	1.48E+01	5.81E-05	8.42E-04	14.5	2.13E+01	8.34E-05	1.21E-03
15	2.00E+01	7.88E-05	1.18E-03	15	1.55E+01	6.08E-05	9.12E-04
15.5	4.15E+01	1.63E-04	2.53E-03	15.5	2.33E+01	9.12E-05	1.41E-03
16.1	1.11E+02	4.37E-04	7.04E-03	16.1	6.78E+01	2.66E-04	4.28E-03
16.6	1.32E+02	5.21E-04	8.64E-03	16.6	1.07E+02	4.18E-04	6.94E-03
17.1	2.19E+02	8.62E-04	1.47E-02	17.1	1.82E+02	7.15E-04	1.22E-02
17.6	3.27E+02	1.29E-03	2.27E-02	17.6	2.74E+02	1.07E-03	1.89E-02
18.1	4.45E+02	1.75E-03	3.17E-02	18.1	3.76E+02	1.48E-03	2.67E-02
18.6	5.93E+02	2.33E-03	4.34E-02	18.6	5.31E+02	2.08E-03	3.87E-02
19.1	7.42E+02	2.92E-03	5.58E-02	19.1	6.80E+02	2.67E-03	5.09E-02
19.6	9.33E+02	3.67E-03	7.20E-02	19.6	8.27E+02	3.24E-03	6.36E-02
20.1	1.12E+03	4.42E-03	8.89E-02	20.1	9.87E+02	3.87E-03	7.78E-02
20.6	1.32E+03	5.19E-03	1.07E-01	20.6	1.21E+03	4.73E-03	9.74E-02
21.2	1.53E+03	6.01E-03	1.27E-01	21.2	1.34E+03	5.26E-03	1.11E-01
21.7	1.68E+03	6.63E-03	1.44E-01	21.7	1.57E+03	6.16E-03	1.34E-01
22.2	1.90E+03	7.49E-03	1.66E-01	22.2	1.68E+03	6.57E-03	1.46E-01
22.7	2.13E+03	8.39E-03	1.90E-01	22.7	1.93E+03	7.58E-03	1.72E-01
23.2	2.29E+03	9.02E-03	2.09E-01	23.2	2.18E+03	8.57E-03	1.99E-01
23.7	2.55E+03	1.01E-02	2.38E-01	23.7	2.26E+03	8.88E-03	2.11E-01
24.2	2.74E+03	1.08E-02	2.61E-01	24.2	2.47E+03	9.70E-03	2.35E-01
24.7	2.93E+03	1.15E-02	2.85E-01	24.7	2.68E+03	1.05E-02	2.59E-01
25.2	3.10E+03	1.22E-02	3.07E-01	25.2	2.86E+03	1.12E-02	2.83E-01
25.8	3.23E+03	1.27E-02	3.28E-01	25.8	2.95E+03	1.16E-02	2.99E-01
26.3	3.38E+03	1.33E-02	3.50E-01	26.3	3.08E+03	1.21E-02	3.18E-01

26.8	3.38E+03	1.33E-02	3.57E-01	26.8	3.06E+03	1.20E-02	3.22E-01
27.3	3.64E+03	1.44E-02	3.92E-01	27.3	3.33E+03	1.31E-02	3.56E-01
27.8	3.71E+03	1.46E-02	4.06E-01	27.8	3.44E+03	1.35E-02	3.75E-01
28.3	3.84E+03	1.51E-02	4.28E-01	28.3	3.54E+03	1.39E-02	3.93E-01
28.8	4.03E+03	1.59E-02	4.57E-01	28.8	3.69E+03	1.45E-02	4.17E-01
29.3	4.06E+03	1.60E-02	4.68E-01	29.3	3.76E+03	1.47E-02	4.32E-01
29.8	4.09E+03	1.61E-02	4.80E-01	29.8	3.82E+03	1.50E-02	4.46E-01
30.3	4.16E+03	1.64E-02	4.96E-01	30.3	3.93E+03	1.54E-02	4.67E-01
30.9	4.28E+03	1.69E-02	5.21E-01	30.9	3.96E+03	1.55E-02	4.79E-01
31.4	4.32E+03	1.70E-02	5.35E-01	31.4	4.06E+03	1.59E-02	5.00E-01
31.9	4.19E+03	1.65E-02	5.26E-01	31.9	3.94E+03	1.55E-02	4.93E-01
32.4	4.30E+03	1.69E-02	5.48E-01	32.4	4.02E+03	1.58E-02	5.11E-01
32.9	4.26E+03	1.68E-02	5.51E-01	32.9	3.97E+03	1.56E-02	5.12E-01
33.4	4.26E+03	1.68E-02	5.60E-01	33.4	3.99E+03	1.56E-02	5.22E-01
33.9	4.29E+03	1.69E-02	5.73E-01	33.9	3.98E+03	1.56E-02	5.30E-01
34.4	4.21E+03	1.66E-02	5.70E-01	34.4	4.06E+03	1.59E-02	5.48E-01
34.9	4.23E+03	1.67E-02	5.82E-01	34.9	3.92E+03	1.54E-02	5.37E-01
35.4	4.19E+03	1.65E-02	5.85E-01	35.4	3.97E+03	1.56E-02	5.52E-01
36	4.18E+03	1.65E-02	5.93E-01	36	3.93E+03	1.54E-02	5.55E-01
36.5	4.22E+03	1.66E-02	6.06E-01	36.5	3.89E+03	1.53E-02	5.57E-01
37	4.10E+03	1.62E-02	5.98E-01	37	3.92E+03	1.54E-02	5.69E-01
37.5	4.07E+03	1.60E-02	6.01E-01	37.5	3.93E+03	1.54E-02	5.78E-01
38	4.15E+03	1.63E-02	6.20E-01	38	3.88E+03	1.52E-02	5.79E-01
38.5	3.98E+03	1.57E-02	6.04E-01	38.5	3.85E+03	1.51E-02	5.81E-01
39	3.96E+03	1.56E-02	6.09E-01	39	3.81E+03	1.49E-02	5.83E-01
39.5	3.92E+03	1.54E-02	6.10E-01	39.5	3.77E+03	1.48E-02	5.84E-01
40	3.87E+03	1.52E-02	6.10E-01	40	3.71E+03	1.46E-02	5.83E-01
40.6	3.81E+03	1.50E-02	6.09E-01	40.6	3.68E+03	1.44E-02	5.86E-01
41.1	3.80E+03	1.49E-02	6.14E-01	41.1	3.62E+03	1.42E-02	5.84E-01
41.6	3.70E+03	1.46E-02	6.06E-01	41.6	3.63E+03	1.43E-02	5.93E-01
42.1	3.67E+03	1.45E-02	6.09E-01	42.1	3.54E+03	1.39E-02	5.85E-01
42.6	3.58E+03	1.41E-02	6.01E-01	42.6	3.50E+03	1.37E-02	5.86E-01
43.1	3.53E+03	1.39E-02	5.99E-01	43.1	3.47E+03	1.36E-02	5.86E-01
43.6	3.48E+03	1.37E-02	5.98E-01	43.6	3.38E+03	1.33E-02	5.78E-01
44.1	3.34E+03	1.32E-02	5.81E-01	44.1	3.32E+03	1.30E-02	5.75E-01
44.6	3.42E+03	1.35E-02	6.00E-01	44.6	3.27E+03	1.28E-02	5.72E-01
45.1	3.30E+03	1.30E-02	5.86E-01	45.1	3.25E+03	1.28E-02	5.75E-01
45.7	3.21E+03	1.26E-02	5.77E-01	45.7	3.16E+03	1.24E-02	5.66E-01

46.2	3.21E+03	1.27E-02	5.85E-01	46.2	3.13E+03	1.23E-02	5.67E-01
46.7	3.07E+03	1.21E-02	5.64E-01	46.7	3.07E+03	1.20E-02	5.62E-01
47.2	2.96E+03	1.17E-02	5.51E-01	47.2	3.03E+03	1.19E-02	5.61E-01
47.7	2.98E+03	1.18E-02	5.61E-01	47.7	2.96E+03	1.16E-02	5.55E-01
48.2	2.93E+03	1.16E-02	5.57E-01	48.2	2.87E+03	1.13E-02	5.44E-01
48.7	2.83E+03	1.11E-02	5.43E-01	48.7	2.87E+03	1.13E-02	5.48E-01
49.2	2.71E+03	1.07E-02	5.25E-01	49.2	2.81E+03	1.10E-02	5.42E-01
49.7	2.72E+03	1.07E-02	5.32E-01	49.7	2.70E+03	1.06E-02	5.26E-01
50.3	2.64E+03	1.04E-02	5.24E-01	50.3	2.68E+03	1.05E-02	5.30E-01
50.8	2.56E+03	1.01E-02	5.13E-01	50.8	2.60E+03	1.02E-02	5.18E-01
51.3	2.48E+03	9.76E-03	5.01E-01	51.3	2.59E+03	1.01E-02	5.20E-01
51.8	2.41E+03	9.48E-03	4.91E-01	51.8	2.55E+03	9.99E-03	5.17E-01
52.3	2.34E+03	9.20E-03	4.81E-01	52.3	2.37E+03	9.31E-03	4.87E-01
52.8	2.26E+03	8.89E-03	4.69E-01	52.8	2.36E+03	9.26E-03	4.89E-01
53.3	2.21E+03	8.69E-03	4.63E-01	53.3	2.25E+03	8.83E-03	4.71E-01
53.8	2.10E+03	8.28E-03	4.46E-01	53.8	2.27E+03	8.90E-03	4.79E-01
54.3	2.08E+03	8.18E-03	4.44E-01	54.3	2.15E+03	8.42E-03	4.57E-01
54.8	1.96E+03	7.72E-03	4.23E-01	54.8	2.11E+03	8.27E-03	4.53E-01
55.4	1.93E+03	7.59E-03	4.20E-01	55.4	2.10E+03	8.24E-03	4.56E-01
55.9	1.85E+03	7.27E-03	4.06E-01	55.9	2.00E+03	7.83E-03	4.38E-01
56.4	1.76E+03	6.92E-03	3.90E-01	56.4	1.93E+03	7.58E-03	4.28E-01
56.9	1.66E+03	6.55E-03	3.73E-01	56.9	1.90E+03	7.46E-03	4.24E-01
57.4	1.59E+03	6.28E-03	3.60E-01	57.4	1.81E+03	7.09E-03	4.07E-01
57.9	1.53E+03	6.04E-03	3.50E-01	57.9	1.80E+03	7.08E-03	4.10E-01
58.4	1.44E+03	5.66E-03	3.30E-01	58.4	1.79E+03	7.00E-03	4.09E-01
58.9	1.37E+03	5.40E-03	3.18E-01	58.9	1.67E+03	6.54E-03	3.85E-01
59.4	1.30E+03	5.12E-03	3.04E-01	59.4	1.58E+03	6.21E-03	3.69E-01
59.9	1.24E+03	4.87E-03	2.92E-01	59.9	1.57E+03	6.18E-03	3.70E-01
60.5	1.16E+03	4.56E-03	2.76E-01	60.5	1.48E+03	5.82E-03	3.52E-01
61	1.08E+03	4.26E-03	2.60E-01	61	1.40E+03	5.47E-03	3.34E-01
61.5	1.03E+03	4.06E-03	2.50E-01	61.5	1.30E+03	5.10E-03	3.14E-01
62	9.70E+02	3.82E-03	2.37E-01	62	1.30E+03	5.09E-03	3.15E-01
62.5	8.79E+02	3.46E-03	2.16E-01	62.5	1.24E+03	4.87E-03	3.04E-01
63	7.80E+02	3.07E-03	1.94E-01	63	1.20E+03	4.70E-03	2.96E-01
63.5	7.10E+02	2.79E-03	1.77E-01	63.5	1.07E+03	4.19E-03	2.66E-01
64	6.36E+02	2.50E-03	1.60E-01	64	1.05E+03	4.11E-03	2.63E-01
64.5	5.44E+02	2.14E-03	1.38E-01	64.5	9.70E+02	3.81E-03	2.46E-01
65.1	4.88E+02	1.92E-03	1.25E-01	65.1	9.43E+02	3.70E-03	2.41E-01

65.6	3.95E+02	1.55E-03	1.02E-01	65.6	8.82E+02	3.46E-03	2.27E-01
66.1	3.08E+02	1.21E-03	8.02E-02	66.1	8.04E+02	3.16E-03	2.09E-01
66.6	2.23E+02	8.76E-04	5.84E-02	66.6	7.33E+02	2.87E-03	1.91E-01
67.1	1.26E+02	4.96E-04	3.33E-02	67.1	7.22E+02	2.83E-03	1.90E-01
67.6	6.35E+01	2.50E-04	1.69E-02	67.6	6.42E+02	2.52E-03	1.70E-01
68.1	1.83E+01	7.19E-05	4.89E-03	68.1	5.71E+02	2.24E-03	1.52E-01
				68.6	4.90E+02	1.92E-03	1.32E-01
				69.1	3.89E+02	1.53E-03	1.05E-01
				69.6	3.00E+02	1.17E-03	8.18E-02
				70.2	1.98E+02	7.76E-04	5.45E-02
				70.7	1.24E+02	4.85E-04	3.43E-02
				71.2	6.65E+01	2.61E-04	1.86E-02
				71.7	3.63E+01	1.42E-04	1.02E-02
	2.54E+05		**3.92E+01**		**2.55E+05**		**4.07E+01**

70 kVp (Gendex)			
E(keV)	Average Photons	Average Intensity	Average Energy
9.9	6.55E+01	2.61E-04	2.58E-03
10.4	1.06E+02	4.22E-04	4.39E-03
11	1.06E+02	4.20E-04	4.62E-03
11.5	1.75E+00	6.97E-06	8.01E-05
12	2.00E+00	7.96E-06	9.56E-05
12.5	1.75E+00	6.97E-06	8.71E-05
13	3.25E+00	1.29E-05	1.68E-04
13.5	4.00E+00	1.59E-05	2.15E-04
14	3.75E+00	1.49E-05	2.09E-04
14.5	3.50E+00	1.39E-05	2.02E-04
15	2.28E+01	9.06E-05	1.36E-03
15.5	2.43E+01	9.66E-05	1.50E-03
16.1	4.15E+01	1.65E-04	2.66E-03
16.6	8.45E+01	3.36E-04	5.58E-03
17.1	1.28E+02	5.09E-04	8.70E-03
17.6	2.43E+02	9.67E-04	1.70E-02
18.1	3.79E+02	1.51E-03	2.73E-02
18.6	4.87E+02	1.94E-03	3.60E-02
19.1	6.34E+02	2.52E-03	4.82E-02
19.6	7.68E+02	3.06E-03	6.00E-02
20.1	9.93E+02	3.95E-03	7.94E-02
20.6	1.21E+03	4.80E-03	9.89E-02
21.2	1.42E+03	5.66E-03	1.20E-01
21.7	1.61E+03	6.41E-03	1.39E-01
22.2	1.85E+03	7.38E-03	1.64E-01
22.7	2.03E+03	8.07E-03	1.83E-01
23.2	2.35E+03	9.34E-03	2.17E-01
23.7	2.49E+03	9.93E-03	2.35E-01
24.2	2.68E+03	1.07E-02	2.58E-01
24.7	2.94E+03	1.17E-02	2.89E-01
25.2	3.12E+03	1.24E-02	3.13E-01
25.8	3.28E+03	1.31E-02	3.37E-01

26.3	3.34E+03	1.33E-02	3.50E-01
26.8	3.39E+03	1.35E-02	3.62E-01
27.3	3.83E+03	1.52E-02	4.16E-01
27.8	3.82E+03	1.52E-02	4.22E-01
28.3	3.93E+03	1.56E-02	4.43E-01
28.8	4.11E+03	1.64E-02	4.72E-01
29.3	4.24E+03	1.69E-02	4.95E-01
29.8	4.23E+03	1.68E-02	5.02E-01
30.3	4.36E+03	1.74E-02	5.26E-01
30.9	4.40E+03	1.75E-02	5.41E-01
31.4	4.43E+03	1.76E-02	5.54E-01
31.9	4.38E+03	1.74E-02	5.56E-01
32.4	4.64E+03	1.85E-02	5.98E-01
32.9	4.54E+03	1.81E-02	5.95E-01
33.4	4.39E+03	1.75E-02	5.83E-01
33.9	4.40E+03	1.75E-02	5.94E-01
34.4	4.37E+03	1.74E-02	5.98E-01
34.9	4.42E+03	1.76E-02	6.14E-01
35.4	4.41E+03	1.76E-02	6.22E-01
36	4.33E+03	1.72E-02	6.21E-01
36.5	4.34E+03	1.73E-02	6.31E-01
37	4.29E+03	1.71E-02	6.32E-01
37.5	4.26E+03	1.69E-02	6.36E-01
38	4.23E+03	1.68E-02	6.39E-01
38.5	4.14E+03	1.65E-02	6.34E-01
39	4.08E+03	1.62E-02	6.33E-01
39.5	3.98E+03	1.59E-02	6.26E-01
40	3.93E+03	1.56E-02	6.26E-01
40.6	3.92E+03	1.56E-02	6.34E-01
41.1	3.73E+03	1.49E-02	6.11E-01
41.6	3.69E+03	1.47E-02	6.10E-01
42.1	3.64E+03	1.45E-02	6.10E-01
42.6	3.59E+03	1.43E-02	6.09E-01
43.1	3.53E+03	1.41E-02	6.06E-01
43.6	3.43E+03	1.36E-02	5.95E-01
44.1	3.41E+03	1.36E-02	5.99E-01
44.6	3.30E+03	1.31E-02	5.86E-01
45.1	3.18E+03	1.27E-02	5.71E-01

45.7	3.10E+03	1.23E-02	5.63E-01
46.2	3.05E+03	1.21E-02	5.61E-01
46.7	2.94E+03	1.17E-02	5.46E-01
47.2	2.90E+03	1.15E-02	5.45E-01
47.7	2.80E+03	1.12E-02	5.32E-01
48.2	2.75E+03	1.10E-02	5.28E-01
48.7	2.62E+03	1.04E-02	5.08E-01
49.2	2.54E+03	1.01E-02	4.98E-01
49.7	2.54E+03	1.01E-02	5.02E-01
50.3	2.42E+03	9.62E-03	4.84E-01
50.8	2.39E+03	9.51E-03	4.83E-01
51.3	2.31E+03	9.18E-03	4.71E-01
51.8	2.20E+03	8.77E-03	4.54E-01
52.3	2.18E+03	8.69E-03	4.54E-01
52.8	2.02E+03	8.06E-03	4.26E-01
53.3	1.98E+03	7.87E-03	4.20E-01
53.8	1.94E+03	7.71E-03	4.15E-01
54.3	1.88E+03	7.47E-03	4.05E-01
54.8	1.81E+03	7.20E-03	3.94E-01
55.4	1.73E+03	6.90E-03	3.82E-01
55.9	1.67E+03	6.65E-03	3.72E-01
56.4	1.53E+03	6.11E-03	3.44E-01
56.9	1.50E+03	5.98E-03	3.40E-01
57.4	1.41E+03	5.60E-03	3.22E-01
57.9	1.37E+03	5.45E-03	3.15E-01
58.4	1.29E+03	5.13E-03	2.99E-01
58.9	1.19E+03	4.74E-03	2.79E-01
59.4	1.18E+03	4.69E-03	2.78E-01
59.9	1.06E+03	4.23E-03	2.54E-01
60.5	9.74E+02	3.88E-03	2.35E-01
61	9.45E+02	3.76E-03	2.30E-01
61.5	8.95E+02	3.56E-03	2.19E-01
62	8.06E+02	3.21E-03	1.99E-01
62.5	7.20E+02	2.87E-03	1.79E-01
63	6.84E+02	2.72E-03	1.71E-01
63.5	6.07E+02	2.42E-03	1.53E-01
64	5.46E+02	2.17E-03	1.39E-01
64.5	5.00E+02	1.99E-03	1.28E-01

65.1	4.32E+02	1.72E-03	1.12E-01
65.6	3.74E+02	1.49E-03	9.76E-02
66.1	3.24E+02	1.29E-03	8.52E-02
66.6	2.74E+02	1.09E-03	7.26E-02
67.1	2.27E+02	9.05E-04	6.07E-02
67.6	1.96E+02	7.81E-04	5.28E-02
68.1	1.59E+02	6.33E-04	4.31E-02
68.6	1.23E+02	4.90E-04	3.36E-02
69.1	9.20E+01	3.66E-04	2.53E-02
69.6	7.63E+01	3.04E-04	2.11E-02
70.2	5.93E+01	2.36E-04	1.66E-02
70.7	5.08E+01	2.02E-04	1.43E-02
71.2	4.45E+01	1.77E-04	1.26E-02
71.7	4.23E+01	1.68E-04	1.21E-02
72.2	4.38E+01	1.74E-04	1.26E-02
	2.51E+05		**3.89E+01**

Appendix F

IPEM SPECTRA USED FOR MCNPX INPUT DECKS

50 kVp

Energy bins

9.50E-03 1.0E-02 10.5E-02 1.10E-02 1.15E-02 1.20E-02 1.25E-02 1.30E-02
1.35E-02 1.40E-02 1.45E-02 1.50E-02 1.55E-02 1.60E-02 1.65E-02 1.70E-02
1.75E-02 1.80E-02 1.85E-02 1.90E-02 1.95E-02 2.00E-02 2.05E-02 2.10E-02
2.15E-02 2.20E-02 2.25E-02 2.30E-02 2.35E-02 2.40E-02 2.45E-02 2.50E-02
2.55E-02 2.60E-02 2.65E-02 2.70E-02 2.75E-02 2.80E-02 2.85E-02 2.90E-02
2.95E-02 3.00E-02 3.05E-02 3.10E-02 3.15E-02 3.20E-02 3.25E-02 3.30E-02
3.35E-02 3.40E-02 3.45E-02 3.50E-02 3.55E-02 3.60E-02 3.65E-02 3.70E-02
3.75E-02 3.80E-02 3.85E-02 3.90E-02 3.95E-02 4.00E-02 4.05E-02 4.10E-02
4.15E-02 4.20E-02 4.25E-02 4.30E-02 4.35E-02 4.40E-02 4.45E-02 4.50E-02
4.55E-02 4.60E-02 4.65E-02 4.70E-02 4.75E-02 4.80E-02 4.85E-02 4.90E-02
4.95E-02 5.00E-02

Intensity Distribution Inherent Filtration

0.00E+00 4.51E-08 4.38E-08 3.03E-07 3.88E-06 4.27E-06 1.18E-05 3.25E-05
7.78E-05 1.59E-04 3.01E-04 5.23E-04 8.47E-04 1.30E-03 1.87E-03 2.60E-03
3.44E-03 4.42E-03 5.52E-03 6.70E-03 7.97E-03 9.27E-03 1.06E-02 1.19E-02
1.32E-02 1.45E-02 1.58E-02 1.70E-02 1.80E-02 1.91E-02 1.99E-02 2.07E-02
2.15E-02 2.21E-02 2.27E-02 2.32E-02 2.35E-02 2.39E-02 2.41E-02 2.43E-02
2.43E-02 2.43E-02 2.43E-02 2.41E-02 2.40E-02 2.37E-02 2.35E-02 2.31E-02
2.28E-02 2.23E-02 2.19E-02 2.14E-02 2.09E-02 2.04E-02 1.98E-02 1.92E-02
1.86E-02 1.80E-02 1.73E-02 1.67E-02 1.60E-02 1.53E-02 1.46E-02 1.38E-02
1.31E-02 1.24E-02 1.16E-02 1.09E-02 1.01E-02 9.33E-03 8.56E-03 7.78E-03
7.00E-03 6.22E-03 5.44E-03 4.66E-03 3.88E-03 3.09E-03 2.32E-03 1.54E-03
7.69E-04 6.41E-05

Intensity Distribution 0.1 mm Cu Filtration

0.00E+00 4.12E-16 3.61E-15 1.85E-13 1.17E-11 5.22E-11 5.30E-10 4.51E-09
2.72E-08 1.28E-07 5.04E-07 1.66E-06 4.76E-06 1.21E-05 2.71E-05 5.63E-05
1.07E-04 1.89E-04 3.16E-04 4.97E-04 7.59E-04 1.09E-03 1.52E-03 2.05E-03
2.70E-03 3.44E-03 4.29E-03 5.26E-03 6.29E-03 7.44E-03 8.60E-03 9.87E-03
1.12E-02 1.25E-02 1.37E-02 1.51E-02 1.64E-02 1.79E-02 1.89E-02 2.01E-02
2.13E-02 2.22E-02 2.33E-02 2.40E-02 2.49E-02 2.55E-02 2.62E-02 2.66E-02
2.70E-02 2.74E-02 2.76E-02 2.76E-02 2.77E-02 2.76E-02 2.74E-02 2.72E-02
2.69E-02 2.65E-02 2.60E-02 2.54E-02 2.47E-02 2.40E-02 2.33E-02 2.24E-02
2.15E-02 2.06E-02 1.96E-02 1.85E-02 1.74E-02 1.63E-02 1.51E-02 1.38E-02
1.26E-02 1.13E-02 9.94E-03 8.58E-03 7.20E-03 5.79E-03 4.37E-03 2.93E-03
1.47E-03 1.23E-04

Intensity Distribution 0.2 mm Cu Filtration

0.00E+00 2.99E-24 2.37E-22 8.95E-20 2.81E-17 5.08E-16 1.89E-14 4.99E-13
7.53E-12 8.25E-11 6.72E-10 4.20E-09 2.13E-08 9.04E-08 3.14E-07 9.71E-07
2.64E-06 6.44E-06 1.44E-05 2.93E-05 5.75E-05 1.02E-04 1.73E-04 2.81E-04
4.37E-04 6.48E-04 9.29E-04 1.30E-03 1.75E-03 2.31E-03 2.95E-03 3.74E-03

4.65E-03 5.62E-03 6.62E-03 7.79E-03 9.10E-03 1.06E-02 1.18E-02 1.32E-02
1.49E-02 1.62E-02 1.77E-02 1.91E-02 2.05E-02 2.19E-02 2.32E-02 2.44E-02
2.55E-02 2.66E-02 2.76E-02 2.84E-02 2.91E-02 2.98E-02 3.02E-02 3.06E-02
3.08E-02 3.10E-02 3.09E-02 3.08E-02 3.05E-02 3.01E-02 2.96E-02 2.89E-02
2.81E-02 2.72E-02 2.63E-02 2.51E-02 2.39E-02 2.26E-02 2.11E-02 1.95E-02
1.79E-02 1.62E-02 1.44E-02 1.26E-02 1.06E-02 8.63E-03 6.55E-03 4.43E-03
2.24E-03 1.89E-04

55 kVp

Energy Bins

9.50E-03 1.00E-02 1.05E-02 1.10E-02 1.15E-02 1.20E-02 1.25E-02 1.30E-02
1.35E-02 1.40E-02 1.45E-02 1.50E-02 1.55E-02 1.60E-02 1.65E-02 1.70E-02
1.75E-02 1.80E-02 1.85E-02 1.90E-02 1.95E-02 2.00E-02 2.05E-02 2.10E-02
2.15E-02 2.20E-02 2.25E-02 2.30E-02 2.35E-02 2.40E-02 2.45E-02 2.50E-02
2.55E-02 2.60E-02 2.65E-02 2.70E-02 2.75E-02 2.80E-02 2.85E-02 2.90E-02
2.95E-02 3.00E-02 3.05E-02 3.10E-02 3.15E-02 3.20E-02 3.25E-02 3.30E-02
3.35E-02 3.40E-02 3.45E-02 3.50E-02 3.55E-02 3.60E-02 3.65E-02 3.70E-02
3.75E-02 3.80E-02 3.85E-02 3.90E-02 3.95E-02 4.00E-02 4.05E-02 4.10E-02
4.15E-02 4.20E-02 4.25E-02 4.30E-02 4.35E-02 4.40E-02 4.45E-02 4.50E-02
4.55E-02 4.60E-02 4.65E-02 4.70E-02 4.75E-02 4.80E-02 4.85E-02 4.90E-02
4.95E-02 5.00E-02 5.05E-02 5.10E-02 5.15E-02 5.20E-02 5.25E-02 5.30E-02
5.35E-02 5.40E-02 5.45E-02 5.50E-02

Intensity Distribution Inherent Filtration

0.00E+00 3.23E-08 2.86E-08 2.03E-07 2.75E-06 2.92E-06 8.17E-06 2.28E-05
5.55E-05 1.15E-04 2.20E-04 3.87E-04 6.35E-04 9.82E-04 1.43E-03 2.00E-03
2.68E-03 3.47E-03 4.37E-03 5.34E-03 6.40E-03 7.49E-03 8.59E-03 9.77E-03
1.09E-02 1.20E-02 1.31E-02 1.41E-02 1.51E-02 1.60E-02 1.68E-02 1.76E-02
1.83E-02 1.89E-02 1.95E-02 2.00E-02 2.04E-02 2.08E-02 2.10E-02 2.13E-02
2.14E-02 2.15E-02 2.16E-02 2.15E-02 2.15E-02 2.14E-02 2.13E-02 2.11E-02
2.09E-02 2.07E-02 2.04E-02 2.01E-02 1.98E-02 1.95E-02 1.91E-02 1.87E-02
1.83E-02 1.79E-02 1.75E-02 1.70E-02 1.66E-02 1.61E-02 1.56E-02 1.51E-02
1.46E-02 1.41E-02 1.36E-02 1.31E-02 1.26E-02 1.20E-02 1.15E-02 1.09E-02
1.04E-02 9.85E-03 9.30E-03 8.76E-03 8.21E-03 7.65E-03 7.10E-03 6.55E-03
5.99E-03 5.44E-03 4.89E-03 4.33E-03 3.78E-03 3.23E-03 2.69E-03 2.15E-03
1.60E-03 1.07E-03 5.32E-04 4.43E-05

Intensity Distribution 0.1 mm Cu Filtration

0.00E+00 2.66E-16 2.12E-15 1.11E-13 7.47E-12 3.22E-11 3.30E-10 2.85E-09
1.74E-08 8.35E-08 3.32E-07 1.11E-06 3.21E-06 8.28E-06 1.87E-05 3.92E-05
7.50E-05 1.34E-04 2.25E-04 3.57E-04 5.49E-04 7.93E-04 1.11E-03 1.51E-03
2.00E-03 2.56E-03 3.21E-03 3.95E-03 4.74E-03 5.64E-03 6.55E-03 7.54E-03
8.60E-03 9.64E-03 1.06E-02 1.17E-02 1.28E-02 1.40E-02 1.49E-02 1.58E-02
1.69E-02 1.77E-02 1.86E-02 1.93E-02 2.01E-02 2.08E-02 2.14E-02 2.19E-02
2.24E-02 2.28E-02 2.31E-02 2.34E-02 2.36E-02 2.37E-02 2.38E-02 2.38E-02
2.38E-02 2.37E-02 2.36E-02 2.33E-02 2.31E-02 2.28E-02 2.24E-02 2.20E-02
2.16E-02 2.11E-02 2.06E-02 2.01E-02 1.95E-02 1.89E-02 1.82E-02 1.75E-02
1.68E-02 1.61E-02 1.53E-02 1.45E-02 1.37E-02 1.29E-02 1.21E-02 1.12E-02
1.03E-02 9.43E-03 8.52E-03 7.61E-03 6.68E-03 5.74E-03 4.80E-03 3.85E-03

2.90E-03 1.93E-03 9.68E-04 8.10E-05

Intensity Distribution 0.2 mm Cu Filtration

0.00E+00 1.77E-24 1.28E-22 4.95E-20 1.65E-17 2.88E-16 1.08E-14 2.90E-13
4.44E-12 4.93E-11 4.07E-10 2.57E-09 1.32E-08 5.66E-08 1.99E-07 6.20E-07
1.70E-06 4.19E-06 9.41E-06 1.94E-05 3.82E-05 6.81E-05 1.16E-04 1.90E-04
2.97E-04 4.43E-04 6.38E-04 8.94E-04 1.21E-03 1.61E-03 2.06E-03 2.63E-03
3.28E-03 3.98E-03 4.70E-03 5.55E-03 6.51E-03 7.63E-03 8.54E-03 9.55E-03
1.08E-02 1.18E-02 1.30E-02 1.41E-02 1.52E-02 1.63E-02 1.74E-02 1.84E-02
1.94E-02 2.04E-02 2.12E-02 2.20E-02 2.28E-02 2.35E-02 2.40E-02 2.46E-02
2.51E-02 2.55E-02 2.58E-02 2.60E-02 2.61E-02 2.62E-02 2.62E-02 2.61E-02
2.59E-02 2.57E-02 2.54E-02 2.50E-02 2.46E-02 2.40E-02 2.34E-02 2.27E-02
2.21E-02 2.13E-02 2.04E-02 1.96E-02 1.86E-02 1.76E-02 1.66E-02 1.56E-02
1.44E-02 1.33E-02 1.21E-02 1.08E-02 9.57E-03 8.26E-03 6.95E-03 5.60E-03
4.24E-03 2.84E-03 1.43E-03 1.20E-04

60 kVp

Energy Bins

9.50E-03 1.00E-02 1.05E-02 1.10E-02 1.15E-02 1.20E-02 1.25E-02 1.30E-02
1.35E-02 1.40E-02 1.45E-02 1.50E-02 1.55E-02 1.60E-02 1.65E-02 1.70E-02
1.75E-02 1.80E-02 1.85E-02 1.90E-02 1.95E-02 2.00E-02 2.05E-02 2.10E-02
2.15E-02 2.20E-02 2.25E-02 2.30E-02 2.35E-02 2.40E-02 2.45E-02 2.50E-02
2.55E-02 2.60E-02 2.65E-02 2.70E-02 2.75E-02 2.80E-02 2.85E-02 2.90E-02
2.95E-02 3.00E-02 3.05E-02 3.10E-02 3.15E-02 3.20E-02 3.25E-02 3.30E-02
3.35E-02 3.40E-02 3.45E-02 3.50E-02 3.55E-02 3.60E-02 3.65E-02 3.70E-02
3.75E-02 3.80E-02 3.85E-02 3.90E-02 3.95E-02 4.00E-02 4.05E-02 4.10E-02
4.15E-02 4.20E-02 4.25E-02 4.30E-02 4.35E-02 4.40E-02 4.45E-02 4.50E-02
4.55E-02 4.60E-02 4.65E-02 4.70E-02 4.75E-02 4.80E-02 4.85E-02 4.90E-02
4.95E-02 5.00E-02 5.05E-02 5.10E-02 5.15E-02 5.20E-02 5.25E-02 5.30E-02
5.35E-02 5.40E-02 5.45E-02 5.50E-02 5.55E-02 5.60E-02 5.65E-02 5.70E-02
5.75E-02 5.80E-02 5.85E-02 5.90E-02 5.95E-02 6.00E-02

Intensity Distribution Inherent Filtration

0.00E+00 1.93E-08 1.62E-08 1.20E-07 1.76E-06 1.84E-06 5.29E-06 1.52E-05
3.77E-05 7.97E-05 1.56E-04 2.79E-04 4.65E-04 7.31E-04 1.08E-03 1.53E-03
2.07E-03 2.72E-03 3.46E-03 4.27E-03 5.16E-03 6.09E-03 7.04E-03 8.06E-03
9.04E-03 1.00E-02 1.10E-02 1.20E-02 1.28E-02 1.37E-02 1.45E-02 1.51E-02
1.59E-02 1.65E-02 1.70E-02 1.75E-02 1.79E-02 1.83E-02 1.86E-02 1.89E-02
1.91E-02 1.92E-02 1.94E-02 1.94E-02 1.95E-02 1.94E-02 1.94E-02 1.93E-02
1.92E-02 1.91E-02 1.89E-02 1.87E-02 1.85E-02 1.83E-02 1.80E-02 1.78E-02
1.75E-02 1.72E-02 1.69E-02 1.66E-02 1.63E-02 1.59E-02 1.56E-02 1.52E-02
1.49E-02 1.45E-02 1.41E-02 1.37E-02 1.34E-02 1.30E-02 1.26E-02 1.22E-02
1.18E-02 1.14E-02 1.10E-02 1.06E-02 1.01E-02 9.73E-03 9.33E-03 8.92E-03
8.50E-03 8.09E-03 7.67E-03 7.26E-03 6.85E-03 6.43E-03 6.02E-03 5.61E-03
5.20E-03 4.79E-03 4.38E-03 3.97E-03 3.56E-03 3.16E-03 2.75E-03 2.35E-03
1.96E-03 1.56E-03 1.17E-03 7.75E-04 3.86E-04 3.21E-05

Intensity Distribution 0.1 mm Cu Filtration

0.00E+00 1.46E-16 1.11E-15 6.08E-14 4.39E-12 1.87E-11 1.97E-10 1.74E-09

1.09E-08 5.33E-08 2.16E-07 7.35E-07 2.17E-06 5.67E-06 1.30E-05 2.75E-05
5.34E-05 9.64E-05 1.64E-04 2.62E-04 4.07E-04 5.93E-04 8.37E-04 1.15E-03
1.53E-03 1.97E-03 2.48E-03 3.07E-03 3.71E-03 4.43E-03 5.17E-03 5.98E-03
6.85E-03 7.71E-03 8.52E-03 9.42E-03 1.03E-02 1.13E-02 1.21E-02 1.29E-02
1.39E-02 1.46E-02 1.54E-02 1.60E-02 1.67E-02 1.73E-02 1.79E-02 1.84E-02
1.89E-02 1.93E-02 1.97E-02 2.00E-02 2.03E-02 2.05E-02 2.07E-02 2.08E-02
2.09E-02 2.10E-02 2.10E-02 2.09E-02 2.09E-02 2.08E-02 2.06E-02 2.04E-02
2.02E-02 2.00E-02 1.97E-02 1.94E-02 1.91E-02 1.87E-02 1.83E-02 1.79E-02
1.75E-02 1.71E-02 1.66E-02 1.61E-02 1.56E-02 1.51E-02 1.46E-02 1.40E-02
1.35E-02 1.29E-02 1.23E-02 1.17E-02 1.11E-02 1.05E-02 9.88E-03 9.25E-03
8.62E-03 7.98E-03 7.33E-03 6.68E-03 6.02E-03 5.36E-03 4.69E-03 4.03E-03
3.36E-03 2.69E-03 2.02E-03 1.34E-03 6.72E-04 5.61E-05

Intensity Distribution 0.2 mm Cu Filtration

0.00E+00 9.12E-25 6.24E-23 2.53E-20 9.07E-18 1.56E-16 6.05E-15 1.66E-13
2.60E-12 2.95E-11 2.48E-10 1.60E-09 8.33E-09 3.63E-08 1.29E-07 4.09E-07
1.14E-06 2.82E-06 6.41E-06 1.33E-05 2.65E-05 4.77E-05 8.22E-05 1.35E-04
2.13E-04 3.19E-04 4.62E-04 6.51E-04 8.87E-04 1.18E-03 1.52E-03 1.95E-03
2.44E-03 2.98E-03 3.53E-03 4.19E-03 4.93E-03 5.80E-03 6.51E-03 7.31E-03
8.31E-03 9.13E-03 1.01E-02 1.09E-02 1.19E-02 1.28E-02 1.37E-02 1.45E-02
1.54E-02 1.62E-02 1.69E-02 1.77E-02 1.84E-02 1.90E-02 1.96E-02 2.02E-02
2.07E-02 2.11E-02 2.15E-02 2.18E-02 2.21E-02 2.23E-02 2.25E-02 2.26E-02
2.27E-02 2.27E-02 2.27E-02 2.26E-02 2.25E-02 2.23E-02 2.20E-02 2.18E-02
2.15E-02 2.11E-02 2.07E-02 2.03E-02 1.98E-02 1.93E-02 1.88E-02 1.82E-02
1.76E-02 1.70E-02 1.63E-02 1.56E-02 1.49E-02 1.41E-02 1.34E-02 1.26E-02
1.18E-02 1.10E-02 1.01E-02 9.29E-03 8.40E-03 7.51E-03 6.60E-03 5.69E-03
4.76E-03 3.83E-03 2.88E-03 1.92E-03 9.66E-04 8.09E-05

66 kVp

Energy Bins

9.50E-03 1.00E-02 1.05E-02 1.10E-02 1.15E-02 1.20E-02 1.25E-02 1.30E-02
1.35E-02 1.40E-02 1.45E-02 1.50E-02 1.55E-02 1.60E-02 1.65E-02 1.70E-02
1.75E-02 1.80E-02 1.85E-02 1.90E-02 1.95E-02 2.00E-02 2.05E-02 2.10E-02
2.15E-02 2.20E-02 2.25E-02 2.30E-02 2.35E-02 2.40E-02 2.45E-02 2.50E-02
2.55E-02 2.60E-02 2.65E-02 2.70E-02 2.75E-02 2.80E-02 2.85E-02 2.90E-02
2.95E-02 3.00E-02 3.05E-02 3.10E-02 3.15E-02 3.20E-02 3.25E-02 3.30E-02
3.35E-02 3.40E-02 3.45E-02 3.50E-02 3.55E-02 3.60E-02 3.65E-02 3.70E-02
3.75E-02 3.80E-02 3.85E-02 3.90E-02 3.95E-02 4.00E-02 4.05E-02 4.10E-02
4.15E-02 4.20E-02 4.25E-02 4.30E-02 4.35E-02 4.40E-02 4.45E-02 4.50E-02
4.55E-02 4.60E-02 4.65E-02 4.70E-02 4.75E-02 4.80E-02 4.85E-02 4.90E-02
4.95E-02 5.00E-02 5.05E-02 5.10E-02 5.15E-02 5.20E-02 5.25E-02 5.30E-02
5.35E-02 5.40E-02 5.45E-02 5.50E-02 5.55E-02 5.60E-02 5.65E-02 5.70E-02
5.75E-02 5.80E-02 5.85E-02 5.90E-02 5.95E-02 6.00E-02 6.05E-02 6.10E-02
6.15E-02 6.20E-02 6.25E-02 6.30E-02 6.35E-02 6.40E-02 6.45E-02 6.50E-02
6.55E-02 6.60E-02

Intensity Distribution Inherent Filtration

0.00E+00 1.81E-08 1.34E-08 9.85E-08 1.47E-06 1.48E-06 4.20E-06 1.20E-05
2.98E-05 6.30E-05 1.23E-04 2.22E-04 3.71E-04 5.85E-04 8.68E-04 1.24E-03
1.69E-03 2.22E-03 2.84E-03 3.52E-03 4.28E-03 5.08E-03 5.89E-03 6.78E-03

7.63E-03 8.52E-03 9.37E-03 1.02E-02 1.10E-02 1.18E-02 1.25E-02 1.31E-02
1.38E-02 1.44E-02 1.49E-02 1.53E-02 1.58E-02 1.62E-02 1.65E-02 1.68E-02
1.69E-02 1.71E-02 1.73E-02 1.74E-02 1.75E-02 1.75E-02 1.75E-02 1.75E-02
1.74E-02 1.74E-02 1.73E-02 1.71E-02 1.70E-02 1.69E-02 1.67E-02 1.65E-02
1.63E-02 1.61E-02 1.59E-02 1.56E-02 1.54E-02 1.52E-02 1.49E-02 1.47E-02
1.44E-02 1.41E-02 1.38E-02 1.36E-02 1.33E-02 1.30E-02 1.27E-02 1.24E-02
1.21E-02 1.18E-02 1.15E-02 1.12E-02 1.09E-02 1.06E-02 1.03E-02 1.00E-02
9.70E-03 9.40E-03 9.09E-03 8.78E-03 8.48E-03 8.17E-03 7.87E-03 7.56E-03
7.26E-03 6.96E-03 6.65E-03 6.35E-03 6.05E-03 5.75E-03 5.45E-03 5.15E-03
4.85E-03 4.55E-03 4.26E-03 3.96E-03 3.67E-03 3.38E-03 3.09E-03 2.80E-03
2.51E-03 2.22E-03 1.94E-03 1.66E-03 1.38E-03 1.10E-03 8.19E-04 5.44E-04
2.71E-04 2.26E-05

Intensity Distribution 0.1 mm Cu Filtration

0.00E+00 1.11E-16 7.54E-16 4.16E-14 3.13E-12 1.28E-11 1.36E-10 1.21E-09
7.58E-09 3.73E-08 1.52E-07 5.22E-07 1.55E-06 4.09E-06 9.43E-06 2.02E-05
3.94E-05 7.16E-05 1.23E-04 1.98E-04 3.09E-04 4.52E-04 6.42E-04 8.86E-04
1.18E-03 1.54E-03 1.94E-03 2.42E-03 2.93E-03 3.52E-03 4.12E-03 4.79E-03
5.50E-03 6.21E-03 6.89E-03 7.64E-03 8.42E-03 9.26E-03 9.92E-03 1.06E-02
1.14E-02 1.20E-02 1.27E-02 1.33E-02 1.39E-02 1.45E-02 1.50E-02 1.55E-02
1.59E-02 1.63E-02 1.67E-02 1.70E-02 1.73E-02 1.76E-02 1.78E-02 1.80E-02
1.81E-02 1.82E-02 1.83E-02 1.84E-02 1.84E-02 1.84E-02 1.83E-02 1.83E-02
1.82E-02 1.81E-02 1.80E-02 1.78E-02 1.76E-02 1.74E-02 1.72E-02 1.70E-02
1.68E-02 1.65E-02 1.62E-02 1.59E-02 1.56E-02 1.53E-02 1.50E-02 1.47E-02
1.43E-02 1.39E-02 1.36E-02 1.32E-02 1.28E-02 1.24E-02 1.20E-02 1.16E-02
1.12E-02 1.08E-02 1.04E-02 9.95E-03 9.52E-03 9.08E-03 8.64E-03 8.20E-03
7.76E-03 7.31E-03 6.86E-03 6.40E-03 5.95E-03 5.49E-03 5.03E-03 4.58E-03
4.12E-03 3.66E-03 3.20E-03 2.74E-03 2.28E-03 1.83E-03 1.37E-03 9.09E-04
4.55E-04 3.79E-05

Intensity Distribution 0.2 mm Cu Filtration

0.00E+00 6.53E-25 4.01E-23 1.64E-20 6.08E-18 1.01E-16 3.92E-15 1.08E-13
1.71E-12 1.94E-11 1.65E-10 1.07E-09 5.62E-09 2.47E-08 8.84E-08 2.82E-07
7.89E-07 1.98E-06 4.52E-06 9.46E-06 1.90E-05 3.43E-05 5.95E-05 9.82E-05
1.55E-04 2.34E-04 3.41E-04 4.83E-04 6.61E-04 8.85E-04 1.15E-03 1.47E-03
1.85E-03 2.26E-03 2.69E-03 3.20E-03 3.78E-03 4.46E-03 5.03E-03 5.66E-03
6.45E-03 7.11E-03 7.86E-03 8.55E-03 9.32E-03 1.01E-02 1.08E-02 1.15E-02
1.22E-02 1.29E-02 1.35E-02 1.42E-02 1.48E-02 1.54E-02 1.59E-02 1.64E-02
1.69E-02 1.73E-02 1.77E-02 1.80E-02 1.83E-02 1.86E-02 1.89E-02 1.91E-02
1.93E-02 1.94E-02 1.95E-02 1.96E-02 1.96E-02 1.96E-02 1.95E-02 1.95E-02
1.94E-02 1.93E-02 1.91E-02 1.89E-02 1.87E-02 1.85E-02 1.82E-02 1.80E-02
1.76E-02 1.73E-02 1.69E-02 1.66E-02 1.62E-02 1.58E-02 1.54E-02 1.49E-02
1.45E-02 1.40E-02 1.35E-02 1.30E-02 1.25E-02 1.20E-02 1.15E-02 1.09E-02
1.04E-02 9.81E-03 9.24E-03 8.64E-03 8.07E-03 7.47E-03 6.87E-03 6.27E-03
5.65E-03 5.04E-03 4.42E-03 3.80E-03 3.17E-03 2.54E-03 1.90E-03 1.27E-03
6.37E-04 5.32E-05

70 kVp

Energy Bins

9.50E-03 1.00E-02 1.05E-02 1.10E-02 1.15E-02 1.20E-02 1.25E-02 1.30E-02
1.35E-02 1.40E-02 1.45E-02 1.50E-02 1.55E-02 1.60E-02 1.65E-02 1.70E-02
1.75E-02 1.80E-02 1.85E-02 1.90E-02 1.95E-02 2.00E-02 2.05E-02 2.10E-02
2.15E-02 2.20E-02 2.25E-02 2.30E-02 2.35E-02 2.40E-02 2.45E-02 2.50E-02
2.55E-02 2.60E-02 2.65E-02 2.70E-02 2.75E-02 2.80E-02 2.85E-02 2.90E-02
2.95E-02 3.00E-02 3.05E-02 3.10E-02 3.15E-02 3.20E-02 3.25E-02 3.30E-02
3.35E-02 3.40E-02 3.45E-02 3.50E-02 3.55E-02 3.60E-02 3.65E-02 3.70E-02
3.75E-02 3.80E-02 3.85E-02 3.90E-02 3.95E-02 4.00E-02 4.05E-02 4.10E-02
4.15E-02 4.20E-02 4.25E-02 4.30E-02 4.35E-02 4.40E-02 4.45E-02 4.50E-02
4.55E-02 4.60E-02 4.65E-02 4.70E-02 4.75E-02 4.80E-02 4.85E-02 4.90E-02
4.95E-02 5.00E-02 5.05E-02 5.10E-02 5.15E-02 5.20E-02 5.25E-02 5.30E-02
5.35E-02 5.40E-02 5.45E-02 5.50E-02 5.55E-02 5.60E-02 5.65E-02 5.70E-02
5.75E-02 5.80E-02 5.85E-02 5.90E-02 5.95E-02 6.00E-02 6.05E-02 6.10E-02
6.15E-02 6.20E-02 6.25E-02 6.30E-02 6.35E-02 6.40E-02 6.45E-02 6.50E-02
6.55E-02 6.60E-02 6.65E-02 6.70E-02 6.75E-02 6.80E-02 6.85E-02 6.90E-02
6.95E-02 7.00E-02

Intensity Distribution Inherent Filtration

0.00E+00 1.96E-08 1.32E-08 9.54E-08 1.42E-06 1.38E-06 3.89E-06 1.10E-05
2.71E-05 5.70E-05 1.11E-04 1.99E-04 3.32E-04 5.24E-04 7.77E-04 1.11E-03
1.51E-03 1.99E-03 2.55E-03 3.17E-03 3.86E-03 4.59E-03 5.34E-03 6.15E-03
6.94E-03 7.77E-03 8.56E-03 9.35E-03 1.01E-02 1.08E-02 1.15E-02 1.21E-02
1.27E-02 1.33E-02 1.37E-02 1.42E-02 1.46E-02 1.50E-02 1.53E-02 1.56E-02
1.58E-02 1.60E-02 1.62E-02 1.63E-02 1.64E-02 1.64E-02 1.65E-02 1.65E-02
1.64E-02 1.64E-02 1.63E-02 1.62E-02 1.61E-02 1.60E-02 1.59E-02 1.57E-02
1.56E-02 1.54E-02 1.52E-02 1.50E-02 1.48E-02 1.46E-02 1.44E-02 1.42E-02
1.39E-02 1.37E-02 1.35E-02 1.32E-02 1.30E-02 1.28E-02 1.25E-02 1.23E-02
1.20E-02 1.18E-02 1.15E-02 1.13E-02 1.10E-02 1.07E-02 1.05E-02 1.02E-02
9.97E-03 9.71E-03 9.45E-03 9.20E-03 8.94E-03 8.68E-03 8.43E-03 8.17E-03
7.92E-03 7.66E-03 7.40E-03 7.15E-03 6.90E-03 6.64E-03 6.39E-03 6.14E-03
5.89E-03 5.69E-03 5.39E-03 5.15E-03 4.99E-03 4.65E-03 4.41E-03 4.17E-03
3.92E-03 3.68E-03 3.44E-03 3.20E-03 2.96E-03 2.73E-03 2.49E-03 2.26E-03
2.03E-03 1.79E-03 1.56E-03 1.36E-03 1.11E-03 8.84E-04 6.61E-04 4.46E-04
2.19E-04 1.82E-05

Intensity Distribution 0.1 mm Cu Filtration

0.00E+00 1.24E-16 7.62E-16 4.08E-14 3.04E-12 1.20E-11 1.25E-10 1.10E-09
6.81E-09 3.32E-08 1.35E-07 4.59E-07 1.36E-06 3.57E-06 8.24E-06 1.76E-05
3.44E-05 6.25E-05 1.07E-04 1.73E-04 2.70E-04 3.96E-04 5.64E-04 7.78E-04
1.04E-03 1.35E-03 1.72E-03 2.14E-03 2.60E-03 3.12E-03 3.66E-03 4.25E-03
4.89E-03 5.53E-03 6.15E-03 6.83E-03 7.53E-03 8.30E-03 8.90E-03 9.54E-03
1.03E-02 1.08E-02 1.15E-02 1.20E-02 1.26E-02 1.31E-02 1.36E-02 1.40E-02
1.44E-02 1.48E-02 1.52E-02 1.55E-02 1.58E-02 1.61E-02 1.63E-02 1.65E-02
1.66E-02 1.68E-02 1.69E-02 1.69E-02 1.70E-02 1.70E-02 1.70E-02 1.70E-02
1.69E-02 1.69E-02 1.68E-02 1.67E-02 1.66E-02 1.65E-02 1.63E-02 1.61E-02
1.60E-02 1.58E-02 1.56E-02 1.54E-02 1.51E-02 1.49E-02 1.46E-02 1.44E-02
1.41E-02 1.39E-02 1.36E-02 1.33E-02 1.30E-02 1.27E-02 1.24E-02 1.21E-02

1.18E-02 1.14E-02 1.11E-02 1.08E-02 1.04E-02 1.01E-02 9.74E-03 9.40E-03
9.05E-03 8.78E-03 8.35E-03 7.99E-03 7.77E-03 7.27E-03 6.91E-03 6.55E-03
6.18E-03 5.82E-03 5.46E-03 5.09E-03 4.73E-03 4.36E-03 3.99E-03 3.62E-03
3.26E-03 2.90E-03 2.53E-03 2.21E-03 1.80E-03 1.44E-03 1.08E-03 7.29E-04
3.58E-04 2.98E-05

Intensity Distribution 0.2 mm Cu Filtration

0.00E+00 7.07E-25 3.93E-23 1.56E-20 5.73E-18 9.20E-17 3.50E-15 9.52E-14
1.49E-12 1.68E-11 1.41E-10 9.13E-10 4.78E-09 2.09E-08 7.49E-08 2.39E-07
6.68E-07 1.67E-06 3.83E-06 8.01E-06 1.61E-05 2.91E-05 5.06E-05 8.36E-05
1.33E-04 2.00E-04 2.92E-04 4.14E-04 5.67E-04 7.61E-04 9.86E-04 1.27E-03
1.60E-03 1.96E-03 2.33E-03 2.78E-03 3.28E-03 3.88E-03 4.37E-03 4.93E-03
5.63E-03 6.21E-03 6.87E-03 7.48E-03 8.16E-03 8.81E-03 9.47E-03 1.01E-02
1.07E-02 1.14E-02 1.19E-02 1.25E-02 1.31E-02 1.36E-02 1.41E-02 1.46E-02
1.50E-02 1.54E-02 1.58E-02 1.61E-02 1.64E-02 1.67E-02 1.70E-02 1.72E-02
1.74E-02 1.76E-02 1.77E-02 1.78E-02 1.79E-02 1.80E-02 1.79E-02 1.79E-02
1.79E-02 1.79E-02 1.78E-02 1.77E-02 1.76E-02 1.74E-02 1.73E-02 1.71E-02
1.69E-02 1.67E-02 1.64E-02 1.62E-02 1.59E-02 1.56E-02 1.53E-02 1.50E-02
1.47E-02 1.44E-02 1.40E-02 1.37E-02 1.33E-02 1.29E-02 1.25E-02 1.21E-02
1.17E-02 1.14E-02 1.09E-02 1.05E-02 1.02E-02 9.59E-03 9.14E-03 8.70E-03
8.23E-03 7.77E-03 7.31E-03 6.84E-03 6.36E-03 5.89E-03 5.40E-03 4.91E-03
4.43E-03 3.94E-03 3.46E-03 3.02E-03 2.47E-03 1.97E-03 1.48E-03 1.01E-03
4.94E-04 4.12E-05

75 kVp

Energy Bins

9.50E-03 1.00E-02 1.05E-02 1.10E-02 1.15E-02 1.20E-02 1.25E-02 1.30E-02
1.35E-02 1.40E-02 1.45E-02 1.50E-02 1.55E-02 1.60E-02 1.65E-02 1.70E-02
1.75E-02 1.80E-02 1.85E-02 1.90E-02 1.95E-02 2.00E-02 2.05E-02 2.10E-02
2.15E-02 2.20E-02 2.25E-02 2.30E-02 2.35E-02 2.40E-02 2.45E-02 2.50E-02
2.55E-02 2.60E-02 2.65E-02 2.70E-02 2.75E-02 2.80E-02 2.85E-02 2.90E-02
2.95E-02 3.00E-02 3.05E-02 3.10E-02 3.15E-02 3.20E-02 3.25E-02 3.30E-02
3.35E-02 3.40E-02 3.45E-02 3.50E-02 3.55E-02 3.60E-02 3.65E-02 3.70E-02
3.75E-02 3.80E-02 3.85E-02 3.90E-02 3.95E-02 4.00E-02 4.05E-02 4.10E-02
4.15E-02 4.20E-02 4.25E-02 4.30E-02 4.35E-02 4.40E-02 4.45E-02 4.50E-02
4.55E-02 4.60E-02 4.65E-02 4.70E-02 4.75E-02 4.80E-02 4.85E-02 4.90E-02
4.95E-02 5.00E-02 5.05E-02 5.10E-02 5.15E-02 5.20E-02 5.25E-02 5.30E-02
5.35E-02 5.40E-02 5.45E-02 5.50E-02 5.55E-02 5.60E-02 5.65E-02 5.70E-02
5.75E-02 5.80E-02 5.85E-02 5.90E-02 5.95E-02 6.00E-02 6.05E-02 6.10E-02
6.15E-02 6.20E-02 6.25E-02 6.30E-02 6.35E-02 6.40E-02 6.45E-02 6.50E-02
6.55E-02 6.60E-02 6.65E-02 6.70E-02 6.75E-02 6.80E-02 6.85E-02 6.90E-02
6.95E-02 7.00E-02 7.05E-02 7.10E-02 7.15E-02 7.20E-02 7.25E-02 7.30e-02
7.35E-02 7.40E-02 7.45E-02 7.50E-02

Intensity Distribution Inherent Filtration

0.00E+00 6.90E-09 4.93E-09 3.94E-08 6.46E-07 6.70E-07 2.01E-06 5.99E-06
1.55E-05 3.39E-05 6.86E-05 1.27E-04 2.19E-04 3.54E-04 5.38E-04 7.87E-04
1.09E-03 1.47E-03 1.92E-03 2.42E-03 2.99E-03 3.61E-03 4.25E-03 4.96E-03
5.66E-03 6.39E-03 7.11E-03 7.85E-03 8.52E-03 9.24E-03 9.87E-03 1.05E-02

1.11E-02 1.16E-02 1.21E-02 1.26E-02 1.30E-02 1.34E-02 1.38E-02 1.41E-02
1.43E-02 1.45E-02 1.48E-02 1.49E-02 1.50E-02 1.51E-02 1.52E-02 1.53E-02
1.53E-02 1.53E-02 1.53E-02 1.52E-02 1.51E-02 1.51E-02 1.50E-02 1.49E-02
1.47E-02 1.46E-02 1.45E-02 1.43E-02 1.42E-02 1.40E-02 1.38E-02 1.37E-02
1.35E-02 1.33E-02 1.31E-02 1.29E-02 1.27E-02 1.25E-02 1.23E-02 1.21E-02
1.19E-02 1.17E-02 1.15E-02 1.13E-02 1.10E-02 1.08E-02 1.06E-02 1.04E-02
1.02E-02 9.97E-03 9.75E-03 9.53E-03 9.32E-03 9.10E-03 8.89E-03 8.67E-03
8.46E-03 8.25E-03 8.03E-03 7.82E-03 7.61E-03 7.39E-03 7.18E-03 6.97E-03
6.76E-03 8.74E-03 6.35E-03 6.14E-03 9.75E-03 5.73E-03 5.52E-03 5.32E-03
5.12E-03 4.91E-03 4.71E-03 4.51E-03 4.31E-03 4.11E-03 3.91E-03 3.72E-03
3.52E-03 3.33E-03 3.13E-03 4.20E-03 2.75E-03 2.56E-03 2.37E-03 2.51E-03
1.98E-03 1.77E-03 1.59E-03 1.41E-03 1.23E-03 1.06E-03 8.77E-04 7.01E-04
5.24E-04 3.49E-04 1.74E-04 1.45E-05

Intensity Distribution 0.1 mm Cu Filtration

0.00E+00 4.41E-17 2.84E-16 1.68E-14 1.36E-12 5.73E-12 6.30E-11 5.82E-10
3.78E-09 1.92E-08 8.04E-08 2.82E-07 8.60E-07 2.32E-06 5.47E-06 1.19E-05
2.38E-05 4.40E-05 7.67E-05 1.26E-04 1.99E-04 2.97E-04 4.27E-04 5.96E-04
8.06E-04 1.06E-03 1.35E-03 1.70E-03 2.08E-03 2.52E-03 2.98E-03 3.49E-03
4.04E-03 4.59E-03 5.13E-03 5.72E-03 6.34E-03 7.02E-03 7.56E-03 8.14E-03
8.78E-03 9.31E-03 9.89E-03 1.04E-02 1.09E-02 1.14E-02 1.19E-02 1.23E-02
1.27E-02 1.31E-02 1.34E-02 1.37E-02 1.40E-02 1.43E-02 1.45E-02 1.47E-02
1.49E-02 1.50E-02 1.52E-02 1.53E-02 1.53E-02 1.54E-02 1.55E-02 1.55E-02
1.55E-02 1.55E-02 1.54E-02 1.54E-02 1.53E-02 1.52E-02 1.51E-02 1.50E-02
1.49E-02 1.48E-02 1.46E-02 1.45E-02 1.43E-02 1.42E-02 1.40E-02 1.38E-02
1.36E-02 1.34E-02 1.32E-02 1.30E-02 1.28E-02 1.25E-02 1.23E-02 1.21E-02
1.19E-02 1.16E-02 1.14E-02 1.11E-02 1.09E-02 1.06E-02 1.03E-02 1.01E-02
9.81E-03 1.27E-02 9.27E-03 8.99E-03 1.43E-02 8.45E-03 8.17E-03 7.90E-03
7.61E-03 7.33E-03 7.05E-03 6.77E-03 6.49E-03 6.21E-03 5.92E-03 5.63E-03
5.35E-03 5.06E-03 4.78E-03 6.43E-03 4.21E-03 3.92E-03 3.64E-03 3.87E-03
3.06E-03 2.74E-03 2.46E-03 2.19E-03 1.92E-03 1.64E-03 1.37E-03 1.09E-03
8.20E-04 5.46E-04 2.73E-04 2.28E-05

Intensity Distribution 0.2 mm Cu Filtration

0.00E+00 2.42E-25 1.41E-23 6.15E-21 2.47E-18 4.22E-17 1.70E-15 4.86E-14
7.93E-13 9.30E-12 8.11E-11 5.40E-10 2.91E-09 1.31E-08 4.78E-08 1.56E-07
4.44E-07 1.13E-06 2.64E-06 5.61E-06 1.14E-05 2.10E-05 3.68E-05 6.16E-05
9.87E-05 1.51E-04 2.22E-04 3.17E-04 4.38E-04 5.92E-04 7.72E-04 9.99E-04
1.27E-03 1.56E-03 1.87E-03 2.24E-03 2.66E-03 3.15E-03 3.57E-03 4.04E-03
4.63E-03 5.13E-03 5.70E-03 6.22E-03 6.81E-03 7.38E-03 7.95E-03 8.50E-03
9.06E-03 9.61E-03 1.01E-02 1.06E-02 1.11E-02 1.16E-02 1.21E-02 1.25E-02
1.29E-02 1.33E-02 1.37E-02 1.40E-02 1.43E-02 1.46E-02 1.48E-02 1.51E-02
1.53E-02 1.55E-02 1.56E-02 1.58E-02 1.59E-02 1.60E-02 1.60E-02 1.61E-02
1.61E-02 1.61E-02 1.61E-02 1.61E-02 1.60E-02 1.59E-02 1.59E-02 1.58E-02
1.56E-02 1.55E-02 1.54E-02 1.52E-02 1.51E-02 1.48E-02 1.47E-02 1.45E-02
1.43E-02 1.40E-02 1.38E-02 1.36E-02 1.33E-02 1.30E-02 1.28E-02 1.25E-02
1.22E-02 1.59E-02 1.17E-02 1.13E-02 1.81E-02 1.07E-02 1.04E-02 1.01E-02
9.73E-03 9.41E-03 9.08E-03 8.74E-03 8.39E-03 8.05E-03 7.69E-03 7.33E-03
6.99E-03 6.63E-03 6.28E-03 8.44E-03 5.54E-03 5.17E-03 4.82E-03 5.13E-03
4.06E-03 3.64E-03 3.28E-03 2.92E-03 2.56E-03 2.20E-03 1.83E-03 1.47E-03
1.10E-03 7.36E-04 3.68E-04 3.07E-05

80 kVp

Energy Bins

9.50E-03 1.00E-02 1.05E-02 1.10E-02 1.15E-02 1.20E-02 1.25E-02 1.30E-02
1.35E-02 1.40E-02 1.45E-02 1.50E-02 1.55E-02 1.60E-02 1.65E-02 1.70E-02
1.75E-02 1.80E-02 1.85E-02 1.90E-02 1.95E-02 2.00E-02 2.05E-02 2.10E-02
2.15E-02 2.20E-02 2.25E-02 2.30E-02 2.35E-02 2.40E-02 2.45E-02 2.50E-02
2.55E-02 2.60E-02 2.65E-02 2.70E-02 2.75E-02 2.80E-02 2.85E-02 2.90E-02
2.95E-02 3.00E-02 3.05E-02 3.10E-02 3.15E-02 3.20E-02 3.25E-02 3.30E-02
3.35E-02 3.40E-02 3.45E-02 3.50E-02 3.55E-02 3.60E-02 3.65E-02 3.70E-02
3.75E-02 3.80E-02 3.85E-02 3.90E-02 3.95E-02 4.00E-02 4.05E-02 4.10E-02
4.15E-02 4.20E-02 4.25E-02 4.30E-02 4.35E-02 4.40E-02 4.45E-02 4.50E-02
4.55E-02 4.60E-02 4.65E-02 4.70E-02 4.75E-02 4.80E-02 4.85E-02 4.90E-02
4.95E-02 5.00E-02 5.05E-02 5.10E-02 5.15E-02 5.20E-02 5.25E-02 5.30E-02
5.35E-02 5.40E-02 5.45E-02 5.50E-02 5.55E-02 5.60E-02 5.65E-02 5.70E-02
5.75E-02 5.80E-02 5.85E-02 5.90E-02 5.95E-02 6.00E-02 6.05E-02 6.10E-02
6.15E-02 6.20E-02 6.25E-02 6.30E-02 6.35E-02 6.40E-02 6.45E-02 6.50E-02
6.55E-02 6.60E-02 6.65E-02 6.70E-02 6.75E-02 6.80E-02 6.85E-02 6.90E-02
6.95E-02 7.00E-02 7.05E-02 7.10E-02 7.15E-02 7.20E-02 7.25E-02 7.30e-02
7.35E-02 7.40E-02 7.45E-02 7.50E-02 7.55E-02 7.60E-02 7.65E-02 7.70E-02
7.75E-02 7.80E-02 7.85E-02 7.90E-02 7.95E-02 8.00E-02

Intensity Distribution Inherent Filtration

0.00E+00 5.91E-09 4.01E-09 3.21E-08 5.26E-07 5.47E-07 1.64E-06 4.90E-06
1.27E-05 2.79E-05 5.65E-05 1.05E-04 1.81E-04 2.95E-04 4.50E-04 6.61E-04
9.22E-04 1.25E-03 1.63E-03 2.07E-03 2.57E-03 3.11E-03 3.69E-03 4.32E-03
4.95E-03 5.62E-03 6.27E-03 6.94E-03 7.57E-03 8.23E-03 8.82E-03 9.38E-03
9.95E-03 1.05E-02 1.09E-02 1.14E-02 1.18E-02 1.22E-02 1.26E-02 1.29E-02
1.31E-02 1.34E-02 1.36E-02 1.37E-02 1.39E-02 1.40E-02 1.41E-02 1.42E-02
1.42E-02 1.42E-02 1.42E-02 1.42E-02 1.42E-02 1.41E-02 1.40E-02 1.40E-02
1.39E-02 1.38E-02 1.37E-02 1.35E-02 1.34E-02 1.33E-02 1.31E-02 1.30E-02
1.28E-02 1.27E-02 1.25E-02 1.23E-02 1.22E-02 1.20E-02 1.18E-02 1.16E-02
1.15E-02 1.13E-02 1.11E-02 1.09E-02 1.07E-02 1.06E-02 1.04E-02 1.02E-02
1.00E-02 9.83E-03 9.64E-03 9.46E-03 9.28E-03 9.09E-03 8.91E-03 8.73E-03
8.54E-03 8.36E-03 8.18E-03 8.00E-03 7.82E-03 7.64E-03 7.46E-03 7.29E-03
7.11E-03 1.22E-02 6.76E-03 6.59E-03 1.57E-02 6.24E-03 6.07E-03 5.89E-03
5.72E-03 5.56E-03 5.39E-03 5.22E-03 5.05E-03 4.89E-03 4.72E-03 4.55E-03
4.39E-03 4.23E-03 4.06E-03 6.99E-03 3.74E-03 3.58E-03 3.42E-03 4.08E-03
3.09E-03 2.84E-03 2.70E-03 2.56E-03 2.41E-03 2.27E-03 2.12E-03 1.98E-03
1.84E-03 1.69E-03 1.55E-03 1.41E-03 1.26E-03 1.12E-03 9.79E-04 8.37E-04
6.96E-04 5.56E-04 4.16E-04 2.77E-04 1.38E-04 1.15E-05

Intensity Distribution 0.1 mm Cu Filtration

0.00E+00 3.63E-17 2.22E-16 1.31E-14 1.07E-12 4.50E-12 4.95E-11 4.58E-10
2.98E-09 1.51E-08 6.36E-08 2.24E-07 6.85E-07 1.85E-06 4.39E-06 9.63E-06
1.93E-05 3.58E-05 6.27E-05 1.03E-04 1.65E-04 2.46E-04 3.55E-04 4.99E-04
6.77E-04 8.92E-04 1.15E-03 1.45E-03 1.78E-03 2.16E-03 2.55E-03 3.00E-03
3.48E-03 3.97E-03 4.45E-03 4.98E-03 5.53E-03 6.14E-03 6.63E-03 7.15E-03
7.73E-03 8.21E-03 8.74E-03 9.19E-03 9.68E-03 1.01E-02 1.06E-02 1.10E-02

1.13E-02 1.17E-02 1.20E-02 1.23E-02 1.26E-02 1.28E-02 1.30E-02 1.33E-02
1.34E-02 1.36E-02 1.37E-02 1.38E-02 1.39E-02 1.40E-02 1.41E-02 1.41E-02
1.41E-02 1.41E-02 1.42E-02 1.41E-02 1.41E-02 1.40E-02 1.40E-02 1.39E-02
1.38E-02 1.37E-02 1.36E-02 1.35E-02 1.34E-02 1.33E-02 1.31E-02 1.30E-02
1.28E-02 1.27E-02 1.25E-02 1.24E-02 1.22E-02 1.20E-02 1.19E-02 1.17E-02
1.15E-02 1.13E-02 1.11E-02 1.09E-02 1.07E-02 1.05E-02 1.03E-02 1.01E-02
9.90E-03 1.71E-02 9.48E-03 9.26E-03 2.21E-02 8.83E-03 8.61E-03 8.40E-03
8.18E-03 7.96E-03 7.74E-03 7.52E-03 7.30E-03 7.08E-03 6.85E-03 6.62E-03
6.41E-03 6.18E-03 5.96E-03 1.03E-02 5.50E-03 5.28E-03 5.06E-03 6.04E-03
4.58E-03 4.22E-03 4.02E-03 3.81E-03 3.60E-03 3.39E-03 3.18E-03 2.97E-03
2.76E-03 2.54E-03 2.33E-03 2.12E-03 1.91E-03 1.69E-03 1.48E-03 1.27E-03
1.06E-03 8.45E-04 6.33E-04 4.21E-04 2.10E-04 1.75E-05

Intensity Distribution 0.2 mm Cu Filtration

0.00E+00 1.93E-25 1.07E-23 4.66E-21 1.87E-18 3.21E-17 1.30E-15 3.71E-14
6.06E-13 7.12E-12 6.22E-11 4.16E-10 2.24E-09 1.01E-08 3.72E-08 1.22E-07
3.49E-07 8.95E-07 2.09E-06 4.47E-06 9.14E-06 1.68E-05 2.97E-05 5.00E-05
8.04E-05 1.23E-04 1.82E-04 2.61E-04 3.62E-04 4.91E-04 6.43E-04 8.34E-04
1.06E-03 1.31E-03 1.57E-03 1.89E-03 2.25E-03 2.68E-03 3.04E-03 3.44E-03
3.95E-03 4.39E-03 4.88E-03 5.34E-03 5.86E-03 6.36E-03 6.87E-03 7.35E-03
7.84E-03 8.34E-03 8.81E-03 9.26E-03 9.71E-03 1.01E-02 1.05E-02 1.09E-02
1.13E-02 1.17E-02 1.20E-02 1.23E-02 1.26E-02 1.29E-02 1.31E-02 1.33E-02
1.35E-02 1.37E-02 1.39E-02 1.40E-02 1.42E-02 1.43E-02 1.43E-02 1.44E-02
1.45E-02 1.45E-02 1.45E-02 1.45E-02 1.45E-02 1.45E-02 1.44E-02 1.44E-02
1.43E-02 1.43E-02 1.42E-02 1.41E-02 1.40E-02 1.38E-02 1.37E-02 1.36E-02
1.34E-02 1.33E-02 1.31E-02 1.29E-02 1.27E-02 1.26E-02 1.24E-02 1.22E-02
1.20E-02 2.07E-02 1.16E-02 1.13E-02 2.71E-02 1.09E-02 1.06E-02 1.04E-02
1.01E-02 9.91E-03 9.66E-03 9.41E-03 9.15E-03 8.91E-03 8.64E-03 8.36E-03
8.12E-03 7.84E-03 7.59E-03 1.31E-02 7.03E-03 6.75E-03 6.49E-03 7.76E-03
5.89E-03 5.45E-03 5.18E-03 4.92E-03 4.66E-03 4.40E-03 4.13E-03 3.86E-03
3.59E-03 3.32E-03 3.05E-03 2.78E-03 2.50E-03 2.22E-03 1.95E-03 1.67E-03
1.39E-03 1.11E-03 8.36E-04 5.57E-04 2.78E-04 2.32E-05

85 kVp

Energy Bins

9.50E-03 1.00E-02 1.05E-02 1.10E-02 1.15E-02 1.20E-02 1.25E-02 1.30E-02
1.35E-02 1.40E-02 1.45E-02 1.50E-02 1.55E-02 1.60E-02 1.65E-02 1.70E-02
1.75E-02 1.80E-02 1.85E-02 1.90E-02 1.95E-02 2.00E-02 2.05E-02 2.10E-02
2.15E-02 2.20E-02 2.25E-02 2.30E-02 2.35E-02 2.40E-02 2.45E-02 2.50E-02
2.55E-02 2.60E-02 2.65E-02 2.70E-02 2.75E-02 2.80E-02 2.85E-02 2.90E-02
2.95E-02 3.00E-02 3.05E-02 3.10E-02 3.15E-02 3.20E-02 3.25E-02 3.30E-02
3.35E-02 3.40E-02 3.45E-02 3.50E-02 3.55E-02 3.60E-02 3.65E-02 3.70E-02
3.75E-02 3.80E-02 3.85E-02 3.90E-02 3.95E-02 4.00E-02 4.05E-02 4.10E-02
4.15E-02 4.20E-02 4.25E-02 4.30E-02 4.35E-02 4.40E-02 4.45E-02 4.50E-02
4.55E-02 4.60E-02 4.65E-02 4.70E-02 4.75E-02 4.80E-02 4.85E-02 4.90E-02
4.95E-02 5.00E-02 5.05E-02 5.10E-02 5.15E-02 5.20E-02 5.25E-02 5.30E-02
5.35E-02 5.40E-02 5.45E-02 5.50E-02 5.55E-02 5.60E-02 5.65E-02 5.70E-02
5.75E-02 5.80E-02 5.85E-02 5.90E-02 5.95E-02 6.00E-02 6.05E-02 6.10E-02
6.15E-02 6.20E-02 6.25E-02 6.30E-02 6.35E-02 6.40E-02 6.45E-02 6.50E-02

6.55E-02 6.60E-02 6.65E-02 6.70E-02 6.75E-02 6.80E-02 6.85E-02 6.90E-02
6.95E-02 7.00E-02 7.05E-02 7.10E-02 7.15E-02 7.20E-02 7.25E-02 7.30e-02
7.35E-02 7.40E-02 7.45E-02 7.50E-02 7.55E-02 7.60E-02 7.65E-02 7.70E-02
7.75E-02 7.80E-02 7.85E-02 7.90E-02 7.95E-02 8.00E-02 8.05E-02 8.10E-02
8.15E-02 8.20E-02 8.25E-02 8.30E-02 8.35E-02 8.40E-02 8.45E-02 8.50E-02

Intensity Distribution Inherent Filtration

0.00E+00 5.10E-09 3.32E-09 2.65E-08 4.30E-07 4.54E-07 1.36E-06 4.08E-06
1.06E-05 2.32E-05 4.72E-05 8.79E-05 1.52E-04 2.48E-04 3.80E-04 5.60E-04
7.85E-04 1.07E-03 1.40E-03 1.79E-03 2.23E-03 2.71E-03 3.22E-03 3.78E-03
4.35E-03 4.96E-03 5.56E-03 6.18E-03 6.75E-03 7.37E-03 7.93E-03 8.45E-03
9.00E-03 9.50E-03 9.95E-03 1.04E-02 1.08E-02 1.12E-02 1.15E-02 1.19E-02
1.21E-02 1.23E-02 1.26E-02 1.27E-02 1.29E-02 1.30E-02 1.31E-02 1.32E-02
1.33E-02 1.33E-02 1.33E-02 1.33E-02 1.33E-02 1.33E-02 1.32E-02 1.32E-02
1.31E-02 1.30E-02 1.29E-02 1.28E-02 1.27E-02 1.26E-02 1.25E-02 1.24E-02
1.22E-02 1.21E-02 1.20E-02 1.18E-02 1.17E-02 1.15E-02 1.14E-02 1.12E-02
1.11E-02 1.09E-02 1.07E-02 1.06E-02 1.04E-02 1.03E-02 1.01E-02 9.93E-03
9.77E-03 9.61E-03 9.45E-03 9.29E-03 9.13E-03 8.96E-03 8.81E-03 8.65E-03
8.49E-03 8.33E-03 8.17E-03 8.02E-03 7.86E-03 7.70E-03 7.55E-03 7.39E-03
7.24E-03 1.56E-02 6.94E-03 6.79E-03 2.16E-02 6.49E-03 6.34E-03 6.19E-03
6.05E-03 5.90E-03 5.76E-03 5.61E-03 5.47E-03 5.33E-03 5.19E-03 5.04E-03
4.91E-03 4.76E-03 4.63E-03 9.50E-03 4.35E-03 4.21E-03 4.08E-03 5.27E-03
3.77E-03 3.48E-03 3.36E-03 3.24E-03 3.13E-03 3.01E-03 2.89E-03 2.77E-03
2.66E-03 2.54E-03 2.42E-03 2.30E-03 2.19E-03 2.07E-03 1.95E-03 1.83E-03
1.72E-03 1.60E-03 1.48E-03 1.37E-03 1.25E-03 1.14E-03 1.02E-03 9.05E-04
7.90E-04 6.76E-04 5.62E-04 4.49E-04 3.36E-04 2.23E-04 1.11E-04 9.27E-06

Intensity Distribution 0.1 mm Cu Filtration

0.00E+00 3.02E-17 1.77E-16 1.05E-14 8.43E-13 3.61E-12 3.97E-11 3.68E-10
2.40E-09 1.22E-08 5.14E-08 1.81E-07 5.55E-07 1.51E-06 3.58E-06 7.88E-06
1.58E-05 2.96E-05 5.20E-05 8.59E-05 1.37E-04 2.06E-04 2.99E-04 4.22E-04
5.75E-04 7.61E-04 9.81E-04 1.24E-03 1.53E-03 1.87E-03 2.22E-03 2.61E-03
3.04E-03 3.48E-03 3.91E-03 4.39E-03 4.88E-03 5.43E-03 5.87E-03 6.35E-03
6.88E-03 7.33E-03 7.81E-03 8.23E-03 8.68E-03 9.10E-03 9.50E-03 9.87E-03
1.02E-02 1.06E-02 1.09E-02 1.11E-02 1.14E-02 1.17E-02 1.19E-02 1.21E-02
1.23E-02 1.24E-02 1.26E-02 1.27E-02 1.28E-02 1.29E-02 1.29E-02 1.30E-02
1.30E-02 1.30E-02 1.31E-02 1.30E-02 1.30E-02 1.30E-02 1.30E-02 1.29E-02
1.29E-02 1.28E-02 1.27E-02 1.26E-02 1.25E-02 1.24E-02 1.23E-02 1.22E-02
1.21E-02 1.20E-02 1.19E-02 1.17E-02 1.16E-02 1.15E-02 1.13E-02 1.12E-02
1.10E-02 1.09E-02 1.07E-02 1.06E-02 1.04E-02 1.02E-02 1.01E-02 9.90E-03
9.74E-03 2.11E-02 9.40E-03 9.22E-03 2.95E-02 8.87E-03 8.70E-03 8.53E-03
8.34E-03 8.17E-03 7.99E-03 7.81E-03 7.63E-03 7.46E-03 7.27E-03 7.08E-03
6.91E-03 6.73E-03 6.55E-03 1.35E-02 6.18E-03 6.00E-03 5.82E-03 7.53E-03
5.41E-03 4.99E-03 4.83E-03 4.66E-03 4.51E-03 4.34E-03 4.18E-03 4.02E-03
3.85E-03 3.69E-03 3.52E-03 3.35E-03 3.19E-03 3.02E-03 2.85E-03 2.68E-03
2.52E-03 2.35E-03 2.18E-03 2.01E-03 1.84E-03 1.67E-03 1.50E-03 1.34E-03
1.17E-03 1.00E-03 8.32E-04 6.65E-04 4.98E-04 3.31E-04 1.65E-04 1.38E-05

Intensity Distribution 0.2 mm Cu Filtration

0.00E+00 1.57E-25 8.32E-24 3.63E-21 1.45E-18 2.51E-17 1.01E-15 2.91E-14
4.75E-13 5.60E-12 4.90E-11 3.28E-10 1.77E-09 8.03E-09 2.96E-08 9.72E-08
2.80E-07 7.20E-07 1.69E-06 3.63E-06 7.45E-06 1.38E-05 2.44E-05 4.12E-05
6.66E-05 1.02E-04 1.52E-04 2.19E-04 3.04E-04 4.14E-04 5.44E-04 7.08E-04
9.02E-04 1.12E-03 1.35E-03 1.62E-03 1.94E-03 2.31E-03 2.62E-03 2.98E-03
3.43E-03 3.82E-03 4.26E-03 4.66E-03 5.12E-03 5.57E-03 6.02E-03 6.46E-03
6.90E-03 7.35E-03 7.77E-03 8.18E-03 8.59E-03 8.99E-03 9.34E-03 9.72E-03
1.01E-02 1.04E-02 1.07E-02 1.10E-02 1.12E-02 1.15E-02 1.17E-02 1.20E-02
1.22E-02 1.23E-02 1.25E-02 1.26E-02 1.28E-02 1.29E-02 1.30E-02 1.30E-02
1.31E-02 1.32E-02 1.32E-02 1.32E-02 1.32E-02 1.32E-02 1.32E-02 1.32E-02
1.32E-02 1.31E-02 1.31E-02 1.30E-02 1.29E-02 1.28E-02 1.28E-02 1.26E-02
1.26E-02 1.24E-02 1.23E-02 1.22E-02 1.21E-02 1.19E-02 1.18E-02 1.16E-02
1.15E-02 2.50E-02 1.12E-02 1.10E-02 3.52E-02 1.06E-02 1.05E-02 1.03E-02
1.01E-02 9.91E-03 9.73E-03 9.54E-03 9.33E-03 9.15E-03 8.94E-03 8.73E-03
8.54E-03 8.33E-03 8.13E-03 1.67E-02 7.69E-03 7.48E-03 7.29E-03 9.44E-03
6.79E-03 6.28E-03 6.08E-03 5.88E-03 5.69E-03 5.50E-03 5.30E-03 5.10E-03
4.90E-03 4.69E-03 4.49E-03 4.28E-03 4.07E-03 3.86E-03 3.66E-03 3.44E-03
3.23E-03 3.02E-03 2.81E-03 2.59E-03 2.38E-03 2.16E-03 1.94E-03 1.73E-03
1.51E-03 1.30E-03 1.08E-03 8.64E-04 6.48E-04 4.31E-04 2.16E-04 1.80E-05

90 kVp

Energy Bins

9.50E-03 1.00E-02 1.05E-02 1.10E-02 1.15E-02 1.20E-02 1.25E-02 1.30E-02
1.35E-02 1.40E-02 1.45E-02 1.50E-02 1.55E-02 1.60E-02 1.65E-02 1.70E-02
1.75E-02 1.80E-02 1.85E-02 1.90E-02 1.95E-02 2.00E-02 2.05E-02 2.10E-02
2.15E-02 2.20E-02 2.25E-02 2.30E-02 2.35E-02 2.40E-02 2.45E-02 2.50E-02
2.55E-02 2.60E-02 2.65E-02 2.70E-02 2.75E-02 2.80E-02 2.85E-02 2.90E-02
2.95E-02 3.00E-02 3.05E-02 3.10E-02 3.15E-02 3.20E-02 3.25E-02 3.30E-02
3.35E-02 3.40E-02 3.45E-02 3.50E-02 3.55E-02 3.60E-02 3.65E-02 3.70E-02
3.75E-02 3.80E-02 3.85E-02 3.90E-02 3.95E-02 4.00E-02 4.05E-02 4.10E-02
4.15E-02 4.20E-02 4.25E-02 4.30E-02 4.35E-02 4.40E-02 4.45E-02 4.50E-02
4.55E-02 4.60E-02 4.65E-02 4.70E-02 4.75E-02 4.80E-02 4.85E-02 4.90E-02
4.95E-02 5.00E-02 5.05E-02 5.10E-02 5.15E-02 5.20E-02 5.25E-02 5.30E-02
5.35E-02 5.40E-02 5.45E-02 5.50E-02 5.55E-02 5.60E-02 5.65E-02 5.70E-02
5.75E-02 5.80E-02 5.85E-02 5.90E-02 5.95E-02 6.00E-02 6.05E-02 6.10E-02
6.15E-02 6.20E-02 6.25E-02 6.30E-02 6.35E-02 6.40E-02 6.45E-02 6.50E-02
6.55E-02 6.60E-02 6.65E-02 6.70E-02 6.75E-02 6.80E-02 6.85E-02 6.90E-02
6.95E-02 7.00E-02 7.05E-02 7.10E-02 7.15E-02 7.20E-02 7.25E-02 7.30E-02
7.35E-02 7.40E-02 7.45E-02 7.50E-02 7.55E-02 7.60E-02 7.65E-02 7.70E-02
7.75E-02 7.80E-02 7.85E-02 7.90E-02 7.95E-02 8.00E-02 8.05E-02 8.10E-02
8.15E-02 8.20E-02 8.25E-02 8.30E-02 8.35E-02 8.40E-02 8.45E-02 8.50E-02
8.55E-02 8.60E-02 8.65E-02 8.70E-02 8.75E-02 8.80E-02 8.85E-02 8.90E-02
8.95E-02 9.00E-02

Intensity Distribution Inherent Filtration

0.00E+00 4.41E-09 2.78E-09 2.23E-08 3.55E-07 3.83E-07 1.15E-06 3.44E-06
8.94E-06 1.97E-05 4.00E-05 7.45E-05 1.29E-04 2.11E-04 3.24E-04 4.80E-04

6.74E-04 9.18E-04 1.21E-03 1.55E-03 1.94E-03 2.37E-03 2.82E-03 3.34E-03
3.85E-03 4.40E-03 4.95E-03 5.52E-03 6.06E-03 6.64E-03 7.16E-03 7.66E-03
8.17E-03 8.65E-03 9.09E-03 9.53E-03 9.92E-03 1.03E-02 1.06E-02 1.10E-02
1.12E-02 1.14E-02 1.17E-02 1.19E-02 1.20E-02 1.22E-02 1.23E-02 1.24E-02
1.25E-02 1.25E-02 1.25E-02 1.26E-02 1.26E-02 1.25E-02 1.25E-02 1.25E-02
1.24E-02 1.24E-02 1.23E-02 1.22E-02 1.21E-02 1.20E-02 1.19E-02 1.18E-02
1.17E-02 1.16E-02 1.15E-02 1.13E-02 1.12E-02 1.11E-02 1.09E-02 1.08E-02
1.07E-02 1.05E-02 1.04E-02 1.02E-02 1.01E-02 9.94E-03 9.81E-03 9.66E-03
9.51E-03 9.37E-03 9.22E-03 9.08E-03 8.94E-03 8.79E-03 8.65E-03 8.51E-03
8.37E-03 8.23E-03 8.08E-03 7.95E-03 7.81E-03 7.67E-03 7.53E-03 7.39E-03
7.26E-03 1.87E-02 6.99E-03 6.86E-03 2.71E-02 6.59E-03 6.46E-03 6.33E-03
6.20E-03 6.08E-03 5.95E-03 5.82E-03 5.70E-03 5.57E-03 5.45E-03 5.32E-03
5.20E-03 5.08E-03 4.96E-03 1.17E-02 4.72E-03 4.60E-03 4.48E-03 6.18E-03
4.20E-03 3.83E-03 3.74E-03 3.64E-03 3.55E-03 3.45E-03 3.35E-03 3.26E-03
3.16E-03 3.06E-03 2.96E-03 2.87E-03 2.77E-03 2.67E-03 2.57E-03 2.48E-03
2.38E-03 2.28E-03 2.18E-03 2.09E-03 1.99E-03 1.89E-03 1.80E-03 1.70E-03
1.60E-03 1.51E-03 1.41E-03 1.31E-03 1.22E-03 1.12E-03 1.03E-03 9.31E-04
8.36E-04 7.42E-04 6.48E-04 5.54E-04 4.61E-04 3.68E-04 2.75E-04 1.83E-04
9.13E-05 7.60E-06

Intensity Distribution 0.1 mm Cu Filtration

0.00E+00 2.54E-17 1.45E-16 8.56E-15 6.74E-13 2.95E-12 3.25E-11 3.01E-10
1.96E-09 1.00E-08 4.22E-08 1.49E-07 4.58E-07 1.25E-06 2.97E-06 6.55E-06
1.32E-05 2.47E-05 4.36E-05 7.24E-05 1.16E-04 1.75E-04 2.55E-04 3.61E-04
4.94E-04 6.56E-04 8.49E-04 1.08E-03 1.33E-03 1.63E-03 1.94E-03 2.30E-03
2.68E-03 3.08E-03 3.47E-03 3.90E-03 4.35E-03 4.85E-03 5.26E-03 5.70E-03
6.19E-03 6.60E-03 7.05E-03 7.44E-03 7.87E-03 8.25E-03 8.63E-03 8.98E-03
9.32E-03 9.64E-03 9.93E-03 1.02E-02 1.05E-02 1.07E-02 1.09E-02 1.11E-02
1.13E-02 1.14E-02 1.16E-02 1.17E-02 1.18E-02 1.19E-02 1.20E-02 1.20E-02
1.21E-02 1.21E-02 1.22E-02 1.22E-02 1.22E-02 1.21E-02 1.21E-02 1.21E-02
1.20E-02 1.20E-02 1.19E-02 1.19E-02 1.18E-02 1.17E-02 1.16E-02 1.16E-02
1.14E-02 1.14E-02 1.12E-02 1.12E-02 1.10E-02 1.09E-02 1.08E-02 1.07E-02
1.06E-02 1.04E-02 1.03E-02 1.02E-02 1.00E-02 9.89E-03 9.75E-03 9.61E-03
9.48E-03 2.46E-02 9.20E-03 9.04E-03 3.59E-02 8.75E-03 8.61E-03 8.47E-03
8.31E-03 8.16E-03 8.02E-03 7.87E-03 7.72E-03 7.57E-03 7.42E-03 7.26E-03
7.12E-03 6.97E-03 6.82E-03 1.61E-02 6.51E-03 6.36E-03 6.21E-03 8.58E-03
5.84E-03 5.34E-03 5.21E-03 5.09E-03 4.96E-03 4.83E-03 4.70E-03 4.58E-03
4.45E-03 4.32E-03 4.18E-03 4.05E-03 3.92E-03 3.79E-03 3.65E-03 3.52E-03
3.38E-03 3.25E-03 3.12E-03 2.98E-03 2.84E-03 2.71E-03 2.57E-03 2.43E-03
2.30E-03 2.16E-03 2.03E-03 1.89E-03 1.75E-03 1.62E-03 1.48E-03 1.34E-03
1.21E-03 1.07E-03 9.38E-04 8.03E-04 6.68E-04 5.34E-04 3.99E-04 2.66E-04
1.33E-04 1.11E-05

Intensity Distribution 0.2 mm Cu Filtration

0.00E+00 1.29E-25 6.64E-24 2.90E-21 1.13E-18 2.01E-17 8.13E-16 2.33E-14
3.81E-13 4.50E-12 3.94E-11 2.64E-10 1.43E-09 6.50E-09 2.40E-08 7.91E-08
2.28E-07 5.90E-07 1.39E-06 2.99E-06 6.17E-06 1.15E-05 2.04E-05 3.46E-05
5.60E-05 8.65E-05 1.29E-04 1.86E-04 2.60E-04 3.54E-04 4.67E-04 6.10E-04
7.79E-04 9.68E-04 1.17E-03 1.41E-03 1.69E-03 2.02E-03 2.30E-03 2.62E-03
3.02E-03 3.37E-03 3.76E-03 4.13E-03 4.55E-03 4.95E-03 5.36E-03 5.76E-03
6.16E-03 6.57E-03 6.95E-03 7.33E-03 7.71E-03 8.08E-03 8.40E-03 8.75E-03

9.07E-03 9.38E-03 9.67E-03 9.93E-03 1.02E-02 1.04E-02 1.07E-02 1.09E-02
1.11E-02 1.12E-02 1.14E-02 1.15E-02 1.17E-02 1.18E-02 1.19E-02 1.20E-02
1.20E-02 1.21E-02 1.21E-02 1.22E-02 1.22E-02 1.22E-02 1.22E-02 1.22E-02
1.22E-02 1.22E-02 1.21E-02 1.21E-02 1.20E-02 1.20E-02 1.19E-02 1.18E-02
1.18E-02 1.17E-02 1.16E-02 1.15E-02 1.14E-02 1.13E-02 1.12E-02 1.11E-02
1.09E-02 2.85E-02 1.07E-02 1.05E-02 4.20E-02 1.03E-02 1.01E-02 1.00E-02
9.85E-03 9.70E-03 9.56E-03 9.41E-03 9.24E-03 9.10E-03 8.93E-03 8.76E-03
8.61E-03 8.44E-03 8.29E-03 1.96E-02 7.94E-03 7.77E-03 7.61E-03 1.05E-02
7.18E-03 6.58E-03 6.43E-03 6.28E-03 6.14E-03 5.99E-03 5.84E-03 5.69E-03
5.54E-03 5.38E-03 5.22E-03 5.07E-03 4.91E-03 4.75E-03 4.59E-03 4.42E-03
4.26E-03 4.09E-03 3.93E-03 3.76E-03 3.59E-03 3.42E-03 3.25E-03 3.09E-03
2.92E-03 2.75E-03 2.58E-03 2.41E-03 2.23E-03 2.06E-03 1.89E-03 1.72E-03
1.54E-03 1.37E-03 1.20E-03 1.03E-03 8.56E-04 6.84E-04 5.13E-04 3.41E-04
1.71E-04 1.42E-05

70 kVp (Gendex)

Energy Bins

9.50E-03 1.00E-02 1.05E-02 1.10E-02 1.15E-02 1.20E-02 1.25E-02 1.30E-02
1.35E-02 1.40E-02 1.45E-02 1.50E-02 1.55E-02 1.60E-02 1.65E-02 1.70E-02
1.75E-02 1.80E-02 1.85E-02 1.90E-02 1.95E-02 2.00E-02 2.05E-02 2.10E-02
2.15E-02 2.20E-02 2.25E-02 2.30E-02 2.35E-02 2.40E-02 2.45E-02 2.50E-02
2.55E-02 2.60E-02 2.65E-02 2.70E-02 2.75E-02 2.80E-02 2.85E-02 2.90E-02
2.95E-02 3.00E-02 3.05E-02 3.10E-02 3.15E-02 3.20E-02 3.25E-02 3.30E-02
3.35E-02 3.40E-02 3.45E-02 3.50E-02 3.55E-02 3.60E-02 3.65E-02 3.70E-02
3.75E-02 3.80E-02 3.85E-02 3.90E-02 3.95E-02 4.00E-02 4.05E-02 4.10E-02
4.15E-02 4.20E-02 4.25E-02 4.30E-02 4.35E-02 4.40E-02 4.45E-02 4.50E-02
4.55E-02 4.60E-02 4.65E-02 4.70E-02 4.75E-02 4.80E-02 4.85E-02 4.90E-02
4.95E-02 5.00E-02 5.05E-02 5.10E-02 5.15E-02 5.20E-02 5.25E-02 5.30E-02
5.35E-02 5.40E-02 5.45E-02 5.50E-02 5.55E-02 5.60E-02 5.65E-02 5.70E-02
5.75E-02 5.80E-02 5.85E-02 5.90E-02 5.95E-02 6.00E-02 6.05E-02 6.10E-02
6.15E-02 6.20E-02 6.25E-02 6.30E-02 6.35E-02 6.40E-02 6.45E-02 6.50E-02
6.55E-02 6.60E-02 6.65E-02 6.70E-02 6.75E-02 6.80E-02 6.85E-02 6.90E-02
6.95E-02 7.00E-02

Intensity Distribution Inherent Filtration

0.00E+00 1.42E-09 1.74E-09 1.73E-08 3.19E-07 4.22E-07 1.44E-06 4.80E-06
1.36E-05 3.20E-05 6.89E-05 1.34E-04 2.41E-04 4.04E-04 6.31E-04 9.45E-04
1.34E-03 1.83E-03 2.41E-03 3.08E-03 3.83E-03 4.65E-03 5.50E-03 6.44E-03
7.37E-03 8.35E-03 9.30E-03 1.03E-02 1.11E-02 1.21E-02 1.29E-02 1.37E-02
1.45E-02 1.52E-02 1.58E-02 1.64E-02 1.69E-02 1.74E-02 1.78E-02 1.82E-02
1.84E-02 1.87E-02 1.89E-02 1.90E-02 1.91E-02 1.92E-02 1.92E-02 1.92E-02
1.91E-02 1.90E-02 1.89E-02 1.88E-02 1.86E-02 1.84E-02 1.82E-02 1.79E-02
1.76E-02 1.74E-02 1.71E-02 1.67E-02 1.64E-02 1.61E-02 1.57E-02 1.54E-02
1.50E-02 1.46E-02 1.42E-02 1.38E-02 1.34E-02 1.30E-02 1.26E-02 1.22E-02
1.17E-02 1.13E-02 1.09E-02 1.04E-02 9.99E-03 9.55E-03 9.11E-03 8.68E-03
8.27E-03 7.88E-03 7.52E-03 7.16E-03 6.83E-03 6.49E-03 6.18E-03 5.86E-03
5.57E-03 5.27E-03 4.99E-03 4.71E-03 4.45E-03 4.19E-03 3.94E-03 3.69E-03
3.46E-03 3.24E-03 3.01E-03 2.80E-03 2.61E-03 2.39E-03 2.20E-03 2.01E-03
1.84E-03 1.67E-03 1.51E-03 1.35E-03 1.20E-03 1.06E-03 9.23E-04 7.93E-04

6.76E-04 5.62E-04 4.60E-04 3.67E-04 2.78E-04 1.97E-04 1.33E-04 7.40E-05
3.51E-05 2.92E-06

Intensity Distribution 0.1 mm Cu Filtration

0.00E+00 1.02E-17 1.13E-16 8.33E-15 7.59E-13 4.07E-12 5.10E-11 5.26E-10
3.75E-09 2.04E-08 9.11E-08 3.36E-07 1.07E-06 2.98E-06 7.23E-06 1.62E-05
3.27E-05 6.16E-05 1.09E-04 1.80E-04 2.87E-04 4.30E-04 6.22E-04 8.73E-04
1.18E-03 1.56E-03 1.99E-03 2.51E-03 3.07E-03 3.72E-03 4.39E-03 5.13E-03
5.94E-03 6.75E-03 7.53E-03 8.39E-03 9.28E-03 1.03E-02 1.10E-02 1.18E-02
1.27E-02 1.35E-02 1.43E-02 1.49E-02 1.57E-02 1.63E-02 1.69E-02 1.74E-02
1.79E-02 1.84E-02 1.88E-02 1.91E-02 1.94E-02 1.96E-02 1.98E-02 2.00E-02
2.01E-02 2.01E-02 2.01E-02 2.01E-02 2.00E-02 1.99E-02 1.98E-02 1.96E-02
1.94E-02 1.91E-02 1.89E-02 1.85E-02 1.82E-02 1.78E-02 1.74E-02 1.70E-02
1.66E-02 1.61E-02 1.56E-02 1.51E-02 1.46E-02 1.41E-02 1.35E-02 1.30E-02
1.25E-02 1.20E-02 1.15E-02 1.10E-02 1.05E-02 1.01E-02 9.64E-03 9.20E-03
8.79E-03 8.36E-03 7.95E-03 7.55E-03 7.15E-03 6.76E-03 6.38E-03 6.01E-03
5.65E-03 5.31E-03 4.96E-03 4.62E-03 4.32E-03 3.97E-03 3.67E-03 3.37E-03
3.08E-03 2.80E-03 2.54E-03 2.28E-03 2.03E-03 1.79E-03 1.57E-03 1.35E-03
1.16E-03 9.64E-04 7.92E-04 6.31E-04 4.79E-04 3.41E-04 2.30E-04 1.28E-04
6.11E-05 5.09E-06

Intensity Distribution 0.2 mm Cu Filtration

0.00E+00 6.20E-26 6.18E-24 3.36E-21 1.52E-18 3.30E-17 1.52E-15 4.84E-14
8.66E-13 1.09E-11 1.01E-10 7.09E-10 3.98E-09 1.85E-08 6.96E-08 2.32E-07
6.75E-07 1.75E-06 4.12E-06 8.84E-06 1.81E-05 3.35E-05 5.92E-05 9.94E-05
1.60E-04 2.44E-04 3.60E-04 5.15E-04 7.11E-04 9.62E-04 1.25E-03 1.62E-03
2.05E-03 2.53E-03 3.02E-03 3.61E-03 4.28E-03 5.08E-03 5.74E-03 6.48E-03
7.40E-03 8.17E-03 9.06E-03 9.86E-03 1.08E-02 1.16E-02 1.25E-02 1.33E-02
1.41E-02 1.49E-02 1.56E-02 1.63E-02 1.70E-02 1.76E-02 1.82E-02 1.87E-02
1.92E-02 1.96E-02 2.00E-02 2.03E-02 2.05E-02 2.08E-02 2.09E-02 2.10E-02
2.11E-02 2.11E-02 2.11E-02 2.09E-02 2.08E-02 2.06E-02 2.03E-02 2.00E-02
1.97E-02 1.94E-02 1.89E-02 1.85E-02 1.80E-02 1.75E-02 1.69E-02 1.64E-02
1.58E-02 1.53E-02 1.47E-02 1.42E-02 1.37E-02 1.31E-02 1.27E-02 1.21E-02
1.17E-02 1.11E-02 1.06E-02 1.02E-02 9.67E-03 9.17E-03 8.70E-03 8.22E-03
7.77E-03 7.33E-03 6.87E-03 6.40E-03 6.01E-03 5.55E-03 5.14E-03 4.74E-03
4.35E-03 3.96E-03 3.60E-03 3.24E-03 2.90E-03 2.57E-03 2.25E-03 1.94E-03
1.67E-03 1.39E-03 1.15E-03 9.14E-04 6.96E-04 4.96E-04 3.36E-04 1.88E-04
8.95E-05 7.46E-06

Appendix G

Radiographic Exposure Measurements

	PLANMECA X-RAY UNITS 50 kVp, 8 mA, 0.100 s														
Rm	445	471	449	409	433	435	483	441	481	443	465	451	475	479	1566
SCD	30.5	30.5	30.5	30.5	30.5	30.5	30.5	30.5	30.5	30.5	30.5	30.5	30.5	30.5	30.5
kVp	50.37	50.97	50.58	50.83	50.4	50.39	50.36	49.9	50.75	50.68	50.82	50.37	50.65	50	50.11
HVL (mm Al)	1.72	1.73	1.67	1.69	1.67	1.69	1.68	1.66	1.67	1.71	1.65	1.73	1.69	1.67	1.63
Air Kerma (µGy)	342.4	356.2	365.2	360.6	354.9	339.4	375.7	334.8	347.6	348.7	376.6	319.3	355.0	335.1	355.3
	339.0	357.6	367.1	363.3	352.8	339.6	373.4	325.5	340.1	351.2	376.3	319.4	365.2	334.7	348.1
	342.3	357.3	364.6	358.0	356.9	339.1	375.1	335.9	338.9	353.2	374.2	318.8	363.9	334.5	351.9
	341.2	354.6	363.5	360.2	352.7	341.4	372.2	336.2	337.6	351.1	374.4	319.5	362.6	333.1	357.6
	340.2	358.3	366.3	361.5	353.0	339.0	375.8	336.0	339.0	351.7	375.2	320.4	366.3	332.7	350.4
	339.3	354.9	362.2	356.1	353.3	342.1	374.7	338.1	340.7	350.9	376.9	316.3	364.1	332.1	350.4
	339.3	359.0	364.7	361.9	350.4	342.1	372.9	333.7	340.4	349.3	376.9	318.3	361.9	332.4	359.0
	339.7	357.6	363.3	358.5	354.9	339.7	374.8	336.2	339.2	353.9	376.1	318.3	364.5	334.0	354.5
	341.8	359.7	365.0	362.1	350.0	339.9	374.0	333.0	337.6	351.8	375.7	321.2	363.4	333.3	354.9
	343.3	357.4	364.5	357.6	354.0	341.2	375.2	337.2	339.2	354.3	374.9	318.2	363.4	337.0	355.1
µGy/mAs	426.0	446.6	455.8	450.0	441.6	425.5	468.0	418.3	425.0	439.5	469.7	398.7	453.8	417.4	442.2
Avg (µGy):	340.8	357.3	364.6	360.0	353.3	340.4	374.4	334.7	340.0	351.6	375.7	319.0	363.0	333.9	353.7
σ_E:	1.54	1.65	1.44	2.33	2.06	1.21	1.21	3.54	2.87	1.82	1.01	1.33	3.08	1.49	3.43

	PLANMECA X-RAY UNITS 52 kVp, 8 mA, 0.100 s														
Rm	445	471	449	409	433	435	483	441	481	443	465	451	475	479	1566
SCD	30.5	30.5	30.5	30.5	30.5	30.5	30.5	30.5	30.5	30.5	30.5	30.5	30.5	30.5	30.5
kVp	52.91	53.2	52.81	53.2	52.71	52.65	52.68	52.34	52.71	53.23	52.76	52.78	53.31	51.92	52.08
HVL (mm Al)	1.79	1.78	1.77	1.76	1.76	1.73	1.72	1.76	1.81	1.79	1.77	1.8	1.73	1.76	1.69
Air Kerma (μGy)	375.0	391.3	401.3	395.8	388.9	377.3	414.4	370.4	371.6	388.0	410.0	351.4	402.1	369.1	388.3
	375.4	392.3	402.7	396.7	386.8	374.7	413.2	369.6	371.0	385.4	405.2	350.1	400.6	368.3	386.9
	378.9	390.5	404.9	398.2	387.2	375.4	415.1	367.8	369.7	381.8	407.6	352.0	401.1	367.7	384.6
	373.5	393.1	400.4	396.1	393.1	375.4	413.3	371.2	372.0	387.0	408.2	351.0	396.0	368.1	382.5
	375.1	394.3	404.3	393.7	390.6	375.7	412.5	369.2	371.9	384.3	411.1	351.8	397.2	369.7	388.6
	372.0	391.8	402.2	396.1	388.3	373.8	412.7	369.0	372.5	385.3	407.6	349.7	401.1	367.0	386.0
	373.7	391.6	400.8	393.9	387.5	376.7	414.3	368.2	370.4	386.4	412.4	351.6	401.8	368.5	389.2
	372.0	392.3	401.8	396.5	389.7	374.0	413.4	369.3	369.0	384.4	409.7	353.3	399.6	367.3	391.1
	374.0	392.8	401.5	397.8	390.8	374.6	410.4	367.6	372.5	386.3	412.0	350.1	401.1	367.7	391.2
	374.0	392.3	402.7	394.5	392.3	372.6	413.9	369.7	371.5	385.3	410.4	348.2	398.9	369.0	384.1
μGy/mAs	467.9	490.3	502.8	494.9	486.9	468.8	516.7	461.5	464.0	481.8	511.8	438.6	499.9	460.3	484.1
Avg (μGy):	374.4	392.2	402.3	395.9	389.5	375.0	413.3	369.2	371.2	385.4	409.4	350.9	399.9	368.3	387.3
σ_E:	1.97	1.03	1.45	1.52	2.14	1.38	1.29	1.15	1.20	1.70	2.25	1.44	2.04	0.85	2.96

	PLANMECA X-RAY UNITS 55 kVp, 8 mA, 0.100 s														
Rm	445	471	449	409	433	435	483	441	481	443	465	451	475	479	1566
SCD	30.5	30.5	30.5	30.5	30.5	30.5	30.5	30.5	30.5	30.5	30.5	30.5	30.5	30.5	30.5
kVp	55.66	56.45	55.85	56.27	55.81	55.74	55.14	55.95	55.82	56.45	55.95	55.9	55.97	55.12	55.1
HVL (mm Al)	1.87	1.88	1.86	1.84	1.84	1.81	1.82	1.88	1.88	1.86	1.84	1.9	1.82	1.85	1.77
Air Kerma (µGy)	418.9	445.2	453.8	448.3	440.8	421.4	458.5	410.5	419.3	433.0	463.8	397.6	447.6	416.4	434.7
	424.1	439.5	452.3	449.4	437.9	419.2	468.1	413.5	417.5	430.5	462.4	396.6	448.8	414.5	436.3
	424.8	441.8	453.7	448.9	437.1	423.1	464.7	410.8	418.8	434.8	458.0	397.2	443.9	415.7	434.0
	423.7	443.4	449.2	448.4	437.3	425.7	464.0	411.0	419.9	433.8	462.4	392.1	491.8	414.5	435.3
	423.1	441.1	447.2	443.1	438.4	425.3	470.0	381.9	420.1	432.4	461.0	394.8	453.1	413.9	430.0
	424.6	445.5	453.2	447.4	436.7	420.7	458.8	392.5	417.5	431.7	460.4	397.6	453.1	411.6	436.7
	420.8	441.0	454.0	445.9	436.7	426.8	462.7	410.2	418.8	433.8	460.4	396.8	447.0	414.3	434.9
	420.1	445.3	451.3	451.7	436.3	423.6	465.9	414.7	420.2	431.0	462.8	396.5	449.2	415.9	435.2
	421.7	443.4	451.8	444.7	434.9	426.4	462.2	410.3	420.9	429.7	467.7	396.0	452.8	416.2	430.3
	423.6	441.9	449.9	444.9	437.8	426.7	465.2	418.3	418.9	432.8	459.8	395.2	453.9	416.4	431.2
µGy/mAs	528.2	553.5	564.5	559.1	546.7	529.9	580.0	509.2	524.0	540.4	577.3	495.1	567.7	518.7	542.3
Avg (µGy):	422.5	442.8	451.6	447.3	437.4	423.9	464.0	407.4	419.2	432.3	461.9	396.0	454.1	414.9	433.9
σ_E:	2.05	2.08	2.27	2.60	1.54	2.74	3.64	11.21	1.12	1.61	2.66	1.67	13.64	1.51	2.46

	PLANMECA X-RAY UNITS 57 kVp, 8 mA, 0.100 s														
Rm	445	471	449	409	433	435	483	441	481	443	465	451	475	479	1566
SCD	30.5	30.5	30.5	30.5	30.5	30.5	30.5	30.5	30.5	30.5	30.5	30.5	30.5	30.5	30.5
kVp	58.27	58.72	58	58.58	57.78	57.76	57.69	57.61	58.16	58.49	58.14	57.96	58.33	57.12	57.44
HVL (mm Al)	1.91	1.92	1.89	1.89	1.93	1.9	1.85	1.92	1.92	1.91	1.89	1.96	1.88	1.9	1.83
Air Kerma (µGy)	461.8	483.0	489.5	486.9	471.6	460.5	503.5	443.1	458.3	468.6	498.7	428.2	486.6	448.7	467.9
	458.8	485.4	493.5	486.0	471.4	461.9	506.7	447.0	459.7	471.4	499.0	431.8	491.0	449.9	463.7
	464.2	479.2	490.9	485.8	474.2	460.1	506.8	444.5	460.4	471.9	497.2	430.9	488.5	448.5	469.9
	458.8	482.4	490.9	482.0	476.4	453.8	501.1	443.9	457.9	469.5	503.7	427.7	490.9	447.4	467.9
	460.6	482.5	488.9	485.2	471.7	458.3	504.4	443.8	458.8	470.1	500.1	429.6	486.9	450.5	469.5
	464.5	484.2	490.0	488.9	468.7	454.5	507.0	449.8	457.7	472.9	497.2	429.8	488.6	451.1	465.4
	459.7	482.2	491.9	487.3	470.6	459.6	507.5	450.3	458.2	470.6	501.8	428.4	487.5	452.8	468.5
	460.4	482.6	493.9	486.5	478.1	456.0	503.8	439.3	457.6	474.6	500.5	428.9	488.7	446.9	467.7
	462.5	486.2	490.6	486.4	475.5	456.1	506.6	448.6	457.0	470.9	499.5	429.2	483.1	449.7	468.8
	460.8	486.6	485.9	485.2	476.5	459.0	504.4	441.1	457.7	471.6	502.8	429.6	481.5	448.7	466.6
µGy/mAs	576.5	604.3	613.3	607.5	591.8	572.5	631.5	556.4	572.9	589.0	625.1	536.8	609.2	561.8	584.5
Avg (µGy):	461.2	483.4	490.6	486.0	473.5	458.0	505.2	445.1	458.3	471.2	500.0	429.4	487.3	449.4	467.6
σ_E:	2.00	2.23	2.31	1.79	3.10	2.71	2.07	3.68	1.04	1.72	2.20	1.25	3.04	1.77	1.90

	PLANMECA X-RAY UNITS 60 kVp, 8 mA, 0.100 s														
Rm	445	471	449	409	433	435	483	441	481	443	465	451	475	479	1566
SCD	30.5	30.5	30.5	30.5	30.5	30.5	30.5	30.5	30.5	30.5	30.5	30.5	30.5	30.5	30.5
kVp	61.15	61.36	60.81	60.4	60.88	60.47	60.46	60.69	60.77	61.46	61.28	60.48	60.95	60	60.67
HVL (mm Al)	1.99	2.01	2.07	2.2	1.97	2.02	2.02	2.02	2	1.99	1.96	2.15	1.99	1.99	1.9
Air Kerma (µGy)	538.7	553.7	520.8	498.4	554.3	530.1	519.6	500.3	521.0	554.2	566.3	467.7	538.8	520.1	518.8
	541.1	554.4	524.0	503.7	555.6	533.6	517.7	506.9	534.9	556.5	566.2	472.1	545.7	528.7	514.7
	540.8	553.0	523.9	505.3	558.6	532.7	516.0	505.1	532.1	555.9	568.8	468.0	549.4	528.3	513.3
	534.4	556.3	527.1	504.5	557.1	533.6	518.3	504.0	536.9	558.6	567.5	468.8	545.6	528.3	514.9
	540.8	555.1	524.9	505.8	555.8	538.4	512.6	507.8	534.2	558.9	563.4	470.6	550.1	524.7	514.4
	537.3	548.4	518.4	504.9	556.9	537.2	520.2	503.2	537.7	551.0	565.9	468.4	549.3	528.5	519.0
	538.5	555.1	520.9	501.4	557.4	529.4	518.7	502.9	534.6	554.5	565.8	466.0	549.4	525.8	512.3
	539.0	548.9	522.8	504.1	557.9	536.5	514.4	501.9	537.8	555.0	564.0	468.4	548.8	527.3	520.8
	536.1	551.3	523.9	505.7	557.9	535.1	515.8	502.9	536.2	556.4	564.1	468.9	548.9	529.4	512.0
	540.6	550.4	526.9	504.8	555.8	530.1	523.3	504.8	536.4	556.6	563.7	467.1	548.0	528.0	514.8
µGy/mAs	673.4	690.8	654.2	629.8	695.9	667.1	647.1	630.0	667.7	694.7	707.0	585.7	684.2	658.6	644.4
Avg (µGy):	538.7	552.7	523.4	503.9	556.7	533.6	517.7	504.0	534.2	555.8	565.6	468.6	547.4	526.9	515.5
σ_E:	2.25	2.75	2.74	2.30	1.34	3.16	3.10	2.25	4.94	2.28	1.77	1.73	3.39	2.76	3.01

	PLANMECA X-RAY UNITS 63 kVp, 8 mA, 0.100 s														
Rm	445	471	449	409	433	435	483	441	481	443	465	451	475	479	1566
SCD	30.5	30.5	30.5	30.5	30.5	30.5	30.5	30.5	30.5	30.5	30.5	30.5	30.5	30.5	30.5
kVp	63.97	64.62	63.8	63.57	63.94	63.31	63.1	63.73	63.52	64.57	64.31	63.68	63.87	63.02	63.35
HVL (mm Al)	2.09	2.08	2.15	2.3	2.05	2.11	2.12	2.13	2.1	2.09	2.03	2.22	2.08	2.07	1.99
Air Kerma (μGy)	596.9	608.5	578.5	552.3	614.2	584.2	569.2	558.5	589.7	610.3	626.5	519.4	600.3	582.3	566.3
	598.8	607.5	576.5	555.1	612.6	585.2	574.1	560.8	589.1	610.7	627.8	519.4	604.0	585.6	567.7
	592.9	606.6	577.1	555.1	608.4	586.4	567.3	559.9	589.7	607.5	627.1	522.2	603.1	584.5	559.6
	597.0	602.0	578.9	549.8	613.7	588.8	567.9	558.5	587.1	614.7	629.4	522.1	603.2	583.6	564.0
	592.2	611.6	570.7	549.9	612.2	588.3	568.5	552.2	591.4	614.4	622.8	521.7	604.3	583.7	569.5
	592.7	610.6	577.4	551.6	614.0	584.3	570.9	553.7	587.6	609.3	623.5	515.9	606.8	580.7	567.5
	595.7	610.2	577.3	550.9	611.6	584.3	568.8	555.8	592.2	612.5	621.8	517.1	606.4	586.3	565.8
	593.4	604.3	574.5	551.1	614.5	585.1	571.1	554.4	590.6	614.1	621.9	517.4	599.5	580.3	567.6
	595.5	604.4	578.3	554.4	615.4	585.2	570.1	548.8	586.6	610.4	623.8	514.6	605.0	582.9	562.9
	593.4	604.8	576.1	553.8	611.9	588.0	572.0	550.4	588.6	610.0	623.3	514.8	603.1	584.0	562.1
μGy/mAs	743.5	758.8	720.7	690.5	766.1	732.5	712.5	694.1	736.6	764.2	781.0	648.1	754.5	729.3	706.6
Avg (μGy):	594.8	607.1	576.5	552.4	612.8	586.0	570.0	555.3	589.3	611.4	624.8	518.5	603.6	583.4	565.3
σ_E:	2.25	3.18	2.42	2.05	2.00	1.79	2.08	4.09	1.83	2.42	2.69	2.93	2.32	1.91	3.08

	PLANMECA X-RAY UNITS 66 kVp, 8 mA, 0.100 s														
Rm	445	471	449	409	433	435	483	441	481	443	465	451	475	479	1566
SCD	30.5	30.5	30.5	30.5	30.5	30.5	30.5	30.5	30.5	30.5	30.5	30.5	30.5	30.5	30.5
kVp	67.13	67.44	66.8	66.36	67.14	66.53	66.2	66.79	66.84	67.65	67.46	66.38	67.19	66.25	66.36
HVL (mm Al)	2.17	2.18	2.25	2.41	2.14	2.19	2.22	2.2	2.17	2.17	2.13	2.31	2.16	2.15	2.07
Air Kerma (µGy)	653.6	661.1	628.5	605.2	666.2	642.1	623.1	610.2	645.6	666.1	679.8	563.8	661.7	641.0	614.3
	651.3	660.5	624.4	602.6	664.5	642.0	622.8	606.0	639.0	662.7	681.2	569.7	659.8	640.6	615.7
	654.0	660.4	626.2	603.8	669.9	641.2	619.5	609.3	643.6	669.0	681.0	566.3	660.6	639.3	607.6
	644.9	658.2	630.3	600.5	671.6	641.0	620.3	609.8	641.4	671.0	679.5	567.8	657.7	640.0	615.1
	646.3	663.6	629.4	599.1	667.4	645.0	623.9	609.9	644.5	673.1	678.1	566.3	661.1	635.2	612.1
	647.8	661.9	627.3	598.0	662.4	645.9	619.3	607.5	642.1	663.6	679.6	563.6	661.9	638.5	605.8
	648.9	662.4	630.1	601.1	666.3	645.0	621.4	603.7	642.1	663.2	677.0	566.5	661.5	638.7	617.1
	649.1	664.7	628.4	601.4	666.3	640.8	622.6	605.6	642.0	665.8	676.2	568.4	658.4	636.8	610.9
	652.0	665.1	629.0	599.5	667.1	642.1	623.4	605.5	644.5	666.6	676.8	562.6	659.5	635.7	611.0
	652.9	666.5	625.0	602.1	665.3	639.4	620.0	602.2	642.8	663.2	676.2	564.6	659.9	639.0	610.0
µGy/mAs	812.6	828.0	784.8	751.7	833.4	803.1	777.1	758.7	803.5	833.0	848.2	707.4	825.2	798.1	765.0
Avg (µGy):	650.1	662.4	627.9	601.3	666.7	642.5	621.6	607.0	642.8	666.4	678.5	566.0	660.2	638.5	612.0
σ_E:	3.15	2.55	2.07	2.20	2.60	2.14	1.73	2.80	1.89	3.57	1.92	2.29	1.43	1.99	3.63

	PLANMECA X-RAY UNITS 70 kVp, 8 mA, 0.100 s														
Rm	445	471	449	409	433	435	483	441	481	443	465	451	475	479	1566
SCD	30.5	30.5	30.5	30.5	30.5	30.5	30.5	30.5	30.5	30.5	30.5	30.5	30.5	30.5	30.5
kVp	71.03	71.61	70.49	70.34	70.86	70.35	70.08	70.43	70.81	71.88	71.35	70.34	71.06	69.79	69.85
HVL (mm Al)	2.28	2.28	2.37	2.54	2.26	2.3	2.32	2.33	2.28	2.27	2.24	2.45	2.27	2.26	2.19
Air Kerma (µGy)	721.3	741.5	696.3	671.7	743.4	717.0	691.3	666.3	718.4	742.4	755.2	628.5	735.6	708.0	680.0
	722.8	740.5	695.2	662.3	736.8	717.0	691.7	676.8	716.1	744.1	757.0	626.6	731.6	707.7	670.5
	724.5	737.6	699.2	669.2	740.1	717.7	692.8	671.2	718.2	738.8	755.8	627.7	732.3	711.9	673.5
	729.4	739.8	695.5	663.5	740.9	713.1	689.4	673.2	714.6	741.4	754.0	629.1	733.6	708.8	674.4
	718.9	737.9	697.1	661.7	737.2	716.1	694.7	675.2	714.3	739.2	756.0	629.2	734.7	709.7	674.5
	716.4	736.6	696.4	663.8	740.6	717.5	693.7	673.9	714.1	740.8	752.9	632.6	737.6	705.6	674.4
	723.3	737.1	695.9	666.4	739.0	715.4	688.5	668.6	720.0	739.3	757.9	632.1	729.2	711.2	677.2
	727.2	743.0	699.3	663.8	745.7	720.4	693.6	669.8	714.3	740.5	756.7	625.9	729.8	715.4	675.6
	722.9	734.9	694.8	661.3	737.1	717.2	692.1	673.1	714.2	738.4	752.4	631.1	729.7	709.8	678.5
	718.1	741.2	699.6	662.7	739.9	720.8	692.2	670.1	719.1	739.6	756.8	629.2	730.2	716.5	671.6
µGy/mAs	903.1	923.8	871.2	830.8	925.1	896.5	865.0	839.8	895.4	925.6	944.3	786.5	915.5	888.1	843.8
Avg (µGy):	722.5	739.0	696.9	664.6	740.1	717.2	692.0	671.8	716.3	740.5	755.5	629.2	732.4	710.5	675.0
σ_E:	4.02	2.56	1.81	3.41	2.85	2.24	1.91	3.19	2.34	1.79	1.83	2.21	2.86	3.40	2.95

Average μGy/mAs (Planmeca Units)								
UNIT	**50**	**52**	**55**	**57**	***60***	***63***	***66***	***70***
445	426.0	467.9	528.2	576.5	673.4	743.5	812.6	903.1
471	446.6	490.3	553.5	604.3	690.8	758.8	828.0	923.8
449	455.8	502.8	564.5	613.3	654.2	720.7	784.8	871.2
409	450.0	494.9	559.1	607.5	629.8	690.5	751.7	830.8
433	441.6	486.9	546.7	591.8	695.9	766.1	833.4	925.1
435	425.5	468.8	529.9	572.5	667.1	732.5	803.1	896.5
483	468.0	516.7	580.0	631.5	647.1	712.5	777.1	865.0
441	418.3	461.5	509.2	556.4	630.0	694.1	758.7	839.8
481	425.0	464.0	524.0	572.9	667.7	736.6	803.5	895.4
443	439.5	481.8	540.4	589.0	694.7	764.2	833.0	925.6
465	469.7	511.8	577.3	625.1	707.0	781.0	848.2	944.3
451	398.7	438.6	495.1	536.8	585.7	648.1	707.4	786.5
475	453.8	499.9	567.7	609.2	684.2	754.5	825.2	915.5
479	417.4	460.3	518.7	561.8	658.6	729.3	798.1	888.1
1566	442.2	484.1	542.3	584.5	644.4	706.6	765.0	843.8
Average:	438.5	482.0	542.4	588.9	662.0	729.3	795.3	883.6
σ:	19.9	21.7	25.1	26.6	31.9	35.1	38.2	43.7
Detector Uncertainty (+/-) :	21.9	24.1	27.1	29.4	33.1	36.5	39.8	44.2
Total Uncertainty (+/-):	29.6	32.4	36.9	39.7	46.0	50.6	55.1	62.1
avg %σ:	6.8%	6.7%	6.8%	6.7%	6.9%	6.9%	6.9%	7.0%

	GENDEX X-RAY UNITS 70 kVp, 7 mA, 6 pulses							
Rm	377	457	378	458	379	425	427	431
SCD	20.5	20.5	20.5	20.5	20.5	20.5	20.5	20.5
kVp	72.44	71.75	69.72	72.3	72.77	74.85	73.65	71.82
HVL (mm Al)	2.01	2.23	2.31	2.05	2.06	2.34	2.26	2.5
Air Kerma (µGy)	842.8	687.1	718.5	868.0	802.3	634.9	847.9	697.0
	845.2	691.4	749.6	870.5	845.7	637.8	852.1	698.8
	851.0	690.8	745.3	869.9	847.9	644.1	851.5	697.1
	847.7	691.7	748.4	869.6	850.5	645.1	852.9	701.0
	847.7	688.0	747.1	871.9	852.0	647.3	850.4	698.7
	848.8	689.3	747.8	866.1	845.7	650.1	854.1	699.0
	848.7	692.0	749.7	871.3	851.3	647.9	852.9	698.5
	846.2	690.4	748.4	870.8	850.7	650.5	850.8	699.9
	847.4	692.2	748.8	873.6	848.8	649.9	853.7	698.6
	846.4	689.8	750.2	871.7	854.0	651.5	852.8	698.2
µGy/mAs	1376.8	1121.9	1211.4	1414.5	1373.1	1049.8	1384.5	1135.5
Avg (µGy):	847.2	690.3	745.4	870.3	844.9	645.9	851.9	698.7
σ_E:	2.2	1.7	9.5	2.1	15.2	5.6	1.8	1.2

Average μGy/mAs (Gendex)

UNIT	***70*** *Gendex*
377	1376.8
457	1121.9
378	1211.4
458	1414.5
379	1373.1
425	1049.8
427	1384.5
431	1135.5
Average:	1258.4
σ:	144.9
Detector Uncertainty (+/-) :	62.92
Total Uncertainty:	158.0
avg %σ:	13%

Appendix H

Carestream Sensor Response Data: Planmeca Units

kVp	Air Kerma (μGy)	Mean PV (100x100 pixel ROI ctr of image)	σ (100x100 pixel ROI ctr of image)	SNR
50	6.1	113.9	5.5	20.6
50	12.3	178.6	6.1	29.1
50	24.5	261.2	6.7	38.9
50	48.5	582.9	9.1	64.0
50	156.0	1694.0	14.1	120.3
50	9.41	59.5	6.0	10.0
50	19.05	213.4	7.0	30.6
50	38.21	511.1	8.7	58.8
50	75.47	864.3	10.6	81.7
50	153.20	1826.3	13.8	131.9
50	9.06	71.5	4.8	15.0
50	18.11	170.7	5.7	30.1
50	35.99	367.4	7.2	50.9
50	71.71	786.9	9.4	83.7
50	113.00	1310.7	12.5	105.0
50	144.64	1628.8	13.4	122.0
50	146.40	1615.0	15.7	103.2
50	73.3	883.8	11.4	77.6
50	36.67	475.7	9.2	51.6
50	18.1	255.5	7.4	34.4
50	9.04	147.9	6.6	22.4
50	192.7	1936.8	14.0	138.2
50	96.28	1041.9	11.3	92.3
50	47.4	512.4	8.9	57.3
50	23.68	267.1	8.1	33.2
50	12.0	146.8	7.2	20.4
55	9.0	103.2	5.5	18.7
55	18.3	276.5	6.9	40.2
55	36.1	505.3	8.5	59.2
55	73.7	872.8	10.8	80.9
55	235.4	2817.6	18.5	152.3
55	14.12	196.4	7.1	27.6
55	28.93	357.1	7.8	45.5
55	57.51	839.6	10.4	80.4
55	115.20	1597.4	13.3	120.3
55	230.00	3023.2	18.3	164.9
55	13.71	103.6	5.2	20.1

55	27.42	402.9	7.2	55.6
55	53.91	766.4	9.6	80.2
55	109.20	1343.0	12.2	109.8
55	171.10	2178.2	14.9	146.2
55	220.70	2775.7	21.6	128.4
55	110.2	1466.1	14.7	99.9
55	54.86	719.3	10.5	68.3
55	27.5	408.1	8.9	45.9
55	13.55	225.9	7.3	31.0
55	225.20	2525.2	17.4	145.0
55	113.7	1384.0	12.4	112.0
55	56.00	739.2	10.2	72.8
55	29.0	406.2	8.6	47.4
55	14.78	206.5	7.9	26.1
60	7.9	65.9	5.1	12.9
60	15.7	154.0	6.0	25.8
60	31.8	404.7	8.0	50.5
60	63.4	456.1	8.4	54.1
60	202.7	2681.2	18.5	145.1
60	20.13	333.3	7.8	43.0
60	40.29	662.3	9.6	69.1
60	80.97	1221.4	12.6	96.6
60	162.50	2375.0	16.1	148.0
60	19.12	174.2	6.0	29.1
60	38.37	603.2	9.1	66.0
60	76.17	1032.7	10.9	94.4
60	152.90	2015.9	15.3	131.6
60	240.20	3208.7	18.1	177.7
60	242.9	3192.3	22.5	141.6
60	120.60	1690.9	16.2	104.2
60	59.9	803.1	11.4	70.7
60	30.65	485.8	9.4	51.9
60	14.9	267.0	7.5	35.5
60	258.0	3152.4	17.7	178.2
60	126.80	1695.3	13.9	122.1
60	63.4	884.8	10.6	83.6
60	31.97	463.0	8.9	52.0
60	16.1	258.5	7.9	32.9
66	4.7	80.2	5.5	14.6
66	11.3	208.5	6.4	32.4
66	22.4	361.6	7.8	46.3
66	43.8	694.2	10.4	66.5
66	87.8	1250.5	12.8	97.5
66	221.4	3078.7	19.6	157.0
66	8.24	179.7	7.1	25.4

66	17.10	207.9	7.1	25.4
66	34.21	321.3	7.8	97.0
66	69.19	1124.1	11.6	97.0
66	139.30	2015.3	15.2	132.2
66	218.00	3130.5	19.1	163.5
66	8.21	141.1	5.8	24.4
66	16.61	169.1	5.8	29.3
66	33.38	565.2	8.8	64.5
66	67.85	1088.7	11.5	94.3
66	134.70	2054.1	15.5	132.3
66	212.80	3061.7	18.1	168.9
66	217.00	3107.1	22.5	138.2
66	107.5	1564.2	16.0	97.9
66	53.68	855.1	11.7	73.2
66	26.3	294.5	8.0	36.8
66	15.59	129.5	7.0	18.5
66	177.0	2445.1	16.9	144.6
66	89.00	1079.3	12.1	89.5
66	45.0	682.3	10.3	66.5
66	23.04	371.2	8.5	43.9
70	5.9	112.2	5.8	19.3
70	13.5	243.8	6.9	35.5
70	26.3	439.9	8.6	51.0
70	53.1	849.1	11.0	77.3
70	106.3	1618.1	14.8	109.1
70	267.3	3677.6	20.7	177.7
70	20.56	239.3	7.4	32.3
70	41.80	715.4	9.8	72.8
70	83.91	1362.9	13.7	99.3
70	167.94	2566.7	17.4	147.9
70	263.26	3771.4	19.2	196.3
70	10.39	202.8	5.9	34.3
70	20.33	370.8	7.2	51.7
70	40.55	699.7	9.4	74.1
70	81.3	1334.7	12.9	103.3
70	163.3	2517.7	17.1	147.2
70	255.7	3607.7	19.9	181.4
70	204.10	2992.4	21.7	137.9
70	101.3	1596.6	15.5	102.7
70	51.80	692.9	11.4	60.6
70	25.0	438.3	9.09	48.2
70	217.80	2962.6	18.6	159.5
70	108.1	1568.0	13.9	113.1
70	54.8	826.5	11.3	73.3

Appendix I

Carestream Sensor Response Data: Gendex Units (70 kVp Only)

Air Kerma (μGy)	Mean PV (100x100 pixel ROI ctr of image)	σ (100x100 pixel ROI ctr of image)	SNR
36.5	480.5	9.0	53.4
56.5	661.8	9.7	68.1
58.9	841.4	11.3	74.2
67.9	833.3	11.2	74.2
68.7	866.9	10.9	79.7
78.4	807.4	11.0	73.1
113.4	1571.2	14.1	111.4
120.7	1725.9	14.9	115.7
125.3	1640.6	15.1	108.4
128.4	1678.0	14.0	120.1
146.1	1862.9	15.9	116.9
158.8	2120.3	17.9	118.4
171.3	2125.2	17.5	121.5
172.1	2390.7	18.3	130.9
176.7	2292.5	15.6	147.0
200.1	2552.0	18.2	140.5
227.2	3025.1	18.6	162.2
235.0	3072.9	20.2	152.2
249.6	3178.0	17.0	187.1
250.1	3572.1	20.8	171.7
280.0	3557.1	19.7	180.1

Appendix J

ScanX® Sensor Response Data: Planmeca Unit

kVp	Air Kerma (μGy)	Mean PV (100x100 pixel ROI ctr of image)	σ (100x100 pixel ROI ctr of image)	SNR
50	1412.9	2224.4	40.6	54.9
50	536.2	1021.0	23.7	43.1
50	203.5	534.9	15.5	34.5
50	77.2	297.1	11.7	25.3
50	29.3	168.3	10.0	16.9
50	1412.9	2199.1	93.2	23.6
50	536.2	1037.1	29.3	35.4
50	203.5	541.1	15.7	34.4
50	77.2	302.8	11.9	25.5
50	29.3	171.7	9.9	17.4
50	1412.9	2184.6	41.0	53.3
50	536.2	1030.7	21.7	47.6
50	203.5	547.0	15.1	36.3
50	77.2	306.1	11.5	26.5
50	29.3	173.6	9.8	17.8
50	1412.9	2171.3	47.8	45.4
50	536.2	1012.0	22.3	45.4
50	203.5	533.1	15.3	34.9
50	77.2	297.0	11.6	25.6
50	29.3	170.1	9.7	17.5
50	1412.9	2265.7	45.9	49.4
50	536.2	1034.3	23.8	43.6
50	203.5	533.4	16.3	32.6
50	77.2	296.1	12.0	24.8
50	29.3	169.5	8.8	19.3
60	1512.0	2983.6	47.6	62.7
60	661.0	1584.6	30.7	51.6
60	289.0	953.0	22.3	42.7
60	126.0	599.8	17.8	33.7
60	55.0	381.9	17.2	22.2
60	1512.0	3015.4	48.5	62.2
60	661.0	1645.5	31.5	52.3
60	289.0	992.8	22.7	43.8
60	126.0	618.2	18.5	19.8
60	55.0	383.8	19.3	19.8

60	1512.0	3033.4	32.0	94.7
60	661.0	1686.9	29.3	57.6
60	289.0	1023.5	21.7	47.1
60	126.0	643.9	18.2	35.3
60	55.0	401.6	18.2	22.1
60	1512.0	2855.3	70.3	40.6
60	661.0	1593.1	29.8	53.5
60	289.0	963.2	21.5	44.8
60	126.0	611.2	17.6	34.8
60	55.0	383.9	15.7	24.4
60	1512.0	3023.9	38.8	78.0
60	661.0	1609.6	35.1	45.8
60	289.0	968.3	23.2	41.7
60	126.0	610.1	18.1	33.8
60	55.0	384.6	18.6	20.7
70	1355.4	3018.8	36.5	82.8
70	654.1	1750.3	32.1	54.6
70	315.7	1126.7	24.2	46.5
70	152.4	762.5	21.2	36.0
70	73.5	515.5	24.8	20.8
70	1355.4	2967.3	68.4	43.4
70	654.1	1781.4	36.2	49.3
70	315.7	1161.8	26.2	44.3
70	152.4	788.7	20.8	26.5
70	73.5	534.0	20.1	26.5
70	1355.4	3020.2	38.2	79.1
70	654.1	1863.1	31.6	59.0
70	315.7	1205.7	24.7	48.8
70	152.4	805.1	20.0	40.2
70	73.5	532.4	22.4	23.8
70	1355.4	2894.8	55.2	52.5
70	654.1	1749.8	32.2	54.4
70	315.7	1128.2	24.4	46.3
70	152.4	759.9	20.4	37.2
70	73.5	506.0	22.1	22.9
70	654.1	1827.1	36.2	50.4
70	315.7	1165.7	27.6	42.2
70	152.4	778.3	22.3	34.8
70	73.5	523.1	25.6	20.5

Appendix K

Contrast Analysis Data: McDavid Contrast Detail Phantom

CARESTREAM/PLANMECA SdNR												
Position	**Unit 1**	**Unit 2**	**Unit 3**	**Unit 4**	**Unit 5**	**Unit 6**	**Unit 7**	**Unit 8**	**Unit 9**	**Unit 10**	**Mean SdNR**	**σ**
R1,C2	2.9	2.7	3.2	1.7	2.9	2.5	3.2	1.9	2.1	3.5	2.7	0.6
R1,C3	3.4	2.6	4.3	3.5	3.1	3.8	3.5	3.8	3.1	3.5	3.5	0.5
R2,C2	6.1	4.5	5.6	5.0	5.1	4.7	4.9	4.6	5.5	5.2	5.1	0.5
R2,C3	1.2	0.3	1.1	0.7	0.5	1.0	1.3	0.4	0.6	0.6	0.8	0.4
R2,C4	4.0	2.8	4.2	3.4	3.3	3.2	4.6	2.8	2.9	4.1	3.5	0.6
R3,C1	3.5	3.0	3.8	2.9	2.5	4.0	3.8	3.3	3.3	3.9	3.4	0.5
R3,C3	6.3	4.9	6.1	5.4	5.5	5.5	6.0	5.1	5.1	6.2	5.6	0.5
R4,C1	2.4	1.6	1.9	1.9	1.1	2.1	2.0	1.6	2.4	2.4	1.9	0.4
R4,C2	2.5	1.5	1.4	1.5	0.6	1.6	1.4	1.0	1.8	1.8	1.5	0.5
R4,C4	1.2	0.2	1.1	1.1	0.4	1.4	0.7	0.7	0.8	1.5	0.9	0.4

CARESTREAM/GENDEX SdNR										
Position	**Unit 11**	**Unit 12**	**Unit 13**	**Unit 14**	**Unit 15**	**Unit 16**	**Unit 17**	**Unit 18**	**Mean SdNR**	**σ**
R1,C2	1.2	2.1	1.7	2.1	2.0	1.9	2.1	1.5	1.8	0.3
R1,C3	2.2	3.5	2.8	2.1	3.3	3.3	2.7	3.2	2.9	0.5
R2,C2	4.3	4.5	4.1	3.5	4.5	4.2	4.2	4.6	4.2	0.3
R2,C3	0.0	0.8	0.7	0.2	0.3	0.2	0.6	0.4	0.4	0.3
R2,C4	1.9	2.9	2.2	2.0	2.0	2.3	2.5	2.3	2.2	0.3
R3,C1	2.2	5.0	2.4	2.0	4.8	4.7	2.0	2.7	3.2	1.3
R3,C3	4.2	5.0	4.2	4.0	4.4	4.5	4.6	5.0	4.5	0.4
R4,C1	1.1	1.7	2.9	0.9	1.7	1.5	0.9	1.3	1.5	0.7
R4,C2	1.4	1.6	1.1	0.6	1.0	1.2	1.3	1.5	1.2	0.3
R4,C4	0.7	0.5	0.9	0.0	0.7	0.2	0.7	0.9	0.6	0.3

Appendix L

Sample Input Deck (Anthropomorphic Phantom; 50 kVp)

```
c Cell Cards
1  0          -1  20  30       imp:p 1 imp:e 1  $macrobody around geometry
2  0           1               imp:p 0 imp:e 0  $outside world
3  2 -0.001294  -3             imp:p 1 imp:e 1  $rpp in center of phantom
20 1 -2.92    -20  3  40       imp:p 1 imp:e 1  $enamel phantom
30 3 -1.00    -30              imp:p 1 imp:e 1  $ICRU TISSUE phantom
40 4 -2.19    -40              imp:p 1 imp:e 1  $dentin phantom

c Surface Cards
1  rcc 0 0 -4.5 0 0 36  3.4                  $macrobody around geometry
3  rpp -0.10 0.10 -0.10 0.10 -2.23 -2.20     $2 mm diam 0.3 mm depth
20 rcc  0 0 -3.18 0 0 0.98 2.0               $enamel 1.25 mm thick
30 rcc 0 0 -2.2 0 0 2.2 2.0                  $30x40x22 mm TISSUE
40 rcc 0 0 -3.055 0 0 0.73 1.875             $dentin 7.3 mm thick
50 cz 2.0                                    $cylinder x0,y0
51 pz 0                                      $cylinder base
61 pz -3.18                                  $cylinder base

c Data Cards
m1 6012 -0.212029  8016 -0.266345 11023 -0.004922  12024 -0.00272  $enamel
     15031 -0.163686  17035 -0.004312  20040 -0.345986
m2 7014 -0.7547  8016 -0.2320  18040 -0.0133                       $air
m3 1001 -0.101174 6012 -0.111000 7014 -0.026000 8016 -0.761826     $ICRU tissue
m4 6012 -0.3705 8016 -0.2886 11023 -0.0057 12024 -0.0049           $dentin
     15031 -0.1139 20040 -0.2164
sdef par=p erg=d1  pos=0 0 30 vec=0 0 -1 dir=d2                    $50kVp
si1 h 9.50E-03 1.00E-02 1.05E-02 1.10E-02 1.15E-02 1.20E-02 1.25E-02 1.30E-02
     1.35E-02 1.40E-02 1.45E-02 1.50E-02 1.55E-02 1.60E-02 1.65E-02 1.70E-02
     1.75E-02 1.80E-02 1.85E-02 1.90E-02 1.95E-02 2.00E-02 2.05E-02 2.10E-02
     2.15E-02 2.20E-02 2.25E-02 2.30E-02 2.35E-02 2.40E-02 2.45E-02 2.50E-02
     2.55E-02 2.60E-02 2.65E-02 2.70E-02 2.75E-02 2.80E-02 2.85E-02 2.90E-02
     2.95E-02 3.00E-02 3.05E-02 3.10E-02 3.15E-02 3.20E-02 3.25E-02 3.30E-02
     3.35E-02 3.40E-02 3.45E-02 3.50E-02 3.55E-02 3.60E-02 3.65E-02 3.70E-02
     3.75E-02 3.80E-02 3.85E-02 3.90E-02 3.95E-02 4.00E-02 4.05E-02 4.10E-02
     4.15E-02 4.20E-02 4.25E-02 4.30E-02 4.35E-02 4.40E-02 4.45E-02 4.50E-02
     4.55E-02 4.60E-02 4.65E-02 4.70E-02 4.75E-02 4.80E-02 4.85E-02 4.90E-02
     4.95E-02 5.00E-02
sp1 d 0.00E+00 4.51E-08 4.38E-08 3.03E-07 3.88E-06 4.27E-06 1.18E-05 3.25E-05
     7.78E-05 1.59E-04 3.01E-04 5.23E-04 8.47E-04 1.30E-03 1.87E-03 2.60E-03
     3.44E-03 4.42E-03 5.52E-03 6.70E-03 7.97E-03 9.27E-03 1.06E-02 1.19E-02
     1.32E-02 1.45E-02 1.58E-02 1.70E-02 1.80E-02 1.91E-02 1.99E-02 2.07E-02
     2.15E-02 2.21E-02 2.27E-02 2.32E-02 2.35E-02 2.39E-02 2.41E-02 2.43E-02
```

```
     2.43E-02 2.43E-02 2.43E-02 2.41E-02 2.40E-02 2.37E-02 2.35E-02 2.31E-02
     2.28E-02 2.23E-02 2.19E-02 2.14E-02 2.09E-02 2.04E-02 1.98E-02 1.92E-02
     1.86E-02 1.80E-02 1.73E-02 1.67E-02 1.60E-02 1.53E-02 1.46E-02 1.38E-02
     1.31E-02 1.24E-02 1.16E-02 1.09E-02 1.01E-02 9.33E-03 8.56E-03 7.78E-03
     7.00E-03 6.22E-03 5.44E-03 4.66E-03 3.88E-03 3.09E-03 2.32E-03 1.54E-03
     7.69E-04 6.41E-05
si2 -1 0.9975 1                $histogram for cosine bin limits r=2 cm
sp2 0 0.99875 0.00125          $fract solid angle for each bin
sb2 0 0 1                      $source bias for each bin
mode p e
phys:e
f2:p 51                                                        $10 keV to 50 keV
e2  1.00E-02 1.05E-02 1.10E-02 1.15E-02 1.20E-02 1.25E-02 1.30E-02 1.35E-02
     1.40E-02 1.45E-02 1.50E-02 1.55E-02 1.60E-02 1.65E-02 1.70E-02 1.75E-02
     1.80E-02 1.85E-02 1.90E-02 1.95E-02 2.00E-02 2.05E-02 2.10E-02 2.15E-02
     2.20E-02 2.25E-02 2.30E-02 2.35E-02 2.40E-02 2.45E-02 2.50E-02 2.55E-02
     2.60E-02 2.65E-02 2.70E-02 2.75E-02 2.80E-02 2.85E-02 2.90E-02 2.95E-02
     3.00E-02 3.05E-02 3.10E-02 3.15E-02 3.20E-02 3.25E-02 3.30E-02 3.35E-02
     3.40E-02 3.45E-02 3.50E-02 3.55E-02 3.60E-02 3.65E-02 3.70E-02 3.75E-02
     3.80E-02 3.85E-02 3.90E-02 3.95E-02 4.00E-02 4.05E-02 4.10E-02 4.15E-02
     4.20E-02 4.25E-02 4.30E-02 4.35E-02 4.40E-02 4.45E-02 4.50E-02 4.55E-02
     4.60E-02 4.65E-02 4.70E-02 4.75E-02 4.80E-02 4.85E-02 4.90E-02 4.95E-02
     5.00E-02
fs2 -50
sd2  12.56637  1    $ first number is pi*(radius of surface 50 cylinder)^2
f22:p 61                                                       $15 keV to 50 keV
e22   1.50E-02 1.55E-02 1.60E-02 1.65E-02 1.70E-02 1.75E-02 1.80E-02 1.85E-02
     1.90E-02 1.95E-02 2.00E-02 2.05E-02 2.10E-02 2.15E-02 2.20E-02 2.25E-02
     2.30E-02 2.35E-02 2.40E-02 2.45E-02 2.50E-02 2.55E-02 2.60E-02 2.65E-02
     2.70E-02 2.75E-02 2.80E-02 2.85E-02 2.90E-02 2.95E-02 3.00E-02 3.05E-02
     3.10E-02 3.15E-02 3.20E-02 3.25E-02 3.30E-02 3.35E-02 3.40E-02 3.45E-02
     3.50E-02 3.55E-02 3.60E-02 3.65E-02 3.70E-02 3.75E-02 3.80E-02 3.85E-02
     3.90E-02 3.95E-02 4.00E-02 4.05E-02 4.10E-02 4.15E-02 4.20E-02 4.25E-02
     4.30E-02 4.35E-02 4.40E-02 4.45E-02 4.50E-02 4.55E-02 4.60E-02 4.65E-02
     4.70E-02 4.75E-02 4.80E-02 4.85E-02 4.90E-02 4.95E-02 5.00E-02
fs22 -50
sd22 12.56637  1               $ first number is pi*(radius of surface 50 cylinder)^2
TIR5:p 0 0 -3.5 0  0 0 1  0 0.5 0     $Transmitted Image Projection Tally
FS5 -0.5 9i 0.5                $segments parallel to y axis
C5 -0.5 9i 0.5                 $cosine bins parallel to x-axis
f6:P 30
nps 100000000
Print
prdmp 2J 1
```

Appendix M

MCNPX OUTPUT DATA FOR OPTIMIZATION

Unfiltered Spectra

	50	52	55	57	60	63	66	70
NPS	1.40E+13	1.32E+13	1.20E+13	1.14E+13	1.05E+13	1.00E+13	9.65E+12	9.05E+12
Entrance Dose (μGy)	1235	1129	971	897	786	723	672	606
mAs	2.78	2.34	1.79	1.54	1.21	1.00	0.85	0.67
Skin Dose (μGy) (per source particle)	5.18E-11	5.06E-11	4.88E-11	4.77E-11	4.62E-11	4.51E-11	4.39E-11	4.27E-11
Skin Dose (μGy)	725	667	585	544	485	451	424	387
Energy Deposited (mJ/cm^2)	7.00	6.75	6.37	6.18	5.89	5.83	5.73	5.57
Well photons/cm^2 (per source particle)	4.83E-06	5.53E-06	6.57E-06	7.28E-06	8.34E-06	9.11E-06	1.03E-05	1.15E-05
Well K_{air} (μGy)	34	35	36	36	37	38	39	40
Bckgrnd photons/cm^2 (per source particle)	4.52E-06	5.20E-06	6.20E-06	6.89E-06	7.92E-06	8.87E-06	9.83E-06	1.10E-05
Bckgrnd K_{air} (μGy)	32	33	34	35	35	36	38	38
Rad Contrast	0.068	0.064	0.059	0.057	0.052	0.049	0.046	0.043

	75	80	85	90	70(G)
NPS	8.35E+12	7.70E+12	7.10E+12	6.65E+12	1.29E+13
Entrance Dose (μGy)	522	459	405	366	907
mAs	0.50	0.39	0.30	0.24	0.72
Skin Dose (μGy) (per source particle)	4.09E-11	3.96E-11	3.85E-11	3.76E-11	4.46E-11
Skin Dose (μGy)	341	305	273	250	573
Energy Deposited (mJ/cm^2)	5.41	5.20	4.99	4.84	7.48
Well photons/cm^2 (per source particle)	1.33E-05	1.49E-05	1.63E-05	1.76E-05	9.44E-06
Well K_{air} (μGy)	41	41	41	41	50
Bckgrnd photons/cm^2 (per source particle)	1.28E-05	1.43E-05	1.57E-05	1.70E-05	9.00E-06
Bckgrnd K_{air} (μGy)	39	40	39	39	47
Rad Contrast	0.039	0.037	0.035	0.033	0.049

0.1 mm Cu Filtration

	50	52	55	57	60	63	66	70
NPS	1.07E+13	1.03E+13	9.70E+12	9.30E+12	8.70E+12	8.38E+12	8.05E+12	7.75E+12
Entrance Dose (μGy)	716	667	593	552	492	458	424	392
mAs	5.20	4.39	3.40	2.78	2.06	1.66	1.34	1.05
Skin Dose (μGy) (per source particle)	4.40E-11	4.29E-11	4.12E-11	4.03E-11	3.90E-11	3.80E-11	3.70E-11	3.61E-11
Skin Dose (μGy)	470	441	400	375	339	318	298	279
Energy Deposited (mJ/cm^2)	5.99	5.90	5.77	5.65	5.47	5.42	5.37	5.35
Well photons/cm^2 (per source particle)	7.31E-06	8.22E-06	9.59E-06	1.05E-05	1.18E-05	1.30E-05	1.42E-05	1.56E-05
Well K_{air} (μGy)	37	39	41	41	42	43	43	45
Bckgrnd photons/cm^2 (per source particle)	6.87E-06	7.76E-06	9.10E-06	9.96E-06	1.12E-05	1.24E-05	1.36E-05	1.50E-05
Bckgrnd K_{air} (μGy)	35	37	38	39	40	41	42	43
Transmission	0.31	0.32	0.32	0.34	0.37	0.38	0.40	0.42
Rad Contrast	0.063	0.060	0.054	0.052	0.049	0.046	0.043	0.040

	75	80	85	90	70(G)
NPS	7.20E+12	6.90E+12	6.50E+12	6.00E+12	1.10E+13
Entrance Dose (μGy)	346	318	290	260	599
mAs	0.65	0.50	0.39	0.30	1.18
Skin Dose (μGy) (per source particle)	3.48E-11	3.39E-11	3.31E-11	3.26E-11	3.80E-11
Skin Dose (μGy)	251	234	215	196	418
Energy Deposited (mJ/cm^2)	5.21	5.20	5.09	4.85	7.16
Well photons/cm^2 (per source particle)	1.75E-05	1.92E-05	2.07E-05	2.20E-05	1.31E-05
Well K_{air} (μGy)	45	46	46	44	56
Bckgrnd photons/cm^2 (per source particle)	1.69E-05	1.86E-05	2.01E-05	2.14E-05	1.25E-05
Bckgrnd K_{air} (μGy)	43	45	44	43	54
Transmission	0.51	0.53	0.55	0.57	0.40
Rad Contrast	0.037	0.034	0.032	0.031	0.044

0.2 mm Cu Filtration

	50	52	55	57	60	63	66	70
NPS	9.71E+12	9.36E+12	8.83E+12	8.62E+12	8.31E+12	8.06E+12	7.80E+12	7.44E+12
Entrance Dose (μGy)	565	527	469	445	409	383	358	329
mAs	8.89	7.28	5.40	4.37	3.23	2.54	2.02	1.53
Skin Dose (μGy) (per source particle)	4.02E-11	3.92E-11	3.76E-11	3.68E-11	3.56E-11	3.48E-11	3.39E-11	3.30E-11
Skin Dose (μGy)	390.8	366.8	332.2	317.6	296.1	280.1	264.4	245.8
Energy Deposited (mJ/cm^2)	5.76	5.69	5.58	5.57	5.55	5.54	5.53	5.47
Well photons/cm^2 (per source particle)	9.07E-06	1.01E-05	1.17E-05	1.27E-05	1.42E-05	1.55E-05	1.68E-05	1.83E-05
Well K_{air} (μGy)	40.7	41.9	43.5	44.6	46.1	47.1	48.2	48.7
Bckgrnd photons/cm^2 (per source particle)	8.56E-06	9.59E-06	1.11E-05	1.21E-05	1.35E-05	1.48E-05	1.61E-05	1.77E-05
Bckgrnd K_{air} (μGy)	38.5	39.6	41.4	42.5	44.1	45.2	46.3	46.9
Transmission	0.143	0.150	0.160	0.174	0.195	0.209	0.223	0.240
Rad Contrast	0.060	0.056	0.051	0.049	0.045	0.042	0.039	0.037

	75	80	85	90	70(G)
NPS	7.09E+12	6.77E+12	6.20E+12	5.86E+12	1.03E+13
Entrance Dose (μGy)	299	276	246	227	487
mAs	0.91	0.68	0.50	0.39	1.64
Skin Dose (μGy) (per source particle)	3.20E-11	3.13E-11	3.08E-11	3.04E-11	3.48E-11
Skin Dose (μGy)	227.1	212.0	190.9	178.2	356.6
Energy Deposited (mJ/cm^2)	5.46	5.43	5.15	5.03	7.11
Well photons/cm^2 (per source particle)	2.03E-05	2.21E-05	2.36E-05	2.49E-05	1.57E-05
Well K_{air} (μGy)	49.8	50.5	48.6	48.0	60.5
Bckgrnd photons/cm^2 (per source particle)	1.97E-05	2.14E-05	2.29E-05	2.41E-05	1.50E-05
Bckgrnd K_{air} (μGy)	48.2	48.9	47.2	46.6	58.1
Transmission	0.316	0.340	0.362	0.384	0.235
Rad Contrast	0.034	0.032	0.031	0.029	0.042

Appendix N

SdNR and FOM Calculations

kVp	Filter	Well Signal	Well Noise	Bkgrd Signal	Bkgrd Noise	SdNR	$x10^3$ FOM_S	FOM_C	FOM_{en}	FOM_f
50	Inherent	387.4	8.5	363.3	8.4	2.0	5.52	0.07	0.57	0.28
	Inherent +0.1mm Cu	427	8.7	402.1	8.6	2.0	8.50	0.06	0.67	0.23
	Inherent +0.2mm Cu	463.4	8.9	438	8.7	2.0	10.23	0.06	0.69	0.16
52	Inherent	412.2	8.5	387.9	8.4	2.0	5.99	0.06	0.59	0.35
	Inherent +0.1mm Cu	458.1	8.8	432.9	8.6	2.0	9.06	0.06	0.68	0.28
	Inherent +0.2mm Cu	494.3	8.9	468.7	8.8	2.0	10.90	0.06	0.70	0.20
55	Inherent	450.8	8.6	426.1	8.5	2.0	6.84	0.06	0.63	0.49
	Inherent +0.1mm Cu	506.6	8.9	481.1	8.7	2.0	10.01	0.05	0.69	0.38
	Inherent +0.2mm Cu	542.4	9	516.6	8.9	2.0	12.04	0.05	0.72	0.29
57	Inherent	472.5	8.6	447.8	8.5	2.0	7.35	0.06	0.65	0.60
	Inherent +0.1mm Cu	529.9	8.9	504.3	8.8	2.0	10.67	0.05	0.71	0.48
	Inherent +0.2mm Cu	574.8	9.1	548.6	9	2.0	12.60	0.05	0.72	0.36
60	Inherent	505.7	8.7	481.2	8.6	2.0	8.24	0.05	0.68	0.81
	Inherent +0.1mm Cu	565.4	8.9	539.8	8.8	2.0	11.79	0.05	0.73	0.68
	Inherent +0.2mm Cu	624.8	9.2	598.4	9.1	2.0	13.51	0.05	0.72	0.49
63	Inherent	546	8.7	521	8.6	2.0	8.87	0.05	0.69	1.00
	Inherent +0.1mm Cu	605.4	9	579.7	8.9	2.0	12.56	0.05	0.74	0.85
	Inherent +0.2mm Cu	669.5	9.2	643	9.1	2.0	14.28	0.04	0.72	0.63
66	Inherent	587.7	8.8	562.4	8.7	2.0	9.43	0.05	0.70	1.20
	Inherent +0.1mm Cu	646.6	9	620.7	8.9	2.0	13.42	0.04	0.74	1.07
	Inherent +0.2mm Cu	715.5	9.3	688.9	9.2	2.0	15.13	0.04	0.72	0.81

							x10^3			
kVp	**Filter**	**Well Signal**	**Well Noise**	**Bkgrd Signal**	**Bkgrd Noise**	**SdNR**	**FOM_S**	**FOM_C**	**FOM_{en}**	**FOM_f**
70	**Inherent**	630.7	8.8	605.4	8.7	2.0	10.34	0.04	0.72	1.56
	Inherent +0.1mm Cu	702.1	9.1	675.9	9	2.0	14.31	0.04	0.75	1.39
	Inherent +0.2mm Cu	765.7	9.3	738.9	9.2	2.0	16.27	0.04	0.73	1.08
75	**Inherent**	693.2	8.9	667.6	8.8	2.0	11.7	2.2	0.0	0.7
	Inherent +0.1mm Cu	757.5	9.1	731.4	9	2.0	16.0	2.3	0.0	0.8
	Inherent +0.2mm Cu	838.1	9.4	811.2	9.3	2.0	17.6	1.8	0.0	0.7
80	**Inherent**	739.6	8.9	714	8.8	2.0	13.1	3.0	0.0	0.8
	Inherent +0.1mm Cu	825.7	9.2	799.3	9.1	2.0	17.1	3.0	0.0	0.8
	Inherent +0.2mm Cu	904.4	9.4	877.3	9.3	2.0	18.9	2.5	0.0	0.7
85	**Inherent**	776.7	8.9	751.1	8.8	2.0	14.6	4.1	0.0	0.8
	Inherent +0.1mm Cu	873.4	9.2	847	9.1	2.0	18.6	4.0	0.0	0.8
	Inherent +0.2mm Cu	925.2	9.3	898.4	9.2	2.0	21.0	3.5	0.0	0.8
90	**Inherent**	818	8.9	792.4	8.8	2.0	16.0	5.3	0.0	0.8
	Inherent +0.1mm Cu	896.1	9.1	870	9	2.0	20.5	5.4	0.0	0.8
	Inherent +0.2mm Cu	965.5	9.3	938.7	9.2	2.0	22.5	4.6	0.0	0.8
70(G)	**Inherent**	626.7	10.7	596	10.6	2.0	6.98	0.05	0.53	0.98
	Inherent +0.1mm Cu	713.2	11	681.5	10.9	2.0	9.57	0.04	0.56	0.82
	Inherent +0.2mm Cu	771.5	11.2	739.2	11.1	2.0	11.22	0.04	0.56	0.69

Appendix O

Figures of Merit Weighting

FOM_S									
kVp Filtration	100%	**kVp Filtration**	75%	**kVp Filtration**	50%	**kVp Filtration**	25%	**kVp Filtration**	0%
90 0.2mm Cu	2.57	90 0.2mm Cu	2.49	90 0.1 mm Cu	2.47	90 0.1 mm Cu	2.53	90 0.1 mm Cu	2.58
85 0.2mm Cu	2.41	90 0.1 mm Cu	2.42	90 0.2mm Cu	2.40	90 Inherent	2.38	90 Inherent	2.55
90 0.1 mm Cu	2.36	85 0.2mm Cu	2.27	90 Inherent	2.20	90 0.2mm Cu	2.32	90 0.2mm Cu	2.23
80 0.2mm Cu	2.18	85 0.1 mm Cu	2.11	85 0.2mm Cu	2.13	85 0.1 mm Cu	2.07	85 Inherent	2.13
85 0.1 mm Cu	2.13	90 Inherent	2.02	85 0.1 mm Cu	2.09	85 Inherent	2.02	85 0.1 mm Cu	2.04
75 0.2 mm CU	2.01	80 0.2mm Cu	2.01	85 Inherent	1.91	85 0.2mm Cu	1.99	85 0.2mm Cu	1.85
80 0.1 mm Cu	1.96	80 0.1 mm Cu	1.89	80 0.2mm Cu	1.83	80 0.1 mm Cu	1.75	80 Inherent	1.69
90 Inherent	1.85	75 0.2 mm CU	1.81	80 0.1 mm Cu	1.82	80 0.2mm Cu	1.65	80 0.1 mm Cu	1.68
70 0.2 mm Cu	1.84	85 Inherent	1.80	75 0.1 mm CU	1.64	80 Inherent	1.64	80 0.2mm Cu	1.48
75 0.1 mm CU	1.82	75 0.1 mm CU	1.73	75 0.2 mm CU	1.62	75 0.1 mm CU	1.54	75 0.1 mm CU	1.45
85 Inherent	1.69	70 0.2 mm Cu	1.62	80 Inherent	1.59	75 0.2 mm CU	1.43	75 Inherent	1.38
66 0.2mm Cu	1.69	80 Inherent	1.54	70 0.2 mm Cu	1.41	75 Inherent	1.37	75 0.2 mm CU	1.24
70 0.1 mm Cu	1.64	70 0.1 mm Cu	1.51	70 0.1 mm Cu	1.38	70 0.1 mm Cu	1.26	70 Inherent	1.18
63 0.2mm Cu	1.62	66 0.2mm Cu	1.49	75 Inherent	1.35	70 0.2 mm Cu	1.19	70 0.1 mm Cu	1.13
60 0.2 mm Cu	1.55	63 0.2mm Cu	1.43	66 0.2mm Cu	1.29	70 Inherent	1.18	66 Inherent	1.09
66 0.1 mm Cu	1.51	66 0.1 mm Cu	1.39	66 0.1 mm Cu	1.26	66 0.1 mm Cu	1.14	66 0.1 mm Cu	1.02
80 Inherent	1.49	60 0.2 mm Cu	1.37	63 0.2mm Cu	1.24	66 Inherent	1.09	63 Inherent	1.00
57 0.2mm Cu	1.43	75 Inherent	1.33	60 0.2 mm Cu	1.19	66 0.2mm Cu	1.09	70 0.2 mm Cu	0.98
63 0.1 mm Cu	1.42	63 0.1 mm Cu	1.30	63 0.1 mm Cu	1.19	63 0.1 mm Cu	1.07	70(G) Inherent	0.97
55 0.2mm Cu	1.36	57 0.2mm Cu	1.28	70 Inherent	1.18	63 0.2mm Cu	1.05	63 0.1 mm Cu	0.96

60 0.1 mm Cu	1.33	60 0.1 mm Cu	1.23	60 0.1 mm Cu	1.12	60 0.1 mm Cu	1.02	60 Inherent	0.95
75 Inherent	1.32	55 0.2mm Cu	1.22	57 0.2mm Cu	1.12	60 0.2 mm Cu	1.02	60 0.1 mm Cu	0.92
52 0.2 mm Cu	1.25	70 Inherent	1.17	66 Inherent	1.09	63 Inherent	1.00	57 Inherent	0.90
70(G) 0.2mm Cu	1.24	52 0.2 mm Cu	1.13	55 0.2mm Cu	1.08	57 0.2mm Cu	0.96	70(G) 0.1 mm Cu	0.89
57 0.1 mm Cu	1.22	70(G) 0.2mm Cu	1.13	57 0.1 mm Cu	1.04	57 0.1 mm Cu	0.95	66 0.2mm Cu	0.89
50 0.2 mm Cu	1.18	57 0.1 mm Cu	1.13	52 0.2 mm Cu	1.02	70(G) 0.1 mm Cu	0.95	55 Inherent	0.88
70 Inherent	1.17	66 Inherent	1.09	70(G) 0.2mm Cu	1.02	60 Inherent	0.95	57 0.1 mm Cu	0.87
55 0.1 mm Cu	1.15	50 0.2 mm Cu	1.08	63 Inherent	1.00	55 0.2mm Cu	0.94	63 0.2mm Cu	0.86
70(G) 0.1 mm Cu	1.10	55 0.1 mm Cu	1.07	70(G) 0.1 mm Cu	1.00	70(G) Inherent	0.93	55 0.1 mm Cu	0.84
66 Inherent	1.09	70(G) 0.1 mm Cu	1.05	55 0.1 mm Cu	1.00	55 0.1 mm Cu	0.92	60 0.2 mm Cu	0.84
52 0.1 mm Cu	1.04	63 Inherent	1.00	50 0.2 mm Cu	0.99	70(G) 0.2mm Cu	0.91	50 0.1 mm Cu	0.83
63 Inherent	1.00	52 0.1 mm Cu	0.99	60 Inherent	0.94	52 0.2 mm Cu	0.91	52 0.1 mm Cu	0.83
50 0.1 mm Cu	0.97	50 0.1 mm Cu	0.94	52 0.1 mm Cu	0.94	50 0.2 mm Cu	0.90	52 Inherent	0.83
60 Inherent	0.92	60 Inherent	0.93	50 0.1 mm Cu	0.90	52 0.1 mm Cu	0.89	50 Inherent	0.81
57 Inherent	0.83	57 Inherent	0.85	70(G) Inherent	0.89	57 Inherent	0.88	57 0.2mm Cu	0.81
70(G) Inherent	0.80	70(G) Inherent	0.84	57 Inherent	0.87	50 0.1 mm Cu	0.87	50 0.2 mm Cu	0.80
55 Inherent	0.77	55 Inherent	0.80	55 Inherent	0.83	55 Inherent	0.85	70(G) 0.2mm Cu	0.80
52 Inherent	0.66	52 Inherent	0.70	52 Inherent	0.74	52 Inherent	0.78	52 0.2 mm Cu	0.79
50 Inherent	0.59	50 Inherent	0.65	50 Inherent	0.70	50 Inherent	0.76	55 0.2mm Cu	0.79

FOM_C							
kVp Filtration	100%	**kVp Filtration**	75%	**kVp Filtration**	50%	**kVp Filtration**	0%
50 Inherent	1.38	90 0.1 mm Cu	1.26	90 0.1 mm Cu	1.89	90 0.1 mm Cu	3.16

52 Inherent	1.31	90 Inherent	1.24	90 Inherent	1.81	90 Inherent	2.95
50 0.1 mm Cu	1.28	50 Inherent	1.17	90 0.2mm Cu	1.75	90 0.2mm Cu	2.89
52 0.1 mm Cu	1.21	90 0.2mm Cu	1.17	85 0.1 mm Cu	1.59	85 0.1 mm Cu	2.54
50 0.2 mm Cu	1.21	85 Inherent	1.15	85 Inherent	1.59	85 Inherent	2.46
55 Inherent	1.20	50 0.1 mm Cu	1.14	85 0.2mm Cu	1.54	85 0.2mm Cu	2.45
57 Inherent	1.14	52 Inherent	1.13	80 0.1 mm Cu	1.40	80 0.1 mm Cu	2.11
52 0.2 mm Cu	1.13	85 0.1 mm Cu	1.12	80 Inherent	1.34	80 0.2mm Cu	1.99
55 0.1 mm Cu	1.10	50 0.2 mm Cu	1.10	80 0.2mm Cu	1.32	80 Inherent	1.94
70(G) Inherent	1.08	52 0.1 mm Cu	1.10	75 0.1 mm CU	1.28	75 0.1 mm CU	1.81
60 Inherent	1.06	55 Inherent	1.09	75 0.2 mm CU	1.18	75 0.2 mm CU	1.68
57 0.1 mm Cu	1.05	85 0.2mm Cu	1.08	75 Inherent	1.18	75 Inherent	1.56
55 0.2mm Cu	1.04	52 0.2 mm Cu	1.06	70 0.1 mm Cu	1.11	70 0.1 mm Cu	1.41
63 Inherent	1.00	57 Inherent	1.06	70 Inherent	1.08	70 0.2 mm Cu	1.34
57 0.2mm Cu	0.99	55 0.1 mm Cu	1.04	66 0.1 mm Cu	1.05	70 Inherent	1.29
60 0.1 mm Cu	0.98	80 0.1 mm Cu	1.04	70 0.2 mm Cu	1.05	66 0.1 mm Cu	1.23
70(G) 0.1 mm Cu	0.97	80 Inherent	1.04	66 Inherent	1.04	66 0.2mm Cu	1.19
66 Inherent	0.93	70(G) Inherent	1.03	63 0.1 mm Cu	1.02	66 Inherent	1.14
63 0.1 mm Cu	0.92	60 Inherent	1.02	60 0.1 mm Cu	1.01	63 0.1 mm Cu	1.12
60 0.2 mm Cu	0.92	57 0.1 mm Cu	1.02	50 0.1 mm Cu	1.01	63 0.2mm Cu	1.11
70(G) 0.2mm Cu	0.91	75 0.1 mm CU	1.01	63 Inherent	1.00	60 0.2 mm Cu	1.05
70 Inherent	0.87	55 0.2mm Cu	1.00	50 0.2 mm Cu	1.00	60 0.1 mm Cu	1.03
66 0.1 mm Cu	0.86	63 Inherent	1.00	66 0.2mm Cu	0.99	63 Inherent	1.00
63 0.2mm Cu	0.85	60 0.1 mm Cu	0.99	52 0.1 mm Cu	0.99	57 0.2mm Cu	0.95
70 0.1 mm Cu	0.80	66 Inherent	0.99	57 0.1 mm Cu	0.99	70(G) 0.1 mm Cu	0.94

66 0.2mm Cu	0.80	75 Inherent	0.99	63 0.2mm Cu	0.98	57 0.1 mm Cu	0.92
75 Inherent	0.79	57 0.2mm Cu	0.98	60 Inherent	0.98	70(G) 0.2mm Cu	0.91
70 0.2 mm Cu	0.75	80 0.2mm Cu	0.98	60 0.2 mm Cu	0.98	60 Inherent	0.91
75 0.1 mm CU	0.74	63 0.1 mm Cu	0.97	52 0.2 mm Cu	0.98	55 0.2mm Cu	0.90
80 Inherent	0.74	70 Inherent	0.97	55 0.1 mm Cu	0.98	70(G) Inherent	0.88
85 Inherent	0.71	70(G) 0.1 mm Cu	0.96	70(G) Inherent	0.98	55 0.1 mm Cu	0.86
75 0.2 mm CU	0.69	66 0.1 mm Cu	0.96	57 0.2mm Cu	0.97	52 0.2 mm Cu	0.83
80 0.1 mm Cu	0.69	70 0.1 mm Cu	0.95	57 Inherent	0.97	57 Inherent	0.80
90 Inherent	0.67	60 0.2 mm Cu	0.95	55 0.2mm Cu	0.97	50 0.2 mm Cu	0.79
85 0.1 mm Cu	0.65	75 0.2 mm CU	0.94	55 Inherent	0.97	52 0.1 mm Cu	0.78
80 0.2mm Cu	0.64	63 0.2mm Cu	0.92	50 Inherent	0.96	55 Inherent	0.73
90 0.1 mm Cu	0.63	70(G) 0.2mm Cu	0.91	52 Inherent	0.96	50 0.1 mm Cu	0.73
85 0.2mm Cu	0.62	70 0.2 mm Cu	0.90	70(G) 0.1 mm Cu	0.95	52 Inherent	0.61
90 0.2mm Cu	0.60	66 0.2mm Cu	0.90	70(G) 0.2mm Cu	0.91	50 Inherent	0.55

FOM_E							
kVp Filtration	100%	**kVp Filtration**	75%	**kVp Filtration**	50%	**kVp Filtration**	0%
90 Inherent	1.22	90 0.1 mm Cu	1.65	90 0.1 mm Cu	2.09	90 0.1 mm Cu	2.96
90 0.1 mm Cu	1.22	90 Inherent	1.61	90 Inherent	1.99	90 Inherent	2.76
85 Inherent	1.19	90 0.2mm Cu	1.55	90 0.2mm Cu	1.94	90 0.2mm Cu	2.70
90 0.2mm Cu	1.17	85 Inherent	1.47	85 0.1 mm Cu	1.76	85 0.1 mm Cu	2.37
85 0.1 mm Cu	1.15	85 0.1 mm Cu	1.46	85 Inherent	1.75	85 Inherent	2.30
85 0.2mm Cu	1.14	85 0.2mm Cu	1.43	85 0.2mm Cu	1.71	85 0.2mm Cu	2.28
80 0.1 mm Cu	1.12	80 0.1 mm Cu	1.33	80 0.1 mm Cu	1.54	80 0.1 mm Cu	1.96
75 0.1 mm	1.12	80 Inherent	1.29	80 0.2mm Cu	1.47	80 0.2mm Cu	1.84

CU							
80 Inherent	1.12	80 0.2mm Cu	1.28	80 Inherent	1.47	80 Inherent	1.81
70 0.1 mm Cu	1.09	75 0.1 mm CU	1.26	75 0.1 mm CU	1.40	75 0.1 mm CU	1.68
80 0.2mm Cu	1.09	75 0.2 mm CU	1.19	75 0.2 mm CU	1.31	75 0.2 mm CU	1.55
66 0.1 mm Cu	1.07	75 Inherent	1.16	75 Inherent	1.27	75 Inherent	1.47
75 0.2 mm CU	1.07	70 0.1 mm Cu	1.15	70 0.1 mm Cu	1.20	70 0.1 mm Cu	1.31
63 0.1 mm Cu	1.06	70 0.2 mm Cu	1.10	70 0.2 mm Cu	1.15	70 0.2 mm Cu	1.24
75 Inherent	1.06	66 0.1 mm Cu	1.10	70 Inherent	1.14	70 Inherent	1.23
60 0.2 mm Cu	1.06	70 Inherent	1.09	66 0.1 mm Cu	1.12	66 0.1 mm Cu	1.16
70 0.2 mm Cu	1.06	63 0.1 mm Cu	1.07	66 0.2mm Cu	1.07	66 Inherent	1.11
60 0.1 mm Cu	1.05	66 0.2mm Cu	1.05	66 Inherent	1.07	66 0.2mm Cu	1.11
63 0.2mm Cu	1.05	66 Inherent	1.05	63 0.1 mm Cu	1.07	63 0.1 mm Cu	1.08
57 0.2mm Cu	1.05	63 0.2mm Cu	1.05	63 0.2mm Cu	1.05	63 0.2mm Cu	1.05
70 Inherent	1.04	60 0.1 mm Cu	1.04	60 0.1 mm Cu	1.03	60 0.1 mm Cu	1.01
55 0.2mm Cu	1.04	60 0.2 mm Cu	1.04	60 0.2 mm Cu	1.03	60 0.2 mm Cu	1.00
66 0.2mm Cu	1.04	57 0.2mm Cu	1.02	63 Inherent	1.00	63 Inherent	1.00
57 0.1 mm Cu	1.03	57 0.1 mm Cu	1.01	57 0.2mm Cu	0.99	70(G) 0.1 mm Cu	0.99
66 Inherent	1.03	55 0.2mm Cu	1.00	57 0.1 mm Cu	0.98	70(G) Inherent	0.98
52 0.2 mm Cu	1.03	63 Inherent	1.00	55 0.2mm Cu	0.97	70(G) 0.2mm Cu	0.95
50 0.2 mm Cu	1.02	52 0.2 mm Cu	0.99	60 Inherent	0.95	60 Inherent	0.94
55 0.1 mm Cu	1.02	55 0.1 mm Cu	0.98	55 0.1 mm Cu	0.95	57 0.2mm Cu	0.93
63 Inherent	1.00	50 0.2 mm Cu	0.98	52 0.2 mm Cu	0.95	57 0.1 mm Cu	0.93
52 0.1 mm Cu	0.99	60 Inherent	0.96	50 0.2 mm Cu	0.94	55 0.2mm Cu	0.90
50 0.1 mm Cu	0.97	52 0.1 mm Cu	0.96	52 0.1 mm Cu	0.92	55 0.1 mm Cu	0.89

60 Inherent	0.97	50 0.1 mm Cu	0.94	70(G) 0.1 mm Cu	0.91	52 0.2 mm Cu	0.87
57 Inherent	0.93	57 Inherent	0.92	50 0.1 mm Cu	0.90	57 Inherent	0.87
55 Inherent	0.91	55 Inherent	0.89	57 Inherent	0.90	50 0.2 mm Cu	0.85
52 Inherent	0.83	70(G) 0.1 mm Cu	0.86	70(G) Inherent	0.88	52 0.1 mm Cu	0.85
70(G) 0.1 mm Cu	0.82	70(G) 0.2mm Cu	0.83	55 Inherent	0.87	50 0.1 mm Cu	0.83
70(G) 0.2mm Cu	0.80	70(G) Inherent	0.83	70(G) 0.2mm Cu	0.87	55 Inherent	0.83
50 Inherent	0.79	52 Inherent	0.82	52 Inherent	0.80	52 Inherent	0.77
70(G) Inherent	0.78	50 Inherent	0.78	50 Inherent	0.77	50 Inherent	0.75

FOM_F							
kVp Filtration	100%	**kVp Filtration**	75%	**kVp Filtration**	50%	**kVp Filtration**	0%
90 0.1 mm Cu	5.91	90 0.1 mm Cu	4.78	90 0.1 mm Cu	3.66	90 0.1 mm Cu	1.40
90 Inherent	5.78	90 Inherent	4.64	90 Inherent	3.51	85 0.1 mm Cu	1.31
90 0.2mm Cu	4.94	90 0.2mm Cu	4.07	90 0.2mm Cu	3.19	80 0.1 mm Cu	1.25
85 Inherent	4.50	85 Inherent	3.68	85 Inherent	2.85	90 Inherent	1.24
85 0.1 mm Cu	4.33	85 0.1 mm Cu	3.58	85 0.1 mm Cu	2.82	75 0.1 mm CU	1.23
85 0.2mm Cu	3.80	85 0.2mm Cu	3.20	85 0.2mm Cu	2.60	85 Inherent	1.20
80 0.1 mm Cu	3.25	80 0.1 mm Cu	2.75	80 0.1 mm Cu	2.25	70 0.1 mm Cu	1.18
80 Inherent	3.21	80 Inherent	2.68	80 Inherent	2.16	66 0.1 mm Cu	1.15
80 0.2mm Cu	2.70	80 0.2mm Cu	2.35	80 0.2mm Cu	2.00	63 0.1 mm Cu	1.13
75 0.1 mm CU	2.49	75 0.1 mm CU	2.17	75 0.1 mm CU	1.86	60 0.1 mm Cu	1.12
75 Inherent	2.30	75 Inherent	1.99	75 Inherent	1.68	80 Inherent	1.11
75 0.2 mm CU	1.96	75 0.2 mm CU	1.78	75 0.2 mm CU	1.61	57 0.1 mm Cu	1.10
70 Inherent	1.65	70 Inherent	1.49	70 Inherent	1.34	55 0.1 mm Cu	1.09
70 0.1 mm Cu	1.49	70 0.1 mm Cu	1.41	70 0.1 mm Cu	1.33	52 0.1 mm Cu	1.08

66 Inherent	1.32	66 Inherent	1.24	70 0.2 mm Cu	1.17	50 0.1 mm Cu	1.07
70 0.2 mm Cu	1.13	70 0.2 mm Cu	1.15	66 Inherent	1.17	75 Inherent	1.06
66 0.1 mm Cu	1.12	66 0.1 mm Cu	1.13	66 0.1 mm Cu	1.13	70 Inherent	1.03
70(G) Inherent	1.06	70(G) Inherent	1.02	63 0.1 mm Cu	1.01	66 Inherent	1.02
63 Inherent	1.00	63 Inherent	1.00	66 0.2mm Cu	1.00	63 Inherent	1.00
70(G) 0.1 mm Cu	0.89	63 0.1 mm Cu	0.95	63 Inherent	1.00	60 Inherent	0.98
63 0.1 mm Cu	0.89	66 0.2mm Cu	0.92	70(G) Inherent	0.97	57 Inherent	0.97
60 Inherent	0.83	70(G) 0.1 mm Cu	0.91	70(G) 0.1 mm Cu	0.93	70(G) 0.1 mm Cu	0.96
66 0.2mm Cu	0.83	60 Inherent	0.87	63 0.2mm Cu	0.92	55 Inherent	0.96
60 0.1 mm Cu	0.71	60 0.1 mm Cu	0.81	60 0.1 mm Cu	0.92	90 0.2mm Cu	0.93
70(G) 0.2mm Cu	0.70	63 0.2mm Cu	0.80	60 Inherent	0.91	52 Inherent	0.93
63 0.2mm Cu	0.67	70(G) 0.2mm Cu	0.77	60 0.2 mm Cu	0.86	50 Inherent	0.92
57 Inherent	0.63	57 Inherent	0.71	70(G) 0.2mm Cu	0.84	70(G) Inherent	0.88
60 0.2 mm Cu	0.54	60 0.2 mm Cu	0.70	57 0.1 mm Cu	0.81	85 0.2mm Cu	0.88
55 Inherent	0.52	57 0.1 mm Cu	0.66	57 Inherent	0.80	80 0.2mm Cu	0.80
57 0.1 mm Cu	0.51	55 Inherent	0.63	57 0.2mm Cu	0.77	75 0.2 mm CU	0.75
55 0.1 mm Cu	0.41	55 0.1 mm Cu	0.58	55 0.1 mm Cu	0.75	70 0.2 mm Cu	0.70
57 0.2mm Cu	0.38	57 0.2mm Cu	0.58	55 Inherent	0.74	66 0.2mm Cu	0.66
52 Inherent	0.35	55 0.2mm Cu	0.51	55 0.2mm Cu	0.72	63 0.2mm Cu	0.64
55 0.2mm Cu	0.30	52 0.1 mm Cu	0.50	52 0.1 mm Cu	0.69	60 0.2 mm Cu	0.62
52 0.1 mm Cu	0.30	52 Inherent	0.49	52 0.2 mm Cu	0.68	57 0.2mm Cu	0.59
50 Inherent	0.27	50 0.1 mm Cu	0.46	50 0.1 mm Cu	0.66	55 0.2mm Cu	0.57
50 0.1 mm Cu	0.25	52 0.2 mm Cu	0.45	50 0.2 mm Cu	0.66	52 0.2 mm Cu	0.54
52 0.2 mm Cu	0.22	50 Inherent	0.43	52 Inherent	0.64	50 0.2 mm Cu	0.53
50 0.2 mm Cu	0.18	50 0.2 mm Cu	0.42	50 Inherent	0.59	70(G) 0.2mm Cu	0.49

FOM_S & FOM_C					
kVp Filtration	100% FOM_S	**kVp Filtration**	50%	**kVp Filtration**	0% FOM_S
90 0.2mm Cu	2.57	90 0.2mm Cu	1.58	50 Inherent	1.38
85 0.2mm Cu	2.41	85 0.2mm Cu	1.52	52 Inherent	1.31
90 0.1 mm Cu	2.36	90 0.1 mm Cu	1.49	50 0.1 mm Cu	1.28
80 0.2mm Cu	2.18	80 0.2mm Cu	1.41	52 0.1 mm Cu	1.21
85 0.1 mm Cu	2.13	85 0.1 mm Cu	1.39	50 0.2 mm Cu	1.21
75 0.2 mm CU	2.01	75 0.2 mm CU	1.35	55 Inherent	1.20
80 0.1 mm Cu	1.96	80 0.1 mm Cu	1.32	57 Inherent	1.14
90 Inherent	1.85	70 0.2 mm Cu	1.29	52 0.2 mm Cu	1.13
70 0.2 mm Cu	1.84	75 0.1 mm CU	1.28	55 0.1 mm Cu	1.10
75 0.1 mm CU	1.82	90 Inherent	1.26	60 Inherent	1.06
85 Inherent	1.69	66 0.2mm Cu	1.25	57 0.1 mm Cu	1.05
66 0.2mm Cu	1.69	63 0.2mm Cu	1.24	55 0.2mm Cu	1.04
70 0.1 mm Cu	1.64	60 0.2 mm Cu	1.23	63 Inherent	1.00
63 0.2mm Cu	1.62	70 0.1 mm Cu	1.22	57 0.2mm Cu	0.99
60 0.2 mm Cu	1.55	57 0.2mm Cu	1.21	60 0.1 mm Cu	0.98
66 0.1 mm Cu	1.51	85 Inherent	1.20	66 Inherent	0.93
80 Inherent	1.49	55 0.2mm Cu	1.20	63 0.1 mm Cu	0.92
57 0.2mm Cu	1.43	50 0.2 mm Cu	1.19	60 0.2 mm Cu	0.92
63 0.1 mm Cu	1.42	52 0.2 mm Cu	1.19	70 Inherent	0.87
55 0.2mm Cu	1.36	66 0.1 mm Cu	1.19	66 0.1 mm Cu	0.86
60 0.1 mm Cu	1.33	63 0.1 mm Cu	1.17	63 0.2mm Cu	0.85
75 Inherent	1.32	60 0.1 mm Cu	1.16	70 0.1 mm Cu	0.80

52 0.2 mm Cu	1.25	57 0.1 mm Cu	1.13	66 0.2mm Cu	0.80
57 0.1 mm Cu	1.22	50 0.1 mm Cu	1.13	75 Inherent	0.79
50 0.2 mm Cu	1.18	55 0.1 mm Cu	1.13	70 0.2 mm Cu	0.75
70 Inherent	1.17	52 0.1 mm Cu	1.12	75 0.1 mm CU	0.74
55 0.1 mm Cu	1.15	80 Inherent	1.12	80 Inherent	0.74
66 Inherent	1.09	75 Inherent	1.06	85 Inherent	0.71
52 0.1 mm Cu	1.04	70 Inherent	1.02	75 0.2 mm CU	0.69
63 Inherent	1.00	66 Inherent	1.01	80 0.1 mm Cu	0.69
50 0.1 mm Cu	0.97	63 Inherent	1.00	90 Inherent	0.67
60 Inherent	0.92	60 Inherent	0.99	85 0.1 mm Cu	0.65
57 Inherent	0.83	55 Inherent	0.99	80 0.2mm Cu	0.64
55 Inherent	0.77	57 Inherent	0.99	90 0.1 mm Cu	0.63
52 Inherent	0.66	50 Inherent	0.99	85 0.2mm Cu	0.62
50 Inherent	0.59	52 Inherent	0.98	90 0.2mm Cu	0.60

$FOM_S + FOM_E$					
kVp Filtration	100% FOM_S	**kVp Filtration**	50%	**kVp Filtration**	0% FOM_S
90 0.2mm Cu	2.57	90 0.2mm Cu	1.87	90 Inherent	1.22
85 0.2mm Cu	2.41	90 0.1 mm Cu	1.79	90 0.1 mm Cu	1.22
90 0.1 mm Cu	2.36	85 0.2mm Cu	1.78	85 Inherent	1.19
80 0.2mm Cu	2.18	85 0.1 mm Cu	1.64	90 0.2mm Cu	1.17
85 0.1 mm Cu	2.13	80 0.2mm Cu	1.64	85 0.1 mm Cu	1.15
75 0.2 mm CU	2.01	80 0.1 mm Cu	1.54	85 0.2mm Cu	1.14
80 0.1 mm Cu	1.96	75 0.2 mm CU	1.54	80 0.1 mm Cu	1.12
90 Inherent	1.85	90 Inherent	1.53	75 0.1 mm CU	1.12

70 0.2 mm Cu	1.84	75 0.1 mm CU	1.47	80 Inherent	1.12
75 0.1 mm CU	1.82	70 0.2 mm Cu	1.45	70 0.1 mm Cu	1.09
85 Inherent	1.69	85 Inherent	1.44	80 0.2mm Cu	1.09
66 0.2mm Cu	1.69	66 0.2mm Cu	1.36	66 0.1 mm Cu	1.07
70 0.1 mm Cu	1.64	70 0.1 mm Cu	1.36	75 0.2 mm CU	1.07
63 0.2mm Cu	1.62	63 0.2mm Cu	1.33	63 0.1 mm Cu	1.06
60 0.2 mm Cu	1.55	80 Inherent	1.30	75 Inherent	1.06
66 0.1 mm Cu	1.51	60 0.2 mm Cu	1.30	60 0.2 mm Cu	1.06
80 Inherent	1.49	66 0.1 mm Cu	1.29	70 0.2 mm Cu	1.06
57 0.2mm Cu	1.43	63 0.1 mm Cu	1.24	60 0.1 mm Cu	1.05
63 0.1 mm Cu	1.42	57 0.2mm Cu	1.24	63 0.2mm Cu	1.05
55 0.2mm Cu	1.36	55 0.2mm Cu	1.20	57 0.2mm Cu	1.05
60 0.1 mm Cu	1.33	60 0.1 mm Cu	1.19	70 Inherent	1.04
75 Inherent	1.32	75 Inherent	1.19	55 0.2mm Cu	1.04
52 0.2 mm Cu	1.25	52 0.2 mm Cu	1.14	66 0.2mm Cu	1.04
57 0.1 mm Cu	1.22	57 0.1 mm Cu	1.12	57 0.1 mm Cu	1.03
50 0.2 mm Cu	1.18	70 Inherent	1.11	66 Inherent	1.03
70 Inherent	1.17	50 0.2 mm Cu	1.10	52 0.2 mm Cu	1.03
55 0.1 mm Cu	1.15	55 0.1 mm Cu	1.08	50 0.2 mm Cu	1.02
66 Inherent	1.09	66 Inherent	1.06	55 0.1 mm Cu	1.02
52 0.1 mm Cu	1.04	52 0.1 mm Cu	1.01	63 Inherent	1.00
63 Inherent	1.00	63 Inherent	1.00	52 0.1 mm Cu	0.99
50 0.1 mm Cu	0.97	50 0.1 mm Cu	0.97	50 0.1 mm Cu	0.97
60 Inherent	0.92	60 Inherent	0.95	60 Inherent	0.97
57 Inherent	0.83	57 Inherent	0.88	57 Inherent	0.93

55 Inherent	0.77	55 Inherent	0.84	55 Inherent	0.91
52 Inherent	0.66	52 Inherent	0.74	52 Inherent	0.83
50 Inherent	0.59	50 Inherent	0.69	50 Inherent	0.79

$FOM_S + FOM_F$					
kVp Filtration	100% FOM_S	**kVp Filtration**	50%	**kVp Filtration**	0% FOM_S
90 0.2mm Cu	2.57	90 0.1 mm Cu	4.14	90 0.1 mm Cu	5.91
85 0.2mm Cu	2.41	90 Inherent	3.81	90 Inherent	5.78
90 0.1 mm Cu	2.36	90 0.2mm Cu	3.76	90 0.2mm Cu	4.94
80 0.2mm Cu	2.18	85 0.1 mm Cu	3.23	85 Inherent	4.50
85 0.1 mm Cu	2.13	85 0.2mm Cu	3.11	85 0.1 mm Cu	4.33
75 0.2 mm CU	2.01	85 Inherent	3.10	85 0.2mm Cu	3.80
80 0.1 mm Cu	1.96	80 0.1 mm Cu	2.60	80 0.1 mm Cu	3.25
90 Inherent	1.85	80 0.2mm Cu	2.44	80 Inherent	3.21
70 0.2 mm Cu	1.84	80 Inherent	2.35	80 0.2mm Cu	2.70
75 0.1 mm CU	1.82	75 0.1 mm CU	2.15	75 0.1 mm CU	2.49
85 Inherent	1.69	75 0.2 mm CU	1.98	75 Inherent	2.30
66 0.2mm Cu	1.69	75 Inherent	1.81	75 0.2 mm CU	1.96
70 0.1 mm Cu	1.64	70 0.1 mm Cu	1.56	70 Inherent	1.65
63 0.2mm Cu	1.62	70 0.2 mm Cu	1.48	70 0.1 mm Cu	1.49
60 0.2 mm Cu	1.55	70 Inherent	1.41	66 Inherent	1.32
66 0.1 mm Cu	1.51	66 0.1 mm Cu	1.32	70 0.2 mm Cu	1.13
80 Inherent	1.49	66 0.2mm Cu	1.26	66 0.1 mm Cu	1.12
57 0.2mm Cu	1.43	66 Inherent	1.20	63 Inherent	1.00

63 0.1 mm Cu	1.42	63 0.1 mm Cu	1.15	63 0.1 mm Cu	0.89
55 0.2mm Cu	1.36	63 0.2mm Cu	1.14	60 Inherent	0.83
60 0.1 mm Cu	1.33	60 0.2 mm Cu	1.04	66 0.2mm Cu	0.83
75 Inherent	1.32	60 0.1 mm Cu	1.02	60 0.1 mm Cu	0.71
52 0.2 mm Cu	1.25	63 Inherent	1.00	63 0.2mm Cu	0.67
57 0.1 mm Cu	1.22	57 0.2mm Cu	0.91	57 Inherent	0.63
50 0.2 mm Cu	1.18	60 Inherent	0.88	60 0.2 mm Cu	0.54
70 Inherent	1.17	57 0.1 mm Cu	0.86	55 Inherent	0.52
55 0.1 mm Cu	1.15	55 0.2mm Cu	0.83	57 0.1 mm Cu	0.51
66 Inherent	1.09	55 0.1 mm Cu	0.78	55 0.1 mm Cu	0.41
52 0.1 mm Cu	1.04	52 0.2 mm Cu	0.73	57 0.2mm Cu	0.38
63 Inherent	1.00	57 Inherent	0.73	52 Inherent	0.35
50 0.1 mm Cu	0.97	50 0.2 mm Cu	0.68	55 0.2mm Cu	0.30
60 Inherent	0.92	52 0.1 mm Cu	0.67	52 0.1 mm Cu	0.30
57 Inherent	0.83	55 Inherent	0.65	50 Inherent	0.27
55 Inherent	0.77	50 0.1 mm Cu	0.61	50 0.1 mm Cu	0.25
52 Inherent	0.66	52 Inherent	0.50	52 0.2 mm Cu	0.22
50 Inherent	0.59	50 Inherent	0.43	50 0.2 mm Cu	0.18

$FOM_C + FOM_E$					
kVp **Filtration**	100% FOM_C	**kVp** **Filtration**	50%	**kVp** **Filtration**	0% FOM_C
50 Inherent	1.38	50 0.1 mm Cu	1.13	90 Inherent	1.22
52 Inherent	1.31	50 0.2 mm Cu	1.11	90 0.1 mm Cu	1.22
50 0.1 mm Cu	1.28	52 0.1 mm Cu	1.10	85 Inherent	1.19

52 0.1 mm Cu	1.21	50 Inherent	1.08	90 0.2mm Cu	1.17
50 0.2 mm Cu	1.21	52 0.2 mm Cu	1.08	85 0.1 mm Cu	1.15
55 Inherent	1.20	52 Inherent	1.07	85 0.2mm Cu	1.14
57 Inherent	1.14	55 0.1 mm Cu	1.06	80 0.1 mm Cu	1.12
52 0.2 mm Cu	1.13	55 Inherent	1.06	75 0.1 mm CU	1.12
55 0.1 mm Cu	1.10	57 0.1 mm Cu	1.04	80 Inherent	1.12
60 Inherent	1.06	57 Inherent	1.04	70 0.1 mm Cu	1.09
57 0.1 mm Cu	1.05	55 0.2mm Cu	1.04	80 0.2mm Cu	1.09
55 0.2mm Cu	1.04	60 0.1 mm Cu	1.02	66 0.1 mm Cu	1.07
63 Inherent	1.00	57 0.2mm Cu	1.02	75 0.2 mm CU	1.07
57 0.2mm Cu	0.99	60 Inherent	1.01	63 0.1 mm Cu	1.06
60 0.1 mm Cu	0.98	63 Inherent	1.00	75 Inherent	1.06
66 Inherent	0.93	63 0.1 mm Cu	0.99	60 0.2 mm Cu	1.06
63 0.1 mm Cu	0.92	60 0.2 mm Cu	0.99	70 0.2 mm Cu	1.06
60 0.2 mm Cu	0.92	66 Inherent	0.98	60 0.1 mm Cu	1.05
70 Inherent	0.87	66 0.1 mm Cu	0.97	63 0.2mm Cu	1.05
66 0.1 mm Cu	0.86	70 Inherent	0.95	57 0.2mm Cu	1.05
63 0.2mm Cu	0.85	63 0.2mm Cu	0.95	70 Inherent	1.04
70 0.1 mm Cu	0.80	85 Inherent	0.95	55 0.2mm Cu	1.04
66 0.2mm Cu	0.80	70 0.1 mm Cu	0.95	66 0.2mm Cu	1.04
75 Inherent	0.79	90 Inherent	0.95	57 0.1 mm Cu	1.03
70 0.2 mm Cu	0.75	75 0.1 mm CU	0.93	66 Inherent	1.03
75 0.1 mm CU	0.74	80 Inherent	0.93	52 0.2 mm Cu	1.03
80 Inherent	0.74	75 Inherent	0.93	50 0.2 mm Cu	1.02
85 Inherent	0.71	90 0.1 mm Cu	0.92	55 0.1 mm Cu	1.02

75 0.2 mm CU	0.69	66 0.2mm Cu	0.92	63 Inherent	1.00
80 0.1 mm Cu	0.69	80 0.1 mm Cu	0.90	52 0.1 mm Cu	0.99
90 Inherent	0.67	70 0.2 mm Cu	0.90	50 0.1 mm Cu	0.97
85 0.1 mm Cu	0.65	85 0.1 mm Cu	0.90	60 Inherent	0.97
80 0.2mm Cu	0.64	85 0.2mm Cu	0.88	57 Inherent	0.93
90 0.1 mm Cu	0.63	90 0.2mm Cu	0.88	55 Inherent	0.91
85 0.2mm Cu	0.62	75 0.2 mm CU	0.88	52 Inherent	0.83
90 0.2mm Cu	0.60	80 0.2mm Cu	0.87	50 Inherent	0.79

$FOM_C + FOM_F$					
kVp Filtration	100% FOM_C	**kVp Filtration**	50%	**kVp Filtration**	0% FOM_C
50 Inherent	1.38	90 0.1 mm Cu	3.27	90 0.1 mm Cu	5.91
52 Inherent	1.31	90 Inherent	3.22	90 Inherent	5.78
50 0.1 mm Cu	1.28	90 0.2mm Cu	2.77	90 0.2mm Cu	4.94
52 0.1 mm Cu	1.21	85 Inherent	2.61	85 Inherent	4.50
50 0.2 mm Cu	1.21	85 0.1 mm Cu	2.49	85 0.1 mm Cu	4.33
55 Inherent	1.20	85 0.2mm Cu	2.21	85 0.2mm Cu	3.80
57 Inherent	1.14	80 Inherent	1.97	80 0.1 mm Cu	3.25
52 0.2 mm Cu	1.13	80 0.1 mm Cu	1.97	80 Inherent	3.21
55 0.1 mm Cu	1.10	80 0.2mm Cu	1.67	80 0.2mm Cu	2.70
60 Inherent	1.06	75 0.1 mm CU	1.62	75 0.1 mm CU	2.49
57 0.1 mm Cu	1.05	75 Inherent	1.55	75 Inherent	2.30
55 0.2mm Cu	1.04	75 0.2 mm CU	1.32	75 0.2 mm CU	1.96
63 Inherent	1.00	70 Inherent	1.26	70 Inherent	1.65
57 0.2mm Cu	0.99	70 0.1 mm Cu	1.15	70 0.1 mm Cu	1.49

60 0.1 mm Cu	0.98	66 Inherent	1.12	66 Inherent	1.32
66 Inherent	0.93	63 Inherent	1.00	70 0.2 mm Cu	1.13
63 0.1 mm Cu	0.92	66 0.1 mm Cu	0.99	66 0.1 mm Cu	1.12
60 0.2 mm Cu	0.92	60 Inherent	0.95	63 Inherent	1.00
70 Inherent	0.87	70 0.2 mm Cu	0.94	63 0.1 mm Cu	0.89
66 0.1 mm Cu	0.86	63 0.1 mm Cu	0.91	60 Inherent	0.83
63 0.2mm Cu	0.85	57 Inherent	0.88	66 0.2mm Cu	0.83
70 0.1 mm Cu	0.80	55 Inherent	0.86	60 0.1 mm Cu	0.71
66 0.2mm Cu	0.80	60 0.1 mm Cu	0.85	63 0.2mm Cu	0.67
75 Inherent	0.79	52 Inherent	0.83	57 Inherent	0.63
70 0.2 mm Cu	0.75	50 Inherent	0.82	60 0.2 mm Cu	0.54
75 0.1 mm CU	0.74	66 0.2mm Cu	0.82	55 Inherent	0.52
80 Inherent	0.74	57 0.1 mm Cu	0.78	57 0.1 mm Cu	0.51
85 Inherent	0.71	50 0.1 mm Cu	0.77	55 0.1 mm Cu	0.41
75 0.2 mm CU	0.69	63 0.2mm Cu	0.76	57 0.2mm Cu	0.38
80 0.1 mm Cu	0.69	55 0.1 mm Cu	0.76	52 Inherent	0.35
90 Inherent	0.67	52 0.1 mm Cu	0.76	55 0.2mm Cu	0.30
85 0.1 mm Cu	0.65	60 0.2 mm Cu	0.73	52 0.1 mm Cu	0.30
80 0.2mm Cu	0.64	50 0.2 mm Cu	0.69	50 Inherent	0.27
90 0.1 mm Cu	0.63	57 0.2mm Cu	0.69	50 0.1 mm Cu	0.25
85 0.2mm Cu	0.62	52 0.2 mm Cu	0.68	52 0.2 mm Cu	0.22
90 0.2mm Cu	0.60	55 0.2mm Cu	0.67	50 0.2 mm Cu	0.18

$FOM_E + FOM_F$					
kVp Filtration	100% FOM_E	**kVp Filtration**	50%	**kVp Filtration**	0% FOM_E

90 Inherent	1.22	90 0.1 mm Cu	3.56	90 0.1 mm Cu	5.91
90 0.1 mm Cu	1.22	90 Inherent	3.50	90 Inherent	5.78
85 Inherent	1.19	90 0.2mm Cu	3.05	90 0.2mm Cu	4.94
90 0.2mm Cu	1.17	85 Inherent	2.84	85 Inherent	4.50
85 0.1 mm Cu	1.15	85 0.1 mm Cu	2.74	85 0.1 mm Cu	4.33
85 0.2mm Cu	1.14	85 0.2mm Cu	2.47	85 0.2mm Cu	3.80
80 0.1 mm Cu	1.12	80 0.1 mm Cu	2.19	80 0.1 mm Cu	3.25
75 0.1 mm CU	1.12	80 Inherent	2.16	80 Inherent	3.21
80 Inherent	1.12	80 0.2mm Cu	1.90	80 0.2mm Cu	2.70
70 0.1 mm Cu	1.09	75 0.1 mm CU	1.80	75 0.1 mm CU	2.49
80 0.2mm Cu	1.09	75 Inherent	1.68	75 Inherent	2.30
66 0.1 mm Cu	1.07	75 0.2 mm CU	1.51	75 0.2 mm CU	1.96
75 0.2 mm CU	1.07	70 Inherent	1.34	70 Inherent	1.65
63 0.1 mm Cu	1.06	70 0.1 mm Cu	1.29	70 0.1 mm Cu	1.49
75 Inherent	1.06	66 Inherent	1.17	66 Inherent	1.32
60 0.2 mm Cu	1.06	66 0.1 mm Cu	1.10	70 0.2 mm Cu	1.13
70 0.2 mm Cu	1.06	70 0.2 mm Cu	1.10	66 0.1 mm Cu	1.12
60 0.1 mm Cu	1.05	63 Inherent	1.00	63 Inherent	1.00
63 0.2mm Cu	1.05	63 0.1 mm Cu	0.98	63 0.1 mm Cu	0.89
57 0.2mm Cu	1.05	66 0.2mm Cu	0.93	60 Inherent	0.83
70 Inherent	1.04	60 Inherent	0.90	66 0.2mm Cu	0.83
55 0.2mm Cu	1.04	60 0.1 mm Cu	0.88	60 0.1 mm Cu	0.71
66 0.2mm Cu	1.04	63 0.2mm Cu	0.86	63 0.2mm Cu	0.67
57 0.1 mm Cu	1.03	60 0.2 mm Cu	0.80	57 Inherent	0.63
66 Inherent	1.03	57 Inherent	0.78	60 0.2 mm Cu	0.54

52 0.2 mm Cu	1.03	57 0.1 mm Cu	0.77	55 Inherent	0.52
50 0.2 mm Cu	1.02	55 Inherent	0.72	57 0.1 mm Cu	0.51
55 0.1 mm Cu	1.02	55 0.1 mm Cu	0.71	55 0.1 mm Cu	0.41
63 Inherent	1.00	57 0.2mm Cu	0.71	57 0.2mm Cu	0.38
52 0.1 mm Cu	0.99	55 0.2mm Cu	0.67	52 Inherent	0.35
50 0.1 mm Cu	0.97	52 0.1 mm Cu	0.65	55 0.2mm Cu	0.30
60 Inherent	0.97	52 0.2 mm Cu	0.62	52 0.1 mm Cu	0.30
57 Inherent	0.93	50 0.1 mm Cu	0.61	50 Inherent	0.27
55 Inherent	0.91	50 0.2 mm Cu	0.60	50 0.1 mm Cu	0.25
52 Inherent	0.83	52 Inherent	0.59	52 0.2 mm Cu	0.22
50 Inherent	0.79	50 Inherent	0.53	50 0.2 mm Cu	0.18

Appendix P

Sample Clinical Validation MCNPX Input Deck

```
Template Dental F2 Tally
c Cell Cards
1  0          -1 20 30          imp:p 1 imp:e 1  $macrobody around geometry
2  0           1                imp:p 0 imp:e 0  $outside world
3  2 -0.001294  -3              imp:p 1 imp:e 1  $rcc in center of phantom
20 1 -2.7       -20  3          imp:p 1 imp:e 1  $Al phantom
30 3 -1.19      -30             imp:p 1 imp:e 1  $PMMA phantom

c Surface Cards
1  rcc 0 0 -4.5  0 0 36  3.4                    $macrobody around geometry
3  rpp -0.10 0.10 -0.10 0.10 -2.03 -2.0         $2 mm diam 0.3 mm depth
20 rcc 0 0 -2.7 0 0 0.7 2.0                     $7 mm Al phantom
30 rcc 0 0 -2.0 0 0 2.0 2.0                     $20 mm PMMA
50 cz 2.0                     $cylinder x0,y0
51 pz 0                       $cylinder base
61 pz -2.7                    $cylinder base

c Data Cards
m1 13027 -0.99 29063 -0.00125 14028 -0.003875        $Type 1100 aluminum
     26056 -0.003875 30064 -0.001
m2 7014 -0.7547  8016 -0.2320  18040 -0.0133          $air
m3 1001 -0.080538  7014 -0.599848  8016 -0.319614    $PMMA
sdef par=p erg=d1  pos=0 0 30 vec=0 0 -1 dir=d2                    $63kVp
si1 h 9.50E-03 1.00E-02 1.05E-02 1.10E-02 1.15E-02 1.20E-02 1.25E-02 1.30E-02
     1.35E-02 1.40E-02 1.45E-02 1.50E-02 1.55E-02 1.60E-02 1.65E-02 1.70E-02
     1.75E-02 1.80E-02 1.85E-02 1.90E-02 1.95E-02 2.00E-02 2.05E-02 2.10E-02
     2.15E-02 2.20E-02 2.25E-02 2.30E-02 2.35E-02 2.40E-02 2.45E-02 2.50E-02
     2.55E-02 2.60E-02 2.65E-02 2.70E-02 2.75E-02 2.80E-02 2.85E-02 2.90E-02
     2.95E-02 3.00E-02 3.05E-02 3.10E-02 3.15E-02 3.20E-02 3.25E-02 3.30E-02
     3.35E-02 3.40E-02 3.45E-02 3.50E-02 3.55E-02 3.60E-02 3.65E-02 3.70E-02
     3.75E-02 3.80E-02 3.85E-02 3.90E-02 3.95E-02 4.00E-02 4.05E-02 4.10E-02
     4.15E-02 4.20E-02 4.25E-02 4.30E-02 4.35E-02 4.40E-02 4.45E-02 4.50E-02
     4.55E-02 4.60E-02 4.65E-02 4.70E-02 4.75E-02 4.80E-02 4.85E-02 4.90E-02
     4.95E-02 5.00E-02 5.05E-02 5.10E-02 5.15E-02 5.20E-02 5.25E-02 5.30E-02
     5.35E-02 5.40E-02 5.45E-02 5.50E-02 5.55E-02 5.60E-02 5.65E-02 5.70E-02
     5.75E-02 5.80E-02 5.85E-02 5.90E-02 5.95E-02 6.00E-02 6.05E-02 6.10E-02
     6.15E-02 6.20E-02 6.25E-02 6.30E-02
sp1 d 0.00E+00 1.87E-08 1.47E-08 1.09E-07 1.61E-06 1.64E-06 4.70E-06 1.34E-05
     3.35E-05 7.07E-05 1.38E-04 2.48E-04 4.15E-04 6.53E-04 9.66E-04 1.38E-03
     1.87E-03 2.45E-03 3.13E-03 3.87E-03 4.69E-03 5.55E-03 6.43E-03 7.38E-03
     8.29E-03 9.23E-03 1.01E-02 1.10E-02 1.18E-02 1.27E-02 1.34E-02 1.41E-02
     1.47E-02 1.53E-02 1.58E-02 1.64E-02 1.68E-02 1.72E-02 1.75E-02 1.78E-02
     1.79E-02 1.81E-02 1.83E-02 1.83E-02 1.84E-02 1.84E-02 1.84E-02 1.84E-02
     1.83E-02 1.82E-02 1.81E-02 1.79E-02 1.77E-02 1.76E-02 1.73E-02 1.71E-02
     1.69E-02 1.67E-02 1.64E-02 1.61E-02 1.59E-02 1.56E-02 1.53E-02 1.50E-02
```

```
     1.47E-02 1.43E-02 1.40E-02 1.37E-02 1.34E-02 1.30E-02 1.27E-02 1.24E-02
     1.20E-02 1.17E-02 1.13E-02 1.10E-02 1.07E-02 1.03E-02 9.96E-03 9.61E-03
     9.25E-03 8.90E-03 8.55E-03 8.19E-03 7.84E-03 7.49E-03 7.14E-03 6.79E-03
     6.43E-03 6.08E-03 5.73E-03 5.39E-03 5.04E-03 4.69E-03 4.34E-03 4.00E-03
     3.66E-03 3.31E-03 2.97E-03 2.64E-03 2.30E-03 1.96E-03 1.63E-03 1.30E-03
     9.72E-04 6.45E-04 3.22E-04 2.67E-05
si2 -1 0.9975 1                          $histogram for cosine bin limits r=2 cm
sp2 0 0.99875 0.00125                    $fract solid angle for each bin
sb2 0 0 1                                $source bias for each bin
mode p e
phys:e
f2:p 51                                                        $10 keV to 63 keV
e2  1.00E-02 1.05E-02 1.10E-02 1.15E-02 1.20E-02 1.25E-02 1.30E-02 1.35E-02
     1.40E-02 1.45E-02 1.50E-02 1.55E-02 1.60E-02 1.65E-02 1.70E-02 1.75E-02
     1.80E-02 1.85E-02 1.90E-02 1.95E-02 2.00E-02 2.05E-02 2.10E-02 2.15E-02
     2.20E-02 2.25E-02 2.30E-02 2.35E-02 2.40E-02 2.45E-02 2.50E-02 2.55E-02
     2.60E-02 2.65E-02 2.70E-02 2.75E-02 2.80E-02 2.85E-02 2.90E-02 2.95E-02
     3.00E-02 3.05E-02 3.10E-02 3.15E-02 3.20E-02 3.25E-02 3.30E-02 3.35E-02
     3.40E-02 3.45E-02 3.50E-02 3.55E-02 3.60E-02 3.65E-02 3.70E-02 3.75E-02
     3.80E-02 3.85E-02 3.90E-02 3.95E-02 4.00E-02 4.05E-02 4.10E-02 4.15E-02
     4.20E-02 4.25E-02 4.30E-02 4.35E-02 4.40E-02 4.45E-02 4.50E-02 4.55E-02
     4.60E-02 4.65E-02 4.70E-02 4.75E-02 4.80E-02 4.85E-02 4.90E-02 4.95E-02
     5.00E-02 5.05E-02 5.10E-02 5.15E-02 5.20E-02 5.25E-02 5.30E-02 5.35E-02
     5.40E-02 5.45E-02 5.50E-02 5.55E-02 5.60E-02 5.65E-02 5.70E-02 5.75E-02
     5.80E-02 5.85E-02 5.90E-02 5.95E-02 6.00E-02 6.05E-02 6.10E-02 6.15E-02
     6.20E-02 6.25E-02 6.30E-02
fs2 -50
sd2  12.56637  1    $ first number is pi*(radius of surface 50 cylinder)^2
f22:p 61                                                       $15 keV to 63 keV
e22 1.50E-02 1.55E-02 1.60E-02 1.65E-02 1.70E-02 1.75E-02 1.80E-02 1.85E-02
     1.90E-02 1.95E-02 2.00E-02 2.05E-02 2.10E-02 2.15E-02 2.20E-02 2.25E-02
     2.30E-02 2.35E-02 2.40E-02 2.45E-02 2.50E-02 2.55E-02 2.60E-02 2.65E-02
     2.70E-02 2.75E-02 2.80E-02 2.85E-02 2.90E-02 2.95E-02 3.00E-02 3.05E-02
     3.10E-02 3.15E-02 3.20E-02 3.25E-02 3.30E-02 3.35E-02 3.40E-02 3.45E-02
     3.50E-02 3.55E-02 3.60E-02 3.65E-02 3.70E-02 3.75E-02 3.80E-02 3.85E-02
     3.90E-02 3.95E-02 4.00E-02 4.05E-02 4.10E-02 4.15E-02 4.20E-02 4.25E-02
     4.30E-02 4.35E-02 4.40E-02 4.45E-02 4.50E-02 4.55E-02 4.60E-02 4.65E-02
     4.70E-02 4.75E-02 4.80E-02 4.85E-02 4.90E-02 4.95E-02 5.00E-02 5.05E-02
     5.10E-02 5.15E-02 5.20E-02 5.25E-02 5.30E-02 5.35E-02 5.40E-02 5.45E-02
     5.50E-02 5.55E-02 5.60E-02 5.65E-02 5.70E-02 5.75E-02 5.80E-02 5.85E-02
     5.90E-02 5.95E-02 6.00E-02 6.05E-02 6.10E-02 6.15E-02 6.20E-02 6.25E-02
     6.30E-02
fs22 -50
sd22 12.56637  1                $ first number is pi*(radius of surface 50 cylinder)^2
TIR5:p 0 0 -3.0 0  0 0 1  0 0.5 0    $Transmitted Image Projection Tally
FS5 -0.5 9i 0.5                      $segments parallel to y axis
C5 -0.5 9i 0.5                       $cosine bins parallel to x-axis
f6:P 30
nps 100000000
Print
prdmp 2J 1
```

Appendix Q

Clinical Validation MCNPX Data

Unfiltered

	63	70	90	70(G)
NPS	1.00E+13	9.33E+12		1.23E+13
Entrance Dose (μGy)	733	635		883
mAs	1.02	0.71		0.70
Skin Dose (μGy) (per source particle)	4.02E-11	3.83E-11		3.98E-11
Skin Dose (μGy)	402	357		490
Energy Deposited (mJ/cm^2)	5.86	5.82		7.26
Well photons/cm^2 (per source particle)	1.55E-05	1.64E-05		1.43E-05
Well K_{air} (μGy)	69	64		79
Bckgrnd photons/cm^2 (per source particle)	1.49E-05	1.59E-05		1.38E-05
Bckgrnd K_{air} (μGy)	67	62		76
Rad Contrast	0.034	0.033		0.036

0.1 mm Copper Filtration

	63	70	90	70(G)
NPS		9.04E+12	7.20E+12	1.16E+13
Entrance Dose (μGy)		466	318	642
mAs		1.25	0.37	1.27
Skin Dose (μGy) (per source particle)		3.25E-11	2.98E-11	3.41E-11
Skin Dose (μGy)		294	214	395
Energy Deposited (mJ/cm^2)		6.33	5.90	7.64
Well photons/cm^2 (per source particle)		2.13E-05	2.70E-05	1.88E-05
Well K_{air} (μGy)		75	69	91
Bckgrnd photons/cm^2 (per source particle)		2.07E-05	2.64E-05	1.82E-05
Bckgrnd K_{air} (μGy)		73	67	88
Transmission		0.42	0.57	0.40
Rad Contrast		0.029	0.024	0.033

SdNR and FOM Calculations

kVp	Filter	Well Signal	Well Noise	Bkgrd Signal	Bkgrd Noise	SdNR	FOM_S x10^3	FOM_F	FOM_C	FOM_E
63	**Inherent**	973.5	10.5	942.2	10.4	2.1	11.0	1.0	0.0	0.8
70	**Inherent**	998.2	10.2	967.4	10.1	2.1	12.3	1.4	0.0	0.8
	Inherent +0.1mm Cu	1171.6	10.9	1138.9	10.7	2.1	15.0	1.0	0.0	0.7
90	**Inherent +0.1mm Cu**	1366.6	10.5	1334.9	10.4	2.1	20.6	3.6	0.0	0.7
70(G)	**Inherent**	1013.9	12	978	11.9	2.1	9.0	1.1	0.0	0.6
	Inherent +0.1mm Cu	1177.1	12.6	1139	12.5	2.1	11.2	0.7	0.0	0.6

Clinical Data: Carestream/Planmeca

Sensor	Entrance Dose (μGy)	kVp	Filter	Well Signal	Well Noise	Bkgrd Signal	Bkgrd Noise	SdNR (measured)	SdNR Predicted)
1	722	63	**Inherent**	898.4	12.2	869.4	11.8	1.7	2.1
2	719	63	**Inherent**	1106.8	12.4	1070.2	12.8	2.0	2.1
3	689	63	**Inherent**	1074.7	12.2	1040.2	12.3	2.0	2.0
4	761	63	**Inherent**	1175.0	14.4	1136.9	13.9	1.9	2.2
5	754	63	**Inherent**	1219.2	13.0	1184.1	13.0	1.9	2.2
AVG:	**729**			**1094.8**	**12.9**	**1060.2**	**12.8**	**1.9**	**2.1**

Sensor	Entrance Dose (μGy)	kVp	Filter	Well Signal	Well Noise	Bkgrd Signal	Bkgrd Noise	SdNR (measured)	SdNR Predicted)
1	611	70	Inherent	1022.2	12.7	993.5	13.1	1.6	2.1
2	610	70	Inherent	1182.9	12.6	1147.3	12.6	2.0	2.1
3	587	70	Inherent	1171.6	13.0	1137.0	12.7	1.9	2.0
4	614	70	Inherent	1200.3	14.2	1163.9	14.1	1.8	2.1
5	637	70	Inherent	1312.1	12.8	1274.0	13.4	2.0	2.2
AVG:	**612**			**1177.8**	**13.1**	**1143.2**	**13.2**	**1.9**	**2.1**

Sensor	Entrance Dose (μGy)	kVp	Filter	Well Signal	Well Noise	Bkgrd Signal	Bkgrd Noise	SdNR (measured)	SdNR Predicted)
1	463	70	0.1 mm Cu	1485.1	15.4	1446.2	15.3	1.8	2.1
2	459	70	0.1 mm Cu	1576.5	15.0	1534.0	15.3	2.0	2.1
3	438	70	0.1 mm Cu	1554.4	14.4	1513.7	15.0	2.0	2.1
4	430	70	0.1 mm Cu	1435.7	15.9	1396.7	15.3	1.8	2.1
5	466	70	0.1 mm Cu	1709.9	14.7	1665.9	15.0	2.1	2.1
AVG:	**451**			**1552.3**	**15.1**	**1511.3**	**15.2**	**1.9**	**2.1**

Carestream/Gendex

Sensor	Entrance Dose (μGy)	kVp	Filter	Well Signal	Well Noise	Bkgrd Signal	Bkgrd Noise	SdNR (measured)	SdNR Predicted)
5	891	70	**Inherent**	1035.7	13.2	1002.9	13.2	1.8	2.1
6	840	70	**Inherent**	936.6	11.3	910.2	11.2	1.7	2.1
7	859	70	**Inherent**	1146.9	13.3	1110.6	13.5	1.9	2.1
8	883	70	**Inherent**	1168.6	14.0	1135.4	13.5	1.7	2.1
AVG:	**868**			**1071.9**	**13.0**	**1039.8**	**12.9**	**1.8**	**2.1**

5	612	70	**0.1 mm Cu**	1503.7	17.0	1456.6	16.4	2.0	2.1
6	595	70	**0.1 mm Cu**	1303.8	12.7	1270.3	12.8	1.9	2.0
7	628	70	**0.1 mm Cu**	1698.8	16.3	1651.4	16.1	2.1	2.1
8	669	70	**0.1 mm Cu**	1665.2	16.4	1621.2	15.9	1.9	2.2
AVG:	**626**			**1542.9**	**15.6**	**1499.9**	**15.3**	**2.0**	**2.1**

Appendix R

Uncertainty Analysis

Planmeca Exposure Response Function: $E(mR) = 12.83 kVp^{2.098} cm^2 / mAs$

Entrance Air KERMA Conversion: $\frac{mAs}{SSD^2} * 8.77$

kVp	σ (kVp)	σ Coef a_1	σ Coef a_2	Total σ	E(mR) cm^2/mAs	%σ
50	1.01	0.471	0.04	7822.5	47061	17%
52	1.06	0.471	0.04	8571.5	51098	17%
55	1.12	0.471	0.04	9763.7	57479	17%
57	1.16	0.471	0.04	10608.9	61952	17%
60	1.22	0.471	0.04	11944.9	68990	17%
63	1.28	0.471	0.04	13373.0	76426	17%
66	1.34	0.471	0.04	14893.1	84262	18%
70	1.41	0.471	0.04	17060.4	95333	18%
					AVERAGE	17.2%

Gendex Exposure Response Function: K(μGy)=1258.4*mAs

Output (μGy/mAs) (20.5 cm)	σ	Detector Uncertainty	Total Uncertainty (μGy)
1258.4	144.9	62.9	158.0

%σ
13%

Carestream/Planmeca Sensor Response: $PV = 0.272 * (kVp * K_{air})^{0.977}$

Carestream/Planmeca Noise Response: $N = 0.0575 * K_{air} + 6.53$

kVp	K_{air} (μGy)	PV	σ_{PV}	$\%\sigma_{PV}$	N	σ_N	$\%\sigma_N$
50	6.1	72.8	10.7	14.7%	6.9	0.2	2.6%
50	12.3	143.8	22.1	15.4%	7.2	0.2	2.6%
50	24.5	281.6	45.2	16.1%	7.9	0.2	2.6%
50	48.5	548.9	92.1	16.8%	9.3	0.3	3.0%
50	156.0	1718.4	310.9	18.1%	15.5	0.7	4.5%
50	9.41	110.7	16.7	15.1%	7.1	0.2	2.6%
50	19.05	220.5	34.9	15.8%	7.6	0.2	2.6%
50	38.21	435.1	71.9	16.5%	8.7	0.2	2.8%
50	75.47	845.7	146.0	17.3%	10.9	0.4	3.4%
50	153.20	1688.3	305.1	18.1%	15.3	0.7	4.5%
50	9.06	106.7	16.1	15.1%	7.0	0.2	2.6%
50	18.11	209.9	33.1	15.8%	7.6	0.2	2.6%
50	35.99	410.4	67.6	16.5%	8.6	0.2	2.7%
50	71.71	804.5	138.5	17.2%	10.7	0.4	3.4%
50	113.00	1254.3	222.3	17.7%	13.0	0.5	4.0%
50	144.64	1596.1	287.4	18.0%	14.8	0.7	4.4%
50	146.40	1615.1	291.0	18.0%	14.9	0.7	4.4%
50	73.3	821.7	141.6	17.2%	10.7	0.4	3.4%
50	36.67	418.0	68.9	16.5%	8.6	0.2	2.8%
50	18.1	209.3	33.0	15.8%	7.6	0.2	2.6%
50	9.04	106.5	16.1	15.1%	7.0	0.2	2.6%
50	192.7	2112.2	387.3	18.3%	17.6	0.9	4.9%
50	96.28	1072.7	188.2	17.5%	12.1	0.5	3.8%
50	47.4	536.8	90.0	16.8%	9.3	0.3	2.9%
50	23.68	272.7	43.7	16.0%	7.9	0.2	2.6%
50	12.0	140.2	21.5	15.3%	7.2	0.2	2.6%
55	9.0	116.7	17.7	15.2%	7.0	0.2	2.6%

55	18.3	233.2	37.0	15.9%	7.6	0.2	2.6%
55	36.1	451.3	74.8	16.6%	8.6	0.2	2.7%
55	73.7	907.0	157.4	17.3%	10.8	0.4	3.4%
55	235.4	2818.6	526.6	18.7%	20.1	1.0	5.2%
55	14.12	180.6	28.2	15.6%	7.3	0.2	2.6%
55	28.93	363.9	59.4	16.3%	8.2	0.2	2.7%
55	57.51	711.8	121.5	17.1%	9.8	0.3	3.1%
55	115.20	1402.7	250.4	17.9%	13.2	0.5	4.0%
55	230.00	2755.4	514.0	18.7%	19.8	1.0	5.1%
55	13.71	175.5	27.3	15.6%	7.3	0.2	2.6%
55	27.42	345.4	56.2	16.3%	8.1	0.2	2.6%
55	53.91	668.3	113.6	17.0%	9.6	0.3	3.0%
55	109.20	1331.4	236.9	17.8%	12.8	0.5	3.9%
55	171.10	2064.1	377.9	18.3%	16.4	0.8	4.7%
55	220.70	2646.6	492.4	18.6%	19.2	1.0	5.1%
55	110.2	1343.3	239.1	17.8%	12.9	0.5	4.0%
55	54.86	679.8	115.7	17.0%	9.7	0.3	3.1%
55	27.5	345.7	56.3	16.3%	8.1	0.2	2.6%
55	13.55	173.5	27.0	15.6%	7.3	0.2	2.6%
55	225.20	2699.2	502.9	18.6%	19.5	1.0	5.1%
55	113.7	1384.9	247.0	17.8%	13.1	0.5	4.0%
55	56.00	693.6	118.2	17.0%	9.7	0.3	3.1%
55	29.0	364.3	59.5	16.3%	8.2	0.2	2.7%
55	14.78	188.9	29.6	15.6%	7.4	0.2	2.6%
60	7.9	111.6	16.9	15.1%	7.0	0.2	2.6%
60	15.7	218.7	34.5	15.8%	7.4	0.2	2.6%
60	31.8	434.9	71.9	16.5%	8.4	0.2	2.7%
60	63.4	852.9	147.4	17.3%	10.2	0.3	3.2%
60	202.7	2651.6	493.4	18.6%	18.2	0.9	4.9%
60	20.13	278.0	44.6	16.0%	7.7	0.2	2.6%
60	40.29	547.5	91.9	16.8%	8.8	0.2	2.8%
60	80.97	1082.3	190.0	17.6%	11.2	0.4	3.5%
60	162.50	2136.8	392.1	18.3%	15.9	0.7	4.6%
60	19.12	264.4	42.3	16.0%	7.6	0.2	2.6%
60	38.37	522.0	87.3	16.7%	8.7	0.2	2.8%
60	76.17	1019.6	178.3	17.5%	10.9	0.4	3.4%
60	152.90	2013.4	368.0	18.3%	15.3	0.7	4.5%
60	240.20	3129.6	588.6	18.8%	20.3	1.1	5.2%

60	242.9	3163.9	595.5	18.8%	20.5	1.1	5.2%
60	120.60	1597.0	287.5	18.0%	13.5	0.6	4.1%
60	59.9	806.5	138.8	17.2%	10.0	0.3	3.2%
60	30.65	419.2	69.1	16.5%	8.3	0.2	2.7%
60	14.9	207.3	32.6	15.7%	7.4	0.2	2.6%
60	258.0	3355.8	634.1	18.9%	21.4	1.1	5.3%
60	126.80	1677.1	302.9	18.1%	13.8	0.6	4.2%
60	63.4	852.6	147.3	17.3%	10.2	0.3	3.2%
60	31.97	436.8	72.2	16.5%	8.4	0.2	2.7%
60	16.1	223.6	35.4	15.8%	7.5	0.2	2.6%
66	4.7	73.4	10.8	14.7%	6.8	0.2	2.6%
66	11.3	173.6	27.0	15.6%	7.2	0.2	2.6%
66	22.4	338.1	55.0	16.3%	7.8	0.2	2.6%
66	43.8	651.2	110.5	17.0%	9.0	0.3	2.9%
66	87.8	1285.2	228.1	17.8%	11.6	0.4	3.6%
66	221.4	3172.1	597.2	18.8%	19.3	1.0	5.1%
66	8.24	127.5	19.4	15.3%	7.0	0.2	2.6%
66	17.10	260.2	41.6	16.0%	7.5	0.2	2.6%
66	34.21	512.2	85.6	16.7%	8.5	0.2	2.7%
66	69.19	1018.8	178.1	17.5%	10.5	0.3	3.3%
66	139.30	2017.7	368.9	18.3%	14.5	0.6	4.3%
66	218.00	3124.5	587.6	18.8%	19.1	1.0	5.0%
66	8.21	127.0	19.4	15.2%	7.0	0.2	2.6%
66	16.61	252.9	40.3	15.9%	7.5	0.2	2.6%
66	33.38	500.0	83.4	16.7%	8.4	0.2	2.7%
66	67.85	999.6	174.5	17.5%	10.4	0.3	3.3%
66	134.70	1952.6	356.2	18.2%	14.3	0.6	4.3%
66	212.80	3051.7	573.1	18.8%	18.8	0.9	5.0%
66	217.00	3110.5	584.8	18.8%	19.0	1.0	5.0%
66	107.5	1566.6	281.7	18.0%	12.7	0.5	3.9%
66	53.68	795.2	136.8	17.2%	9.6	0.3	3.0%
66	26.3	395.9	65.0	16.4%	8.0	0.2	2.6%
66	15.59	237.8	37.8	15.9%	7.4	0.2	2.6%
66	177.0	2549.3	473.2	18.6%	16.7	0.8	4.7%
66	89.00	1302.8	231.5	17.8%	11.6	0.4	3.6%
66	45.0	669.4	113.8	17.0%	9.1	0.3	2.9%
66	23.04	348.2	56.7	16.3%	7.9	0.2	2.6%
70	5.9	96.9	14.5	15.0%	6.9	0.2	2.6%

70	13.5	218.1	34.5	15.8%	7.3	0.2	2.6%
70	26.3	420.1	69.3	16.5%	8.0	0.2	2.6%
70	53.1	833.2	143.8	17.3%	9.6	0.3	3.0%
70	106.3	1640.8	295.9	18.0%	12.6	0.5	3.9%
70	267.3	4038.2	772.1	19.1%	21.9	1.2	5.4%
70	20.56	329.9	53.6	16.2%	7.7	0.2	2.6%
70	41.80	659.7	112.1	17.0%	8.9	0.3	2.8%
70	83.91	1302.7	231.4	17.8%	11.4	0.4	3.6%
70	167.94	2565.1	476.3	18.6%	16.2	0.7	4.6%
70	263.26	3978.6	760.0	19.1%	21.7	1.2	5.3%
70	10.39	169.4	26.3	15.5%	7.1	0.2	2.6%
70	20.33	326.3	52.9	16.2%	7.7	0.2	2.6%
70	40.55	640.5	108.6	17.0%	8.9	0.2	2.8%
70	81.3	1263.0	223.9	17.7%	11.2	0.4	3.5%
70	163.3	2496.4	462.7	18.5%	15.9	0.7	4.6%
70	255.7	3867.6	737.4	19.1%	21.2	1.1	5.3%
70	204.1	3103.1	583.3	18.8%	18.3	0.9	4.9%
70	101.3	1565.7	281.5	18.0%	12.4	0.5	3.8%
70	51.80	813.4	140.1	17.2%	9.5	0.3	3.0%
70	25.0	398.9	65.6	16.4%	8.0	0.2	2.6%
70	217.8	3306.3	624.1	18.9%	19.1	1.0	5.0%
70	108.1	1668.3	301.2	18.1%	12.7	0.5	3.9%
70	54.8	859.4	148.6	17.3%	9.7	0.3	3.1%
70	28.1	447.6	74.1	16.6%	8.1	0.2	2.6%
			AVG:	**17%**			**3.4%**

Carestream/Gendex Signal Response: $PV = 13.3 * K_{air} - 33.7$

Carestream/Gendex Noise Response: $N = 0.047 * K_{air} + 8.36$

K_{air} (μGy)	PV	σ_{PV}	$\%\sigma_{PV}$	N	σ_N	$\%\sigma_N$
36.5	452.4	67.5	15%	10.1	0.7	6.7%
56.5	718.5	79.9	11%	11.0	0.7	6.4%
58.9	750.2	81.6	11%	11.1	0.7	6.4%
67.9	870.3	88.3	10%	11.5	0.7	6.4%
68.7	881.0	88.9	10%	11.6	0.7	6.4%
78.4	1009.9	96.5	10%	12.0	0.8	6.3%
113.4	1476.1	126.2	9%	13.6	0.9	6.4%
120.7	1573.8	132.8	8%	14.0	0.9	6.4%
125.3	1634.5	136.9	8%	14.2	0.9	6.4%
128.4	1675.8	139.7	8%	14.3	0.9	6.4%
146.1	1912.0	156.0	8%	15.2	1.0	6.5%
158.8	2080.6	167.8	8%	15.8	1.0	6.6%
171.3	2247.0	179.5	8%	16.3	1.1	6.7%
172.1	2258.2	180.3	8%	16.4	1.1	6.7%
176.7	2318.9	184.6	8%	16.6	1.1	6.7%
200.1	2630.4	206.8	8%	17.7	1.2	6.8%
227.2	2991.2	232.9	8%	19.0	1.3	7.0%
235.0	3095.1	240.4	8%	19.3	1.4	7.1%
249.6	3289.5	254.5	8%	20.0	1.4	7.1%
250.1	3295.6	254.9	8%	20.0	1.4	7.1%
280.0	3694.8	284.1	8%	21.4	1.6	7.3%
		AVG:	**8.9%**			**6.7%**

Carestream/Planmeca SdNR and FOM_S

kVp	Filter	SdNR	σ SdNR	%σ SdNR	Skin Dose (μGy)	FOM_S	$\sigma_{FOM(S)}$	$\%\sigma_{FOM(S)}$
50	Inherent	2	0.1	4%	725	5.52	0.57	10%
50	Inherent +0.1mm Cu	2	0.1	4%	470	8.50	0.91	11%
50	Inherent +0.2mm Cu	2	0.1	4%	391	10.23	1.14	11%
52	Inherent	2	0.1	4%	667	5.99	0.64	11%
52	Inherent +0.1mm Cu	2	0.1	4%	441	9.06	1.01	11%
52	Inherent +0.2mm Cu	2	0.1	5%	367	10.90	1.27	12%
55	Inherent	2	0.1	4%	585	6.84	0.76	11%
55	Inherent +0.1mm Cu	2	0.1	5%	400	10.01	1.18	12%
55	Inherent +0.2mm Cu	2	0.1	5%	332	12.04	1.48	12%
57	Inherent	2	0.1	5%	544	7.35	0.85	12%
57	Inherent +0.1mm Cu	2	0.1	5%	375	10.67	1.30	12%
57	Inherent +0.2mm Cu	2	0.1	5%	318	12.60	1.60	13%
60	Inherent	2	0.1	5%	485	8.24	0.99	12%
60	Inherent +0.1mm Cu	2	0.1	5%	339	11.79	1.50	13%
60	Inherent +0.2mm Cu	2	0.1	6%	296	13.51	1.80	13%
63	Inherent	2	0.1	5%	451	8.87	1.12	13%
63	Inherent +0.1mm Cu	2	0.1	6%	318	12.56	1.67	13%
63	Inherent +0.2mm Cu	2	0.1	6%	280	14.28	2.01	14%
66	Inherent	2	0.1	6%	424	9.43	1.24	13%
66	Inherent +0.1mm Cu	2	0.1	6%	298	13.42	1.87	14%
66	Inherent +0.2mm Cu	2	0.1	6%	264	15.13	2.22	15%
70	Inherent	2	0.1	6%	387	10.34	1.44	14%
70	Inherent +0.1mm Cu	2	0.1	6%	279	14.31	2.11	15%
70	Inherent +0.2mm Cu	2	0.1	7%	246	16.27	2.52	15%
75	Inherent	2	0.1	7%	341	11.72	1.74	15%
75	Inherent +0.1mm Cu	2	0.1	7%	251	15.97	2.50	16%
75	Inherent +0.2mm Cu	2	0.1	7%	227	17.61	2.91	17%
80	Inherent	2	0.1	7%	305	13.12	2.05	16%
80	Inherent +0.1mm Cu	2	0.2	8%	234	17.11	2.85	17%

80	Inherent +0.2mm Cu	2	0.2	8%	212	18.87	3.33	18%
85	Inherent	2	0.1	7%	273	14.63	2.38	16%
85	Inherent +0.1mm Cu	2	0.2	8%	215	18.56	3.24	17%
85	Inherent +0.2mm Cu	2	0.2	8%	191	20.96	3.81	18%
90	Inherent	2	0.2	8%	250	16.00	2.72	17%
90	Inherent +0.1mm Cu	2	0.2	8%	196	20.46	3.68	18%
90	Inherent +0.2mm Cu	2	0.2	9%	178	22.45	4.23	19%
			AVG:	**6.0%**				**14.0%**

Carestream/Planmeca FOM_E and FOM_F

kVp	Filter	En Dep (mJ/cm^2)	FOM_E	σFOM(E)	%σ FOM(E)	mAs	FOM_F	σFOM(F)	%σ FOM(F)
50	Inherent	7.00	0.57	0.05	9%	2.78	0.282	0.036	13%
50	Inherent +0.1mm Cu	5.99	0.67	0.06	9%	5.20	0.232	0.030	13%
50	Inherent +0.2mm Cu	5.76	0.69	0.07	10%	8.9	0.163	0.021	13%
52	Inherent	6.75	0.59	0.05	9%	2.34	0.349	0.045	13%
52	Inherent +0.1mm Cu	5.90	0.68	0.07	10%	4.39	0.282	0.037	13%
52	Inherent +0.2mm Cu	5.69	0.70	0.07	10%	7.3	0.205	0.026	13%
55	Inherent	6.37	0.63	0.06	10%	1.79	0.493	0.065	13%
55	Inherent +0.1mm Cu	5.77	0.69	0.07	10%	3.40	0.380	0.050	13%
55	Inherent +0.2mm Cu	5.58	0.72	0.08	11%	5.4	0.288	0.038	13%
57	Inherent	6.18	0.65	0.07	10%	1.54	0.596	0.080	13%
57	Inherent +0.1mm Cu	5.65	0.71	0.08	11%	2.78	0.479	0.064	13%
57	Inherent +0.2mm Cu	5.57	0.72	0.08	11%	4.4	0.359	0.047	13%

60	Inherent	5.89	0.68	0.07	11%	1.21	0.807	0.111	14%
60	Inherent +0.1mm Cu	5.47	0.73	0.08	11%	2.06	0.678	0.093	14%
60	Inherent +0.2mm Cu	5.55	0.72	0.09	12%	3.2	0.495	0.067	13%
63	Inherent	5.83	0.69	0.08	11%	1.00	0.997	0.142	14%
63	Inherent +0.1mm Cu	5.42	0.74	0.09	12%	1.66	0.853	0.120	14%
63	Inherent +0.2mm Cu	5.54	0.72	0.09	13%	2.5	0.633	0.088	14%
66	Inherent	5.73	0.70	0.08	12%	0.85	1.199	0.176	15%
66	Inherent +0.1mm Cu	5.37	0.74	0.10	13%	1.34	1.074	0.158	15%
66	Inherent +0.2mm Cu	5.53	0.72	0.10	14%	2.0	0.806	0.116	14%
70	Inherent	5.57	0.72	0.09	13%	0.67	1.557	0.243	16%
70	Inherent +0.1mm Cu	5.35	0.75	0.10	14%	1.05	1.386	0.216	16%
70	Inherent +0.2mm Cu	5.47	0.73	0.11	14%	1.5	1.082	0.164	15%
75	Inherent	5.41	0.74	0.10	14%	0.50	2.209	0.386	17%
75	Inherent +0.1mm Cu	5.21	0.77	0.11	15%	0.65	2.326	0.426	18%
75	Inherent +0.2mm Cu	5.46	0.73	0.11	16%	0.9	1.830	0.322	18%
80	Inherent	5.20	0.77	0.11	15%	0.39	3.019	0.603	20%
80	Inherent +0.1mm Cu	5.20	0.77	0.12	16%	0.50	3.018	0.633	21%
80	Inherent +0.2mm Cu	5.43	0.74	0.12	17%	0.7	2.451	0.496	20%
85	Inherent	4.99	0.80	0.12	15%	0.30	4.073	0.952	23%
85	Inherent +0.1mm Cu	5.09	0.79	0.13	17%	0.39	3.996	0.990	25%
85	Inherent +0.2mm Cu	5.15	0.78	0.13	17%	0.5	3.484	0.840	24%
90	Inherent	4.84	0.83	0.13	16%	0.24	5.258	1.460	28%

90	**Inherent +0.1mm Cu**	4.85	0.82	0.14	17%	0.30	5.393	1.623	30%
90	**Inherent +0.2mm Cu**	5.03	0.80	0.14	18%	0.4	4.559	1.313	29%
				AVG:	**12.8%**				**17%**

Carestream/Gendex SdNR and FOM_S

kVp	Filter	SdNR	σ SdNR	%σ SdNR	Skin Dose (μGy)	FOM_S	$\sigma_{FOM(S)}$	$\%\sigma_{FOM(S)}$
70	**Inherent**	2	0.1	3%	573	7.0	0.95	14%
70	**Inherent +0.1mm Cu**	2	0.1	3%	418	9.6	1.32	14%
70	**Inherent +0.2mm Cu**	2	0.1	3%	357	11.2	1.56	14%
			AVG:	**3%**				**14%**

Carestream/Gendex FOM_E and FOM_F

kVp	Filter	En Dep (mJ/cm^2)	FOM_E	σFOM(E)	%σ FOM(E)	mAs	FOM_F	σFOM(F)	%σ FOM(F)
70	**Inherent**	7.48	0.53	0.04	7%	0.72	0.984	0.142	14%
70	**Inherent +0.1mm Cu**	7.16	0.56	0.04	7%	1.18	0.822	0.116	14%
70	**Inherent +0.2mm Cu**	7.11	0.56	0.04	7%	1.6	0.692	0.097	14%
				AVG:	**7%**				**14%**

Effective Dose Estimate

DAP to effective dose conversion coefficients for bitewing radiography were roughly estimated with a kVp correction factor calculated using the DAP to effective dose conversion factors published by Looe, et al (2008) for panoramic radiography (Panoramic unit).

1. A linear fit to the published data was performed:

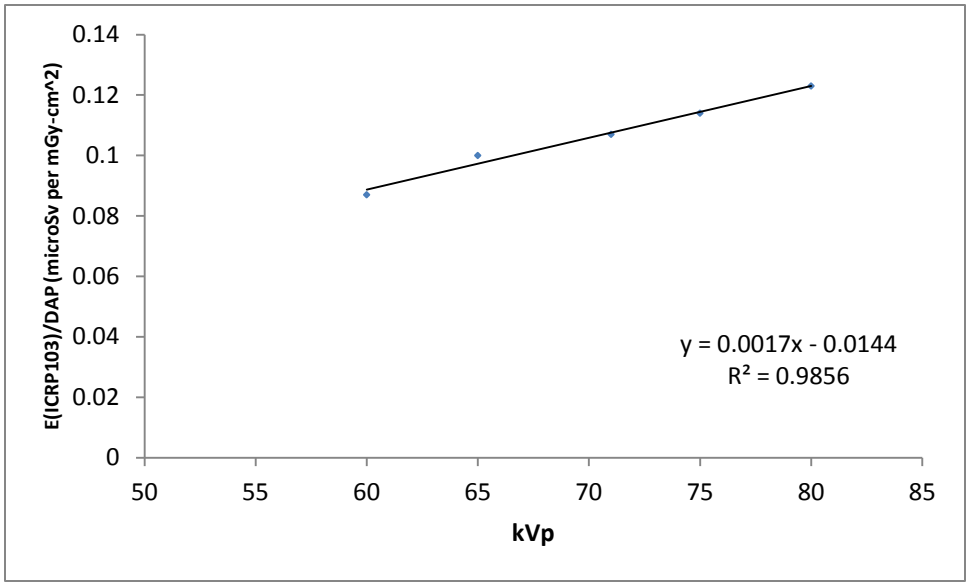

2. An estimate of the bitewing coefficient at 63, 70, and 90 kVp was calculated:

$$E(BW) = \frac{0.0017 * kVp - 0.0144}{E(Pano)_{65kVp}} * E(BW)_{65kVp}$$

3. The uncertainty in the estimated coefficient was calculated:

$$\sigma_{E(BW)} = \sqrt{\left[\left(\frac{a_1 * E_{\text{int } ra}}{E_{Pano}}\right)\sigma_{kVp}\right]^2 + \left[\left(\frac{E_{Intra} * (a_2 - a_1 * kVp)}{E_{Pano}^2}\right)\sigma_{E(Pano)}\right]^2 + \left[\left(\frac{a_1 * kVp - a_2}{E_{Pano}}\right)\sigma_{E(Intra)}\right]^2}$$

Where:

Effective Dose Estimate			
kVp	Peak Kilovoltage	Multiple Values (kVp)	Table 4-2
σ_{kVp}	Uncertainty in Peak Kilovoltage	Multiple Values (kVp)	Table 4-2
E(Pan)	Estimated E(ICRP103/DAP) for Panoramic radiography at 65 kVp	0.100 ($\mu Sv\ mGy^{-1}cm^{-2}$)	Looe, et al
σ E(Pan)	E(Pan) estimated uncertainty	0.02 ($\mu Sv\ mGy^{-1}cm^{-2}$)	Looe, et al
E(Intra)	Estimated E(ICRP103/DAP) for bitewing ("back") radiography at 65 kVp	0.107 ($\mu Sv\ mGy^{-1}cm^{-2}$)	Looe, et al
σ E(Intra)	Coefficient a_2 Standard Error	0.03 ($\mu Sv\ mGy^{-1}cm^{-2}$)	Looe, et al
a_1	Coefficient (X Variable)	0.0017 (Constant)	
σ_{a1}	Coefficient a_1 Standard Error	4E-19 (~0) Not considered an uncertainty for analysis	
a_2	Coefficient (Intercept)	-0.0144	
σ_{a2}	Coefficient a_2 Standard Error	3E-17 (~0) Not considered an uncertainty for analysis	

kVp	σ (kVp)	E(Pan) 65 kVp ($\mu Sv\ mGy^{-1}cm^{2}$)	σ E(Pan)	E(Intra) 65 kVp ($\mu Sv\ mGy^{-1}cm^{2}$)	σ E(Intra)	E(BW) ($\mu Sv\ mGy^{-1}cm^{2}$)	σ(E)	%σ(E)
63	1.34	0.100	0.020	0.107	0.030	0.103	0.034	33%
70	1.49	0.100	0.020	0.107	0.030	0.116	0.041	35%
90	1.92	0.100	0.020	0.107	0.030	0.154	0.054	35%

References

American Association of Physicists in Medicine, *Acceptance Testing and Quality Control of Photostimulable Storage Phosphor Imaging Systems, Report of AAPM Task Group 10* (College Park, MD: American Association of Physicists in Medicine, 2006).

American Association of Physicists in Medicine, *An Exposure Indicator for Digital Radiography, Report of AAPM Task Group 116* (College Park, MD: American Association of Physicists in Medicine, 2009).

American College of Radiology, *The Mammography Quality Control Manual, 1999,* (Reston, VA: American College of Radiology, 1999).

American College of Radiology, *CT Accreditation Phantom Instructions,* 2013, (Reston VA: American College of Radiology, 2013).

Araki, K., Endo, A., and Okano, T., "An Objective Comparison of Four Digital Intra-Oral Radiographic Systems: Sensitometric Properties and Resolution", Dentomaxillofacial Radiology, 29, 2000, pp. 76-80.

Attaelmanan, A.G., Borg, E., and Gröndahl, H., "Assessments of the Physical Performance of 2 Generations of 2 Direct Digital Intraoral Sensors", Oral Surgery Oral Medicine Oral Pathology Oral Radiology Endodontics, 88(4), 1999, pp. 517-523.

Attaelmanan, A.G., Borg, E., and Gröndahl, H., "Signal-to-Noise Ratios of 6 Intraoral Sensors", Oral Surgery Oral Medicine Oral Pathology Oral Radiology Endodontics, 91(5), 2001, pp. 611-615.

Borg, E., Attaelmanan, A.G., and Gröndahl, H., "Image Plate Systems Differ in Physical Performance", Oral Surgery Oral Medicine Oral Pathology Oral Radiology Endodontics, 89(1), 2000, pp. 118-124.

Brettle, D.S., et al, "The Imaging Performance of a Storage Phosphor System for Dental Radiography", The British Journal of Radiology 69, 1996, pp. 256-261.

Brian, J.N., and Williamson, G.F., "Digital Radiography in Dentistry: A Survey of Indiana Dentists:, Dentomaxillofacial Radiology, 36, 2007, pp. 18-23.

Bushberg, J.T., et al, *The Essential Physics of Medical Imaging,* 2nd Edition, (Philadelphia: Lippincott Williams and Wilkins, 2002).

Carr, R., "Simulated Annealing", MathWorld—A Wolfram Web Resource, created by Eric W. Weisstein. (2009) Available on-line at: http://mathworld.wolfram.com/SimulatedAnnealing.html

Coklica, V., Brudevold, F., and Amdur, B.H., "The Distribution and Composition of Density Fractions From Human Crown Dentine", Archives of Oral Biology, 14, 1969, pp. 451-460.

Couture, R.A., "Comments on Noise and Resolution of the DenOptix Radiography System", Oral Surgery Oral Medicine Oral Pathology Oral Radiology Endodontics, 95(6), 2003, pp. 746-751.

Cranley, K., et al., *Catalogue of Diagnostic X-ray Spectra and Other Data,* Report #78, (York, United Kingdom: Institute of Physics and Engineering in Medicine), 1997).

DeMarco, J.J., Solberg, T.D., and Smathers, J.B., "A CT-based Monte Carlo Simulation for Dosimetry Planning and Analysis," *Medical Physics,* vol 25, no. 1 (January 1998), pp. 1-11.

Dobbins, J.T., et al., "Chest Radiography: Optimization of X-ray Spectrum for Cesium Iodide-Amorphous Silicon Flat-Panel Detector", Radiology 226, 2003, pp. 221-230.

ECRI Institute, *Radiographic Units, Dental; Radiography Systems, Digital, Dental,* (Plymouth Meeting, PA: ECRI), July 2002.

Farman, A.G., et al, "Computed Dental Radiography: Evaluation of a New Charge-Coupled Device-Based Intraoral Radiographic System", Quintessence International, 26(6), 1995, pp. 399-404.

Farman, A.G., and Farman, T.T., "A Comparison of 18 Different X-Ray Detectors Currently Used in Dentistry", Oral Surgery Oral Medicine Oral Pathology Oral Radiology Endodontics, 99(4), 2005, pp. 485-489.

Fensin, M.L., et al, *MCNPX Introductory Workshop,* Document# LA-UR-5258 (Computational Analysis and Simulation Group), (Los Alamos, NM: Los Alamos National Laboratory, 2007)

Freund, R., "The Steepest Descent Algorithm for Unconstrained Optimization and a Bi-section Line Search Method", (Boston: Massachusetts Institute of Technology), February 2004.

Geijer, H., et al, "Image Quality vs Radiation Dose for a Flat-Panel Amorphous Silicon Detector: A Phantom Study", European Radiology 11, 2001, pp. 1704-1709.

Geijer, H., "Radiation Dose and Image Quality in Diagnostic Radiology: Optimization of the Dose-Image Quality Relationship with Clinical Experience from Scoliosis Radiography, Coronary Intervention, and a Flat-Panel Digital Detector", Acta Radiologica Supplement 43(427), 2002, pp. 1-43

Gendex Corporation, *GX-770 Intra-Oral X-Ray System User Manual,* (Milwaukee, WI, Gendex Corporation, no publication date).

General Electric Medical Systems, Technical Publication 46-014427, Revision 9: *Tube Ratings Maxiray 100: 50 and 60 Hz,* (Milwaukee, WI: General Electric Co.), 1990).

Gutierrez-Salazar, M., and Reyes-Gasga, J., "Microhardness and Chemical Composition of Human Tooth", Materials Research, 6(3), 2003, pp. 367-373.

Hamer, O.W., et al, "Contrast-Detail Phantom Study for X-Ray Spectrum Optimization Regarding Chest Radiography Using a Cesium Iodide-Amorphous Silicon Flat-Panel Detector", Investigational Radiology 39(10), 2004, pp. 610-618.

Harpen, M.D., "A Mathematical Spread Sheet Application for Production of Entrance Skin Exposure Nomograms", Medical Physics, 23(2), 1996, pp. 241-242.

Hasegawa, B. H., *Medical X-Ray Imaging,* 2nd Edition, (Madison, WI: Medical Physics Publishing, 1991).

Hellén-Halme, K., "Effect of Two X-Ray Tube Voltages on Detection of Approximal Caries in Detection of Digital Radiographs. An In Vitro Study", Clinical Oral Investigations, 15, 2011, pp. 209-213.

Hendricks, J.S., et al, *MCNPX, Version 26C,* Report # LA-UR-06-7991 (Los Alamos, NM: Los Alamos National Laboratory, 2006).

Hubbell, J.H., and Seltzer, S.M., Tables of X-Ray Mass Attenuation Coefficients and Mass Energy-Absorption Coefficients from 1 keV to 20 MeV for elements $Z = 1$ to 92 and 48 Additional Substances of Dosimetric Interest, Gaithersburg, MD: National Institute of Standards and Technology), 1996). Available online at: http://physics.nist.gov/PhysRefData/XrayMassCoef/tab4.html

Huda, W., et al, "Comparison of a Photostimulable Phosphor System with Film for Dental Radiology", Oral Surgery Oral Medicine Oral Pathology Oral Radiology Endodontics 83(6), 1997, pp. 725-731.

International Commission on Radiation Units and Measurements, *Tissue Substitutes in Radiation Dosimetry and Measurement, Report #44,* (Bethesda, MD: ICRU, 1989).

Jansson, M., et al, "Reducing Dose in Urography While Maintaining Image Quality—A Comparison of Storage Phosphor Plates and a Flat-Panel Detector", European Radiology 16, 2006, pp. 221-226.

Jones, A.K., "Dose Versus Image Quality in Pediatric Radiology: Studies Using a Tomographic Newborn Physical Phantom with an Incorporated Dosimetry System", Dissertation presented to the Graduate School of the University of Florida in Partial Fulfillment of the Requirements for the Degree of Doctor of Philosophy, (University of Florida: Jones), 2006.

Kaeppler, et al. "Factors Influencing the Absorbed Dose in Intraoral Radiology", Dentomaxillofacial Radiology, 36(8), 2007, pp. 506-513.

Knoll, G.F., *Radiation Detection and Measurement,* 3rd Edition, (Hoboken, NJ: John Wiley & Sons, Inc., 2000).

Ljungberg, M., Strand, S.E., and King, M.A., *Monte Carlo Calculations in Nuclear Medicine,* (Philadelphia: Institute of Physics Publishing, 1998).

Looe, H.K., et al, "Conversion Coefficients for the Estimation of Effective Doses in Intraoral Radiology From Dose-Area Product Values", Radiation Protection Dosimetry, 131(3), 2008, pp. 365-373.

Manson-Hing, L.R., "An Investigation of the Roentgenographic Contrast of Enamel, Dentine, and Aluminum", Oral Surgery Oral Medicine Oral Pathology 14(12), 1961, pp. 1456-1472.

Månsson, L.G., "Methods for the Evaluation of Image Quality: A Review". Radiation Protection Dosimetry 90(1-2), 2000, pp. 89-99.

McDavid, et al. "The Intrex-A Constant-Potential X-Ray Unit for Periapical Dental Radiography", Oral Surgery 53, 1982, pp. 433-436.

Miyajima, S., "Thin CdTe Detector in Diagnostic X-Ray Spectroscopy", Medical Physics 30(5), 2003, pp. 771-777.

Mouyen F., Benz C., Sonnabend E, Lodter JP. "Presentation and Physical Evaluation of RadioVisioGraphy". Oral Surgery Oral Medicine Oral Patholology Oral Radiology Endodontics 68(2), 1989, pp. 238–42.

National Council on Radiation Protection and Measurements, *Report #172: Reference Levels and Achievable Doses in Medical and Dental Imaging: Recommendations for the United States*. (Bethesda: NCRP, 2012)

Ohio State University College of Dentistry, "Radiographic Caries Identification", (available on-line at: http://dent.osu.edu/Instructional-Resources/RadiologyCarie)

Pelowitz, D. (editor), *MCNPX™ User's Manual, Version 2.5.0,* Report # LA-CP-05-0369 (Los Alamos, NM: Los Alamos National Laboratory, 2005)

Pitcher, C.D., "Quantitative Metrics to Evaluate Image Quality for Computed Radiographic Images", Dissertation presented to the Graduate School of the University of Florida in Partial Fulfillment of the Requirements for the Degree of Doctor of Philosophy, (University of Florida: Pitcher), 2004.

Radcal 9095, (Monrovia, CA: Radcal Corporation, 2004).

Redus, B., "Efficiency of Amptek XR-100T-CdTe and –CZT Detectors Application Note ANCZT-1 Rev. 2", (Amptek, Inc. December 13, 2002).

Redus, B., "CdTe Measurement of X-Ray Tube Spectra: Escape Events Application Note ANCDTE1 Rev A1", (Amptek, Inc., February 4, 2008).

Samei, E., et al., "A Framework for Optimising the Radiographic Technique in Digital X-Ray Imaging", Radiation Protection Dosimetry 114(1-3), 2005, pp. 320-229.

Sandborg, M., Carlsson, C.A., and Carlson, G.A., "Shaping X-Ray Spectra with Filters in X-Ray Diagnostics", Medical and Biological Engineering and Computing 32, 1994, pp. 384-390.

Shibuya, H., Nishikawa, K., and Kuroyanagi, K., "Effect of K-shell Absorption Edge Filters on Image Quality in Digital Intraoral Radiography", Oral Surgery Oral Medicine Oral Pathology 90(3), 2000, pp. 377-384.

Shultis, J.K., and Faw, R.E., *Radiation Shielding,* (La Grange Park, IL: American Nuclear Society, Inc., 2000).

Seibert, J.A., "Digital Radiography: Image Quality and Radiation Dose", Digital Radiography 95(5), 2008, pp. 586-598.

Smith, T.M., et al, "Modern Human Molar Enamel Thickness and Enamel-Dentine Junction Shape", Archives of Oral Biology 51, 2006, pp. 974-995.

Sogur, E., et al, "Effect of Tube Potential and Image Receptor on the Detection of Natural Proximal Caries in Primary Teeth", Clinical Oral Investigations 15, 2011, pp. 901-907.

Stamatakis, H.C., Welander, U., and McDavid, W.D., "Physical Properties of a Photostimulable Phosphor System for Intra-Oral Radiography", Dentomaxillofacial Radiology 29, 2000, pp. 28-34.

Taylor, J.R., *An Introduction to Error Analysis: The Study of Uncertainties in Physical Measurements,* 2nd Edition, (Sausalito, CA: University Science Books, 1997)

Thijssen, M.A.O., et al, "A Definition of Image Quality: The Image Quality Figure", in BIR Report 20: Optimization of Image Quality and Patient Exposure in Diagnostic Radiology 1989, pp. 29-34.

Thilander-Klang, A, and Helmrot, E., "Methods of Determining the Effective Dose in Dental Radiology", Radiation Protection Dosimetry, 139(1), 2010, pp. 306-309.

Ullman, G., "Quantifying Image Quality in Diagnostic Radiology Using Simulation of the Imaging System and Model Observers", Linköping University Medical Dissertations No. 1050, (Linköping University: Ullman), 2008.

Van der Stelt, P.F., "Filmless Imaging: The Uses of Digital Radiography in Dental Practice", Journal of the American Dental Association 136, 2005, pp. 1379-1387.

Wakoh, M., et al., "Perceptibility of Defects in an Aluminum Test Object: A Comparison of the RVG-S and First Generation VIXA Systems With and Without Added Niobium Filtration", Dentomaxillofacial Radiology, 24(4), 1995, pp. 211-214.

Waters, L.S., et al, "The MCNPX Radiation Transport Code", American Institute of Physics Conference Proceedings, 896, 2007, pp. 81-90.

Welander, U., et al., “Resolution as Defined by Line Spread and Modulation Transfer Functions for Four Digital Intraoral Radiographic Systems”, Oral Surgery Oral Medicine Oral Pathology Oral Radiology Endodontics, 78(1), 1994, pp. 109-115.

Welander, U., et al, “Absolute Measures of Image Quality for the Sens-A-Ray Direct Digital Intraoral Radiography System”, Oral Surgery Oral Medicine Oral Pathology Oral Radiology Endodontics, 80(3), 1995, pp. 345-350.

Weidmann, S.M., Weatherell, J.A., and Hamm, S.M., “Variations of Enamel Density in Sections of Human Teeth”, Archives of Oral Biology, 12, 1967, pp. 85-97.

Williams, M.B., et al., “Optimization of Exposure Parameters in Full Field Digital Mammography”, Medical Physics 35(6), 2008, pp. 2414-2423.

Willner, M., et al, “Quantitative X-Ray Phase-Contrast Computed Tomography at 82 keV”, Optics Express, 21(4), 2013, pp. 4155-4166.

Workman, A. and Brettle, D.S. “Physical Performance Measures of Radiographic Imaging Systems”, Dentomaxillofacial Radiology 26, 1997, pp. 139-146.

Yaffe, M.J., and Rowlands, J.A., “X-ray Detectors for Digital Radiography”, Physics in Medicine and Biology, 42, 1997, pp. 1-39.

Yoshiura, K., et al., “Physical Evaluation of a System for Direct Digital Intra-Oral Radiography Based on a Charge-Coupled Device”, Dentomaxillofacial Radiology 28, 1999, pp. 277-283.

Zong, W.G., Kang, S.L., and Park, Y., “Application of Harmony Search to Vehicle Routing”, American Journal of Applied Sciences, 2(12), 2005, pp. 1552-1557

Vita

Kelli Silverstrim was born in Kendallville, Indiana. She graduated from East Noble High School in 1982 and attended Manchester College and Purdue University before entering the United States Air Force in 1984. Kelli graduated Summa Cum Laude with a Bachelor of Science in Radiologic Technology from Midwestern State University in 1987. She obtained a Master of Science in Radiologic Science from Midwestern State University in 2001 and a Master of Science in Engineering from The University of Texas at Austin in 2008. Kelli has remained on active duty since 1984, working as a radiologic technologist, diagnostic medical sonographer, radiation therapist, and medical dosimetrist before becoming a medical health physicist in 2000. She is a diplomate of the American Board of Radiology (diagnostic medical physics), a certified medical dosimetrist (Medical Dosimetrist Certification Board), a registered diagnostic medical sonographer (American Registry for Diagnostic Medical Sonography), and a registered radiologic technologist in both radiography and radiation therapy (American Registry of Radiologic Technologists). Kelli is retiring from the Air Force July 1st, 2014, and will be working as a medical physicist with a private consulting group.

Permanent e-mail address: kelli.silverstrim@gmail.com

This dissertation was typed by Kelli J. Silverstrim.